



Molecular simulations of ion permeation and selectivity in sodium selective ion channels

A thesis submitted in fulfilment of the requirements
for the degree of Doctor of Philosophy

Emelie Flood
BSc, MSc Lund University

School of Science
College of Science, Engineering and Health
RMIT University

December 2017

Declaration of Candidature

I certify that except where due acknowledgement has been made, the work is that of the author alone; the work has not been submitted previously, in whole or in part, to qualify for any other academic award; the content of the thesis is the result of work which has been carried out since the official commencement date of the approved research program; any editorial work, paid or unpaid, carried out by a third party is acknowledged; and, ethics procedures and guidelines have been followed.

Emelie Flood 2017-12-18

Acknowledgements

I would like to acknowledge my supervisor Prof. Toby W Allen for his time, help and support in supervising this project, as well as my associate supervisor Prof. David Adams. I would also like to thank the rest of the Allen group, in particular Dr. Celine Boiteux for your help and guidance and Dr. Bogdan Lev for your support. I am grateful to RMIT University for funding and the Department of Physics for inspiring and educating me during my Ph.D. Furthermore, I would like to express my gratitude to Rupert Weaver and Jenny Gustavsson for providing support concerning language and illustrations.

List of Publications

Peer-reviewed Publications

Emelie Flood, Celine Boiteux, Toby W. Allen. Mechanisms of ion permeation and selectivity in a model human sodium channel. Plos Comp Biol, (2017), undergoing submission.

Lynagh, Timothy, Emelie Flood, Celine Boiteux, Matthias Wulf, Janne M. Colding, Vitaly V. Komnatnyy, Toby W. Allen, and Stephan A. Pless. A Selectivity Filter at the Lower End of ASIC1a. eLife (2017).

Conference Presentations

Australian Biophysics Conference presentation, poster, Multi-ion/carboxylate clusters underpin sodium selectivity in membrane ion channels (2017).

Molecular Mechanics Meeting conference presentation, talk, Mechanisms of Na channel permeation and selectivity (2017).

Biophysical Society Conference presentation, poster, Comparison of ion selectivity in a mammalian and a bacterial sodium channel (2017).

Australian Biophysics Conference presentation, poster, Simulations of ion selectivity in the acid-sensing ion channel ASIC1a (2016).

Australian Biophysics Conference presentation, poster, The origins of ion selectivity in a bacterial sodium channel and its extension to mammalian channels (2015).

VLSCI Molecular Mechanics meeting presentation, talk, Ion Selectivity In Sodium Channels: Investigation of Ion-Carboxylate Interaction (2014).

Table of Content

<i>Declaration of Candidature</i>	i
<i>Acknowledgements</i>	ii
<i>List of Publications</i>	iii
<i>Table of Content</i>	iv
<i>List of Tables</i>	vii
<i>List of Figures</i>	viii
<i>Abstract</i>	1
1. Ion channels	3
1.1 Overview	3
1.2 Introduction	4
1.3 Historical perspective	7
1.4 The action potential.....	11
1.5 Ion permeation and selectivity.....	13
1.6 Molecular determinants of ion selectivity	21
2. Structure and function of Na^+ -selective ion channels.....	27
2.1 Overview	27
2.2 Introduction	28
2.3 Voltage gated Na^+ channels.....	28
2.3.1 Structure of Na_vs	28
2.3.2 Gating mechanisms of Na_vs	30
2.3.3 Selectivity in Na_vs	32
2.3.3.1 Selectivity in bacterial Na_vs	33
2.3.3.2 Selectivity in human Na_vs	37
2.4 Na^+ selective Acid Sensing Ion Channels	39
2.4.1 Structure of ASICs.....	39
2.4.2 Gating mechanisms of Acid Sensing Ion Channels.....	40
2.4.3 Selectivity in ASICs	41
3. Computational methods for molecular modelling	44
3.1 Overview	44
3.2 Introduction	45
3.3 Molecular Dynamics	45
3.4 The ergodic hypothesis	47
3.5 Force fields.....	49
3.5.1 Polarisable models.....	55
3.6 Boundary conditions.....	57

3.7	Non-bonded interactions	59
3.8	Electrostatics with periodic boundary condition.....	60
3.9	Maintaining constant temperature and pressure	62
3.10	Free energy calculations	64
3.10.1	Thermodynamic integration	65
3.10.2	Umbrella sampling	66
3.10.3	Free energy perturbation.....	68
4.	Reparameterisation and validation of interaction specific parameters for ions in additive force fields	72
4.1	Overview	72
4.2	Introduction	73
4.3	Methods	79
4.3.1	Free energies of ion-carboxylate pair interactions	79
4.3.2	Determination of K _D	81
4.3.3	Osmotic pressure simulations.....	82
4.3.4	Simulation details.....	83
4.3.5	<i>Ab initio</i> calculation details	84
4.4	Results	85
4.4.1	Cation-Acetate pair interaction in aqueous solution	85
4.4.2	FF parameter comparison for Na ⁺ -OAc ⁻	86
4.4.3	Force field parameter comparison for KOAc.....	89
4.4.4	FF parameter comparison for Ca ²⁺ - OAc ⁻	90
4.4.5	A NBFIX for Ca ²⁺ interacting with Acetate	92
4.5	Conclusions	95
5.	Selective ion permeation involves complexation with carboxylates and lysine in a human sodium channel.	98
5.1	Overview	98
5.2	Introduction	99
5.3	Methods	106
5.3.1	Model of a human Na _v	106
5.3.2	Simulation details.....	109
5.3.3	Analysis.....	111
5.4	Results and Discussion.....	115
5.4.1	A stable human Na _v model with asymmetric and flexible selectivity filter	
	115	
5.4.2	Selectivity filter with neutral lysine exhibits bacterial-like multi-ion complex formation and conduction.....	119

5.4.3 Charged lysine forms a high field-strength complex to enhance pass-by conduction	127
5.4.4 K ⁺ exhibits less multi-ion complex formation, and is partially blocked by lysine 132	132
5.4.5 Multi-ion complex stability underpins selective conduction	137
5.5 Conclusions	140
5.6 Supplementary information	145
5.6.1 Model dependence of the results	145
6. Ion selectivity in the acid sensing ion channel ASIC1.....	147
6.1 Overview	147
6.2 Introduction	148
6.3 Methods	151
6.3.1 System.....	151
6.3.2 Simulation details.....	151
6.3.3 Analysis.....	152
6.3.4 Model dependence	157
6.3.5 Experimental methods	158
6.4 Results	159
6.4.1 Free simulations of ions in PDB:4NTW show no preference for Na ⁺ in the GAS-belt	159
6.4.2 Umbrella sampling in ASIC PDB:4NTW reveals Na ⁺ preference in the lower part of the pore	160
6.4.3 Umbrella sampling in ASIC PDB:2QTS shows a strong Na ⁺ preference in the lower part of the pore.....	163
6.4.4 Mutagenesis and unnatural amino acid substitution experiments validate MD results.....	164
6.4.5 Free simulations suggest an important roll of multi-ion/multi-carboxylate complexes in selective ion permeation	169
6.4.6 Model dependence	172
6.5 Conclusions	175
7. Concluding remarks and future directions	178
8. References	184

List of Tables

Table 1.1. Ion concentrations and equilibrium potentials in a mammalian muscle cell	12
Table 1.2. Ion radii and hydration free energies	17
Table 4.1. LJ parameters in the standard CHARMM FF and Drude CHARMM FF for Na ⁺ , Ca ⁺ and the oxygen from carboxylate	78
Table 4.2. Experimentally measured osmotic pressure at different concentrations of Ca ²⁺ (OAc ⁻) ₂	82
Table 5.1. Summary of ion bindings in the SF of the NavRh/Nav1.2 mutant	123

List of Figures

Figure 1.1. Cartoon of an ion channel in a lipid bilayer, the ion channel is simplistically represented as a pore.....	4
Figure 1.2. Cartoon showing different types of membrane transport.....	5
Figure 1.3. Illustration of the opening and inactivation of a voltage-gated Na_v	6
Figure 1.4. Ion channels in a membrane with the SF occupied by cations.....	7
Figure 1.5. Cartoon of a classic patch clamp set up.....	8
Figure 1.6. Structure of KcsA.....	9
Figure 1.7. Single ion channel recording and MD simulations are used to determine the free energy profile on ion permeation through the channel and to pinpoint the mechanisms involved	10
Figure 1.8. Cartoon of an action potential.....	13
Figure 1.9. An ion enters the SF from above and knocks the ions already in the SF into the channel.....	20
Figure 1.10. The SF of a K_v and a Na_v	21
Figure 1.11. Illustration of an oversimplified ‘snug fit’ mechanism.	23
Figure 1.12. The SF of a bacterial Na_v	24
Figure 2.1. Sketch of the structure of a bacterial and mammalian Na_v	29
Figure 2.2. Structure of a bacterial Na_v	30
Figure 2.3. Structure on an open and closed Na_v	31
Figure 2.4. Sequence alignment of NaChBac, Na_vAb , Ca_vAb and $\text{Na}_v1.2$	33
Figure 2.5. The SF of Na_vAb	34
Figure 2.6. PMFs of Na^+ in the SF of Na_vAb	36
Figure 2.7. Structure of ASIC1a (PDB:2QTS)	40
Figure 2.8. Sequence alignment of TM2 for a range of ENaC/DEG channels...	42
Figure 2.9. Structure of ASIC1a (PDB:4NTW).....	43
Figure 3.1. Coordinates for bonded interactions	50
Figure 3.2. Illustration of the Lennard-Jones potential with the pair-specific r_{min} and ϵ marked.....	52
Figure 3.3. Periodic boundary condition.....	58
Figure 3.4. Typical MD simulation box containing a voltage-gated ion channel in a lipid membrane surrounded by water and ions.....	59
Figure 3.5. Illustration of the Ewald summation	61
Figure 4.1. A periodic water box containing one ion and one acetate	81
Figure 4.2. Computational setup for measurement of the osmotic pressure	83
Figure 4.3. Comparison of the free energy for different sized boxes for the raw CHARMM FF between OAc^- and Na^+ using LB, K^+ using LB and Ca^{2+} using the new NBFIX created in this chapter.....	85
Figure 4.4. The free energy for OAc^- interacting with Na^+	87
Figure 4.5. The free energy for OAc^- interacting with K^+	90

Figure 4.6. The free energy for OAc ⁻ interacting with Ca ²⁺	92
Figure 4.7. Osmotic pressure as a function of concentration for Ca(OAc) ₂	93
Figure 4.8. Determination of NBFIX for Ca ²⁺ - OAc ⁻	94
Figure 4.9. The free energy of OAc ⁻ interacting with Ca ²⁺ , only free energies over -20 kcal/mol are shown.	95
Figure 5.1. Na _v Rh/Na _v 1.2 channel embedded in a hydrated DPPC bilayer surrounded by water with Na ⁺ and Cl ⁻ ions	100
Figure 5.2. Alignment of Na _v 1.2 and Na _v PaS	102
Figure 5.3. PMFs of Na ⁺ in the SF of Na _v Ab	104
Figure 5.4. Radial distribution function for Na ⁺ -Na ⁺ , K ⁺ -K ⁺ , Na ⁺ -carboxylate and K ⁺ -carboxylate	113
Figure 5.5. RMSD for the backbone of the mutated residues.....	116
Figure 5.6. Residue position of the DEKA and EEDD rings over time in Na _v Rh/Na _v 1.2	117
Figure 5.7. RMSF of residue 178 to 184 in Na _v Rh/Na _v 1.2 and Na _v Ab	118
Figure 5.8. Solvation of the first shell relative to bulk for Na ⁺ in Na _v Rh/Na _v 1.2	119
Figure 5.9. Time series showing the z-positions of K ₁₄₂₂ and Na ⁺ ions in the SF of Na _v 1.2 with deprotonated (neutral) Lys.....	120
Figure 5.10. Electrostatic map of the filter of Na _v 1.2 with deprotonated Lys and Na _v Ab	121
Table 5.1. Summary of ion bindings in the SF of the NavRh/Nav1.2 mutant	123
Figure 5.11. Occupancy analysis in the SF (-15<z<15) with deprotonated K ₁₄₂₂	124
Figure 5.12. Permeation of Na ⁺ in the SF of Na _v 1.2 with deprotonated (neutral) Lys.....	126
Figure 5.13. Time series showing the z-positions of K ₁₄₂₂ and Na ⁺ ions in the SF of Na _v 1.2 with protonated (charged) Lys.....	127
Figure 5.14. Permeation of Na ⁺ in the SF of Na _v 1.2 with protonated (charged) Lys showing the 1-ion conduction mechanism.....	130
Figure 5.15. Permeation of Na ⁺ in the SF of Na _v Rh/Na _v 1.2 with protonated (charged) Lys showing the 2-ion conduction mechanism	132
Figure 5.16. Time series showing the z-positions of K ₁₄₂₂ and K ⁺ ions in the SF of Na _v 1.2 with protonated (charged) Lys	133
Figure 5.17. Occupancy analysis in the SF (-15<z<15) with charged K ₁₄₂₂	134
Figure 5.18. Permeation of K ⁺ in the SF of Na _v Rh/Na _v 1.2 with protonated (charged) Lys	136
Figure 10. Results from FEP simulations	139
Figure S5.1 Distribution of ion occupancy in the SF of Na _v Rh/Na _v 1.2 with Na ⁺ and K ⁺ where NBFIX has been used	146

Figure 6.1. ASIC1 channel embedded in a hydrated DPPC bilayer surrounded by water with Na^+ and Cl^- ions.....	149
Figure 6.2. Sequence alignment of the intracellular domain of PDB:4NTW, PDB:2QTS and rat ASIC1	150
Figure 6.3. Free energy convergence and lateral sampling of ions for umbrella sampling of PDB:4NTW and PDB:2QTS	154
Figure 6.4. Amide-ester substitution A11'a and 4-nitro-2-aminobutyric acid of E18'	159
Figure 6.5. The GAS-belt of PDB:4NTW with a Na^+ ion and K^+ ion in	159
Figure 6.6. Results from free simulations in the TMD of PDB:4NTW	160
Figure 6.7. Results from US simulations in the TMD of PDB:4NTW	162
Figure 6.8. Radial distribution function for Na^+ and K^+	163
Figure 6.9. Results from US simulations in the TMD of PDB:2QTS	164
Figure 6.10. Relative permeability ratios for WT and mutant ASIC1a channels	166
Figure 6.11. Relative permeability ratios of WT and A11' α channels and current voltage relationship channel in NaCl and KCl of WT and channel with mutant E18' ϵ	167
Figure 6.12. Relative permeability ratios for concatemeric channels	169
Figure 6.13. Occupation and conformation of the sites formed by residues E18' and D21' in unbiased simulation of PDB:4NTW and PDB:2QTS	171
Figure 6.14. FEP binding free energy difference $\Delta\Delta G$ and convergence	172
Figure 6.15. Estimates of free energy and coordination results for modified CHARMM27* NBFIIX	174
Figure 6.16. Estimated $\text{Na}^+ \rightarrow \text{K}^+$ free energy perturbations for PDB:4NTW and PDB:2QTS with modified ion parameters.....	175
Figure 7.1. CaCl_2 in Na_vAb	181
Figure 7.2. Na^+ binding sites in Na^+ bound Na^+/K^+ -ATPase	184

Abstract

Na⁺-selective ion channels play key roles in a wide range of both physiological bodily functions and pathological disease processes including propagation of nervous signals, cardiac function and pain sensation. Different channels achieve Na⁺ selectivity despite differences in structure, function and evolutionary origin. For example, voltage gated sodium channels (Na_vs) are tetramers that open and close in response to cell membrane depolarisation, whereas acid sensing ion channels (ASICs) are trimeric channels that respond to a change in extracellular pH. A key function of Na⁺ channels is their ability to select for Na⁺ while discriminating against other ions. To achieve this selectivity, Na_vs makes use of a highly flexible selectivity filter (SF) where ion coordination is facilitated by the side chains of the amino acids. In contrast, ASICs have been proposed to rely on a size-constriction mechanism. However, the utilisation of size-constriction for ion selectivity has not been proven. Furthermore, the amino acids of the SF present diverse chemistries to achieve selectivity in these channels, with the mammalian Na_v using a DEKA ring (Glu, Asp, Lys and Ala), the bacterial Na_v an EEEE ring (four Glus), and ASIC a GAS-belt (Gly, Ala and Ser). Therefore it has been proposed that different Na⁺-selective channels employ different mechanisms to achieve Na⁺ selectivity. There are a number of recently solved atomic scale Na⁺ channel structures of Na_vs and ASICs which presents an opportunity to elucidate these mechanisms and understand the origins of ion selectivity at the molecular level.

Computer simulations are becoming increasingly useful to complement physical experiments in the investigation of biological systems. Molecular Dynamics (MD) simulations can be used to study the properties of macromolecules at the atomic scale. In this thesis, we use MD to explore the mechanisms of ion selectivity in sodium-selective channels. To provide insight into the ion-protein interactions relevant to ion discrimination, we require that these interactions are described with a high level of accuracy. We have therefore investigated the parameters defining the interactions between ions and the chemical groups of interest, and tested them against quantum mechanical calculations and experimental data to determine

accurate models for use in our simulations.

We have explored ion permeation in Na_v s and ASICs using multi- μs fully atomistic simulations, as well as enhanced sampling methods. Our results demonstrate that low free energy multi- Na^+ /multi-carboxylate complexes facilitate selective ion permeation in a similar fashion in all of these channels. In the bacterial Na_v s, these complexes are formed with carboxylates from the EEEE ring. To investigate conduction and selectivity in mammalian Na_v channels, we have constructed a model of the human $\text{Na}_v1.2$ channel by grafting core functional sequences into a structurally well-defined bacterial channel scaffold. We report that Na^+ ion conduction in $\text{Na}_v1.2$ relies on the formation of energetically stable multi- Na^+ /multi-carboxylate complexes formed by both the DEKA and vestibular EEDD rings. These stable complexes facilitate a knock-on conduction mechanism. Furthermore, we have observed that the positively charged DEKA Lys forms a similar $\text{Na}^++\text{Lys}/\text{multi-carboxylate}$ complex deep in the pore to facilitate low barrier ion pass-by permeation for Na^+ , but not K^+ . In contrast Lys acts as an electrostatic plug that partially blocks the channel, leading to discrimination. In the ASIC channel, we have found that Na^+ and K^+ are equally favoured around the GAS constriction, not supporting its previously postulated role in Na^+ selectivity. Instead, we have identified a preference for Na^+ at the lower end of the pore where a ring of Glu and Asp side chains participate in multi- Na^+ /multi-carboxylate complexes, with similar K^+ ion complexes disfavoured, suggesting a SF at the intracellular end of the ASIC pore. These results are supported by mutagenesis and novel unnatural amino acid substitution experiments performed by collaborators.

Our studies of these evolutionarily, structurally and functionally different ion channels have revealed essential high-field strength carboxylate binding events that underscore selective permeation. These key carboxylates form tight multi-ion/multi-carboxylate complexes that thermodynamically select for Na^+ over K^+ . This suggests a common mechanism for the selection of Na^+ ions in membrane ion transport. These studies reveal the principles governing Na^+ selectivity across several ion channels, with the potential to extend to the whole family of Na^+ -selective ion channels and pumps in nature.

Chapter 1

1 Ion channels

1.1 Overview

The cell is surrounded by a membrane made up by phospholipids. The lipids have hydrophobic tails and hydrophilic head groups and to minimise hydrophobic exposure to water the lipids can orient themselves into a lipid bilayer (Fig.1.1). Whether the cell is eukaryotic or prokaryotic, communication between the intracellular and extracellular sides of the cell is vital for function. Therefore ions and molecules need to be able to cross the cell membrane. However, due to the hydrophobic core of the lipid bilayer, very few molecules can efficiently cross a cell membrane by themselves. In particular, charged molecules and ions in bulk are interacting with the water molecules and have a so-called hydration shell. To dehydrate and instead enter a hydrophobic surrounding would be very expensive and the lipid bilayer is therefore basically impermeable to ions and charged molecules. Instead, membrane transport proteins dispersed in the lipid bilayer aid in the crossing of the cell membrane, these can simplistically be thought of as a water-filled pores through the membrane (Fig.1.1).

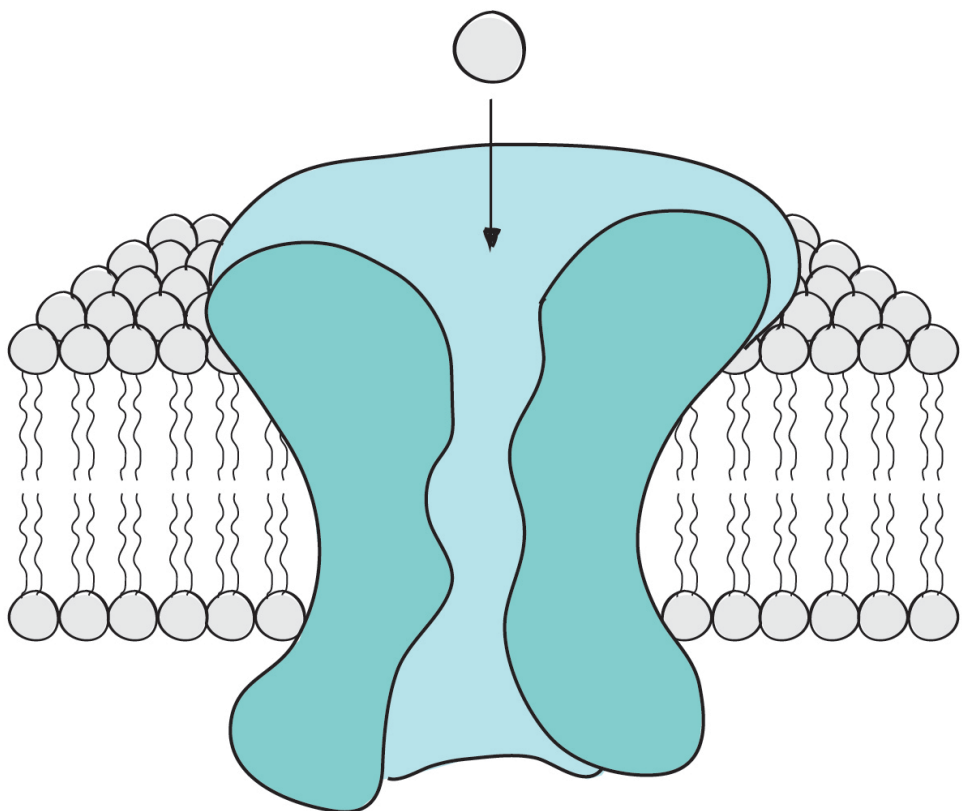


Figure 1.1. Cartoon of an ion channel in a lipid bilayer, the ion channel is simplistically represented as a pore.

1.2 Introduction

The transport mechanism of a membrane transport protein can either be passive or active; in a passive transporter permeation of the ions or molecules is along their electrochemical gradient (Fig.1.2a&b), whereas an active transporter uses energy to transport ions back against their chemical gradient (Fig.1.2c) [1]. Passive transporters can further be broken down into ion channels and carriers. Carriers transfer ions and molecules across the cell membrane by binding to them and undergoing a number of conformational changes. This process is therefore relatively slow (Fig.1.2b). Ion channels instead create water-filled pores through the membrane, which allows for a rapid, diffusion-like permeation along the chemical gradient (Fig.1.2a) [2].

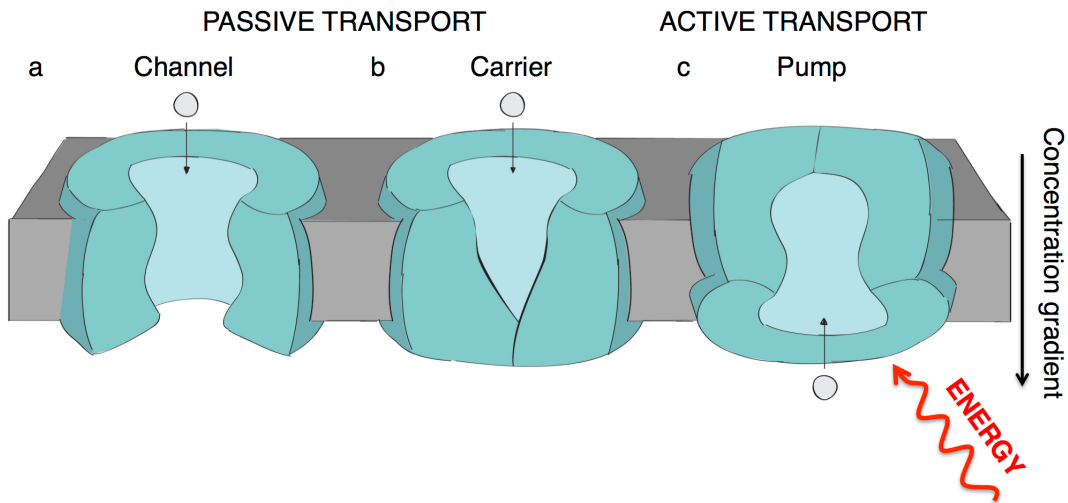


Figure 1.2. Cartoon showing different types of membrane transport.

The opening and closing of the channels, known as gating, is controlled by a stimulus that triggers the opening. This ensures that signals are transmitted only when initiated by a particular stimulus. The channels respond to different stimuli depending on the ion channel. Voltage-gated ion channels are gated by a change in the voltage across the membrane. Their primary function is signal propagation and excitability of various cells. In ligand-gated ion channels, the opening is controlled by the binding to a chemical messenger, including molecules and ions [2]. The ligand itself does not get transported. Mechanosensitive channels open due to mechanical stimulation, including pressure and membrane deformation. Ligand-gated and mechanosensitive ion channels convert chemical and mechanical messages into electrical signals [3].

The gating mechanism varies between channels; some channels move whole segments that open up a permeable pore while other just reorient specific residues in the channel to, for example, change the hydrophobicity of the pore and in that way create a permeable channel. Voltage-gated ion channels have been shown to have gating charges that responds to a change in voltage. These are made up by a number of positively charged amino acids, generally Arg or Lys, that move towards the extracellular side of the membrane during depolarisation, and then move back towards the intracellular side during repolarisation. The movement of gating charges translates to movement of the pore that opens a gate at the bottom of the channel (Fig.1.3a&b).

Inactivation of the ion channels are complex mechanisms, there are generally two types of inactivation, fast inactivation (N-type) and slow inactivation (C-type). After prolonged activation of the channel, it generally enters a N-type inactivated state. During this state the channel is non-conducting and cannot be activated again. This fast inactivation is an inherent mechanism of ion channels. It is necessary for regulation of activity during prolonged stimulation. Different ion channels achieve this inactivation in different ways [4]. Na_v s make use of a “ball and chain” method where an intracellular part of the protein swings in and blocks the gate (Fig.1.3c). The slow inactivation takes longer time and is coupled to the activation. It generally entails an overall change in the ion channel, which brings the channel back to its closed resting state. The channel can then be activated again (Fig.1.3a) [5].

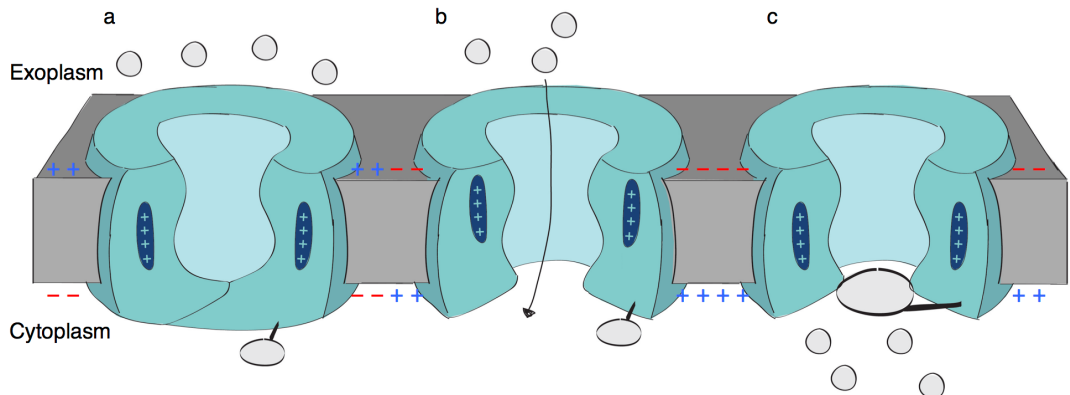


Figure 1.3. Illustration of the opening and inactivation of a voltage-gated Na_v [6].

Furthermore, to control the signalling, permeation through the ion channels is limited by the channel’s ion selectivity; only certain types of ions can easily permeate the channel. There are several types of ions in and around cells. Most abundant are Na^+ , K^+ and Cl^- , but there are also Ca^{2+} , Mg^{2+} , H^+ , Zn^{2+} , as well as other ions. The selectivity process is extremely delicate and the ability of the ion channels to be able to select and conduct the right ion key to its function. The area of the channel that is responsible for exercising this selectivity is called the selectivity filter (SF) (Fig.1.4). Different channels have been known to do this by different processes, but in general, selectivity takes place in a narrow part of the channel where the amino acids of the channel can interact closely with the ions [7].

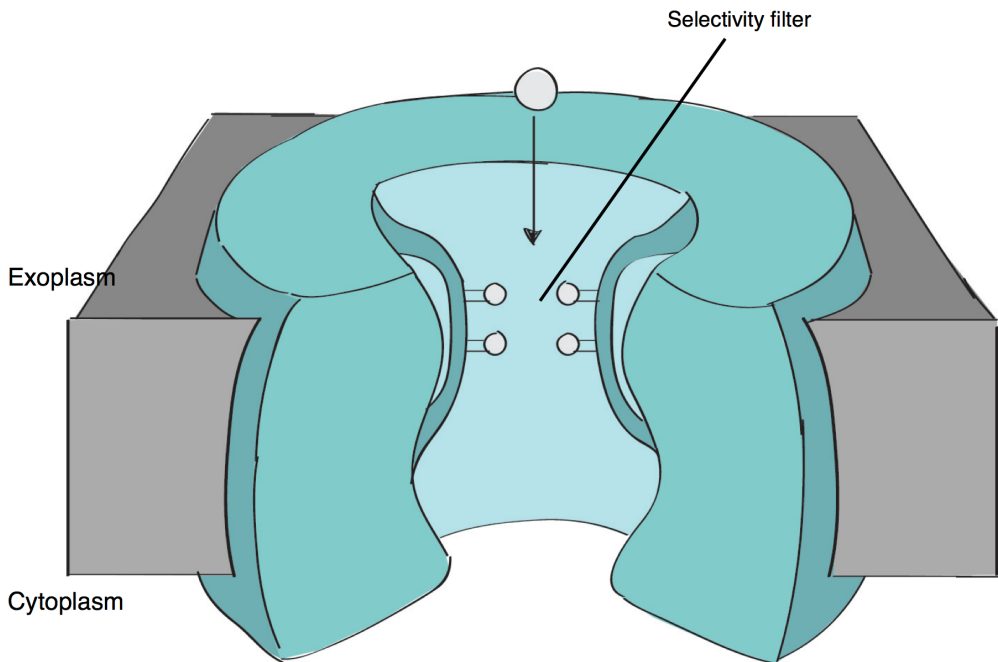


Figure 1.4. Ion channels in a membrane with the SF occupied by cations.

1.3 Historical perspective

The involvement of ions channels in the excitement of muscles and nerves has been known since the end of the 19th century. Sidney Ringer showed that a frog's heart would keep beating when it was submerged in solutions containing salts, in particular, Na^+ , K^+ and Ca^{2+} in certain proportions [8]. There were several competing theories as to why this was necessary until the beginning of the 20th century when Julius Bernstein theorised that semi-permeable ion-selective membranes surround nerves and muscle cells and in that manner, ions can create excitation in the cells [7]. In the 1950s, squid neurons became a major focus of research and experimentation, in particular for Hodgkin and Huxley [9]. The electrical currents conducted through these neurons were much stronger than previously studied, which made important new experiments possible. Through these experiments, the different roles of sodium and potassium were established. Hodgkin and Huxley were the first to develop an empirical model consisting of mathematical equations for ion conduction [9].

Shortly after, the patch-clamp was invented [10]. In the patch-clamp method, glass micropipettes are used to create a 'giga-seal' on the cell membrane, trapping single ion channels. A voltage is applied to the membrane and the

ionic current in and out of the cell can be measured (Fig.1.5) [10]. This made it possible to measure single channel currents and confirmed the existence of ion channels, as well as distinguishing the different channels from each other. The patch clamp method became an essential tool in cell biology and the majority of knowledge about ion channels has come from it.

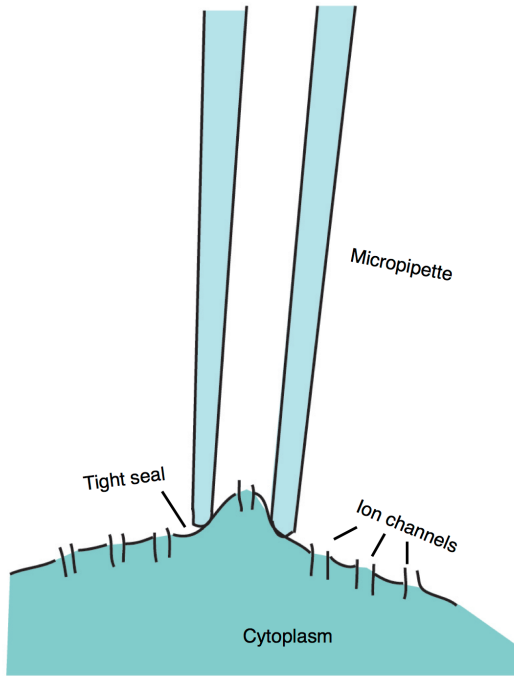


Figure 1.5. Cartoon of a classic patch clamp set up.

However, to be able to fully understand how ion channels work we need to know atomic-scale details about their structure. Advances in bimolecular technology made it possible to determine the sequence of ion channels [11]. However, due to the complicated nature of protein folding it was not until the turn of the century when a structure in atomic detail from x-ray crystallography was determined; it was a bacterial potassium selective channels, KcsA, in 1998 [12]. The structure showed a tetrameric channel where each subunit consists of two transmembrane-spanning α -helices that together form a pore (Fig.1.6) [12]. Since then, several ion channels have been solved to atomic resolution and are available in the Protein Data Bank [13]. However, crystallising a protein can be complicated as well as the process itself is putting the channels in non-physiological environments. Recently cryo-electron microscopy (cryo-EM) has started to show the potential to revolutionise the

field, as the resolution of the EM is increasing, and the first near atomic structure of a eukaryotic Na_v has been solved thanks to cryo-EM [14]. In cryo-EM, the protein is not crystallised but instead frozen. An electron beam is then used to investigate the structure.

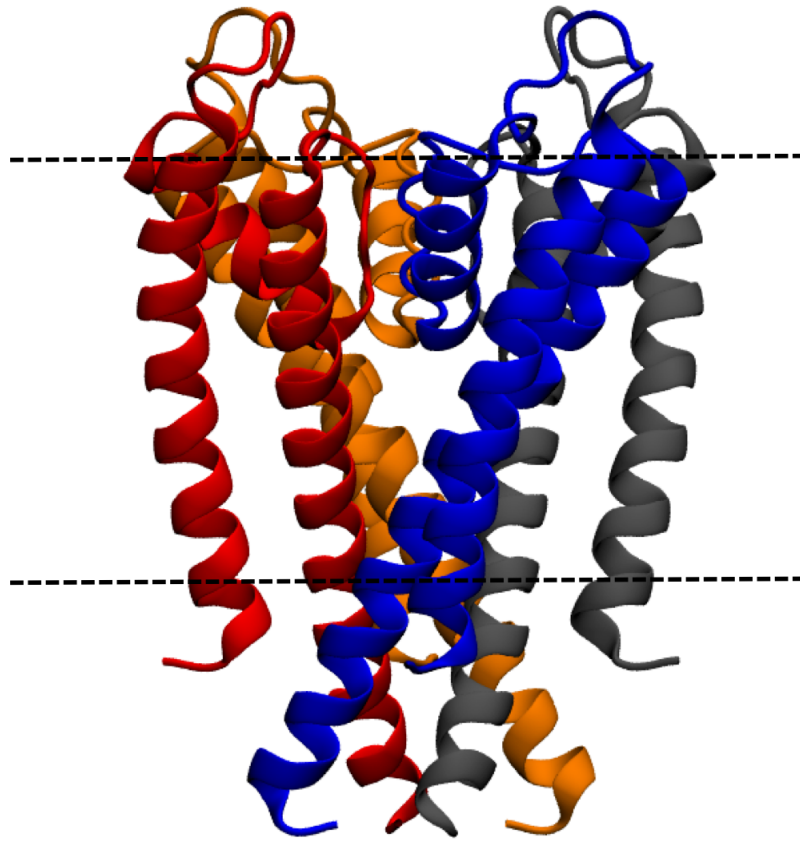


Figure 1.6. Structure of KcsA where the different subunits are coloured in different colours and the black dashed line represent the membrane (PDB:1R3J).

The availability of high-resolution structures has instigated a take-off of computational studies in biophysical research and MD simulations have become an essential tool for studying ion channels. Macroscopic properties of ion channels can be determined from experiments, however, the dynamics of the ions can only be theorised. In MD the dynamics of the behaviour of the ions can be observed and quantified and the exact mechanisms determined. As an illustration, the patch clamp method can tell us which ions can and cannot permeate a channel, but it does not explain the underlying physical principles

involved in permeation. This way MD connects theory to experiments. MD simulations have thus far provided valuable information in ion channel research. In Fig.1.7a single Na^+ currents recordings and the current voltage relationship in an ASIC are shown. The effect from a number of mutants in part of the channel has been investigated and it can be seen that the current decreases for mutants of residue E18' suggesting its importance for functionality. However, the current voltage relationship cannot tell us why this mutant affects the function of the ASIC. When investigating Na^+ ions permeating the channel with MD simulations it can be seen that the Na^+ ions are energetically favoured around E18', Fig.1.7b. Analysis of the simulations show that Na^+ ions bind to E18' when permeating the channel and thus, when E18' is being mutated the channel function is altered. MD simulations allow us to investigate atomic scale details on long and short time scales. The ion permeation and selectivity in ASICs is further discussed in Chapter 6.

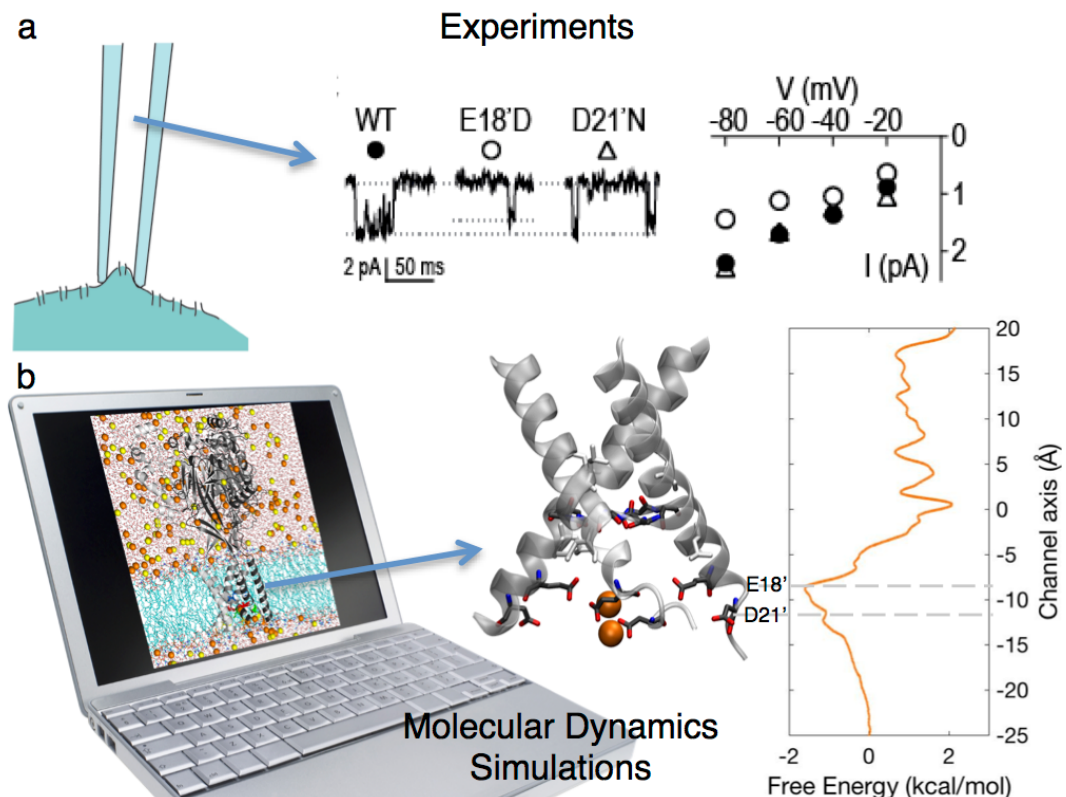


Figure 1.7. a) single ion channel recording showing the effects from different mutants. b) MD simulations are then used to determine the free energy profile on ion permeation through the channel and to pinpoint the mechanisms involved and explain the channel recordings. The investigation is discussed in Chapter 6 [15].

1.4 The action potential

The ions in the body exist in different concentrations inside and outside of the cell, in particular, Na^+ and Cl^- dominates the exoplasm, with a small number of K^+ and Ca^{2+} , whereas K^+ dominates the cytoplasm, with a small number of Na^+ and Cl^- (Table 1.1). These concentration gradients are maintained by the adenosine triphosphate (ATP) powered pumps, most significantly the pump that exchanges three intracellular Na^+ for two extracellular K^+ , Na^+/K^+ -ATPase [16]. The ion pumps also helps to establish a charge difference across the membrane. This creates a potential difference across the cell membrane. Hence, there are two forces acting across the membrane; thermal forces due to the concentration gradient and electrical forces due to the charge difference. When the thermal forces balance the electrical forces a potential is established and equilibrium is reached. This potential is called the equilibrium potential, as it is the voltage that exactly opposes the force from the chemical gradient. The equilibrium potential can be determined by the Nernst equation [17]. The probability of finding a particle, p , in system 1 or system 2 at equilibrium is given by the difference in their energy, $U_2 - U_1$, and can be determined with the Boltzmann distribution

$$\frac{p_2}{p_1} = e^{-(U_2 - U_1)/k_B T} \quad (1.1)$$

where k_B is Boltzmann constant and T the temperature. An ion with charge q has the potential $\phi = U/q$ giving

$$\phi_2 - \phi_1 = -\frac{k_B T}{q} \ln \frac{p_2}{p_1} \quad (1.2)$$

the probability is proportional to the concentration, c , which gives us the Nernst equation

$$\phi_s = \phi_2 - \phi_1 = -\frac{k_B T}{q} \ln \frac{c_2}{c_1} \quad (1.3)$$

The membrane potential is defined as being measured as the potential inside minus the potential outside the cell. This equation can be used to calculate the equilibrium potentials for the ions across a cell membrane, e.g. $E_{\text{Na}^+} \sim 70$ mV,

$E_{K^+} \sim -100$ mV and $E_{Ca^{2+}} \sim 130$ mV (Table 1.1) [18]. In fact, the contribution from K^+ dominates, as the number of open K^+ channels is greater than the number on Na^+ and Ca^{2+} channels, and the resting potential for a cell membrane can be measured to be ~ -70 mV [18].

Table 1.1. Ion concentrations and equilibrium potentials in a mammalian muscle cell [18].

Ion	Extracellular concentration (mM)	Intracellular concentration (mM)	Equilibrium potential at 37°C (mV)
Na^+	150	12.0	67.0
K^+	4.00	155	-98.0
Ca^{2+}	1.80	2.00×10^{-4}	128
Cl^-	150	4.20	-90.0

The membrane potential is used to, among other things, transmit nerve signals (Fig.1.8). A stimulus depolarises the membrane (Fig.1.8b), if this depolarisation crosses a threshold and the membrane potential reaches ~ -45 mV the fast responding Na_v s opens up. This leads to a selective in-flow of Na^+ ions, down its concentration gradient, which further depolarises the membrane (Fig.1.8c). This in-flow would stop when the electrical forces start opposing the forces due to the concentration gradient and the equilibrium potential of Na^+ is reached. However, Na_v s has an inherent property that makes them inactivate after a very short time, which stops the in-flow ahead of time. Furthermore, the depolarisation also triggers the K_v s to open up, however, their opening response is slower and opening is delayed compare to the Na_v s. In a similar way, the K_v s selectively let K^+ ions out of the cell, along its concentration gradient, which repolarises the membrane (Fig.1.8d). The deactivation of the K_v s is slow and it lacks a fast inactivation mechanism, which leads to an overpolarisation of the membrane (Fig.1.8e). This overpolarisation together with the non-responsive inactivated Na_v s ensures that action potentials only propagate in one direction. It takes a larger change in voltage of the membrane to reach the threshold for Na_v opening and only the Na_v s ahead of the action potential can open, whereas the ones behind are inactivated and non-responsive to a change in membrane potential. When the resting potential has been restored the Na_v s becomes

deactivated, and the process can take place again, however, by then the action potential just propagated will be too far away to stimulate the Na_v s and only new action potentials can be transmitted. This mechanism is reliant on the Na_v s and K_v s ability to effectively being able to select for their native ion while discriminating against other ions [18].

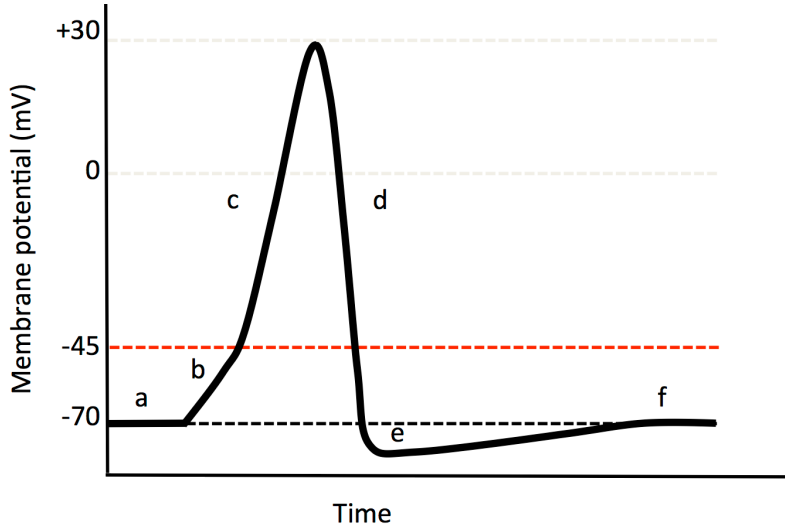


Figure 1.8. Cartoon of an action potential, letters showing the a) resting potential, b) stimulation period, c) depolarisation, d) repolarization, e) overpolarisation and f) resting potential.

1.5 Ion permeation and selectivity

The action potential is fundamental for a wide range of bodily functions. It is necessary for transmitting signals through nerves, muscles and cardiac tissue [19]. Transmission of these signals is dependent on the Na_v s and K_v s to select for their native ions, while discriminating against other ions. This makes the Na^+ ion selectivity mechanism crucial to understand. Both Na^+ and K^+ are physiologically abundant and similar in concentration, have the same charge and their radius differs by only 0.38 Å (Table 1.2). Nonetheless, selective ion channels function with a high degree of fidelity [20]. Furthermore, Na^+ and Ca^{2+} are comparable in size, with the minimal difference in radius of 0.04 Å (Table 1.2). They both have the highest concentration in the exoplasm and their concentration gradients are thus in the same directions. Nonetheless, the cell membrane can maintain the Na^+ gradient while conducting Ca^{2+} . The $\text{Na}^+/\text{Ca}^{2+}$ selectivity mechanism can be explored as a valence based discrimination.

However, mutation of only a few residues makes a Na^+ selective channel instead select for Ca^{2+} . Furthermore, voltage gated Ca^{2+} channels (Ca_v s) and Na_v s have been shown to be evolutionarily connected [21]. The mechanism of $\text{Na}^+/\text{Ca}^{2+}$ selectivity is therefore likely more sophisticated and requires greater attention.

To investigate ion selectivity and permeation from experimental methods, like the patch clamp method mentioned above, we need to determine the relationship between the current and the voltage. Ohms law in simple conductors tells us that membrane potential, ϕ , and the current, I , are related by

$$I = \sigma\phi \quad (1.4)$$

where σ is the channel conductance. However, the concentration gradient derived from the Nernst equation above adds a driving force from the ion, ϕ_s , that can be thought of as an electromotive force (emf), instead giving the following equation for a single ion system

$$I_s = \sigma_s(\phi - \phi_s) \quad (1.5)$$

This can be used when creating a current-voltage relationship from experimental techniques, including the patch-clamp method, to determine the conductance for a specific ion, σ_s

$$\sigma_s = \frac{I_s}{\phi - \phi_s} \quad (1.6)$$

Furthermore, to be able to investigate ion selectivity in experiments we determine the relative permeabilities for the different type of ions.

Ion permeation can be simplified down to a 1D movement across a membrane of size l of a charge affected by diffusion and conductance. The contribution to the ionic flow through an electric field can be determined by Ohms law, which also can be formulated with current density, J

$$J = -\sigma \frac{d\phi}{dz} \quad (1.7)$$

where σ is the channel conductance which is the ability to transfer electricity and for an ion of type S is dependent on the ionic mobility, v_s , and the concentration, c_s , giving Planck's equation

$$J_s = -v_s c_s \frac{d\phi}{dz} \quad (1.8)$$

The contribution due to diffusion can be described with Fick's law, which tells us the relationship between the concentration gradient, $\frac{dc_s}{dz}$, and the current density

$$J_{D,S} = -D_s \frac{dc_s}{dz} \quad (1.9)$$

Where D_s is the diffusion coefficient and is related to the drift velocity by the Einstein relationship

$$D_s = \frac{v_s R T}{z_s F} \quad (1.10)$$

where z_s is the charge of the ion, F the Faraday constant, T the temperature and R the gas constant. The total current density for ion type S is given by combining the contributions from the concentration and the potential gradients, eq.1.8 and eq.1.9, and is the given by the Nernst-Planck equation

$$J_s = J_s + J_{D,S} = -D_s \left(\frac{dc_s}{dz} + \frac{c_s z_s F}{RT} \frac{d\phi}{dz} \right) \quad (1.11)$$

At equilibrium, there is no current and $J_s = 0$, giving

$$\frac{dc_s}{dz} + \frac{c_s z_s F}{RT} \frac{d\phi}{dz} = 0 \quad (1.12)$$

which gives us

$$\frac{d\Phi}{dz} = -\frac{RT}{c_S z_S F} \frac{dc_S}{dz} = -\frac{RT}{z_S F} \frac{d}{dz} \ln c_S \quad (1.13)$$

If we integrate eq.1.13 across the membrane we get the Nernst equation, eq.1.3, back using that $\frac{RT}{z_S F} = \frac{k_B T}{q}$.

We are interested in the current carried across the membrane and its relation to the membrane potential. To determine this we need to make a number of assumptions; the membrane is neutral and homogenous, the intra- and extra-cellular environments are unchanging and that the field in the membrane is constant with $\frac{d\phi}{dz} = \frac{\phi}{l}$. Integration of eq.1.11 across the membrane of length l , if we assume that the concentration inside the membrane at $x = 0$ is $\beta_S c_1$, outside at $x = l$ is $\beta_S c_2$, and β_S is the partition coefficient, then gives us

$$J_S = P_S z_S^2 \frac{\phi F^2}{RT} \frac{c_2 - c_1 e^{-z_S \frac{\phi F}{RT}}}{1 - e^{-z_S \frac{\phi F}{RT}}} \quad (1.14)$$

Where P_S , is the permeability of the membrane for ion S and is defined as $P_S = \frac{D_S \beta_S}{l}$

If there are several ions surrounding the membrane, and we assume that the ions are moving independent of each other, the flow of ions can be added. Physiologically the main contributors to the current are K^+ , Na^+ and Cl^- and we will get the following expression at equilibrium

$$J_K + J_{Na} + J_{Cl} = 0 \quad (1.15)$$

by putting eq.1.14 into eq.1.15 and solving for the potential we obtain the Goldman-Hodgkin-Katz (GHK) equation for relative permeability [22, 23]

$$\phi_{rev} = \frac{RT}{zF} \ln \frac{P_K c_{K,2} + P_{Na} c_{Na,2} + P_{Cl} c_{Cl,2}}{P_K c_{K,1} + P_{Na} c_{Na,1} + P_{Cl} c_{Cl,1}} \quad (1.16)$$

Where ϕ_{rev} is the reversal potential which corresponds to no net flow through the membrane. The relative permeabilities can be calculated if we know the intracellular and extracellular concentrations of the different ions [7].

Table 1.2. Ion radii [7] and hydration free energies [24, 25].

Ion	Radius (Å)	Hydration Free Energy (kcal/mol)
Na⁺	0.95	-98
K⁺	1.33	-80
Ca²⁺	0.99	-381

The relative permeability of ion channels can be determined by the GHK equation using results from e.g. a patch clamp experiment. The relative permeability of, for example, Na_vs has been well studied. Na_vs are permeable to several ions and has a sequence of permeability, also called the ion preference "fingerprint", of Li⁺~Na⁺>K⁺~Cs⁺~Rb⁺, [7, 26, 27]. Na_vs select for Na⁺ over K⁺ with P_{Na⁺}/P_{K⁺}~10-20 [7]. Quite differently, K_vs are only permeable to a few ions and molecules other than K⁺, these being Tl⁺, Rb⁺ and NH₄⁺, and they have a high K⁺ to Na⁺ permeability ratio, P_{K⁺}/P_{Na⁺}~100-250 [7]. The difference in permeability can start to teach us about the SF of these channels; far larger ions, as well as a bigger range of sizes, can permeate the Na⁺ channel whereas only smaller ions can permeate the SF of the K⁺ channel. From the size of the permeating ions and molecules, it was hypothesised that the K_v SF is ~3 Å in diameter and that the SF of the Na_v has an opening of ~3×5 Å [28].

By varying the concentration of ions the independence of the ion movement can also be tested; if the ions are independent the permeability should increase linearly with concentration. This has been extensively investigated in Na_vs and it has been shown that the linear relationship is not satisfied and hence the ions do not move independently in these channels [29-32]. The conclusion was that the ions bind at a number of specific sites within the channel during the permeation event. In particular, several investigations of the single channel current have shown that Na_vs likely have a two-site/three-barrier profile [29-32]. A channel like this is generally thought to be able to hold up to two ions at one time [29, 30]. Some of these experiments suggest a saturating concentration

dependence suggesting a single ion mechanism [29-31], whereas others, who have examined a larger variety of concentration and may therefore be more reliable [7], see a more complex relationship which may be explained by a multi ion conduction mechanism [32].

Furthermore, when there are several ions participating cooperatively in ion conduction in a single file pore, the ion fluxes are thought to be coupled [33]. If there is no flux coupling, the influx and efflux at a certain membrane potential should depend linearly on the ion concentration [34]. As eq.1.14 is assuming independence, it can be separated into the efflux, $J_{s,out}$, and the influx, $J_{s,in}$, as

$$J_{s,out} = P_S z_S^2 \frac{\phi F^2}{RT} \frac{c_1}{1 - e^{-z_S \frac{\phi F}{RT}}} \quad (1.17)$$

$$J_{s,in} = P_S z_S^2 \frac{\phi F^2}{RT} \frac{c_2}{1 - e^{z_S \frac{\phi F}{RT}}} \quad (1.18)$$

These equations simplify considerably if the ratio between the influx and efflux instead is studied. The Ussing flux ratio expression [34] is then obtained

$$\frac{J_{s,out}}{J_{s,in}} = \frac{c_1}{c_2} e^{z_S \frac{\phi F}{RT}} \quad (1.19)$$

However, it can be shown that this is not always the case and that the ions act more like several ions moving as one multivalent unit rather than as single ions. The likelihood of a unit of n ions to form is dependent on the concentration. An increase in concentration increases this chance. The flux then varies with the electrochemical activities raised to the power of a constant, the flux coupling exponent, n' , [33]

$$\frac{J_{s,out}}{J_{s,in}} = \left(\frac{c_1}{c_2} e^{z_S \frac{\phi F}{RT}} \right)^{n'} = e^{n' z_S (\phi - \phi_s) F / RT} \quad (1.20)$$

When $n' > 1$ the conduction mechanism involves multiple ions. Measurements of n' in K_v channels show an n' of 1.5-3.3, suggesting permeation in a multi-ion pore [35]. The existence of multiple ions in the pore of K_{vs} has further been

confirmed by structures of the K_vs [12, 36]. The flux coupling has been investigated also in mammalian Na_vs and n' has been found to be 1-1.15, suggesting a single ion mechanism [30, 37, 38]. However, as mentioned above, the flux coupling experiment is reliant on a single file conduction mechanism as the flux coupling exponent in effect is measuring how one ion is pushing another ion along [33]. The effect is also enhanced by a longer SF as it takes more collisions to translocate an ion through the whole SF [33]. In a wider SF where ions interact but could pass each other this effect would be lost. As mentioned above, the SF of Na_vs is both wider and shorter than that of K_vs. Furthermore, our simulations have shown that ions can pass by each other in the SF of the mammalian Na_vs (see Chapter 5 for further discussion). This is supported by the large size, $\sim 3 \times 5$ Å [28], and high flexibility of the SF [39]. Therefore, the correlation between ion occupancy and the flux ratio exponent may not be as direct in Na_vs as it is in the single file K_vs [40].

A consequence from eq.1.16 is that if the mole fraction of a bionic mixture is varied while the total concentration is held fixed the conductance decreases with decreasing fraction of the highest conducting ion [22, 23]. However, sometimes anomalous mole fraction effects, where the conductance goes through a minimum, can be observed. In these cases the channel conductance is higher for the single ion solutions than the mixed solutions for both ion species [41, 42]. This has been explained by lack of independence due to an single file conduction that is reliant on multiple ions that cooperate [43]. Investigations in K_vs and bacterial Na_vs have shown an anomalous mole fraction effect [27, 42], whereas mammalian Na_vs lack this effect [32]. However, recent investigations have shown that the anomalous mole fraction effect is dependent on what theory is used to interpret the data and can instead be explained by other reasons, including preferential binding of one splices over the other and localized ion binding [44-46]. Traditionally ion channels are studied assuming rigid narrow channels where ions move over static barriers and bind to static sites. However, ion channels are not static but rather dynamic macromolecules [39, 47-49]. The energetic profile of ion conduction is therefore also dynamical and may change according to conditions [49, 50]. The proofs for multi ion conduction in K_vs are overwhelming [12, 35, 36], whereas there are several contradictory theories about the conduction mechanism in Na_vs. Therefore MD simulations can act as a useful tool to help us elucidate the ion conduction

mechanism of Na_vS.

Furthermore, mutagenesis experiments, where specific residues in an ion channel are changed, can be used to pinpoint exactly which residues are likely to be part of these binding sites by showing a loss of permeability for the native ion and/or increase in permeability for non-native ions [51]. Multiple sites and multiple ion occupancy lead to a complex permeation mechanism that can be responsible for the ion selectivity (Fig.1.9).

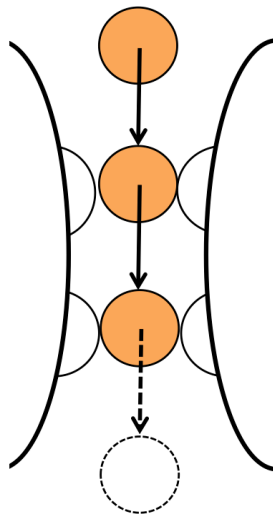


Figure 1.9. An ion enters the SF from above (orange ball) and knocks the ions already in the SF into the channel.

K_vs have a funnel-like SF fitting a dehydrated K⁺ ion perfectly. The SF is lined with the backbone carbonyls of the amino acids that form the SF (Fig.1.10). There are five K⁺ binding sites in the SF, S₀-S₄, these are all made up by a cage of eight neighbouring carbonyl oxygen atoms that coordinate the K⁺ ion. There are 2-3 K⁺ ions in the SF at each time and the ions are separated by one single water molecule. Each of the K⁺ ions and water molecules occupies a binding site [48]. The K⁺ ion conduction has been shown to be reliant on a single file multi-ion knock on mechanism. When an additional ion approaches the channel from the intracellular side it knocks on the ions in the SF resulting in the bottom ion getting knocked into the channel (Fig.1.9) [47, 52, 53].

Recent atomic-scale structures of bacterial Na_vS [54-58] have shown a SF that is flexible and lined with the side chains of the amino acids in the SF. Thus it is

the side chains that are responsible for interactions with the Na^+ ions in the Na_v , rather than the backbone, as in the K_v s. Three binding sites have been identified, S_{HFS} , S_{CEN} and S_{IN} where S_{HFS} is a high field strength site made up by a ring of four Glus (EEEE) (Fig.1.10b) [54]. The conduction mechanism has been proposed to be reliant on a multi-ion knock-on mechanism also in bacterial Na_v s [49, 59, 60]. However, rather than a single file mechanism, the wide Na_v filter allows for a more complicated mechanism [49, 59]. Furthermore, experiments have shown that it is possible to create a Ca^{2+} selective channel by mutating a few of the residues in and around the SF of the bacterial Na_v . This voltage-gated calcium channel (Ca_v) has three Asp rings that make it Ca^{2+} selective [21].

These are examples of ion selective channels, however, the features of selectivity are subtle and subject to a number of factors, for reasons to be explored below. There are several different types of ion channels and they are more or less ion selective. To understand where this selectivity originates from we need to investigate the underlying molecular determinants.

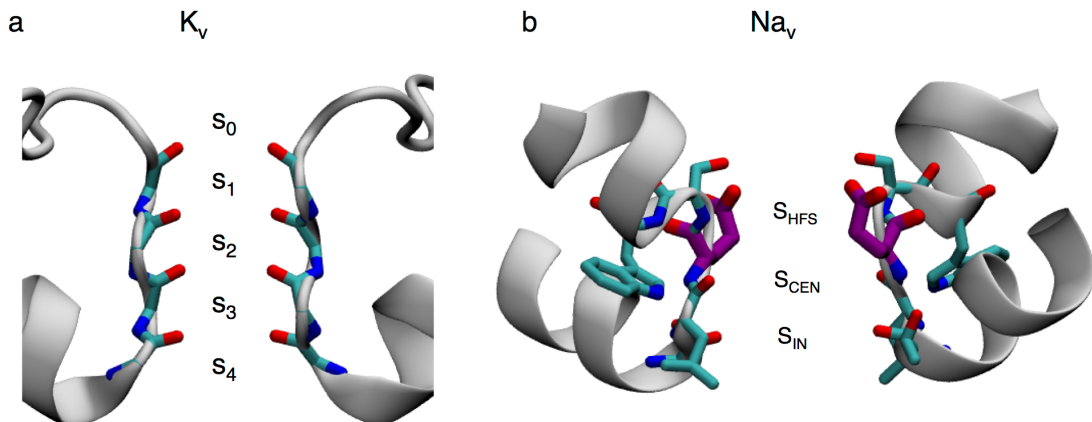


Figure 1.10. The SF of a) a K_v with the backbone of the SF residues shown(KcsA, PDB:1R3J) and b) a Na_v with the side chains and backbone of the SF shown as well as the S_{HFS} Glus highlighted in purple (Na_vAb , PDB:3RVY). Their respective binding sites are marked out. Only two out of four domains are shown.

1.6 Molecular determinants of ion selectivity

The size/charge ratio of an ion determines the strength of the ion-anion/dipole interaction; increasing the charge and/or decreasing the radius increases the

charge density and therefore also the interaction energy. Due to the polar nature of water molecules, a hydration shell surrounds ions in the aqueous bulk surrounding. The strength of the water-ion interaction depends on the size and charge of the ion. Both Na^+ and K^+ are strongly hydrated in bulk, however the smaller Na^+ ions more so than K^+ , with a hydration free energy of -98 kcal/mol and -80 kcal/mol respectively (Table 2) [24]. Due to the high charge and small size Ca^{2+} has a very large hydration energy of -381 kcal/mol (Table 1.2) [25].

To enter a channel the ions need to at least partly dehydrate, however, the pore of an ion channel is commonly lined with polar amino acids that can make up for the dehydration. In that way, ion selectivity can arise from the competition between the loss in hydration interactions and the energetic gain from interactions with protein groups in the channel [61]. The SF of K_vs is lined with carbonyl ligands creating a perfectly sized SF for K^+ ions (Fig.1.10a). Thus, in an oversimplified way selectivity has been hypothesised to be based on a snug fit mechanism that arises from a narrow pore fitting the preferred ion perfectly and being unable to adapt to other ions (Fig.1.11) [62]. This snug fit would allow direct interaction between the ion and the protein and therefore compensate for the hydration free energy for the preferred ion but not for smaller ions. However, numerous investigations of K_vs have shown that ion channels are flexible macromolecules with highly adaptable SF [47-49, 53]. This is emphasising the notion of size exclusion as being over simplified and that the SF in reality looks more like Fig.2.11b. The adaption of the SF to an initially poor fitting ion causes strain on the protein and adds an additional energetic component of strain energy. If the amino acids in the SF would be completely free to move this strain energy would be zero and selectivity would instead be governed by the ion-ligand and ligand-ligand interactions [63]. However, investigations of the strain energy in K_vs have shown that the SF is highly adaptable and that the strain energy is very small for the SF to adapt from fitting the larger K^+ to the smaller Na^+ [64].

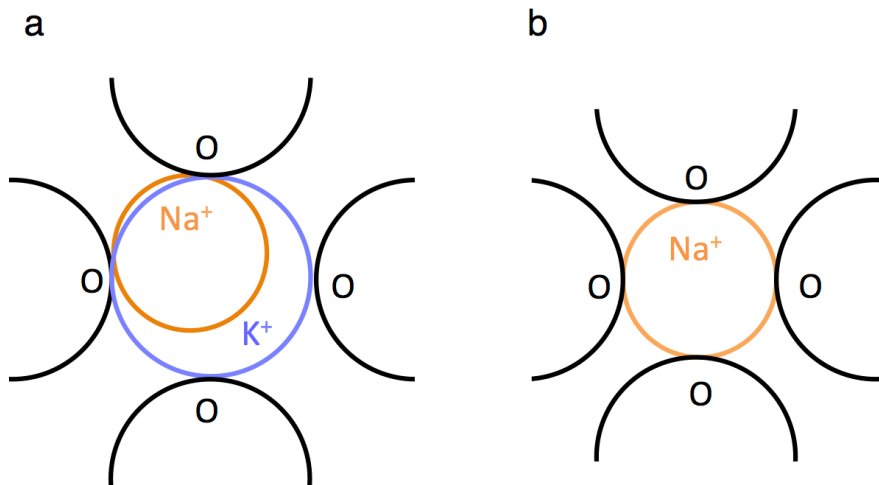


Figure 1.11. a) Illustration of an oversimplified ‘snug fit’ mechanism where the oxygen atoms of a K_v forms a cage that fits the K^+ ion perfectly but is too big for Na^+ which ends up with an interaction deficit. b) However, in reality, ion channels are flexible and can adapt to the size of the Na^+ ion.

The chemical properties of the ligands are important as increasing the charge and dipole moment of a ligand creates a stronger electric field. An ion with higher charge density prefers a strong field strength ligand as it can make up for the large partial dehydration cost whereas a ligand with low field strength can not [61]. Asp and Glu both have a side chain with a carboxylate group ($RCOO^-$) that is deprotonated in aqueous surroundings. The side chains of these are examples of strong field strength ligands, whereas carbonyl backbone of the protein creates comparatively weaker fields. As an illustration, the strongly hydrated Na^+ prefers binding to the side chains of the Na_v SF Glu as they can make up for the partial dehydration of the Na^+ ion.

A larger ligand coordination number can make up for weaker ion-ligand interactions [65]. However, there is a competition between the favourable ion-ligand energy and the unfavourable ligand-ligand energy [47]. A larger ion with a weaker ion-ligand interaction has a larger separation between the ions and the ligands and a smaller ligand-ligand repulsion [63]. K^+ , therefore, prefers a higher coordination number, which helps explain why the K_v SF is lined with sites consisting of a cage of eight backbone carbonyl oxygen atoms (Fig.1.10a). It has in fact been shown that decreasing the number of coordinating carbonyls in the K_v creates a Na^+ selective site [47].

However, to offset the high ligand-ligand cost of several high field strength ligands an additional ion can be added to the binding site. A binding site can thus consist of several ions collectively bound by a number of coordinated ligands. This increases the ion-ligand binding, in particular for an ion with a high electron density [66]. Therefore a binding site consisting of several high field strength ligands would prefer to bind several smaller ions like Na^+ . It has been shown that multi Na^+ complexes are indeed formed in the bacterial Na_v (Fig.1.12) [67].

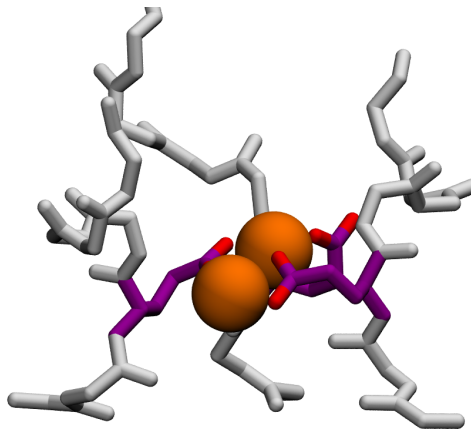


Figure 1.12. The SF of a bacterial Na_v (Na_vAb , PBD:3RVY). The S_{HFS} Glus (purple) are cooperatively binding 2 Na^+ ions in a tight complex. Only three out of four subunits are shown for clarity.

These arguments all have a basis in a thermodynamic preference, however, the kinetics of the ion conduction is also important. Even though the eight carbonyl atoms in the K_v creates a K^+ selective site, it can be shown that by positioning Na^+ in-between the carbonyl cages, a site consisting of four carbonyl oxygen atoms and two water molecules is created. Thus creating a site suited for Na^+ [52]. Therefore, also the kinetics of the ion selectivity must be taken into account. Ion conduction in K_v s has been shown to function via a multi-ion knock on mechanism (Fig.1.9) [48, 49, 68]. The principle is based on a balancing between the ion-ligand attraction and the ion-ion repulsion, creating a near barrier-less conduction. This multi-ion knock on principle infers that there will be a permanent ion in the SF that also makes it harder for other ions to enter it [69].

Furthermore, also the selectivity for Na^+ ions has been proposed to be reliant on a multi ion mechanism [59, 67]. However, the exact mechanisms involved

have not been elucidated yet. But the answer is likely a combination of the thermodynamical and kinetic factors. Moreover, the bacterial Na_v s accomplish Na^+ selectivity via a key site made up by four Glus, whereas the mammalian Na_v s make use of a ring of Glu, Asp, Lys and Ala (DEKA) [20, 51, 70]. The differences between these two key selectivity sites are remarkable; the bacterial Na_v s have four amino acids with negatively charged side chains whereas the mammalian only has two. Additionally, the mammalian Na_v has a positively charged residue, Lys. The ability of these two channels to select for the same ion further confirms the notion of Na^+ selectivity being a complicated mechanism. Because of this, it is important to study the whole energetic landscape rather than just the energetics of the specific interactions to understand ion selectivity.

Ion selectivity has been subject to extensive investigation both theoretically and experimentally for almost a century. Due to the availability of a range of atomic-scale structures for K^+ selective channels for ~20 years [12] the physical principles governing K^+ selectivity has been well described. However, it was only recently (2011) that the first structure of a Na^+ -selective channel was solved [54]. The recent structural information provides us with an excellent opportunity to investigate what governs ion selectivity in Na^+ selective channels. Together with the large quantity of experimental and theoretical data available, discussed in this chapter, we will clarify the mechanisms of Na^+ selectivity in ion channels.

Increased knowledge of ion selectivity will not only provide important fundamental knowledge about the function of ion channels, it will also have further applications. An example is in aiding the development of potential therapeutics. As ion channels take part in several vital functions of the body they are connected to several diseases, including epilepsy, pain and atrial and ventricular fibrillation [71, 72]. However, different types and subtypes of ion channels are responsible for different diseases, e.g. $\text{Na}_v1.1$ and $\text{Na}_v1.2$ has been connected to epilepsy whereas $\text{Na}_v1.3$ and $\text{Na}_v1.7-1.9$ to pain [73]. However, due to the similarity of these ion channels and the lack of the specificity of the drug, drugs that target one type of ion channel often influence the functions of other channels leading to toxicity [73]. These drugs sometimes work by blocking the pore and outcompeting the binding of the native ion of the channel [74]. By

understanding the interactions between the ion and the channel we can learn about this competition and map down the key participants. This knowledge has the potential of being used to create more potent and precise drugs with lower toxicity.

Chapter 2

2 Structure and function of Na^+ -selective ion channels

2.1 Overview

Na^+ selective ion channels play key roles in the body where they participate in functions including propagation of nervous signals. These functions depend on them being able to select for Na^+ while discriminating against other ions. As discussed in Chapter 1, there are numerous factors involved in ion selectivity. The underlying molecular mechanisms of ion selectivity in Na^+ channels are unknown but the recently solved atomic scale Na^+ channel structures present an opportunity for elucidating these mechanisms.

There are only a few strongly Na^+ selective ion channels; these include $\text{Na}_{\text{v}s}$, epithelial sodium channels, degenerins (ENaC/DEGs) and ASICs. Furthermore, atomic scale structural information about these channels is limited to that of $\text{Na}_{\text{v}s}$ and ASICs. The structure and function of these channels differ substantially from each other; $\text{Na}_{\text{v}s}$ are tetramers that open and close in response to a membrane depolarisation, whereas ASICs are trimeric channels that are voltage independent, ligand gated ion channels that instead respond to a change in pH. Furthermore, it has been proposed that the selectivity mechanism is governed by different mechanisms. With the mammalian $\text{Na}_{\text{v}s}$ making use of a highly flexible ring of Asp, Glu, Lys and Ala to select for Na^+ , whereas the selectivity mechanism in ASICs have been proposed to rely on a size-constriction site made up by Gly, Ala and Ser. However, the evidence for

such a constriction site in ASICs are incomplete [15]. To understand what governs the mechanism of Na^+ selective ion channels we have investigated these evolutionarily, structurally and functionally distinct ion channel systems in the search for the underlying fundamentals of selective Na^+ conduction.

2.2 Introduction

The evolutionarily connection between ion channels appears to generally be through gating mechanisms and structure rather than selectivity type. Therefore, it is an open question of how Na^+ selective ion channels developed selectivity for the same ionic species regardless of evolutionary path. Na_vs , ENaCs and ASICs are all strongly Na^+ selective ion channels. The magnitude of the Na^+/K^+ selectivity in these channels differ with ENaCs being the most selective with $P_{\text{Na}^+}/P_{\text{K}^+} \sim 100-500$ [75, 76] and ASICs the least with $P_{\text{Na}^+}/P_{\text{K}^+} \sim 3-13$ [77]. Mammalian Na_vs select for Na^+ with $P_{\text{Na}^+}/P_{\text{K}^+} \sim 10-20$ [7] and bacterial Na_vs with $P_{\text{Na}^+}/P_{\text{K}^+} \sim 5-170$ [26, 27, 78]. There are a number of other channels that conduct Na^+ ions, including, nicotine acetylcholine receptors, glutamate receptors and cyclic nucleotide gated channels; however, these are all regarded as low or non-selective.

2.3 Voltage gated Na^+ channels

Voltage-gated sodium channels (Na_vs) play an essential role in electrical signalling in the body and are necessary for many functions including heart rate and rhythm, muscle contraction and brain activity [7]. These functions rely on the ability of Na_vs to select for Na^+ over K^+ with a great precision (1:10-20) [7] and at a fast pace [79]. Recently, the first high-resolution x-ray structure of a Na_v was solved, the bacterial Na_vAb [54]. After this, a number atomic detail structures of bacterial Na_vs have been presented, including Na_vRh [55], $\text{Na}_v\text{Aep1}$ [56] and the proposed open Na_vMs [57, 58]. These structures have provided knowledge about the architecture of the Na_v on a molecular level and provide an opportunity to investigate these.

2.3.1 Structure of Na_vs

The structures of the mammalian and bacterial Na_vs have a high level of homology. Importantly, the pore forming subunit of the channels share several

features including their structure/fold [20]. Mammalian Na_v s consist of four domains, DI-DIV, linked together to form one long polypeptide chain, whereas the simpler bacterial channels are made up of four identical subunits (Fig.2.1) [20]. Each of the domains/subunits consists of 6 helical trans-membrane spanning segments, S1-S6. S1-S4 make up a voltage sensor responsible for opening and closing the channel and S5-S6 make up a pore domain that creates a funnel through the cell membrane. Between S5-S6 is a pore-loop (P-loop) where the narrow ion SF is located (Fig.2.2) [20]. This P-loop is made up by two short helices, P1 and P2, connected by the SF. In eukaryotes P2 is connected to a large extracellular loop. Regardless, the SF is similarly positioned at the entrance of the pore both in eukaryotic and prokaryotic Na_v s (Fig.2.2) [20]. The eukaryotic Na_v also have intracellular loops connecting the different domains, where the DIII-DIV loop is important for rapid inactivation of the channel (Fig.2.1, red loop) [80].

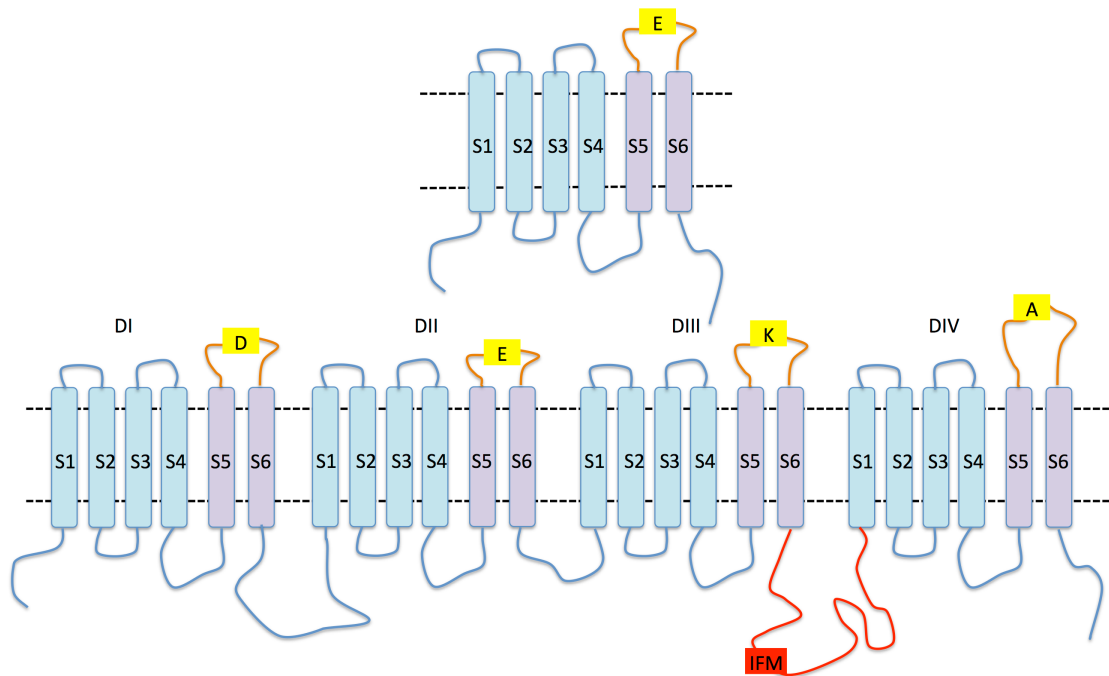


Figure 2.1. Sketch of the structure of a bacterial (top) and mammalian (bottom) Na_v . The mammalian sodium channel has four domains linked into one long polypeptide chain whereas the bacterial sodium channel has four homologous subunits, DI-IV. Each domain/subunit consists of six segments, S1-6. The voltage sensor domains, S1-S4, are shown in blue, the pore domains, S5-S6, in purple, the p-loops in orange and the DIII-DIV loop in red.

2.3.2 Gating mechanisms of Na_v s

Na_v s cycle through three states: activated, inactivated and closed. The inactivated and closed states are both non-conducting. An action potential stimulates the voltage sensor and opens the gate. This leads to a selective inflow of ions. The activation and deactivation mechanisms of the Na_v s have been shown to be reliant on four to seven positively charged residues, usually Arg (R1-R7), at three residue intervals on the S4 helix, that form salt bridges with neighbouring negatively charged residues (Fig.2.2) [81]. When the membrane depolarises S4 moves outwards and rotates and the gating residues break and reform with the new neighbours, which stabilises the channel in an open confirmation (Fig.2.3) [5]. The movement of S4 pulls the S4-S5 linker out which interacts with residues in S3 and the intracellular end of S6. This allows a kink and rotation to form in the middle of S6 not present in the closed state, that widens the gate (Fig.2.3) [58].

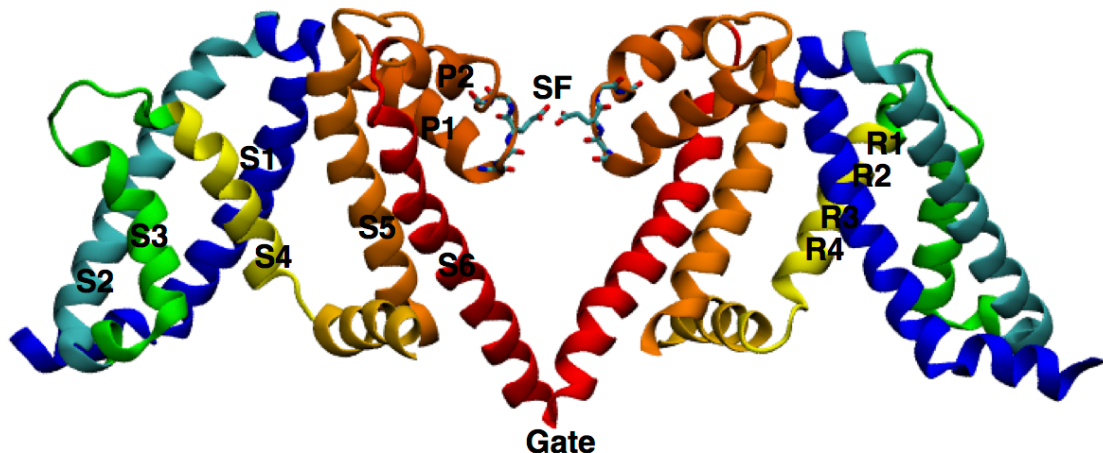


Figure 2.2. Structure of a bacterial Na_v , showing 2 of the four subunits for clarity, with each segment (S1-S6), P1 and P2 helices, the SF, intracellular gate and gating charges (R1-R4) marked.

Shortly, on the scale of milliseconds, after the opening, the channel becomes inactivated. The inactivation period acts as a refractory period during which the channel is unresponsive to membrane depolarisation [20]. A ball and chain swings into the intracellular end of the pore stopping the influx of ions and inactivates the channel. The DIII-DIV loop has been found to be responsible for this mechanism and in particular the hydrophobic residues Ile, Phe and Met (IFM), which acts as a latch that stabilises the blocking of the gate [80]. This fast inactivation is important for rapid firing of impulses through the axon as it

ensures that the action potential can only travel in one direction and that the membrane potential is restored [20]. Prokaryotic Na_vs lack the DIII-DIV loop and do not undergo fast inactivation [20]. Furthermore, the crystal structure of a bacterial Na_v in the deactivated state [55][37][37][37][37][37] has shown a narrower SF assumed to be collapsed/closed [55]. Therefore, a collapsed SF has been proposed to relate to the inactivated state [55].



Figure 2.3. Structure on an open (red) and closed (grey and gold) Na_v [58].

When the resting potential has been restored the channel becomes deactivated and closed, this can take ms to minutes. Deactivation is distinctly different from inactivation in that it is not attributed to a specific part of the channel but is rather an overall change in the conformational state of the channel. Mutagenesis has shown changes in deactivation rates when alterations to the residues in and around the SF and gate of the S6 helices are made [67].

The activation state for the available atomic scale structures of bacterial Na_vs

varies. The pore domain of the Na_vAb and Na_vAe [54, 56] are in a deactivated state, Na_vRh is in an inactivated state [55] and Na_vMs in a proposed activated state [57, 58]. Recently, an additional structure of Na_vAb has been presented, where it has been proposed to be in an activated state [82]. The structures that are deactivated or inactivated have a closed gate. Therefore no continuous pore can be seen. However, the SF is open and can therefore be investigated [49, 54, 56, 59].

Recently the first eukaryotic Na_v was presented; Na_vPaS from American cockroach [14]. It has a 36-46% sequence identity to human Na_v [14], compared to 25-30% sequence identity between bacterial and human Na_vs [58]. It is shorter than the mammalian Na_v with 1553 residues compared to 1800-2050 residues. However, it has the same key SF residues as the mammalian Na_v (made up by DEKA) but differences in other part of the SF. The structure shows that the residues of the SF are asymmetrical in height [14].

2.3.3 Selectivity in Na_vs

Early mutagenesis experiments suggested that it is the chemistry of the side chains of the amino acids in the SF of Na_vs that is responsible for ion selectivity [7, 51, 70], as opposed to the backbone of the amino acids in K_vs [7]. The key residues responsible for this selectivity have been shown to be a ring of Glu, Asp, Lys and Ala (DEKA) in the SF of the human Na_v (Fig.2.4) [54]; while in its place the bacterial Na_v have four Glus (EEEE) [20, 51, 70]. This bacterial EEEE ring makes up a high field strength site (S_{HFS}) that is thought to be ideal for binding small cations such as Na^+ [54]. Regardless of these differences in SFs, bacterial and human Na_vs share the same ion preference fingerprint [7, 26, 27]. However, whether or not they are using the same or different mechanism to achieve this selectivity is yet to be determined.

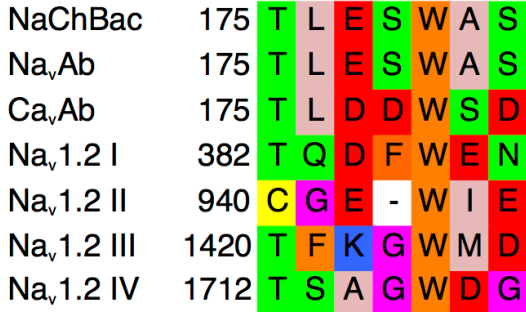


Figure 2.4. Sequence alignment of NaChBac, Na_vAb, Ca_vAb and Na_v1.2. Colour signifies amino acid properties. The amino acids are coloured according to their properties using the Zappo colouring scheme (Pink=Aliphatic/hydrophobic, orange=aromatic, blue=positive, red=negative, green=hydrophilic, magenta=conformationally special and yellow=cysteine) [83].

2.3.3.1 Selectivity in bacterial Na_vs

The first identification of a bacterial Na_v, NaChBac, was in 2001 by Ren *et al.* [26]. Experiments have shown a preference for Na⁺ over K⁺ of P_{Na+}/P_{K+}~5-171 and Na⁺ over Ca²⁺ of P_{Na+}/P_{Ca2+}~7-70 in bacterial Na_vs [26, 27, 78]. Sequence alignment of NaChBac with the mammalian Na_v identified the SF to be made up by the residues TLESWAS (Fig.2.4) [26]. The Glus (TLESWAS) were also identified as a key SF binding site. Furthermore, mutagenesis studies confirmed that these residues were responsible for selectivity as mutation of them altered the selectivity of NaChBac [78]. In particular, it has been shown that the preference for Na⁺ over K⁺ is decreased when the key Glus are mutated to Asps (TLDSWAS) [84]. Implying that not only the charge but also length of the Glu is important.

The S_{HFS} Glus of the bacterial Na_vs are also present in the SFs of bacterial and mammalian voltage gated Ca²⁺ channels [21]. Site directed mutagenesis has shown that adding Glus to the bacterial Na_v creates a Ca²⁺ selective channel [21]. In particular, it can be shown that increasing the number of charged residues in the SF steadily increases Ca²⁺ over Na⁺ selectivity (TLESWAS: P_{Na+}/P_{Ca2+}=6.7, TLESWAD: P_{Na+}/P_{Ca2+}=0.059, TLEDWAD: P_{Na+}/P_{Ca2+}=0.014, TLDDWAD: P_{Na+}/P_{Ca2+}=0.0075) [78]. The more residues that are transformed the more Ca²⁺ selective the channel becomes and when the Na_vAb SF is mutated to TLDDWAD a Ca²⁺ selective Ca_vAb can be created (Fig.2.4) [20].

The crystallisation of the first atomic scale structure of a bacterial Na_v, Na_vAb [54], provided further structural insight into their SF. The SF of Na_vAb is made up of a loop between P1 and P2 (Fig.2.2). The P2 helix breaks at Ser180 creating a funnel like SF that extends to Thr175 where the P1 helix forms (Fig.2.5). The width of the SF allows partly hydrated Na⁺ ions to permeate [85]. The SF is made up of the side chains of the Glu177 and the backbone carbonyls of the Thr175 and Leu176 [54], where the ring of Glus forms a high field strength ion binding site (S_{HFS}) [54]. It has been postulated that two additional sites ideal for binding Na⁺ ions are comprised of the backbone carbonyls of Leu (S_{CEN}) and carbonyl and hydroxyls of Thr (S_{IN}) (TLESWAS) [27, 49, 54, 68]. Furthermore, an additional external site has been identified in the vestibule of the SF [56, 60].

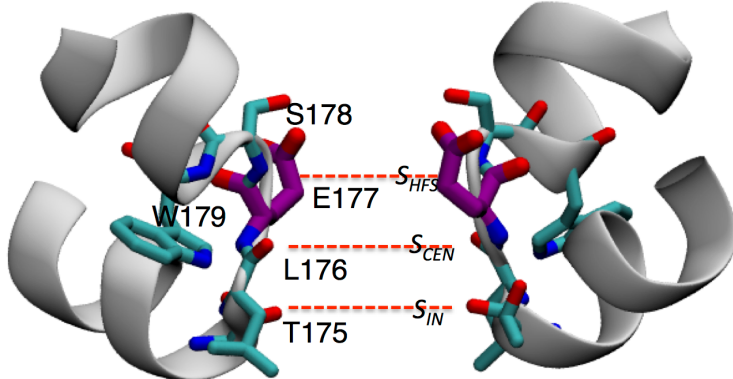


Figure 2.5. SF of Na_vAb with the residues 175-178 shown in cyan and marked out. The S_{HFS} Glus are shown in purple and the binding sites are shown in red dashed lines.

This structural information is highly informative, however, its limitations should be noted. Namely, the x-ray structure is only a snapshot of the ion channel in a non-physical environment. Crystallisation and freezing, as well as the lack of a membrane, may result in the protein being in a conformation different to that of its native state. Furthermore, flexible parts of the protein are complex to fit with certainty due to their electron density map being less well defined. Therefore, it is paramount not to draw conclusions from the structures alone [86]. MD stimulations provide the ability to investigate these structures in a dynamic context where the structural flexibility of the channels is accounted for.

MD simulations have shown an ion occupancy of one to four ions in the SF of the bacterial Na_v [49, 59, 84] and a conduction reliant on the transition between these states [49, 59]. Furthermore, they have shown that when a lone Na^+ ion occupies the SF it binds to the S_{HFS} Glus [27, 60]. Due to the charged and highly polar nature of the Glus, combined with the high charge/size ratio of Na^+ , this binding is strong and therefore single-ion conduction is associated with high energetic barriers [27, 49, 87].

Fig.2.6 show Na^+ ions in a bacterial Na_v where the movement of the ions is represented in terms of free energy projections (reproduced free energy maps and snapshots from Boiteux *et al.* [49]). When there are two ions in the SF, Fig.2.6a, the z-position of the top ion z_2 is shown with respect to the z-position of the bottom ion z_1 . The ions move between the S_{HFS} , S_{CEN} and S_{IN} and three states can be seen; A, B_1 and C_1 . There is always an ion occupying the S_{HFS} . In state A, the bottom ion is occupying S_{IN} and in state B_1 the bottom ion is occupying S_{CEN} . In state C_1 both ions are bound together by the Glus in the S_{HFS} . When there are two ions in the SF the ions appear trapped.

When a third ion enters the SF, with z-position z_3 , four states can be seen; A, B_2 , C_2 and D_2 . Fig.2.6b shows the centre of mass of the two top ions at z_{23} with respect to the bottom ion, z_1 . State A is the same state as in the two-ion case but with an additional ion entering from above. In state B_2 the top ion has moved into the SF and binds above the S_{HFS} ($z_{23}=4 \text{ \AA}$) while the bottom ion occupies the S_{IN} ($z_{13}=-4 \text{ \AA}$). In state C_2 the top two ions are both bound by the S_{HFS} Glus ($z_{23}=2 \text{ \AA}$). This knocks the bottom ion into the cavity by Coulomb repulsion while the top two ions stay bound to the S_{HFS} , leading to state D_2 . In Fig.2.6c the projection of the top two ions can be seen, at z_2 and z_3 . It is interesting to note that, due to the width and flexibility of the SF, the top ion can either knock-on or pass-by the middle ion in the S_{HFS} , with both paths showing similar energetic barriers (Fig.2.6c dashed line). It is evident that the addition of an ion lowers the energetic barrier for translocation by increasing the electrostatic repulsion, pushing the bottom ion into the cavity. This leads to a multi-ion knock-on or pass-by conduction reliant on a transition between two and three ion occupations. This 2/3-ion knock-on mechanism has been demonstrated to be reliant on the conformational isomerisation of the S_{HFS} Glus (Fig.2.6; insets) [49, 59].

Binding of Na^+ to the S_{HFS} Glus is central to understanding selectivity of Na^+ over K^+ . Furthermore, the permeation mechanism is reliant on a multi-ion knock-on mechanism where the dynamics of the ions and the amino acid side chains play an integral role [27, 49, 60, 87]. Other studies have found similar results [59]. However, studies focusing on 2-ion occupancies or fewer have proposed a 2-ion knock on mechanism where the top ion enters the SF and knocks the bottom ion into the cavity [60, 87].

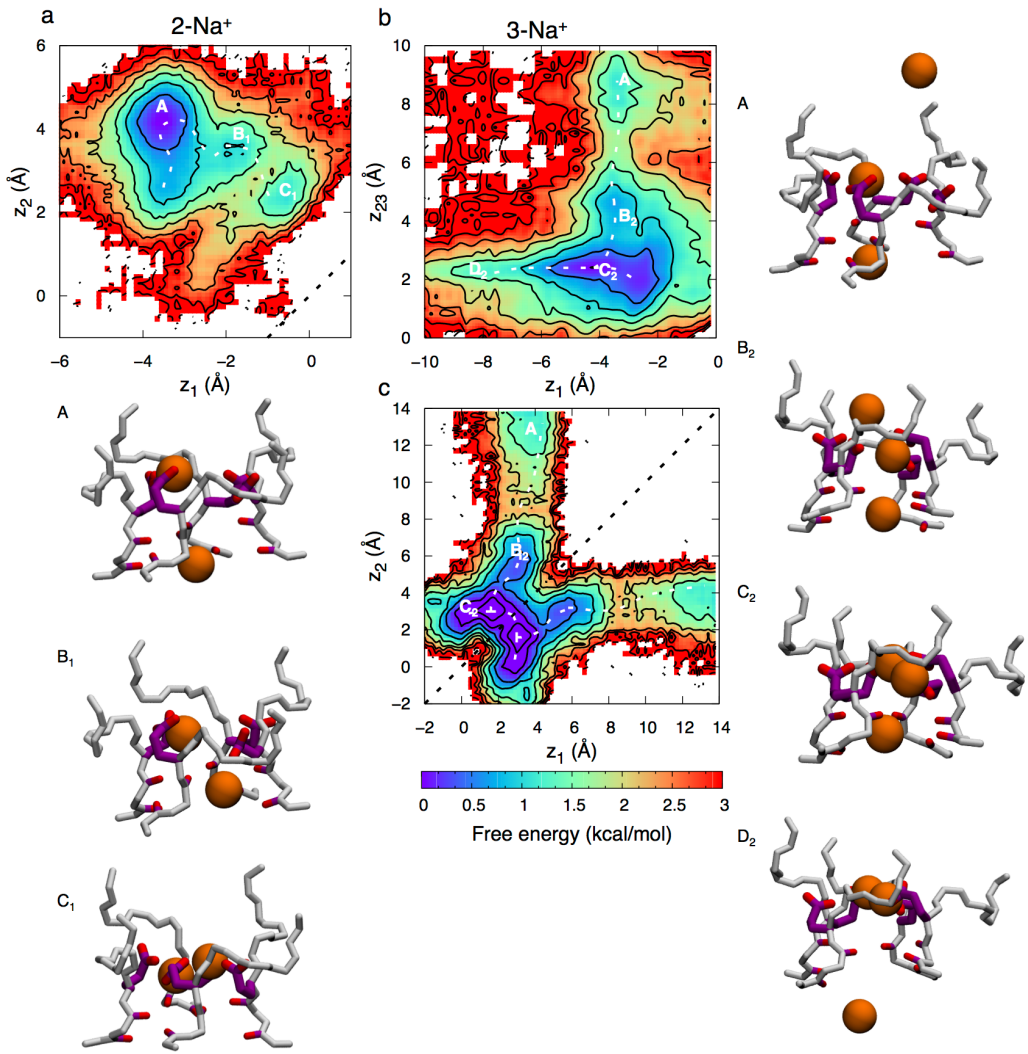


Figure 2.6. Na^+ in the SF of Na_vAb . 2D free energy projections showing a) 2-ion occupancy and b) 3-ion occupancy. z_1 corresponds to the z position of the bottom ion, z_{23} the z position of COM of the top two ions and z_3 the z position of the top ion. Snapshots with the EEEE ring in purple indicate the corresponding Na^+ ion (orange balls) movements [49].

To date, there has been limited use of MD simulations to investigate the selectivity mechanisms of Na^+ over Ca^{2+} in bacterial Na_v s. Previous MD simulations have proposed that $\text{Na}^+/\text{Ca}^{2+}$ selectivity originates from the large energetic cost of partial dehydration of Ca^{2+} not compensated for by the SF amino acids. Therefore, Ca^{2+} is energetically unfavourable in the SF of the bacterial Na_v [88]. Furthermore, it has been suggested that Na^+ ions can pass the Ca^{2+} in the SF and therefore Ca^{2+} is not a Na_v blocker [88, 89]. However, MD simulations have thus far not been able to contribute to our understanding of $\text{Na}^+/\text{Ca}^{2+}$ selectivity due to limitations in the MD force fields parameters related to the divalent Ca^{2+} ion (see Chapter 3 and 4 for more in depth discussion).

2.3.3.2 Selectivity in human Na_v s

The SF in mammalian sodium channels has a ring comprised of residues: Asp, Glu, Lys and Ala (DEKA) in contrast to the bacterial Na_v SF which has four Glus [51, 70]. Additionally, it has a charged ring in the outer vestibule of the SF made up of Glu, Glu, Asp and Asp ($\text{E}_\text{I}\text{E}_\text{II}\text{D}_\text{III}\text{D}_\text{IV}$) (Fig.2.4) [90]. Both of these rings are well conserved throughout all Na_v subtypes [91]. The residues in these two rings have been demonstrated to be asymmetrical in height [92] and highly flexible [39].

Site directed mutations have shown that the DEKA ring is crucial for the selectivity of Na^+ over K^+ [51, 70, 93]. In particular, it has been shown that having at least one of D and E preserves Na^+/K^+ selectivity [51]. The most important carboxylate in the DEKA ring is the E which together with the K_{1422} (the DEKA K is referred to by its $\text{hNa}_v1.2$ residue number to distinguish it from potassium), maintains WT selectivity despite mutation of D (WT: $P_K/P_{Na} = 0.03$, AEKA: $P_K/P_{Na} = 0.03$, DAKA: $P_K/P_{Na} = 0.09$) [51]. However, if the positions of these two residues are swapped, into DKEA, the selectivity is reduced (WT: $P_K/P_{Na} = 0.10$, DKEA: $P_K/P_{Na} = 0.37$) [93]. This demonstrates the importance of the positions of the residues; potentially due to their interactions with surrounding amino acids. Mutagenesis experiments have also shown that both the charge and length of K_{1422} is important for maintaining Na^+ selectivity. In these models, substitution of K_{1422} for amino acids with neutral side chains results in a complete loss of Na^+ selectivity [51].

Furthermore, substitution of K₁₄₂₂ with amino acids with negatively charged side chains shows a removed, or even reversed, selectivity (WT: P_{Na+}/P_{K+}=33, DEAA: P_{Na+}/P_{K+}=0.91, DECA: P_{Na+}/P_{K+}=0.83, DEFA: P_{Na+}/P_{K+}=1.0, DEHA: P_{Na+}/P_{K+}=1.4, DERA: P_{Na+}/P_{K+}=1.4) [51].

The vestibular EEDD-ring has also been shown to be important for ion conduction, presumably because it increases the electrostatic attraction of extracellular cations [91, 93-95]. Although all four residues are not equally important as cysteine mutations have shown that the greatest decrease in conduction occurs when domain II Glu is mutated (effect on conduction: E_{II}>E_I>D_{IV}~D_{III}) [92, 93]. The involvement of the EEEE ring in selectivity is unclear as some mutagenesis experiments have shown substitution of these residues have minimal to no effect on ion selectivity [93, 96]. However, other studies have found that ion selectivity, in particular for Li⁺ and K⁺, is altered when the outer ring is mutated [90, 92, 97].

Substitution experiments have also identified the K₁₄₂₂ and the A from the DEKA ring as being important for the selectivity of Na⁺ over Ca²⁺. Increasing the charge by mutating one or both of shows a channel highly permeable to Ca²⁺ [70]. The sequences of the Na_v and the Ca_v SFs show a higher number of amino acids with negatively charged side chains in Ca_v than Na_v (Fig.2.4). We would expect that by adding negative charges to the SF of the Na_v the channel would become more permeable to Ca²⁺. In fact, this is also seen when K₁₄₂₂ is mutated to neutral amino acids, with dramatic shift to Ca²⁺ selectivity (DEKA: P_{Na+}/P_{Ca2+}>100 [98], DEAA: P_{Na+}/P_{Ca2+}=0.054, DECA: P_{Na+}/P_{Ca2+}=0.060, DEFA: P_{Na+}/P_{Ca2+}=0.089, DEHA: P_{Na+}/P_{Ca2+}=0.29) [51].

Due to the lack of high-resolution structural data we are limited to results from experiments like these for understanding of what governs the selectivity of the mammalian Na_vs. Favre et al., who performed some of these experiments, speculated that selectivity in the Na_vs is a static process that is governed by a size constriction site made up by the Lys-Asp/Glu bond, creating a size and electrostatic environment more favourable to Na⁺ than K⁺ and Ca²⁺ [51]. However, models based on K_vs have proposed that selectivity is instead a dynamic process governed by the ability of Na⁺ to displace the ammonium group of the Lys [99, 100]. The static and dynamic theories are the two main

competing theories of Na^+ selectivity in Na_vs . Other models based on bacterial Na_vs have implied a greater thermodynamic preference for Na^+ in the lower SF, and an additional outer binding site at the EEDD-ring [68, 101]. To fully understand the movement of the Lys and the potentially dynamic multi-ion process of ion selectivity in Na_vs , we need to look at free simulations where the system is allowed to progress unconstrained for timescales that are physiologically relevant ($\sim\mu\text{s}$).

2.4 Na^+ selective Acid Sensing Ion Channels

ASICs are voltage independent, ligand gated channels activated by a change in extracellular pH [102]. They can only be found in mammals and they were only discovered in the mid 90s [103, 104]. Since the discovery, six different ASICs have been identified (ASIC1a, ASIC1b, ASIC2a, ASIC2b, ASIC3 and ASIC4) encoded by four different genes (ASIC1-4) [105]. ASICs are widely distributed both in the central and peripheral nervous system where they primarily participate in neuronal sensitivity to acidosis, as well as pain, taste, anxiety, retinal function and memory [106-109]. They have a high degree of homology between species, with, for example, mouse and human ASIC1a sharing 99% of their amino acid sequence [110]. ASICs are a proton-gated subgroup of the larger family of ENaCs/DEGs, with which they share high degree of sequence homology [111].

2.4.1 Structure of ASICs

A number of atomic scale structures of mammalian ASIC1 in different conformations have been described, including the closed PDB:2QTS [112], the psalmotoxin bound PDB:4FZ0 and PDB:4FZ1 [113] and the MitTx bound open PDB:4NTW [114]. This structural information has helped delineate the structure of the channel. ASICs consists of three homomeric or heteromeric subunits each containing 2 trans-membrane spanning domains (TM1 and TM2) connected by a large extracellular loop (Fig.2.7a). This loop makes up 60-70% of the protein and extends as far as 80 Å away from the membrane [112]. The trans-membrane domains are α -helical and together they create an hourglass shaped pore linking the extracellular side to the intracellular side of the membrane. On the intracellular side of the channel, connected to TM1 and

TM2, are a N and C termini, however these are not resolved in any of the existing x-ray structures [112-114]. At the extracellular side of the membrane the α -helices break and form coupled β -strands that form a wrist like junction connecting the TM domain and the extracellular loop [112]. The extracellular loop can be described with the shape of a hand (Fig.2.7b), with the palm being made up by 12 β -sheets connected to the wrist. Above the palm domain are α -helices connected by loops that make up a knuckle domain and a finger domain surrounding a β -ball. Also connected to the palm domain is a cysteine rich thumb domain that contains 7 disulphide bonds that stabilises the structure of the extracellular loop [112].

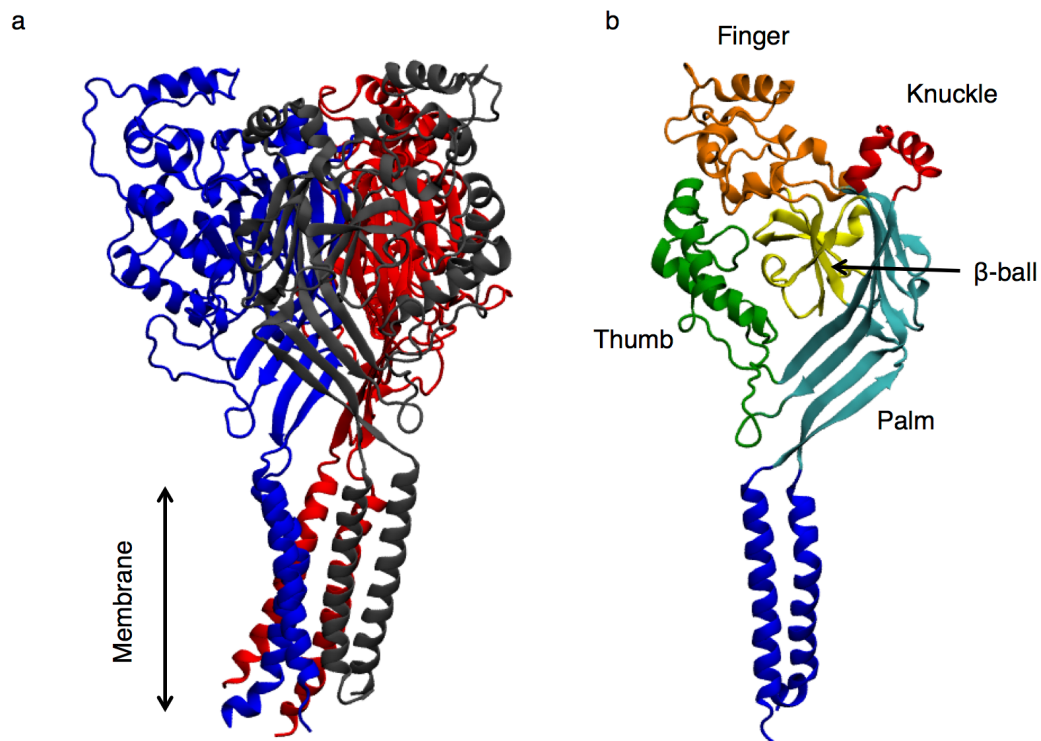


Figure 2.7. ASIC1a (PDB:2QTS) a) showing all three subunits and b) only showing one subunits with the domains in different colours: the palm in cyan, the knuckle in red, the finger in orange, the β -ball in yellow, the thumb in green and the trans-membrane domain in blue.

2.4.2 Gating mechanisms of Acid Sensing Ion Channels

At neutral pH the ASICs are closed or deactivated. A rapid decrease in extracellular pH opens the channel. After this, the channel quickly becomes desensitised and unresponsive to extracellular protons. When the pH increases the channel returns to a closed state. The pH sensitivity varies between the different types of channel, ASIC1 and ASIC3 open after only a slight decrease

in pH ($\text{pH} < 7.0$) whereas ASIC2 needs a substantial decrease in pH to open ($\text{pH} < 5.0$) [104, 115-119]. If the pH decrease is not large or rapid enough, the channel becomes desensitised and unresponsive to further change in pH [120].

The exact residues involved in proton sensing have not been established. However, Asp, Glu and His are likely candidates to respond to a change in pH [121]. It has been proposed that there are several proton-sensing sites spread out over the extracellular loop. There is an acidic pocket located between the thumb, β -ball and finger domains where a number of pH sensitive residues, that are well conserved throughout ASICs but not in other ENaC/DEGs, are located. These form carboxyl-carboxylate interactions in the open state of the channel and are therefore assumed to be protonated. This acidic pocket is thus hypothesised to be key to pH sensing. Furthermore, mutation of these residues show diminished functionality of the channel [112]. The proton binding in these sites is suggested to translate into movement of the thumb domain by binding and unbinding of the disulphide bond, this in turn moves and/or rotates the TMD and creates a permeable pore (Fig.2.7a) [112].

2.4.3 Selectivity in ASICs

ASICs are Na^+ selective, but also permeable to Li^+ , K^+ , Ca^{2+} and H^+ , and select Na^+ over K^+ with a ratio of 1:13 ($P_{\text{Na}^+}/P_{\text{Li}^+}=1.3$, $P_{\text{Na}^+}/P_{\text{K}^+}=13$, $P_{\text{Ca}^{2+}}/P_{\text{Li}^+}=2.5$ and $P_{\text{Na}^+}/P_{\text{H}^+}=0.8$) [104], similarly to Na_v channels. The extracellular concentration of Ca^{2+} influences the activity of ASIC; an increase in Ca^{2+} concentration has been shown to decrease the current, indicating that Ca^{2+} works as a ASIC blocker [104].

A highly conserved region throughout the whole family of ENaC/Degs, made up of Gly/Ser, X and Ser, can be found in the middle of TM2 (Fig.2.8). Experiments on ENaCs show a decrease in selectivity when the Ser of this triplet is mutated and it is therefore believed that these residues are responsible for ion selectivity [122]. Due to the similarities between ENaCs and ASICs, the idea that these residues make up the SF has been transferred to ASICs. In ASICs the residues in this location are Gly, Ala and Ser (GAS) (Fig.2.8) [111]. Furthermore, a recent ASIC1 crystal structure, PDB:4NTW [114], shows how the TM2 helix breaks into two short α -helices, TM1 and TM2, at the GAS

residues (Fig.2.9). The kinks from the three subunits together create a narrow constriction site of ~3.8 Å that appears, based on the crystal structure, to accommodate a hydrated Na⁺ ion precisely, while being too small for K⁺ [114] (Fig.2.9) [114]. Na⁺/K⁺ selectivity has therefore been suggested to be reliant on a size exclusion mechanism. However, the SF can accommodate the larger Cs⁺, and is therefore likely flexible [113]. Furthermore, the role of GAS as a SF has not been tested experimentally, because mutations in this part of the channel render ASICs non-functional [123-125].

	-8'	0'	4'	7'	10'	12'	15'	18'	21'	UniProt ID	
Chick_ASIC1	YEVAGLLGDI	GQMGLFIGASIL	T	VLELF	D					Q1XA76	
Mouse_ASIC1a	YEIAGLLGDI	GGQMGLFIGASIL	T	VLELF	D					Q6NXK8	
Mouse_ASIC2a	YEVAALLGD	I	GGQMGLFIGASIL	T	L	I	E	L	F	Q925H0	
Mouse_ASIC3	YEVSELLGD	I	GGQMGLFIGASLL	T	I	L	E	I	D	Q6X1Y6	
Mouse_ENaCa	VTMVSLLSNLGSQWSI	WFGSSVL	S	V	V	E	M	A	E	Q61180	
Mouse_ENaCb	NNIVWLLSNLGGQFGFW	MGGSVL	C	L	I	E	F	G	E	Q9WU38	
Mouse_ENaCg	NSIEMLLSNFGGQLGLW	MSCS	V	V	C	V	I	E	I	Q9WU39	
C. el_DEG-1	YGLVNLIADFGGHGLWL	GFSV	I	T	V	M	E	V	C	P24585	
C. el_MEC-4	YGFVNLLADFGQLGLW	CGIS	F	L	T	C	C	E	F	P24612	
Aplys_FaNaC	YGLADLFADIGGT	LGLWMG	I	S	V	L	T	I	M	E	Q4H3X6
Hydra_HyNaC2	YDFYKLIGDVGGQLGL	LLLGASV	L	T	V	E	F	V	D	A8DZR6	

Figure 2.8. Sequence alignment of TM2 for a range of ENaC/DEG channels. Conserved residues are highlighted in yellow. The numbering system of Lynac *et al.* is used [15].

Several other regions of the TM2 are well conserved throughout the ENaC/DEG family, in particular, E18' (Fig.2.8) (the numbering system of Lynac *et al.* is used [15]). Furthermore, one helical turn down is another charged ring of Asp in ASICs and Glu in ENaCs (E/D21') (Fig.2.8). Together these residues form two charged rings where the residues are close to each other (Fig.2.9). Moreover, the E18' has been noted in a study focusing on proton binding where they were found to bind Na⁺ ions [121].

Due to the high flexibility of ion channels, size exclusion is generally not thought to be responsible for ion selectivity [47-49]. Furthermore, there is a lack of experimental verification of the GAS selectivity mechanism in ASICs. This raises doubts to whether or not the GAS residues are responsible for selectivity in ASICs and leaves an open-ended question about how ASICs select for Na⁺ ions. As discussed above, Na⁺ selective channels often utilise a number of Glus

and Asps to select for Na^+ . The sequence alignment of ASICs show well conserved rings of Glus and Asps in the pore. This, together with the similarity in Na^+/K^+ permeability ratio for mammalian Na_v s and ASIC, may suggest that these channels utilise a similar mechanism for Na^+ selectivity and that there is an underlying common mechanism in how ion channels selects for Na^+ .

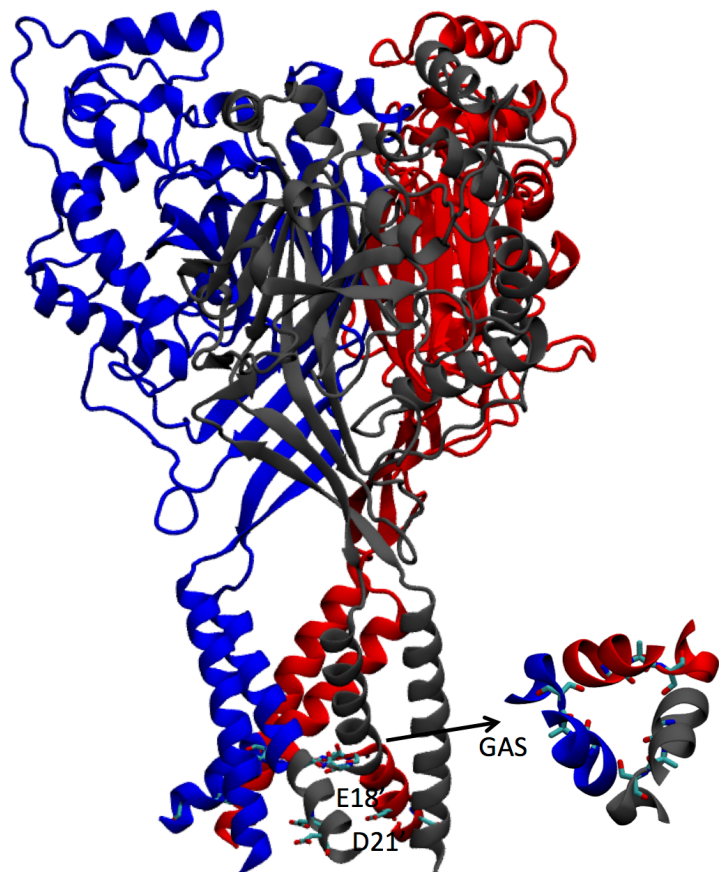


Figure 2.9. ASIC1a (PDB:4NTW) a) showing all three subunits with the GAS residues as well as E18' and D21' marked out and shown in cyan. Inset shows a top view of the GAS belt.

Chapter 3

3 Computational methods for molecular modelling

3.1 Overview

Computer simulations are becoming increasingly common and popular to complement experiments in the investigation of biological systems. Furthermore, they are very useful for investigating properties hard to examine in experiments, like those on short time and length scales. In MD simulations a classical view of the system is assumed and the atoms propagate according to Newton's equation of motion. The atoms in MD simulations interact according to a force field (FF) that consists of a potential energy function and pre-calculated parameters. In MD simulations we make use of a number of techniques to, for example, maintain thermodynamic ensemble, simulate a macroscopic system and calculate long-range forces. To be able to extract macroscopic properties, for comparison to experiments, from these microscopic simulations, statistical mechanics is used. Even though computers are becoming increasingly powerful, enhanced sampling methods are sometimes necessary. Umbrella sampling (US) holds the system near regular positions along a reaction coordinate to allow calculation of an equilibrium free energy profile. In free energy perturbation (FEP) the system is transformed from one state to another to give a path independent estimate of free energy differences between the two states. These are two techniques that are very useful when investigating ion selectivity and permeation. In Chapter 4, 5 and 6 I have used super computing with enhanced sampling methods to explore the short and long time scale processes associated with ion binding and permeation. This has

allowed me to quantify the mechanisms of ion selectivity and discrimination in a number of Na^+ selective ion channels.

3.2 Introduction

Most of our general understanding of ion selectivity and permeation comes from experiments. However, in experiments we often average over long time and/or length scales that encompass ensembles of systems. As discussed in Chapter 1, the speed of ion permeation through a channel fast, $>10^7$ ions can pass through an ion channel every second [20]. Furthermore, the atoms and molecules involved in this permeation are of the size scale of Å (10^{-10} m) [7]. For this reason molecular modelling is a useful tool to study biological systems at the atomic level. Furthermore, in molecular modelling theoretical predictions can be tested in simulations. Statistical mechanics can be used to connect the microscopic simulations to macroscopic experiments, that way connecting theory to experiments. There are several different levels of molecular modelling of biological systems. The most detailed way is to take a quantum mechanical view with Car-Perrinello Molecular Dynamics (CPMD) [126] where the valence electrons are explicitly taken into account. However, this is very computationally costly for large systems. If we assume that the electronic structure does not change sufficiently during the simulation a classical view of the system can be used with MD simulations. In MD simulations only the movement of the nucleus of the atom is considered. Further simplified methods can be used such as coarse-grained methods where fewer degrees of freedom are traced and a larger system can be studied. Classical atomistic MD provides a good compromise between speed and detail and is a powerful tool for biological systems due to their size and timescales [127].

3.3 Molecular Dynamics

In MD simulations the particles are allowed to interact and the trajectories are determined by numerical integration of Newton's equations of motion

$$\mathbf{F}_i(\mathbf{r}^N) = -\nabla_i U(\mathbf{r}^N) \quad (3.1)$$

$$\frac{\mathbf{F}_i(\mathbf{r}^N)}{m_i} = \frac{d^2\mathbf{r}_i}{dt^2} \quad (3.2)$$

where m_i , \mathbf{r}_i and \mathbf{a}_i are the mass, position and acceleration of the particle. MD assumes a classical description of the system and the propagation the particles are determined from the potential energy function $U(\mathbf{r}^N)$, where $\mathbf{r}^N = (\mathbf{r}_1, \mathbf{r}_2, \dots, \mathbf{r}_N)$ are the 3N coordinates of the system and \mathbf{r} a three dimensional position vector.

The differential equations are numerically solved by an integration algorithm. One of the most common ones is the Verlet algorithm [128] which is based on the Taylor expansion

$$\mathbf{r}_i(t + \delta t) = \mathbf{r}_i(t) + \frac{d\mathbf{r}_i(t)}{dt} \delta t + \frac{d^2\mathbf{r}_i(t)}{dt^2} \frac{\delta t^2}{2} + \dots \quad (3.3)$$

Given the position of the particle at time t we can determine their position at time $t + \delta t$. The Verlet algorithm combines $\mathbf{r}_i(t + \delta t)$ and $\mathbf{r}_i(t - \delta t)$, which gives

$$\mathbf{r}(t + \delta t) = 2\mathbf{r}_i(t) - \mathbf{r}_i(t - \delta t) + \delta t^2 \mathbf{a}_i(t) \quad (3.4)$$

which can be used to determine the propagation of the atoms. However, the Verlet algorithm lacks an explicit velocity term, although not needed to solve Newton's equation of motion, more commonly the Velocity-Verlet algorithm is used [129]. The Velocity-Verlet gives position, velocity and acceleration

$$\mathbf{r}_i(t + \delta t) = \mathbf{r}_i(t) + \mathbf{v}_i(t)\delta t + \frac{1}{2}\delta t^2 \mathbf{a}_i(t) \quad (3.5)$$

$$\mathbf{v}_i(t + \delta t) = \mathbf{v}_i(t) + \frac{\mathbf{a}_i(t) + \mathbf{a}_i(t + \delta t)}{2}\delta(t) \quad (3.6)$$

The time step decides the possible length of the trajectory but also the error. Furthermore, the fastest molecular motions limit the time step. To capture the vibrations of bonds to hydrogen atoms a time step of at most 1 fs should be used. However, in most MD simulations, all bonds with hydrogen atoms are

fixed at their equilibrium value to allow for a larger time step of ~ 2 fs. However, ion channel functions of interest span ns to μ s. For instance, the permeation of an ion through a channel can take 100s of ns [20] which means that we have to iterate the simulation $\sim 10^8$ times to observe a full permeation.

3.4 The ergodic hypothesis

We want to compare simulations to experiments, however, measurements from experiments generally tell us average properties over a large number of particles and over time. In MD we can measure the microscopic properties of the system; position and velocity. To be able to compare the two we need to be able to compute macroscopic properties from microscopic simulations. The positions, \mathbf{r} , and momenta, \mathbf{p} , of the particles define the microscopic state and the Hamiltonian, H , of a system with N particles can be written as

$$H(\mathbf{p}^N, \mathbf{r}^N) \quad (3.7)$$

The positions and momenta of these particles make up a phase space consisting of $6N$ dimensions. The system can be in any of these microstates and the collections of all states with the same macroscopic properties make up a macrostate that belongs to a thermodynamic ensemble. The ensemble is classified by its interaction with the surrounding. If it has constant number of particles, N , volume, V , and temperature, T , it belongs to the canonical NVT ensemble. However, the thermodynamic ensemble can instead be defined by constant number of particles, N , volume, V , and energy, E , and then belongs to the microcanonical NVE ensemble. For a biological system, where experimental measurements are made at constant temperature and pressure, it can be useful to instead define the system within the isothermal-isobaric NPT ensemble. The isothermal-isobaric ensemble has constant number of particles, N , pressure, P , and temperature, T .

For simplicity let's assume the canonical NVT ensemble for derivations. The canonical partition function, Z , counts the number of non-identical microstates corresponding to the particular NVT

$$Z(N, V, T) = \frac{1}{N! h^{3N}} \int \int e^{-H(\mathbf{p}^N, \mathbf{r}^N)/k_B T} d\mathbf{p}^N d\mathbf{r}^N \quad (3.8)$$

where k_B is Boltzmann's constant, h is Plank's constant and $N!$ appears due to over counting indistinguishable states.

The probability of finding the system in a particular state, $P(\mathbf{p}^N, \mathbf{r}^N)$, can be determined with the canonical Boltzmann distribution function

$$P(\mathbf{p}^N, \mathbf{r}^N) = \frac{e^{-H(\mathbf{p}^N, \mathbf{r}^N)/k_B T}}{Z} \quad (3.9)$$

Knowing the probability distribution we can determine the ensemble average of some observable $O(\mathbf{p}^N, \mathbf{r}^N)$

$$\langle O \rangle_{ensemble} = \int \int O(\mathbf{p}^N, \mathbf{r}^N) P(\mathbf{p}^N, \mathbf{r}^N) d\mathbf{p}^N d\mathbf{r}^N \quad (3.10)$$

However, to be able to calculate this we need to know the Boltzmann distribution function, eq.3.9. A system generally consists of a large number of particles and these can exist in a huge number of conformations. Therefore, it is extremely difficult to calculate eq.3.10. In MD we let the system evolve and, rather than knowing every state at one time, we follow the system for a certain time and instead determine the time average.

$$\langle O \rangle_{time} = \frac{1}{\tau} \int_1^\tau O(\mathbf{p}^N, \mathbf{r}^N) dt \quad (3.11)$$

Where t is the simulation time and τ the duration of the simulation. If we let the MD system evolve long enough so that its path passes through all states and is independent of initial configurations, we can reach the conclusion that the ensemble average and the time average will be the same

$$\lim_{\tau \rightarrow \infty} \langle O \rangle_{time} = \langle O \rangle_{ensemble} \quad (3.12)$$

This is called the ergodic hypothesis and also requires the system to be at equilibrium and that the whole phase space must be accessible to the particle. The ergodic hypothesis is central to MD simulations [130].

3.5 Force fields

In molecular dynamics, we ignore the motions of the electrons and instead only regard the motion of the centre of mass (COM) of the atom. This classical view uses an approximate potential energy function for the electronic quantum ground state and takes interaction within and between the molecules of the system into account. The potential energy function is called a force field (FF). The most common all-atom FFs are CHARMM [131], GROMOS [132] and AMBER[133].

The potential energy is determined as a pairwise additive sum for the atoms. It is calculated as the sum both of the intramolecular interactions: bond stretching, angle bending, dihedral angles, Urey-Bradley interactions and backbone dihedral pairs, and the intermolecular interactions: the van der Waals interaction, the short ranged electron repulsion and the electrostatic interaction

$$U(r^N) = U_B(r^N) + U_{NB}(r^N) \quad (3.13)$$

The intramolecular interactions in CHARMM FF are determined by

$$\begin{aligned} U_B(r^N) = & \sum_{bonds} K_b(b - b_0)^2 + \sum_{angles} K_\theta(\theta - \theta_0)^2 \\ & + \sum_{dihedrals} K_\phi(1 + \cos(n\phi - \delta)) \\ & + \sum_{Urey-Bradley} K_{ub}(r_{ik} - r_{ub})^2 \\ & + \sum_{impropers} K_u(u - u_0)^2 \end{aligned} \quad (3.14)$$

The first term in eq.3.14 describes the vibrational motion of the covalent bond between two atoms (i,j) at distance b (Fig.3.1a). The second term describes the angular vibrations, θ , that three bonded atoms create (i,j,k) (Fig.3.1b). The third term describes the dihedral angle, ϕ , between the planes, (i,j,k) and

(j,k,l) , created by four bonded atoms (i,j,k,l) (Fig.3.1c). The fourth term describes the non-covalent bond, r_{ik} , between the two outer atoms (i,k) of a group of three atoms (Fig.3.1d), and the fifth term is the improper dihedral angle, u , of 4 bonded atoms (i,j,k,l) , where i,j,l are all bonded to k (Fig.3.1e). The vibrational motion, angular bond, improper dihedral angle and Urey-Bradley are all strong and only fluctuate slightly from their equilibrium positions and they are therefore calculated with a harmonic potential, where X_0 is the equilibrium value and K_x the stiffness of the bond. The harmonic potential is used as it has a low computational cost and is accurate in low energy systems, such as biological systems. The behaviour of the dihedral angle is more complicated as dihedral rotations do not have a single deep distinct minimum but can rather rotate throughout all 360° . Furthermore, the rotations result in more dramatic movement of the atoms. Due to the periodic nature the potential energy for the dihedral angle, ϕ , is calculated with a sum of cosine functions that is dependent on the barrier high, K_ϕ , multiplicity, n , and the phase angle, δ .

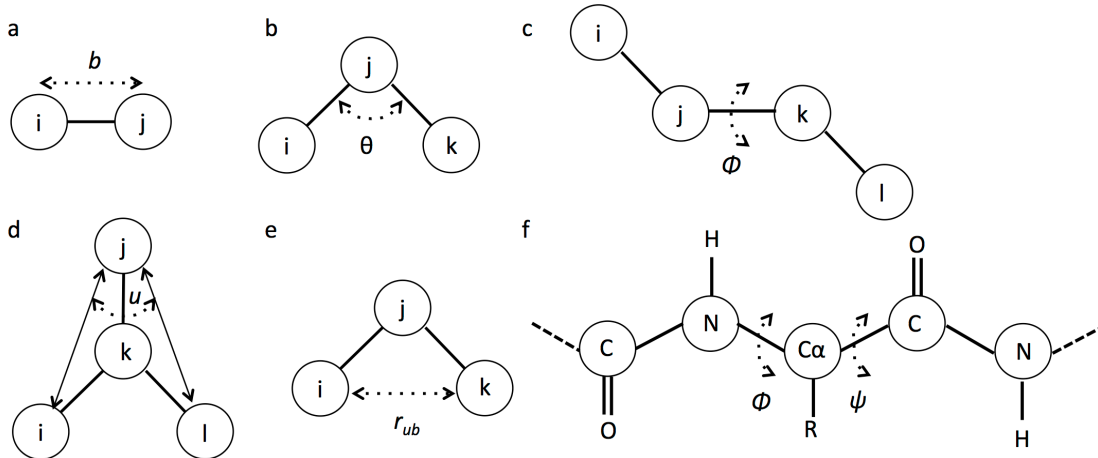


Figure 3.1. Coordinates for bonded interactions a) vibrations, b) angles, c) dihedral, d) improper dihedral, e) Urey-Bradley and f) the backbone dihedral pair for CMAP.

The coupled torsional rotation of the backbone of the protein is important for proper sampling of its confirmations. Studies have shown that the behaviour of certain peptides was deviating both from quantum mechanical calculations and experimental crystallographic data [134-137]. In particular, alanine dipeptides and glycine dipeptides show α -helical secondary structure experimentally,

whereas MD simulations of these showed them in a π -helical confirmation. To improve the torsional rotation a grid based coupled torsion correction map (CMAP) was created and added to the more recent CHARMM FF [138]. The CMAP adds a correction term based on the Ramachandran dihedral pair of the protein backbone torsion of two neighbouring dihedral angles (Fig.3.1f) [138]. The addition of the CMAP improves the conformational sampling of these peptides, as well as of the protein in general [139].

The CHARMM FF further uses the Lennard Jones 6-12 potential (LJ) to calculate the Van der Waals forces that appear due to the attraction between induced dipoles and the short range repulsion originating in the Pauli exclusion principle. The electrostatic interaction is determined with the Coulomb potential. The potential energy function for calculation of the non-bonded interactions thus becomes

$$U(r^N)_{NB} = \sum_{i \neq j} \left(\epsilon_{ij} \left(\left(\frac{r_{ij}^{min}}{r_{ij}} \right)^{12} - 2 \left(\frac{r_{ij}^{min}}{r_{ij}} \right)^6 \right) + \frac{q_i q_j}{4\pi\epsilon_0 r_{ij}} \right) \quad (3.15)$$

where r_{ij}^{min} represent the location of the energy minimum of depth ϵ_{ij} between atoms i and j (Fig.3.2). These are usually determined for self-interactions, therefore approximate combination rules are used to calculate the parameters between different types of atoms. Lorentz-Berthelot (LB) mixing rules are often used and combinations are determined as $\epsilon_{ij} = \sqrt{\epsilon_{ii}\epsilon_{jj}}$ and $r_{ij}^{min} = (r_{ii}^{min} + r_{jj}^{min})/2$ [140]. The intermolecular interactions apply to atoms not bonded to each other and are represented by a pairwise addition of forces. Interactions between atoms bonded by one, or more, common neighbours can be excluded or scaled. Many-body interactions are not explicitly taken into account in the intermolecular interaction potential. Occasionally the LB mixing rule is overridden and specific non-bonded fix (NBFIX) between the atom pair is introduced. These NBFIX parameters are made by adjusting the radius of the atoms involved and then comparing results from MD simulations to experimental results and, sometimes, quantum mechanical calculations. This way the pair specific interaction energy is optimised [141].

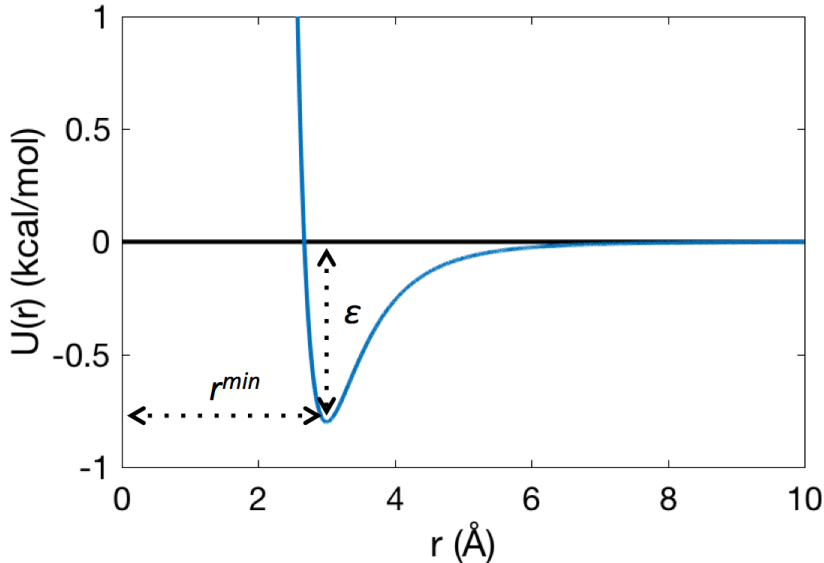


Figure 3.2. Illustration of the Lennard-Jones potential with the pair-specific r^{min} and ϵ marked.

The electrostatic interaction is determined by the Coulomb's potential. It is a long-range slowly decaying function that is inversely proportional to the separation between the atoms. The FF does not explicitly take polarisation into account instead the atomic charges, q_i , are fixed and placed so that they approximately represent the electronic distribution of the atom or molecule. It is well known that the charge distribution of an atom changes depending on its environment, and therefore this lack of polarisation reduces the FFs accuracy. Polarisation of atoms is prominent for the interaction of, for example, multi-ion complexes and multivalent ions.

The interaction potentials, eq.3.14 and eq.3.15, contain a number of atom specific parameters that generally are determined from a combination of experimental and theoretically calculated data. An optimisation is usually involved where results are fitted to experimental data, *i.e.* it is an empirical FF. This data includes solvation free energies, x-ray diffraction, vibrational spectra and densities [131]. Furthermore, parameters are commonly fitted to quantum mechanical calculations [131]. It is important to consider what phase simulations will be in; parameters optimised to mimic gas-phase may not properly represent behaviour in the condensed phase. Rather than determining the parameters for every single atom, the atoms are sorted into transferable groups where the contributions of the functional groups are assumed the same

and parameters for each groups are developed. These parameters are then used for every atom in that group regardless if they belong to different molecules [138].

The equilibrium positions, X_0 , multiplicity, n , and phase, δ , of the intramolecular parameters are generally determined by fitting model compounds to x-ray crystal structures, microwave diffraction structures or electron diffraction structures. The force constants, K_x , are then determined by fitting to vibrational spectra and conformational energies [131]. Quantum mechanical calculations are generally used as a complement to experimental data for fitting parameters to [131].

The parameters for the intermolecular interactions are created to properly represent protein-protein and protein-water interactions as the same non-bonded parameters are used both for protein-protein and protein-water interactions. Furthermore, the FF parameterisation aims to balance the protein-protein, protein-water and water-water interactions. CHARMM FF has been parameterised together with the TIP3P water model [131].

Water models can be separated by the number of interaction points they have. Increasing the number of interaction points improves the electrostatic distribution, however, the computational strain is also increased. The most commonly used water models are the 3-site models, which have three interaction sites. TIP3P [142] is a common type of 3-site water model and is used by CHARMM, AMBER and OPLS. Another common 3-site water model is SPC [143]. TIP3P and SPC have rigid H-O-H angles of 104.5 degrees and 109.5 degrees, respectively. Both the TIP3P and the SPC water models have been shown to overestimate the pure solvent diffusion coefficient compared to experiment, however, TIP3P more so than SPC [144]. When used in a biomolecular simulation, the solvent-solute and solvent-solvent interactions need to compensate each other, therefore, most crucial is to use a water model that has been developed to work together with the force field [142]. The parameters of the water molecules are usually fitted to experimental liquid density and the heat of vaporisation. There is a wide range of other water models available, including flexible models, 4 and 5 site models and models fitted to quantum mechanical data.

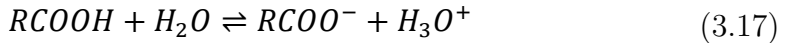
The assignment of partial atomic charges is based on reproduction of interaction energies and geometries from quantum mechanical calculations using the Hartree-Fock approximation with the 6-31G* basis set [131, 145]. The interaction between a model compound and a single water molecule (monohydrate) is calculated for a number of different orientations and positions and the interaction energy and distance determined. This allows for induced polarisation at each of the interaction sites to be taken into account. Although this approach has shown great success, this pre-polarisation sometimes lead to an overestimation of electrostatic charges [131].

The LJ parameters are optimised by performing condensed phase simulations of model compounds in infinite dilution. These are then fitted to experimentally measured data, including heat of vaporisation and molecular volumes [131]. However, investigations have shown that a number of different combinations of parameters can reproduce the same experimental data [146]. Therefore, quantum mechanical calculations of model compound interactions can be used as a complement to optimise the LJ parameters [147]. The interactions for the model compounds are optimised by an iterative procedure going through both bonded and non-bonded interactions until self consistent [131]. When the parameters for the model compounds are determined they are hierarchically transferred to the molecules by choosing the best-fit model.

The protonation state of the amino acids in the FF is fixed. The probability, p , of protonation of a residue depends on its equilibrium constant, $pK_a = -\log_{10} K_a$, and the pH of the surroundings, $pH = -\log_{10} H^+$, as

$$p = \frac{1}{1 + K_a/[H^+]} = \frac{1}{1 + K_a 10^{pH}} = \frac{1}{1 + 10^{pH - pK_a}} \quad (3.16)$$

Asp and Glu are common participants in ion selectivity and can be found in the SF of both eukaryotic and prokaryotic Navs. Asp and Glu have the side chain $RCOOH$ and both are deprotonated in a aqueous solution where they have $pK_a = 3.71$ and $pK_a = 4.15$ respectively



Another important amino acid for ion selectivity in eukaryotic Na_vs is Lys. The side chain of Lys has an amine group, RNH_2 . Lys is basic and is protonated in an aqueous bulk solution where it has $pK_a = 10.6$



However, in a protein all residues effect each other instead of acting independently and the protonation state of a residue can be very hard to determine [148]. Large pK_a shifts have been recorded in channel environments leading to altered protonation states compared to in an aqueous surrounding [149].

3.5.1 Polarisable models

The shapes of the electron distribution around molecules are known to change when they are in electric fields [150]. This is especially prevalent for highly polarisable molecules in a highly polar environment like the SF of an ion channel. As mentioned above, the fixed charge model does not explicitly take polarisability into account. This is one of the largest drawbacks with the FF described. However, there are a number of ways of adding polarisability to the classical FF. This is generally done by adding a polarisability term to the potential energy function, eq.3.13. Methods include using induced point dipole models [151], fluctuating charge models [152] and Drude particle models [153]. The induced dipole point model adds a polarisation energy to all polarisable atoms. The electrostatic field created by the rest of the atoms in the system is determined and used, together with the atomic polarisability for each atom of interest, to calculate the polarisation energy of the atom [151]. In the fluctuating charge model the charges of the atoms are treated as fictitious particles with mass and velocities. The charge positions are allowed to fluctuate and adapt their position according to the surrounding electric field [152]. A common way of adding polarisability is with the Drude particle model. In this model, polarisability is added via a virtual Drude particle to each non-hydrogen atom. The atomic charge is then distributed between the atom and the Drude particle [154]. The Drude particle can move in response to the electrostatic environment, which creates a redistribution of the atomic charge. An

interaction term is added to the potential energy function, eq.3.13, in which the electrostatic interactions between the Drude particle and the surrounding atoms are determined

$$U(r^N)_{Drude} = \sum_{i,j} \frac{q_{i,D}(q_j - q_{j,D})}{|r_{i,D} - r_j|} + \sum_{i,j} \frac{q_{i,D}(q_{j,D} - q_{j,D})}{|r_{i,D} - r_{j,D}|} + \frac{1}{2} \sum_{i,j} k_D |r_{i,D} - r_i|^2 \quad (3.19)$$

The Drude particle has a charge q_D and is attached to each atom with a spring with force constant k_D . This introduces the polarisability $\alpha_i = q_D^2/k_D$ to the atom. In the absence of an electric field the atom is unpolarised and the Drude particle is at $r_{i,D} = r_i$. To avoid instabilities in the simulations and polarisation catastrophes the Drude-atom bond distance, $|r_{i,D} - r_i|$, is not allowed to be longer than generally ~ 0.2 Å. Furthermore, minimal oscillations are ensured by keeping the Drude particle at a very low temperature. To avoid interaction between atoms bound to each other or bound by a common neighbour, 1-2 and 1-3 pairs are scaled with a Thole screening parameter [155]. This screening parameter can also be set to included non-bonded pairs within a cut-off distance, or specifically defined pairs, where over-polarisation is a problem [156].

An important aspect to have in mind when contemplating the use of polarisable FFs is that the parameters in the FF need to be optimised for inclusion of polarisability. Therefore a specific polarisable FF must be used. CHARMM has implemented and optimised a polarisable FF to use with Drude oscillators [157]. This Drude FF goes through a similar parameterisation procedure as the CHARMM FF [158]. Furthermore, a specific water model should be used. Commonly, a 3-point or a 4-point model is used where a Drude particle attached to the oxygen molecule. SWM4 is a 4-point model that either has a positively charged Drude particle, SWM4-DP, or negatively charged Drude particle, SWM4-NDP [157].

The addition of particles adds to the computational demands of the system, compounded by the fact that the forces need to be evaluated every ≤ 1 fs (compared to 2 fs for non-polarisable MD). Although, the computational time has been shown to scale only by a factor of 1.2-1.8 compared to non-polarisable

FFs [159]. Due to its potential for higher accuracy of electrostatic interactions, polarisable FFs are being widely explored [154].

3.6 Boundary conditions

Ion channels sit in large cellular membranes surrounded by water and ions stretching for μm . To be able to put the simulated system in a realistic environment we would need to simulate a system of this size. However, even though the computer power available is continuously increasing, it would be impossible to explicitly simulate this many molecules. Instead, a simulation system generally comprises of the order of $\sim 10^5$ atoms. Another artefacts arise by the atoms near the edge of the simulation box. In a biological system this portion is small compared to the total number of atoms, however, in a smaller system it becomes a large proportion of the particles and starts affecting the overall behaviour of the system.

To overcome the problem of size and boundary artefacts the system can be simulated with an implicit surrounding [160]. However, more commonly a periodic boundary condition (PBC) is used (Fig.3.3). The system is simulated in a box that is surrounded by an infinite number of images of itself leading to an infinite periodic lattice of boxes. The particles in all the image boxes move the same way as in the main box. As such, only the particles in the main box are simulated and kept track of and the computational cost kept to a minimum. Furthermore, if a particle leaves the main box it is translated and enters from the neighbouring box on the opposite face [129]. This way the number of particles in the box is conserved and boundary effects minimised. Several types of boxes can be used, most commonly, however, is to use an orthorhombic box (Fig.3.4).

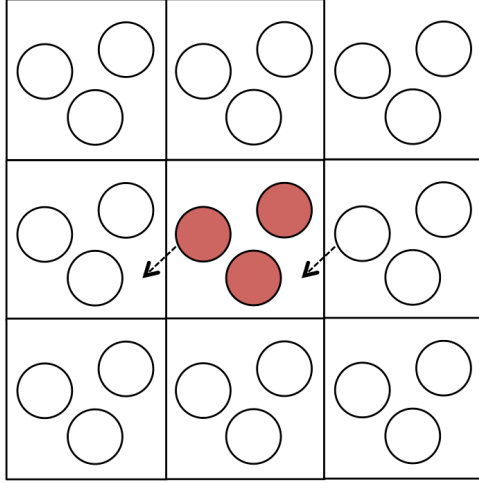


Figure 3.3. Periodic boundary condition. Every particle is mirrored in all boxes, as a particle moves out of the box, its mirror moves in to the box on the opposite side, red circles show the particles in the main box.

It is important to not use a too small box where the protein can interact with the image of itself. Furthermore, introducing an infinite number of images of the system introduces a problem of how to calculate long range (r_{ij}^{-x}) dependent interactions of the non-bonded potential energy, eq.3.15. The particles interact with their own images as well as the images of all other particles, for this reason the minimal image convention is introduced; a particle can only interact with the closest image of another particle, all other images are neglected [129]. Furthermore, the long range electrostatic interactions are conditionally convergent, *i.e.* the result depends on the order of summation, and are instead treated with the Ewald summation technique discussed below [130].

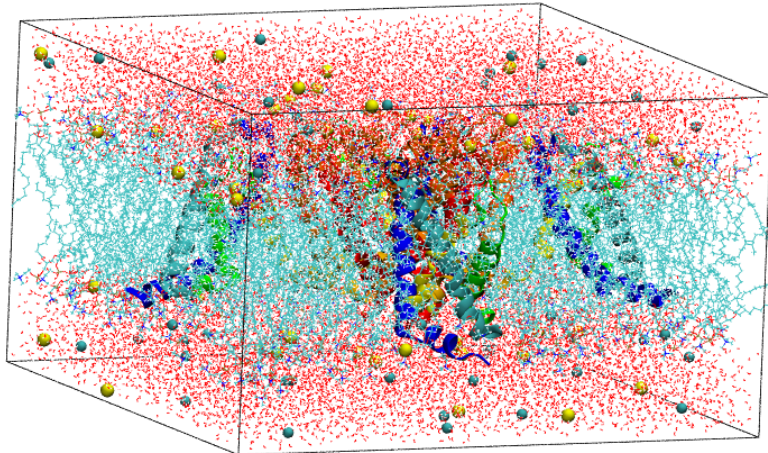


Figure 3.4.Typical MD simulation box containing a voltage-gated ion channel in a lipid membrane surrounded by water and ions.

3.7 Non-bonded interactions

Due to their long-ranged nature, calculation of non-bonded interactions can be very time-consuming in MD simulations. However, the interatomic potential energy that two atoms feel from each other is strongest at small distances, whereas due to its reciprocal relationship to r it plateaus at zero and the interaction energy becomes very small. Fig.3.2 shows the LJ interaction potential for two typical atoms, the energy can be seen to be very small for $r>8$ Å. Therefore, a common way to treat the LJ parameters is to use a cut off distance, r_c , where interactions beyond this are disregarded; this is generally a sphere of radius ~ 12 Å. The cut off distance must be large enough to take all non-negligible forces into account but must be smaller than half the size of the simulation box. To avoid a discontinuity a switching distance can be determined where the interatomic potential will be smoothed. To make the calculation of non-bonded interactions even more efficient, a Verlet neighbour list is can be used [128]. Rather than determining which atoms are within the cut-off distance at every step, a neighbour's list, with a larger radius, r_l , is made and only updated when the largest sum of the movement of a particle exceeds $r_l - r_c$. However, the Verlet neighbour list scales as $\mathcal{O}(N^2)$, hence, when the size of the system is large also this method is slow. Instead a grid based neighbour list is more commonly used. The simulation cell is divided up into M grid points with the sides larger than the cut of distance. The neighbours of

every particle in each box must therefore be within its own box or in one of the neighbouring boxes. This method is sufficiently faster and scales as $\mathcal{O}(N)$ [129].

3.8 Electrostatics with periodic boundary condition

The long range and electrostatic potential, eq.3.15, is dependent on $1/r_{ij}$ and is thus very slowly decaying. Furthermore, when PBC is used these interactions must be calculated for every image. The electrostatic potential with PBC can be written as

$$U_{electrostatic} = \frac{1}{2} \frac{1}{4\pi\epsilon_0} \sum_{\mathbf{n}} \sum_i \sum_j \frac{q_i q_j}{|\mathbf{r}_{ij} + \mathbf{nL}|} \quad (3.20)$$

Where \mathbf{n} is the lattice vector and \mathbf{L} is the dimension of the box. \mathbf{n} excludes all $i = j$ pairs and generally also pairs that are bound to each other and by a common neighbour, 1-3 pairs, in the same box, when $\mathbf{n} = 0$. The factor of $1/2$ has been introduced to correct for double counting. This is the most time consuming part of MD simulations. It converges slowly and the result is conditionally convergent. Instead, the electrostatic potential energy is calculated with Ewald summation [161]. The Ewald summation method splits the electrostatic energy into a fast converging part and a slowly converging part. The long ranged electrostatic interactions can be calculated with Fourier transformation, which converges quickly and absolutely. The electrostatic interactions originate from the electrical potential, ϕ , generated by the ions

$$U_{electrostatic} = \frac{1}{2} \sum_n q_i \phi_i(\mathbf{r}_i) \quad (3.21)$$

This potential originates from the charge distribution, ρ , according to Poisson's equation

$$\nabla^2 \phi_i(\mathbf{r}) = -\frac{\rho_i}{\epsilon_0} \quad (3.22)$$

The charge distribution from a number of point charges can be described by delta functions (Fig.3.5a). The idea is to add and subtract a Gaussian screening

distribution, $f(r)$, of exactly the same magnitude but opposite sign of the charges. This can be done by

$$\frac{1}{r} = \frac{f(r)}{r} + \frac{1-f(r)}{r} \quad (3.23)$$

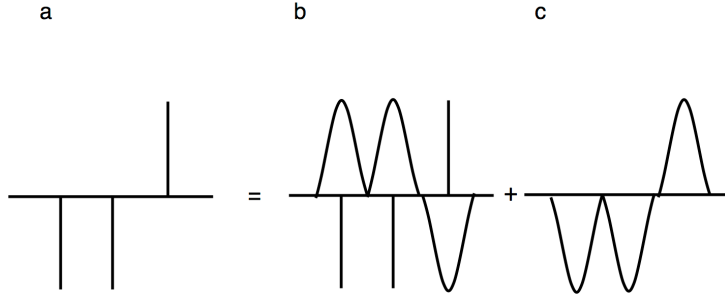


Figure 3.5. Illustration of the Ewald summation where a) represents the point charges and is equal to b) the point charges and the added Gaussian screening charges and c) the correction for the Gaussian screening charges.

This gives us one quickly converging part consisting of the charges and the opposite Gaussian distribution (Fig.3.5b), and one periodic part that can be calculated in the reciprocal space (Fig.3.5c). Poisson's equation is then solved for the contribution to the electrostatic potential energy. However, we also need to add a correction term for the self-interaction between the Gaussian screening charges giving $U^{el} = U^r + U^k + U^0$. The following expressions are obtained for the electrostatic potential energy

$$U^r = \frac{1}{2} \frac{1}{4\pi\epsilon_0} \sum_{\mathbf{n}} \sum_i \sum_j q_i q_j \frac{\text{erfc}(\alpha|\mathbf{r}_{ij} + \mathbf{n}|)}{|\mathbf{r}_{ij} + \mathbf{nL}|} \quad (3.24)$$

$$U^k = \frac{1}{2} \frac{1}{\epsilon_0 V} \sum_{\mathbf{k}} \sum_i \sum_j q_i q_j \frac{4\pi}{k^2} e^{-k^2/4\alpha^2} e^{-i\mathbf{kr}_{ij}} \quad (3.25)$$

$$U^0 = -\frac{\alpha}{\sqrt{\pi}} \sum_i q_i^2 \quad (3.26)$$

Where erfc is the complementary error function, α is the space partition parameter and \mathbf{k} a reciprocal lattice vector of periodic cell images. If the total charge of the system is non-zero additional terms are added [130].

Particle Mesh Ewald method [162] is an extension to Ewald summation where the reciprocal term U^k is approximated with the Fast-Fourier transform (FFT) onto a discrete grid. This reduces the computational cost from $\mathcal{O}(N^{3/2})$ to $\mathcal{O}(N \log N)$. The accuracy and speed is controlled by the space partitioning parameter, α , and the mesh size [129, 130].

3.9 Maintaining constant temperature and pressure

To simulate a physiologically relevant system we want to keep temperature constant with an isothermal-isobaric ensemble. A seemingly obvious way to obtain constant temperature is to rescale the velocities of the particles so that the kinetic energy gives the right temperature. The equipartition theorem relates the temperature to the kinetic energy

$$\langle K \rangle = \frac{3}{2} N k_B T \quad (3.27)$$

Rescaling of the velocities can be done with velocity scaling or Berendsen thermostat [163]. However, rescaling the temperatures gives a kinetic energy without fluctuations [130]. Hence, the Berendsen thermostat does not properly represent energy fluctuations in the system [130].

Instead, in the Andersen thermostat the velocity is at intervals randomly chosen and reassigned from the Maxwell-Boltzmann distribution; this represent exchange with a heat bath [163].

$$P(v_i) = \left(\frac{m_i}{2\pi k_B T} \right)^{1/2} e^{-\left(\frac{m_i v_i^2}{2\pi k_B T} \right)} \quad (3.28)$$

This can either be done for one particle at a time, fairly frequently, or all particles at once less frequently. The Anderson thermostat properly represents the ensemble probabilities. However, due the velocity change of the particles the velocities becomes uncorrelated ($v(t)$ is uncorrelated from $v(t-1)$) and the true molecular kinetics of the system is lost [130].

In the extended ensemble approach introduced by Nose [164] and modified by Hoover [165], called the Nose-Hoover thermostat, additional degrees of freedom are introduced into the Hamiltonian to represent a heat reservoir. The Hamiltonian can then be written as

$$H_{NVT} = \sum_i^N \frac{\mathbf{p}_i^2}{m_i} + U(\mathbf{r}^N) + \frac{p_\xi^2}{2Q} + 3Nk_B T \xi \quad (3.29)$$

where s is the position and Q the effective mass of the heat reservoir and frictional term determined from $\frac{d \ln s}{dt} = \xi$. The term $\frac{\xi^2}{2Q}$ can be thought of as the kinetic energy of the heat reservoir. The Nose-Hoover algorithm generates a canonical ensemble where the particles are deterministic. The choice of the parameter Q is important as it affects the size of the fluctuations for a given temperature. A small Q means low inertia of the system and leads to a rapidly fluctuating system, whereas a large Q leads to a slowly fluctuating one.

Additionally, pressure is constant in most biological systems; therefore an isothermal-isobaric ensemble is desirable. Furthermore, as most experiments are performed under constant pressure and temperature, use of an isothermal-isobaric model allows greater congruence between MD simulations and experimental results. Simulations discussed in Chapters 4-6 were performed in the isothermal-isobaric ensemble. An intuitive way of ensuring that the pressure is constant is to allow for an exchange of volume with the surrounding; this can be thought of as using a piston [166]. The pressure can be determined by

$$PV = Nk_B T - \frac{1}{3} \langle \sum_{i,j}^N \mathbf{r}_{ij} \mathbf{F}_{ij} \rangle \quad (3.30)$$

An extra term that represents a pressure bath is added to the Hamiltonian. The volume is scaled to the desired volume at each step of the simulation [163]. However, a piston is associated with a mass which makes this method very sensitive to the size of the mass; a too low mass leads to a quickly oscillating box size and a too high mass to inefficiencies. Furthermore, just as the Berendsen thermostat, this method does not maintain the ensemble [130]. In a similar way as to the Nose-Hoover thermostat for maintain a constant

temperature, constant pressure can be achieved by coupling the system to a pressure bath, using Nose-Hoover barostat adopted by Martyna *et al.* [167]. Additional degrees of freedom are added to the Hamiltonian where ξ , p_ξ and Q are related to the thermostat, similar to in eq.3.29. A barostat with mass W and momentum p_ϵ related to the volume coordinate $\epsilon = \ln V/V_0$ is introduced giving the isothermal-isobaric Hamiltonian

$$H_{NPT} = \sum_i^N \frac{\mathbf{p}_i^2}{m_i} + U(\mathbf{r}^N) + \frac{p_\epsilon^2}{2W} + \frac{p_\xi^2}{2Q} + (N+1)k_B T \xi + P_{ext} V \quad (3.31)$$

In the same way that $\frac{p_\xi^2}{2Q}$ can be thought of as the kinetic energy for the heat bath, $\frac{p_\epsilon^2}{2W}$ is related to the kinetic energy of the piston. The masses, Q and W , determine the fluctuations of the volume and pressure, ω_ϵ and ω_ξ , by $Q = 3k_B T / \omega_\xi^2$ and $W = 3k_B T / \omega_\epsilon^2$. These should be chosen so that the volume and pressure fluctuations are approximately one order of magnitude smaller than the smallest fluctuation of the system [168].

This method can be extended by controlling the fluctuations in the barostat with Langevin dynamics [169]. An extra friction term, γ , representing viscous dampening as and a term for stochastic forces, \mathbf{R}_i , is added to the equations of motion

$$\frac{d\mathbf{p}_{i,Langevin}}{dt} = \gamma \mathbf{p}_i + \mathbf{R}_i \quad (3.32)$$

The choice of the friction term, γ , is a compromise between sampling efficiency and accuracy. It can be related to the thermostat frequency, $\omega_p \gamma = 2\pi/\omega_p$ and should be, similarly to above, smaller than the smallest fluctuation of the system [168].

3.10 Free energy calculations

The free energy of a system is the energy available for it to do work. By knowing the free energy of a system we can determine the probability of finding

it in a given state. Helmholtz free energy, A , can be related to the partition function, eq.3.8, by

$$A = -k_B T \ln Z \quad (3.33)$$

To determine the free energy we would need to evaluate all configurations in phase space, however, this would be extremely time-consuming. If we instead focus on the difference in free energy between two states, X and Y, connected by a specific reaction coordinate, ξ , we can evaluate the change in free energy along that coordinate

$$\Delta A(\xi) = A_Y(\xi) - A_X(\xi) = -k_B T \ln \left(\frac{Z_Y}{Z_X} \right) = -k_B T \ln \rho(\xi) \quad (3.34)$$

This can be described with the configurational integral

$$\rho(\xi) = \frac{\int \delta(\xi'(\mathbf{r}^N) - \xi) e^{-U(\mathbf{r}^N)/k_B T} d\mathbf{q}^N}{\int e^{-U(\mathbf{r}^N)/k_B T} d\mathbf{q}^N} \quad (3.35)$$

where δ is the Dirac delta function. This does not provide us with the absolute free energy of each state but rather the difference between the states, which is sufficient when we are interested in the transition between the states. In this thesis I have investigated ion selectivity and permeation by evaluating the free energy for ions going from a bulk environment along a reaction coordinate through the channel and/or SF of a model of a human Na_v and an ASIC.

3.10.1 Thermodynamic integration

According to the thermodynamic integration method the energy between two states connected by the reaction coordinate ξ can be calculated by integrating along ξ

$$\begin{aligned} \Delta A &= \int \frac{\partial A(\xi)}{\partial \xi} d\xi = - \int \frac{k_B T}{Z} \frac{\partial Z}{\partial \xi} d\xi \\ &= - \int \frac{k_B T}{Z} \sum \frac{1}{k_B T} e^{-\frac{U(\xi)}{k_B T}} \frac{\partial U(\xi)}{\partial \xi} d\xi \\ &= - \int \langle \frac{\partial U(\xi)}{d\xi} \rangle_\xi \end{aligned} \quad (3.36)$$

Plugging eq.3.1 into eq.3.36 gives

$$\Delta A = - \int < F(\xi) >_\xi \quad (3.37)$$

This is the negative integral of the mean force driving the particle along the reaction coordinate, and as such, ΔA is called the potential of mean force (PMF). The reaction coordinate can be physical, like a positional variable or an angle, or non-physical, like the transition from Na^+ to K^+ [170].

3.10.2 Umbrella sampling

Ion conduction can take several μs , yet the forces driving the MD simulations need to be evaluated every fs . Therefore, simulating this takes extensive computational power, as such, enhanced sampling methods can be used. In US [171], sampling of the path is enforced by holding the ion in windows along the reaction coordinate. A biasing potential, $w_i(\xi)$, is added to each window so that $U(\mathbf{r}^N) \rightarrow U(\mathbf{r}^N) + w_i(\xi)$. This biasing potential should be chosen carefully so that sufficient overlap between energetic states is obtained but also so that all states are sampled. If the free energy profile would be known ahead of time, the ideal $w_i(\xi)$ would be $-\Delta A_i(\xi)$, which would yield a flat surface and good sampling. However, this is usually not the case and a common choice is instead to use a harmonic biasing potential $w_i(\xi) = \frac{k_i}{2}\Delta\xi^2$, where k_i is the force constant in window i [146]. The biased probability density in window i can be described as

$$\begin{aligned} \rho_i^{biased}(\xi) &= \frac{\int \delta(\xi'(\mathbf{r}^N) - \xi) e^{-(U(\mathbf{r}^N) + w_i(\xi))/k_B T} d\mathbf{q}^N}{\int e^{-(U(\mathbf{r}^N) + w_i(\xi))/k_B T} d\mathbf{q}^N} \\ &= e^{-w_i(\xi)/k_B T} \frac{\int \delta(\xi'(\mathbf{r}^N) - \xi) e^{-U(\mathbf{r}^N)/k_B T} d\mathbf{q}^N}{\int e^{-U(\mathbf{r}^N)/k_B T} d\mathbf{q}^N e^{-w_i(\xi)/k_B T}} \\ &= e^{-w_i(\xi)/k_B T} \rho(\xi) < e^{-w_i(\xi)/k_B T} >^{-1} \end{aligned} \quad (3.38)$$

The unbiased probability distribution can be extracted

$$\rho_i(\xi) = e^{w_i(\xi)/k_B T} \rho_i^{biased}(\xi) < e^{-w_i(\xi)/k_B T} > \quad (3.39)$$

and putting eq.3.39 into eq.3.34 gives the unbiased free energy dependent on the biased probability density.

$$\begin{aligned}\Delta A_i(\xi) &= -k_B T \ln(e^{w_i(\xi)/k_B T} \rho_i^{biased}(\xi) < e^{-w_i(\xi)/k_B T} >) + C \\ &= -k_B T \ln \rho_i^{biased}(\xi) - w_i(\xi) + F_i + C\end{aligned}\quad (3.40)$$

where F_i is a constant that represent the free energy cost of introducing the biasing potential

$$e^{-\frac{F_i}{k_B T}} = < e^{-w_i(\xi)/k_B T} >\quad (3.41)$$

The different F_i can be determined with the Weighted Histogram Analysis Method (WHAM) [172]. It is important that two neighbouring windows are sufficiently overlapped. WHAM determines the optimal distribution function by creating histograms with discrete bins along the reaction coordinate. From these, the relative probability of observing the system in a bin is determined. Each of the simulations carries a statistical uncertainty dependent on the energies in each bin. A weight is determined to minimise the error by giving less weight to the ones with higher uncertainty. This way all simulations are taken into account and the variance is then minimised to create an optimal free energy profile. Furthermore, as this is done an estimation of the statistical error involved is obtained [172].

The unbiased probability distribution in eq.3.39, can be determined by a linear combination of the unbiased probability functions in each window

$$\rho(\xi) = \sum_{i=1}^N c_i(\xi) \rho_i(\xi) = \sum_{i=1}^N c_i(\xi) e^{w_i(\xi)/k_B T} \rho_i^{biased}(\xi) e^{-F_i/k_B T}\quad (3.42)$$

where $c_i(\xi)$ is the weight of $\rho_i(\xi)$ in each window, i . To determine $c_i(\xi)$ a normalisation is performed

$$\sum_{i=1}^N c_i(\xi) = 1\quad (3.43)$$

and the variance in $\rho(\xi)$ is minimised with respect to c_i

$$\frac{\partial \sigma^2 \rho(\xi)}{\partial c_i} = 0 \quad (3.44)$$

giving the weight

$$c_i(\xi) = \frac{n_i e^{-(w_i(\xi) - F_i)/k_B T}}{\sum_{j=1}^N n_j e^{-(w_j(\xi) - F_j)/k_B T}} \quad (3.45)$$

by inserting this expression into eq.3.42 we get the WHAM equation

$$\rho(\xi) = \sum_{i=1}^N n_i \rho(\xi)_i^{biased} \left(\sum_{j=1}^N n_j e^{-(w_j(\xi) - F_j)/k_B T} \right)^{-1} \quad (3.46)$$

where n_i the number of data points in window i . Since F_i depends on $\rho(\xi)$ according to eq.3.41 these equations are solved iteratively until they are self-consistent, or meeting a self-consistency criterion, and the optimal probability distribution is found [173]. Self-consistency is generally determined by evaluating the change in free energy between iterations. However, a small change in free energy does not necessarily mean that it has converged. I have used US combined with WHAM to map out the free energies of ions permeating the ASIC in Chapter 6.

3.10.3 Free energy perturbation

The difference in free energy between two states X and Y can be determined by

$$\begin{aligned} \Delta A_{X-Y} &= -k_B T \ln \left(\frac{Z_Y}{Z_X} \right) = -k_B T \ln \frac{\int e^{-\frac{U_Y(r^{3N})}{k_B T}} dr^{3N}}{Z_X} \\ &= -k_B T \ln \frac{\int e^{-\frac{U_X(r^{3N})}{k_B T}} e^{-(U_Y(r^{3N}) - U_X(r^{3N}))/k_B T} dr^{3N}}{Z_X} \\ &= -k_B T \ln \langle e^{-(U_Y - U_X)/k_B T} \rangle_X \end{aligned} \quad (3.47)$$

Every time we determine the energy in state X we also need to calculate it in system Y . Therefore, this method only yields good results when there is sufficient phase space overlap between the two states. However, that is not usually the case and instead the reaction path can be broken up into several intermediate steps. These steps are made to overlap with each other and are connected by a coupling parameter λ . An energy scaling is introduced

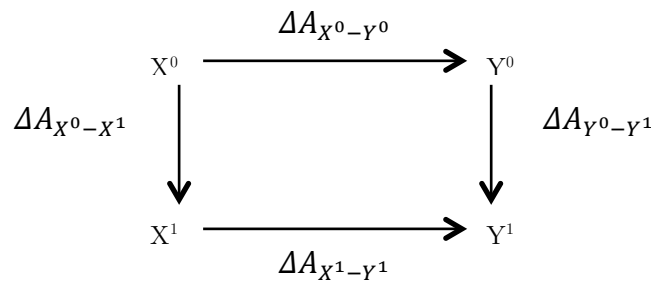
$$U_\lambda = \lambda U_Y(r^{3N}) + (1 - \lambda) U_X(r^{3N}) \quad (3.49)$$

and the change in free energy can be calculated by

$$\Delta A_{X-Y} = -k_B T \sum_{\lambda=0}^{\lambda=1} \ln \langle e^{-(U_{\lambda+1} - U_\lambda)/k_B T} \rangle_\lambda \quad (3.49)$$

FEP does not require that the changes are physical, therefore this is sometimes called alchemical transformation [174]. This is particularly useful when determining the relative binding affinity in a site for two ions where the reaction path is a non-physical one.

The transformation between states can be summarised with a thermodynamic cycle. If we want to examine the free energy difference of system X and system Y going from state 0 to state 1 it would look like the following



Depending on the situation it may be difficult to determine $\Delta A_{X^0-X^1}$ and $\Delta A_{Y^0-Y^1}$. The thermodynamic cycle then tell us that we instead can determine $\Delta A_{X^0-Y^0}$ and $\Delta A_{X^1-Y^1}$, eq.3.50. This can be very useful when, for example, investigating the relative binding of two ions in a binding site.

$$\Delta \Delta A_{X-Y} = \Delta A_{X^0-X^1} - \Delta A_{Y^0-Y^1} = \Delta A_{X^0-Y^0} - \Delta A_{X^1-Y^1} \quad (3.50)$$

To ensure sampling the free energy difference can be determined by combining the sampling sets from both the reference and target states [175]. This can be done by introducing a midway state, k , with energy U_k between the two neighbouring states, i and j ,

$$\Delta A_{i-j} = -k_B T \ln \frac{\langle e^{-(U_k - U_i)/k_B T} \rangle}{\langle e^{-(U_k - U_j)/k_B T} \rangle} \quad (3.54)$$

When a linear relationship is assumed and $U_k = (U_j + U_i)/2$ it obeys the simple overlap sampling (SOS) method [176] giving

$$\Delta A_{i-j} = -k_B T \ln \frac{\langle e^{-(U_j - U_i)/2k_B T} \rangle}{\langle e^{(U_j - U_i)/2k_B T} \rangle} \quad (3.55)$$

However, to be able to optimise k a weighing function can be introduced $\omega = e^{(U_k - (U_i + U_j)/2)/k_B T}$ so that

$$\Delta A_{i-j} = -k_B T \ln \frac{\langle \omega e^{-(U_j - U_i)/2k_B T} \rangle}{\langle \omega e^{(U_j - U_i)/2k_B T} \rangle} \quad (3.56)$$

In the Bennet Acceptance Ratio (BAR) method [177] the weighing function is optimised to minimise the variance $(\Delta A_{i-j} - \Delta A_{i-j}^{est})^2$, giving

$$\omega = \frac{2}{e^{((U_j - U_i) - c)/2k_B T} + e^{(-(U_j - U_i) - c)/2k_B T}} \quad (3.57)$$

Where $c = \Delta A_{i-j} + k_B T \ln(N_j/N_i)$. Plugging eq.3.56 into eq.3.57 gives the BAR equation

$$\Delta A_{i-j}^{est} - c = -k_B T \ln \frac{\sum \langle f(-(U_j - U_i) + c) \rangle}{\sum \langle f((U_j - U_i) + c) \rangle} \quad (3.58)$$

Where $f(x) = 1/(1 + e^x)$ is the Fermi function. The equation is solved iteratively until self-consistent or until a self-consistence criterion is met. The

free energy in each window can also be obtained using WHAM, discussed above.

FEP is very useful when investigating the relative binding affinity between two ions in a binding site. The relative thermodynamical stability is investigated without taking any kinetic considerations into account. I have used FEP in Chapter 5 and 6, where I have analysed the relative binding affinity of Na^+ and K^+ in the SF of a model of the human Na_v (Chapter 5) and in an ASIC (Chapter 6).

Chapter 4

4 Reparameterisation and validation of interaction specific parameters for ions in additive force fields

4.1 Overview

The ability of MD simulations to properly describe biological systems depends on the accuracy of the FF. In classical FFs redistribution of the electronic distribution is not explicitly accounted for, instead fixed atomic charge is assumed. Furthermore, the non-bonded parameters are generally made by fitting parameters to experiments in high dilution and by performing monohydrate quantum mechanical calculations, making them suitable for these types of environments but potentially not for other different surroundings. We therefore need to investigate these ion parameters and test them against well-defined high-level theory and experimental data, and if necessary, reparameterise them. There are a number of ways of adding polarisability to a FF, including with the Drude particle model. In the Drude particle model polarisability is explicitly taken into account by adding a particle to each atom between which the charge is distributed. This allows for polarisation of the atoms in response to fields from the surrounding molecules. However, polarisable FFs suffer from the same potential environment-dependent parameterisation problems as non-polarisable FF. To be able to properly account for the molecular interactions, including polarisability, quantum mechanical effects should be taken into account. CPMD takes the electronic structure into account and therefore allows for redistribution of charge in an

electric field. However, this is an extremely computationally costly method.

A common way of adding polarisability is with the Drude particle model. In this model, polarisability is added via a virtual Drude particle to each non-hydrogen atom. The atomic charge is then distributed between the atom and the Drude particle [154]. The Drude particle can move in response to the electrostatic environment, which creates a redistribution of the atomic charge.

As discussed in Chapter 1 and 2, and further explored in Chapters 5 and 6, the interactions of ions with the amino acids in the SF is vital for the ion channel function. In particular, Glus and Asps seem to be reoccurring in SFs that select for Na^+ ions. Here we assess the parameters for interaction between Na^+ , K^+ and Ca^{2+} and these Glus and Asps from the CHARMM FF and compare to CPMD simulations as well as experiments. Furthermore, when it comes to parameters for the pair specific interactions of Ca^{2+} and Asp and Glu, there has been a lack of attention to such careful benchmarking. We therefore create a Glu/Asp- Ca^{2+} pair specific parameter by performing osmotic pressure simulations and comparing to experiments and CPMD.

4.2 Introduction

Numerous biological processes rely on the ion channels ability to discriminate between different ions. This selectivity takes place in the narrow SF. The SF is lined with amino acids that interact with the ions during the ion conduction [7]. The precision of this selectivity relies on the ion-protein interactions. Furthermore, selectivity relies on a delicate balance of these ion-ion interactions and the ion-water and water-water interactions. In particular, Na^+ selectivity is achieved by using a ring of four Glus in bacterial Na_vs and a ring of Asp, Glu, Lys and Ala in human Na_vs [20]. Furthermore, Glus may be involved in selectivity also in the ASICs [15]. Changing only a few of these key residues alter ion selectivity [91]. This suggests that the selectivity mechanism is an extremely sensitive process. Glu and Asp, which have the same functional carboxylate side chain group (RCOO^-), are reoccurring in these key sites. To properly be able to describe ion conduction and selectivity we want to make sure that the interaction between the key residues and the ions are depicted accurately. Of particular interest is the selectivity of Na^+ over K^+ as both these exist in similar, high, concentrations in the body and are of the same charge

and similar sizes (differ only by ~ 0.4 Å (Table 1.2)) [7]. Furthermore, also $\text{Na}^+/\text{Ca}^{2+}$ selectivity is of interest as these have the same size (differ only by ~ 0.04 Å (Table 1.2)) and the key residues for the selectivity of Na^+ in bacterial Na_vs , a ring of four Glus, is very similar to that the Ca_v use to select for Ca^{2+} , a ring of four Asp [21].

MD simulations are useful tools when studying ion selectivity as they enable investigation of interactions at the atomic level. The system is classically described and the molecular interaction energies are determined with pairwise additive, non-polarisable FFs [131]. It is integral to the success of the use of computer models that these FFs accurately describe the atomic interactions. Rather than determining the parameters for every single atom or atomic interaction, the atoms are sorted into transferable groups and parameters for each type are developed. These parameters are then used for every atom in that group regardless if they belong to different molecules [138].

The CHARMM FF uses the LJ 6-12 potential and the Coulomb potential to calculate the non-bonded interactions, eq.3.15. The LJ parameters, ϵ_{ij} and r_{ij}^{min} , are generally made to match single atom properties like the experiential hydration free energies in infinite dilution [178]. In particular, the LJ parameters for Na^+ , K^+ and Ca^{2+} were made this way (fitting to -82.5 kcal/mol, -103.1 kcal/mol and -381 kcal/mol for K^+ , Na^+ and Ca^{2+}) [179, 180]. This has the potential of yielding good parameters for that type of experimental condition. However, the ions can exist in vastly different microenvironments when permeating an ion channel. In the cytoplasm and exoplasm, they are surrounded mainly by water whereas in the ion channel they are in a limited space surrounded by several charged or polar amino acids, as well as other ions. The FF parameters therefore need to be able to describe a variety of environments correctly [181]. Furthermore, the interaction between two different types of atoms may not be properly depicted by the geometric and arithmetic mean [141]. Experiments have shown that different LJ parameters can reproduce the same macroscopic properties [146], it is therefore important that the LJ parameters reproduce both macroscopic experiments and electronic properties of the atoms. Furthermore, classical additive force fields does not allow redistribution of the electronic distribution of the atom instead the atomic

charges are approximated as being fixed [140, 182]. The charges are determined by quantum mechanical calculations of the interaction energies in the gas phase [131]. The electrostatic interactions are then adjusted to act according to an “average” environment assumed to be water [131]. However, when investigating ion selectivity there is usually several ions involved and they are contained in a small environment surrounded by amino acids, this can hardly be compared to single ions in an aqueous solution. Therefore, the lack of explicit polarisation may not correctly represent interactions where induced polarisation is important [131]. These effects are most important for divalent ions, as the polarisability of the environment becomes a key factor in their interactions.

One way of explicitly adding polarisability to the atom is by using polarisable Drude oscillators. The electronic distribution is modelled by redistributing the atomic charge between the atom and an additional particle, a Drude particle, which is attached to each atom. A change in electric field creates a redistribution of the atomic charge between the atom and Drude particle and that way explicitly induces polarisability [154]. This allows for a higher order comparison. However, polarisable Drude FFs are also dependent on predetermined parameters and therefore suffer similar problems to the classical FFs [131].

In CPMD, just like for MD, the progressions of the atoms are performed with Newton’s equation of motion. But rather than using pre-calculated parameters and relying on the parameterisation technique, the Schrödinger equation is solved in each step and the energy of the nucleus determined. This energy is then used to determine the interaction with the rest of the atoms in the system. CPMD therefore explicitly takes the electrons of the atoms into account [126]. For this reason, we can use CPMD calculations as a higher order guide for the FF parameters. Although it should be noted that CPMD is highly reliant on approximations for solving the Schrödinger equation [183]. Methods taking quantum mechanical effects into account are extremely computationally costly compared to classical MD. The electronic structure need to be evaluated and hence the time step needs be short enough to take the movement of the electrons into account, $\Delta t \sim 0.1$ fs. Furthermore the number of particles in the system increases as the electrons are taken into account. Therefore only very small systems can be simulated and for time scales of fs. This leads to a trade

off between losing important bulk properties when gaining electronic precision. CPMD is not suitable for systems that consist of more than a few 100s of atoms [183]. However, CPMD can be useful for small systems where the chemical interactions play a key role and to fit properties for specific interactions to. In particular for charged atoms and molecules in strong electric fields. CPMD simulations with the BLYP (Becke-Lee-Yang-Parr) [184] density functional has been shown to be good at representing the structure and electronic properties of liquid water [185, 186]. In fact, it was shown to be superior compared to other density functional when compared to experimental neutron diffraction data [185]. However, the water oxygen-oxygen pair correlation function has been found to show some over structuring [187]. Furthermore, CPMD simulations using the BLYP density functional have been extensively used to calculate hydration structures of ions and shown results consistent with experimental from x-ray diffraction [188-190]. This together makes this a suitable method for studying ion pair interactions in a water box. One of the biggest limitations of CPMD simulations is the computational cost sometimes leading to convergence problems [191].

The specific pair interaction of two molecules can be investigated by performing simulations of ion binding and determine the PMF. These simulations can be done in small simple systems and are therefore suitable also for CPMD. The results from the classical simulations can be compared to result from the CPMD simulations and we can fine-tune the fixed charge parameters to try to capture polarisation effects properly. Furthermore, the PMFs can be used to determine the relative binding affinity which can be compared to experimental data from Raman spectroscopy and potentiometry [191]. This gives us an indication of the accuracy of the ion binding both according to electronic and thermodynamical properties. However, these simulations are still only representative of an infinite dilution.

To better represent the pair interaction in a physiologically relevant environment, higher concentrations must be used. The pair-interactions of a solute lead to deviations from the ideal behaviour for colligative properties; therefore the aggregation of the solute can be evaluated using the osmotic

pressure. This way we can directly measure the strength of the solvent-mediated pair interaction, which makes it suitable for studying pair interactions. Furthermore, the osmotic pressure for a solution is one of the few thermodynamic properties that can be both experimentally and computationally measured for a range of conditions. The osmotic pressure for a non-ideal solution can be described as a product of the osmotic coefficient, φ , and the osmotic pressure for an ideal solution, Π^* , $\Pi = \varphi\Pi^*$. Which in turn is described by the Van't Hoff equation $\Pi^* = cRT$, where c is the concentration of ions, R the gas constant and T the temperature [141].

By combining these two methods we can create a good benchmarking system. The higher concentration environment of a SF is taken into account by adjusting strength of the pair interaction to fit osmotic pressure data. And by investigating the pair interaction PMF we can compare to CPMD taking the charge distribution into account. However, there are inherent challenges in matching data representing individual interactions with QM effects to bulk solution thermodynamics and try to create “one fits all” parameters; when one is adjusted, a disagreement may occur in the other. Therefore, we need compromise to get parameters that approximate all relevant situations as well as possible.

The LJ parameters are directly connected to the strength and distance of the pair interaction, it is therefore suitable to adjust these when calibrating the pair interaction. For simplicity, the ϵ_{ij} is generally left unchanged and only r_{ij}^{min} is adjusted. r_{ij}^{min} can either be adjusted for self interactions or for a specific pair. The latter is more common as it only affects the two specific atoms and leaves the FF otherwise unmodified. In this case, the new pair specific non-bonded fix (NBFIX) is used to override the LB mixing rule [192].

Excessive aggregation of ions and over binding of ions to protein and lipids has been noted in several previous studies (including [49, 141, 193]). Therefore, a number of NBFIX values for ion-ion, ion-protein and ion-lipid interactions have previously been created [141, 193-196]. In particular, NBFIX parameters for Na^+ interacting with Glu and Asp was created using osmotic pressure simulations of Na^+ and acetate ($\text{CH}_3\text{COO}^- = \text{OAc}^-$) and experimental osmotic

pressures in a range of concentrations (0.4-3.2 M) ($r_{ij}^{min}=3.23$ Å) [193]. Furthermore, another set of NBFIX parameters have been made for Na⁺ and K⁺ using similar methods ($r_{ij}^{min}=3.19$ Å for Na⁺-O and $r_{ij}^{min}=3.65$ Å for K⁺-O) (Table 4.1) [196]. The reparametarisation of ion-carboxylate interactions have been explored for monovalent ions. However, it is a gap in the research regarding Ca²⁺. As discussed in Chapter 2, the Na⁺/Ca²⁺ selectivity is important, both ions have the same radius (Table 4.1) and the respective SF of bacterial Na_vs and Ca_vs by are very similar. Furthermore, Ca²⁺ presents an additional issue for FFs as it is divalent and polarisation effects, therefore, are very important. Fixed charge models do not represent this well. In particular, excessive Ca²⁺ binding has been observed using classical FFs [49, 197, 198]. NBFIX has been created for the interaction between Ca²⁺ and Asp/Glu for the addition to the polarisable Drude FF. These have been determined by calibrating simulation of ions in propionic acid to experimentally measured hydration free energies (Table 4.1) [199].

Table 4.1. LJ parameters in the standard CHARMM FF and Drude CHARMM FF for Na⁺, Ca⁺ and the oxygen from carboxylate, ^a from Beglov *et al.* [179] ^b from Noskov *et al.* [194], ^c from Marinelli *et al.* [196], ^d from Venable *et al.* [193], ^e from Marchand *et al.* [180], ^f from this work and ^g from Li *et. al.* [199]. Other parameters are from the CHARMM Drude FF.

Atom pair (O on carboxylate)	ϵ_{ij} (kcal/mol)	r_{ij}^{min} (Å)
Na ⁺ - O ^a	-0.0750	3.06
Na ⁺ - O ^b	-0.0750	3.12
Na ⁺ - O ^c	-0.0750	3.19
Na ⁺ - O ^d	-0.0750	3.23
K ⁺ - O ^a	-0.102	3.46
K ⁺ - O ^d	-0.102	3.56
Ca ²⁺ - O ^e	-0.120	3.06
Ca ²⁺ - O ^f	-0.120	3.19
Drude		
Na ⁺ - O	-0.197	3.37
K ⁺ - O	-0.245	3.60
Ca ²⁺ - O	-0.290	3.18
Ca ²⁺ - O ^f	-0.110	3.52

We have investigated the binding between Na^+ , K^+ and Ca^{2+} and Glu/Asp for CHARMM FF with a number of different ion parameters as well as with the addition of explicit polarisation by the use of the polarisable Drude FF. Due to the high charge/size ratio of Na^+ and Ca^{2+} polarisation effects play an important role in binding charged molecules. The pair interaction of $\text{Na}^+/\text{Ca}^{2+}$ and carboxylate was therefore compared to results from CPMD, taking the redistribution of electrons of the atoms into account. The interaction between the divalent Ca^{2+} and carboxylate showed extreme over binding and an osmotic pressure that deviated from experimental results, we have therefore created a new NBFIX for Ca^{2+} -carboxylate by performing osmotic pressure simulations. These were compared to experimental data and adjusted to find a pair specific NBFIX.

4.1 Methods

4.1.1 Free energies of ion-carboxylate pair interactions

We have determined the PMF for the pair interaction between Na^+ , K^+ and Ca^{2+} and carboxylate both with MD and CPMD simulations. Acetate ($\text{CH}_3\text{COO}^- = \text{OAc}^-$) was used as it is the simpler form of the carboxylate side chain that is the functional group of both Asp and Glu (RCH_2COO^-) in ion coordination.

Umbrella sampling [200] was used to explore the binding of the OAc^- and the ion along the reaction coordinate λ . Sampling was enforced by adding a harmonic constraint to the potential holding the atom at separation r_0

$$U(\lambda) = U_0 + \frac{1}{2}k(r - r_0(\lambda))^2 \quad (4.1)$$

According to the thermodynamic integration method, eq.3.37, the energy between two states connected by the coupling parameter λ can be calculated by

$$\Delta G = - \int_{r_r}^r \left(\langle k(r - r_0) \rangle_{r_0} \right) dr_0 + 2k_B T \ln r \quad (4.3)$$

when $(r - r_0)$ is very small [200]. By choosing a large force constant this can be achieved. r_r is a reference point where the PMF is set to zero and the $2k_B \ln r$ term appears due to the reduction in entropy when we fix the atom-atom distance. We have assumed that the mean force exerted on the atoms is equal and opposite to the constraint force acquired from the simulations.

The molecules were constrained with a separation distance, r_0 , of 1-7 Å. To ensure that $(r - r_0)$ was small while still obtaining overlap between the windows a force constant, k , of 230 kcal/mol/Å² and step size of 0.1 Å was used in the MD simulations and force constant 627.51 kcal/mol/Å² and step size of 0.58 Å in the CPMD simulations (Fig. 4.1). The relationship between step size and force constant was determined from the equipartition theorem $\langle x^2 \rangle = \sqrt{k_B T/k}$. Each umbrella window was equilibrated and simulated for 20 ns, totalling in 1 μs long simulations for each system. A convergence criterion of within 0.5 kcal/mol was used and the first 0.2 ns discarded for each window. The remaining trajectory was used to calculate the PMF for the MD simulations. The CPMD systems were simulated for 20 fs and converged to within 0.4 kcal/mol. A time step of 2 fs was used for simulations with the raw CHARMM FF, a time step of 1 fs was used with the polarisable FF and a time step of 0.1 fs was used for the CPMD simulations. The pair interactions were investigated for four different system sizes to evaluate the smallest size possible to achieve an accurate representation of the pair interaction.

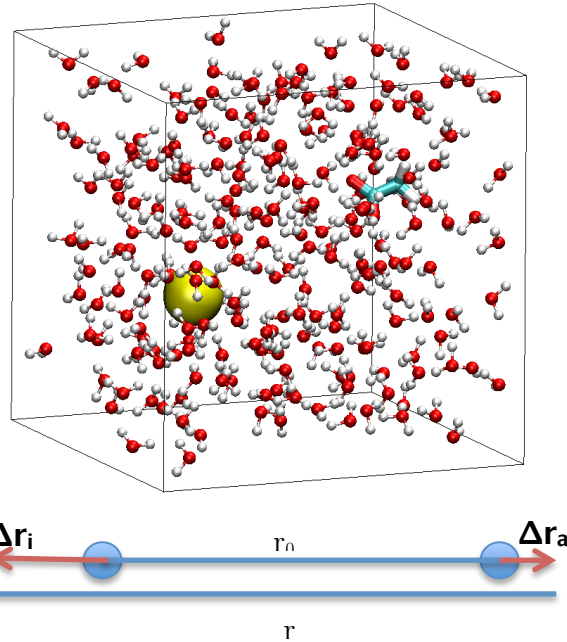


Figure 4.1. A periodic water box containing one ion and one acetate. The reaction coordinate is shown below.

4.1.2 Determination of K_D

The binding affinity was evaluated by determining the dissociation constant, K_D , which can be determined from a pair interaction PMF. K_D can be measured experimentally using methods including Raman spectroscopy and potentiometry [201]. It is therefore useful to compare to evaluate consistency between MD, CPMD and experiments.

When there is low concentration and multi-ion clusters can be neglected the dissociation constant can be determined by

$$1/K_D = 4\pi \int_0^{r_{ref}} e^{-\Delta G(r)/k_B T} r^2 dr \quad (4.4)$$

where the volume element is taken into account $\frac{d}{dr}V(r) = 4\pi r^2$ [202]. r_{ref} is the distance that defines the region of binding and $\Delta G(r) = 0$ for the dissociate state at large r . This depends on the distance that separates the paired and unpaired states, and what states are regarded as paired. Therefore it needs to be carefully considered and chosen to match experiments. r_{ref} was chosen to be

6 Å to include both the contact binding and solvent separated binding as the experimental data identifies both of these as bound states. This gives us a K_D in molecules/Å³, however, conventionally K_D is described in M. There are $N_A=6.022\times 10^{23}/\text{mol}$ and $1 \text{ Å}^3 = 10^{-27} \text{ L}$ giving a conversion from Å⁻³ to M of 1660.5 M.

4.1.3 Osmotic pressure simulations

The osmotic pressure for the Ca(OAc)₂ solutions was determined in the simulations by introducing virtual walls only permeable to water according to the method introduced by Luo et. al [141]. The virtual walls represent semipermeable membranes that create a high ion concentration volume and a pure water volume (Fig.4.1). The osmotic pressure could then be directly measured by the mean force exerted by the wall on the ions [141]. This force is equal and opposite to the force exerted on the wall due to the concentration gradient, *i.e.* the osmotic pressure. A half harmonic boundary potential with 10 kcal/mol/Å² was positioned at $z=\pm 24 \text{ Å}$ in a $48\times 48\times 96 \text{ Å}^3$ box to represent the semi-permeable membrane, only letting water through (Fig.4.2). The system was equilibrated and simulated for 200 ns for each of the investigated concentrations. A convergence criterion of r^{min} within 0.005 Å was used and the first 130 ns were discarded for each system. In order to fine-tune the interaction parameters for Ca²⁺, osmotic pressure simulations were performed for Ca²⁺(OAc⁻)₂ with a range of concentrations (0.1-0.5 M) to match experiments (Table 4.2)). r_{ij}^{min} was systematically increased from $r_{ij}^{min} = \frac{r_{ii}^{min} + r_{jj}^{min}}{2}$ to 3.25 Å in steps of 0.05 Å. Preliminary simulations (not shown) suggested that r_{ij}^{min} would be within this range.

Table 4.2. Experimentally measured osmotic pressure at different concentrations of Ca²⁺(OAc⁻)₂ (unpublished work by Dr. Rong Shen, University of Chicago).

c (mol)	Π (bar)
0.1	5.11 ± 0.09
0.2	10.6 ± 0.1
0.3	15.9 ± 0.1
0.4	20.9 ± 0.1
0.5	26.7 ± 0.1

The osmotic pressures obtained from the MD simulations were compared to experimentally measured values (unpublished work by Dr. Rong Shen, University of Chicago). A linear regression was made and the optimal value of r_{ij}^{min} found for each concentration. To match all concentrations, the final r_{ij}^{min} was determined by taking the mean of these. Standard errors were calculated by dividing the data into 10 blocks.

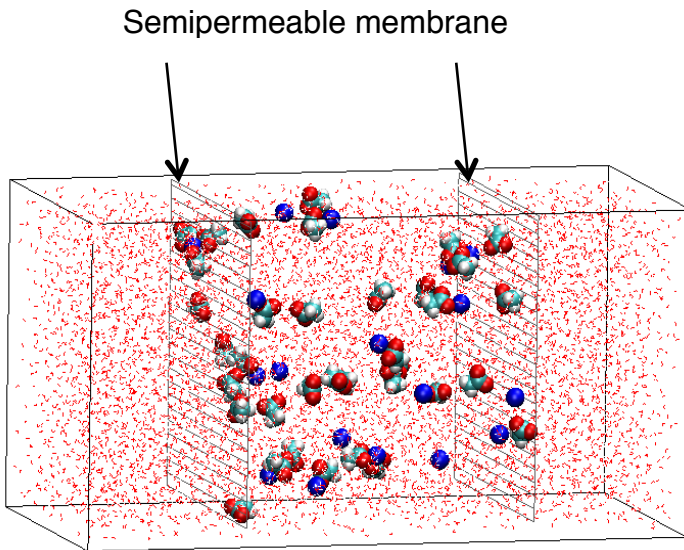


Figure 4.2. Computational setup for measurement of the osmotic pressure. Ca^{2+} and Ac^- are placed in a water box with semipermeable membranes only allowing water to pass through.

4.1.4 Simulation details

To determine the PMFs, four systems were created for each ion-carboxylate interaction, K^+ , Na^+ and Ca^{2+} , totalling in 12 systems. One ion and one acetate molecule were placed in a cubic box of 73 explicit TIP3P water molecules [142] creating a 75 molecule system. Additional systems totalling in 125, 175 and 225 molecules were also created for each ion type. Due to the small sizes of the boxes the non-bonded interaction parameters had to be adjusted and a switching distance of 5, 7, 8 and 8 Å, a real cut of at 7, 9, 10 and 10 Å and a pair interaction list distance of 9.5, 11, 12 and 12 Å was used for the box of 75, 125, 175 and 225 molecules, respectively. A cubic boundary condition was used in boxes of size 15, 18, 20 and 21 Å respectively.

For the osmotic pressure simulations, five systems were created containing, 0.1, 0.2, 0.3, 0.4 and 0.5 M of Ca(OAc)_2 respectively. The solute was placed in a box of size $48 \times 48 \times 96 \text{ \AA}^3$ together with explicit TIP3P molecules. The switching distance, cut-off and pair list distance used were 10, 12 and 14 \AA .

All systems were built with CHARMM [140] and equilibrated using NAMD2.9 [131] using CHARMM general FF for acetate and CHARMM27 FF for ion parameters [131]. An NPT ensemble was used and maintained by a Langevin piston to maintain constant pressure [166, 169] and a Nose-Hoover thermostat to maintain constant temperature [164, 165]. A temperature of 300 K was used. The RATTLE algorithm [203] was used to maintain the bonds to hydrogen atoms. Electrostatic interactions were calculated with Particle Mesh Ewald [204] with grid spacing of 1.5 \AA and 6th order B-spline for mesh interpolation.

The polarisable system using Drude oscillators was prepared online with Drude Prepper using the non-polarisable systems as starting systems. They were energy minimised and equilibrated with CHARMM38 [140]. The system was then further equilibrated and simulated with NAMD2.10 [131]. The Drude SWM4-NDP water model [157] was used. A hard wall was used to prevent the separation of the Drude particle and the atom from becoming too large (0.25 \AA). A dual Langevin thermostat was used to maintain the cold oscillator while maintaining the desired temperature of the system [159] with a Drude damping coefficient of 5 ps^{-1} and a temperature of 1 K for the Drude oscillators.

4.1.5 *Ab initio* calculation details

Collaborators have performed CPMD simulations of Na^+ - Ac^- and Ca^{2+} - Ac^- pair interactions (unpublished work by Dr. Hui Li, University of Chicago). The CPMD 3.15 package that uses the BLYP exchange correlation function with Kleinman-Bylander pseudopotential was used [205, 206]. A temperature of 300K was used together with an energy cut-off of 80.0 Ry and an electron friction mass of 400 a.u. Errors were calculated by dividing the PMF into two blocks.

4.2 Results

4.2.1 Cation-Acetate pair interaction in aqueous solution

The pair interactions of Acetate with Na^+ , K^+ or Ca^{2+} all show two large wells separated by a barrier (Fig.4.3). The first well represents contact binding whereas the second well appears because of solvent separated binding. The barrier in-between is the dehydration barrier, which appears due to the cost of the ion to partly dehydrate to be able to bind to the acetate. For both Na^+ and Ca^{2+} interacting with OAc^- we observe two local minima at the contact binding. This double minimum appears due to the symmetry of the OAc^- ; the ions can bind to either one of the two hydrogen atoms or to both in-between them. The larger K^+ ion does not experience this effect. The small monovalent Na^+ ion shows a tight binding radius; with solvent separated binding within $\sim 6.4 \text{ \AA}$ and contact binding within $\sim 3.8 \text{ \AA}$ (Fig.4.3a). The minimum appears at contact binding with a depth of $\sim -2 \text{ kcal/mol}$ at $\sim 2.7 \text{ \AA}$. The small divalent Ca^{2+} shows a similar binding radius of $\sim 6.4 \text{ \AA}$ and $\sim 3.8 \text{ \AA}$, for solvent separated and contact binding respectively. There is a deep binding of $\sim -6 \text{ kcal/mol}$ in the contact binding site, at $r \sim 2.7 \text{ \AA}$, for $\text{Ca}^{2+}\text{-OAc}^-$ (Fig.4.3b). The larger K^+ shows a solvent separated binding within $r \sim 7 \text{ \AA}$ and a contact binding within $r \sim 4.2 \text{ \AA}$. The free energy for contact binding between K^+ and OAc^- is less; $\sim -1 \text{ kcal/mol}$ (Fig.4.3c).

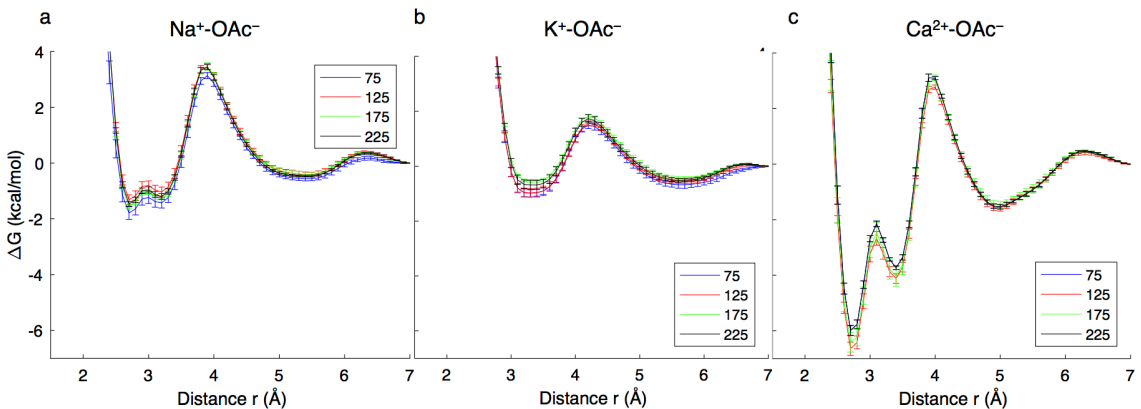


Figure 4.3. Comparison of the free energy for different sized boxes for the raw CHARMM FF between OAc^- and a) Na^+ using LB, b) K^+ using LB and c) Ca^{2+} using the new NBFIX created in this chapter.

To be able to create an ion- OAc^- system, that is also suitable for the costly CPMD calculations, PMFs were computed for four different sized boxes, and

size dependence evaluated. The comparisons in Fig.4.3 show that the PMFs for interaction in different sized boxes are very similar. In fact, they overlap almost completely everywhere except in the dehydration maxima and the contact binding minima. The largest difference between the PMFs of different sizes is 1 kcal/mol. Due to the high computational cost of CPMD, we chose the smallest box consisting of 75 molecules.

4.2.2 FF parameter comparison for $\text{Na}^+\text{-OAc}^-$

The results from the $\text{Na}^+\text{-OAc}^-$ pair interaction study are presented in Fig.4.4. There is a huge discrepancy between the $\text{Na}^+\text{-OAc}^-$ interaction energy depending on which available interaction parameters are used. The blue, green, red and cyan lines in Fig.4.4 show the PMF using CHARMM FF. The PMF in blue and green is made using LB mixing rule, where the blue line is made with CHARMM27 parameters ($r_{ij}^{min}=3.06 \text{ \AA}$, yielding -103.1 kcal/mol) and the green line with CHARMM36 parameters ($r_{ij}^{min}=3.12 \text{ \AA}$, fitted to -98.2 kcal/mol). Both of these parameters originate from adjusting the self-self LJ parameters to experimentally measured hydration free energies (-98.2 kcal/mol and -98.1 kcal/mol , respectively). In PMFs plotted with red and cyan lines the pair interaction is overridden with NBFIX where the pair specific interactions have been optimised according to osmotic pressure data. The PMF with the red line is made using NBFIX from Marinelli *et al.* ($r_{ij}^{min}=3.19 \text{ \AA}$) [196] and the cyan line is made with NBFIX from Venable *et al.* ($r_{ij}^{min}=3.23 \text{ \AA}$) [193]. Furthermore, PMFs with the use of polarisable Drude oscillators and LB mixing rule ($r_{ij}^{min}=3.37 \text{ \AA}$) is shown with a black line. Results from CPMD calculations are presented as a pink line. We will start by going through the PMFs from the non-polarisable CHARMM FF and then compare the results to each other. We will then compare to the results using the polarisable Drude oscillators and ultimately the CPMD.

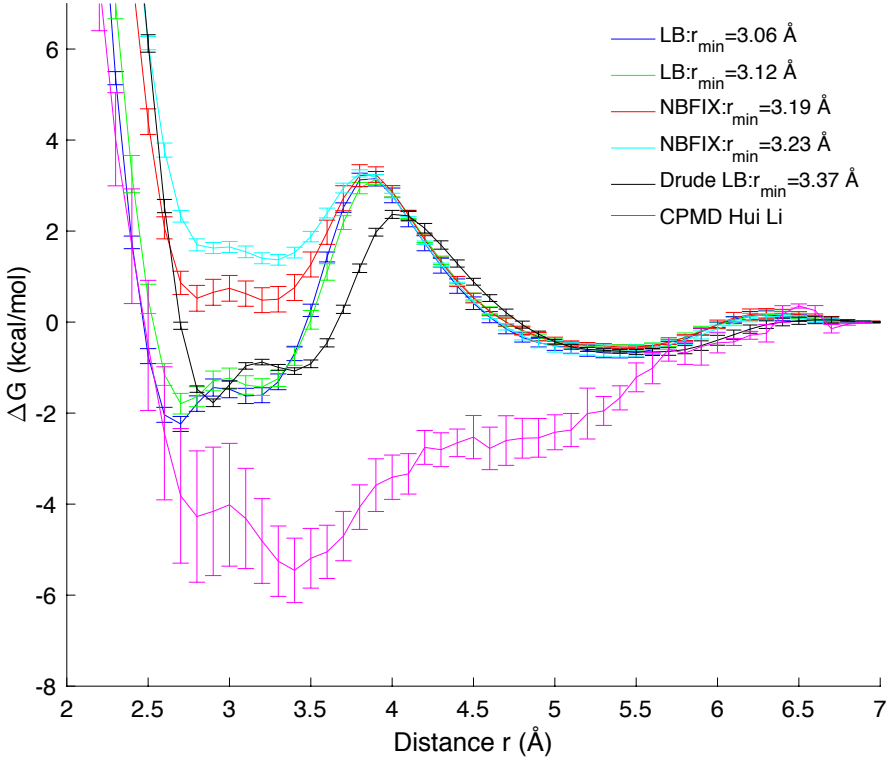


Figure 4.4. The free energy for OAc^- interacting with Na^+ for simulations with raw CHARMM FF and Drude polarizable FF with and without NBFIX as well as results from CPMD simulations.

The PMFs with raw CHARMM FF all show a barrier of ~ 3.5 kcal/mol at ~ 3.7 Å and a solvent separated well of ~ -0.5 kcal/mol around ~ 5.2 Å (Fig.4.4; blue, green, red and cyan lines). However, the direct binding differs between parameters. Both the PMFs using LB mixing rule (blue and green lines) show a binding of ~ -2 kcal/mol at a distance of ~ 3 Å. In fact, the PMFs are within errors of each other. The similarity in binding using these parameters, regardless of the difference in r_{ij}^{min} of 0.06 Å, is likely due to the change in r_{ij}^{min} coming solely from Na^+ . Therefore the altered Na^+ - OAc^- interaction is made up for by the change in Na^+ -water interactions. In the PMFs where NBFIX with larger LJ parameters are used contact binding is greatly decreased and a solvent separated binding is preferred. r_{ij}^{min} is shifted out by 0.2 Å and the contact binding is reduced to ~ 1 kcal/mol and ~ 1.5 kcal/mol for $r_{ij}^{min}=3.19$ Å, red line, and $r_{ij}^{min}=3.23$ Å, cyan line, respectively.

The use of polarisable Drude oscillators (black lines) does not alter the behaviour of the interaction dramatically. The strength of the contact binding

is ~ -2 kcal/mol, however, the minimum is shifted out ~ 0.2 Å and instead at ~ 3 Å. The result from the CPMD simulation is shown with a pink line in Fig.4.4. It shows a wide and deep contact binding. The wide minimum consists of a global minimum at ~ 3.5 Å of $\sim -5.5 \pm 1.5$ kcal/mol and a local slightly shallower minimum at ~ 2.8 Å of $\sim -4.0 \pm 1.5$ kcal/mol. It should be noted that the CPMD results lack a distinct dehydration barrier at 3.7 Å, and only a faint saddle point is seen in its place. This suggests that the barrier has not been properly explored and that the PMF is not fully converged at these distances. The dehydration of an ion, especially a strong Lewis acid like Na^+ is costly, therefore the simulation may not have reached equilibrium at this dehydration distance. Furthermore, we assume that the system has explored the full rotations and therefore correct for the volume element. However, it is possible that this is not true at larger distances for the short CPMD calculations. However, neither of these factors influence binding at short distances and we therefore use the contact binding as an indicator for the Na^+ - OAc^- contact binding. When comparing the depth of the contact binding between the different parameters and FFs, we see that simulations using the LB mixing rule with CHARMM FF parameters best reproduce the CPMD results.

The investigation of the binding affinity for the pair interaction of Na^+ - OAc^- with the LB CHARMM FF parameter gives a $K_D = 0.6 \pm 0.2$ M and $K_D = 0.9 \pm 0.2$ M for CHARMM27 ($r_{ij}^{min} = 3.06$ Å) and CHARMM36 ($r_{ij}^{min} = 3.12$ Å) respectively. With the use of NBFIX, we get $K_D = 1.8 \pm 0.2$ M and $K_D = 1.9 \pm 0.3$ M respectively for $r_{ij}^{min} = 3.19$ Å and $r_{ij}^{min} = 3.23$ Å. Usage of the Drude polarizable FF gives $K_D = 1.6 \pm 0.3$ M and CPMD of $K_D = 0.0055 \pm 1.3556$ M. Experimental data using potentiometry in dilute NaOAc solutions at 298 K shows a K_D in the range of 1.17-1.51 M [207] and 1.0-1.6 M [201]. The results from simulations with the LB CHARMM FF give a K_D that is at the lower end of the experimental range and the results for the addition of NBFIX gives a K_D that is at the upper end. The use of Drude polarizable FF seems to best fit experimental K_D values.

Results from CPMD show a PMF that is in more agreement to that of the non-polarisable FF using LB mixing rule. Furthermore, previous MD simulations where the ion selectivity in LeuT [194], a $\text{Na}^+/\text{Ca}^{2+}$ exchanger [196], and an

ASIC [15] were investigated showed similar results with and without modified parameters. Thus, we conclude that the addition of NBFIX on Na^+ interacting with carboxylate is not necessary.

4.2.3 Force field parameter comparison for KOAc

The resultant PMF from the US of K^+ interacting with OAc^- can be seen in Fig.4.5. The PMF plotted using a blue line show the results using LB mixing rule in CHARMM FF ($r_{ij}^{min}=3.46 \text{ \AA}$). These parameters originate from adjusting the LJ parameters to experimentally measured hydration free energies (yielding -80.6 kcal/mol). Green line shows the use of NBFIX, optimised according to osmotic pressure data [196], in a non-polarisable FF ($r_{ij}^{min}=3.56 \text{ \AA}$) and red line shows the results when using polarisable Drude oscillators ($r_{ij}^{min}=3.60 \text{ \AA}$).

The binding is less tight and deep than that observed for $\text{Na}^+ \text{-} \text{OAc}^-$, as we would expect for the larger K^+ ion. As the molecules get closer to each other they encounter a minimum as they bind to each other while separated by one layer of solvent. This well is similar both in position and depth, at $\sim 5.5 \text{ \AA}$ and $\sim 0.5 \text{ kcal/mol}$, for simulations with the non-polarisable CHARMM FF using LB mixing rule ($r_{ij}^{min}=3.46 \text{ \AA}$) and NBFIX ($r_{ij}^{min}=3.56 \text{ \AA}$) as well as for simulations using the polarisable Drude FF. As the K^+ ion and OAc^- continue to get closer to each other they encounter a barrier when dehydrating. This barrier is the same for simulations using parameters from the raw CHARMM FF and of height $\sim 1.5 \text{ kcal/mol}$ at $\sim 4.3 \text{ \AA}$. For results using the Drude polarisable FF, the barrier is lower and shifted outward. Both usage of the raw CHARMM FF and the Drude polarisable FF show a contact binding of $\sim -1 \text{ kcal/mol}$.

Although we do not have any CPMD calculations available for $\text{K}^+ \text{-} \text{OAc}^-$ we can calculate the binding affinity for the different parameters and FFs and compare to experimental results. These can then be used as a guide to the accuracy of the pair interaction. The calculated K_D for the pair interaction of K^+ and OAc^- with the raw CHARMM FF parameters gives a $K_D=1.9\pm0.2 \text{ M}$, when NBFIX is added $K_D=2.3\pm0.5 \text{ M}$ and for the usage of the polarisable Drude FF $K_D=2.3\pm0.3 \text{ M}$. Experimental data measuring from potentiometry in dilute KOAc solutions at 298K show a biding affinity of $K_D=1.9 \text{ M}$ [207]. The K_D from

simulations without NBFIX shows a close match with experimental results. However, all the K_D s calculated from the PMFs from our MD simulations are within error of each other. Furthermore, also for the K^+ ion parameters, previous MD simulations investigating ion selectivity in a $\text{Na}^+/\text{Ca}^{2+}$ exchanger [196] and an ASIC [15] show similar results both with and without the addition of NBFIX to the K^+ -carboxylate interaction.

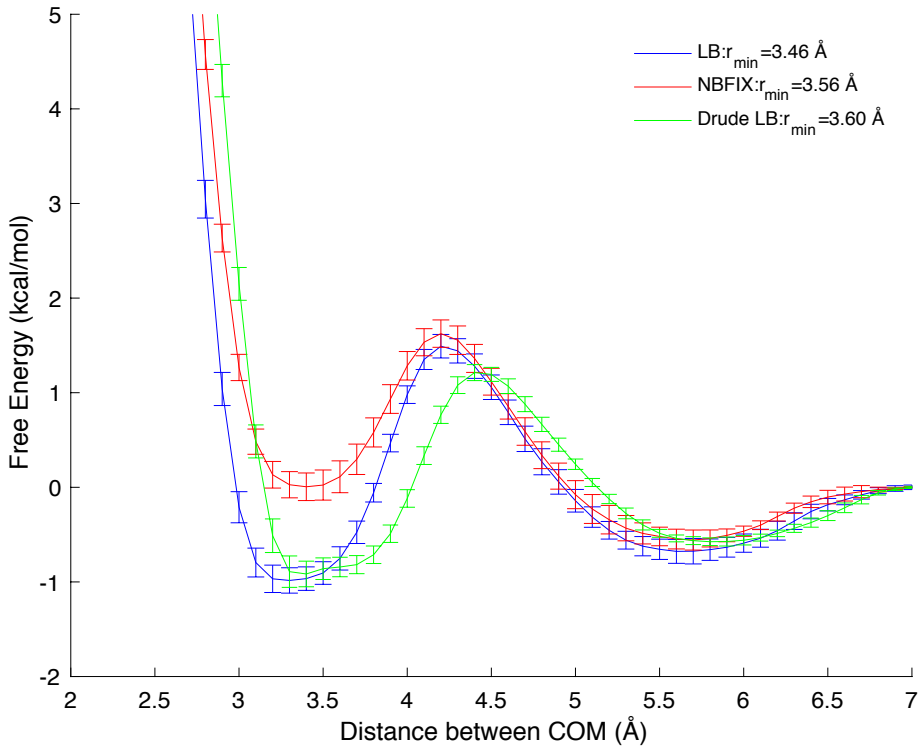


Figure 4.5. The free energy for OAc^- interacting with K^+ for simulations with raw CHARMM FF and Drude polarizable FF with and without NBFIX as well as results from CPMD simulations.

4.2.4 FF parameter comparison for Ca^{2+} - OAc^-

The investigation of ion pairing between Ca^{2+} and OAc^- in Fig.4.6 shows deep binding. The PMFs using the non-polarisable CHARMM FF with LB mixing rule is shown in blue ($r_{ij}^{min}=3.06 \text{ \AA}$). In the same manner, as for Na^+ and K^+ , these parameters were made by adjusting the LJ parameters to reproduce the hydration free energy (-381 kcal/mol). The FF with polarisable Drude oscillator using LB mixing rule is shown in green ($r_{ij}^{min}=3.18 \text{ \AA}$), and NBFIX in black ($r_{ij}^{min}=3.52 \text{ \AA}$). The NBFIX for the polarisable Drude FF was made by

fitting energies from Ca^{2+} in propanoic acid to experimentally measured hydration free energies [199]. Results from CPMD calculations are shown in pink.

All PMFs in Fig.4.6 show a barrier around $\sim 4 \text{ \AA}$ and a well around $\sim 2.7 \text{ \AA}$. The second, solvent separated, well appears around $\sim 5 \text{ \AA}$ with a depth of $\sim -2 \text{ kcal/mol}$. The height of the dehydration barrier vary between $\sim 3 \text{ kcal/mol}$ for the use of NBFIX and $\sim 1.5 \text{ kcal/mol}$ for the use of LB mixing rule. Simulations using the LB mixing rule with CHARMM FF ($r_{ij}^{\min}=3.06 \text{ \AA}$) show a double minimum with a deep contact binding of $\sim -18 \text{ kcal/mol}$ in the global minimum at $\sim 2.6 \text{ \AA}$. Usage of the polarisable Drude CHARMM FF ($r_{ij}^{\min}=3.18 \text{ \AA}$) shows extreme binding of $\sim -50 \text{ kcal/mol}$ also at $\sim 2.6 \text{ \AA}$. The addition of explicit polarisation on top of the already included implicit polarisation creates a very attractive $\text{Ca}^{2+}\text{-OAc}^-$ binding. When NBFIX ($r_{ij}^{\min}=3.56 \text{ \AA}$) is added to the polarisable Drude CHARMM FF the result becomes similar to that of the raw CHARMM FF. The PMF from the CPMD simulations shows a contact binding well that is less than half as deep, with a minimum of $\sim -8 \text{ kcal/mol}$, than those from the MD simulations. However, it should be noted that the dehydration barrier is low for the CPMD simulation, which again may be explained by lack of sampling exploring the barrier and volume element. The calculated K_D is extremely small for all simulations, including CPMD; between 10^{-11} and 10^{-4} M , compared to experimental results of $K_D=0.076, 0.12, 0.12, 0.13 \text{ M}$ [208].

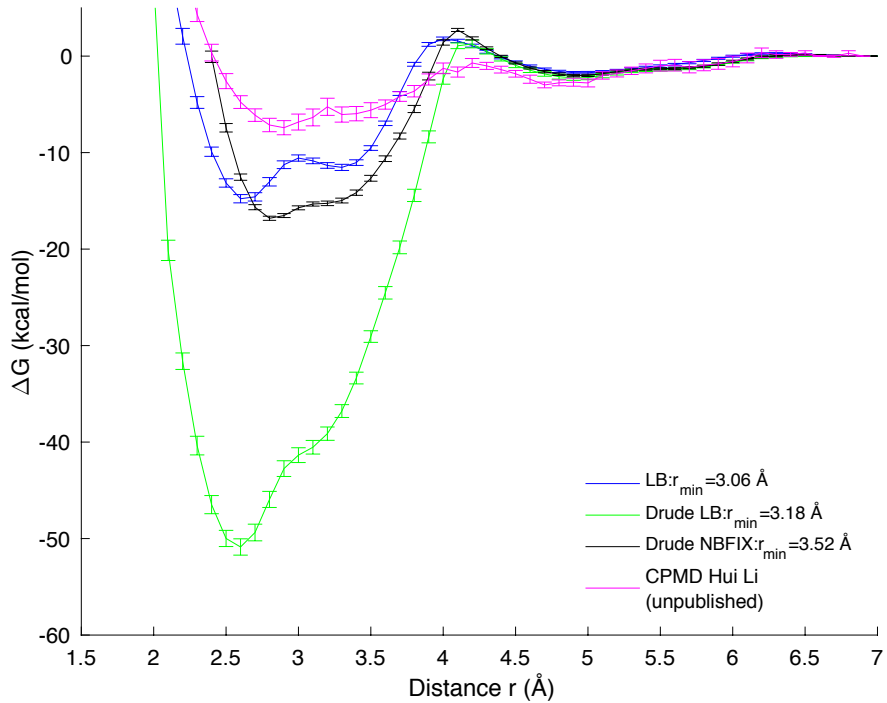


Figure 4.6. The free energy for OAc^- interacting with Ca^{2+} for simulations with raw CHARMM FF and Drude polarizable FF with and without NBFIX as well as results from CPMD simulations.

4.2.5 A NBFIX for Ca^{2+} interacting with Acetate

When comparing the osmotic pressure from MD simulations using LB mixing rule, blue curve, to that from experiments, green curve, in Fig.4.7 we see how the osmotic pressure for $\text{Ca}(\text{OAc})_2$ from the MD simulations is lower than the experimental results for all concentrations. For low concentrations, $c=0.1 \text{ M}$, it is within the margin of error (Fig.4.7). However, for higher concentrations the osmotic pressure from MD simulations is significantly lower than the experimentally measured osmotic pressure (Fig.4.7). This is caused by the excessive ion paring of $\text{Ca}^{2+}\text{-OAc}^-$.

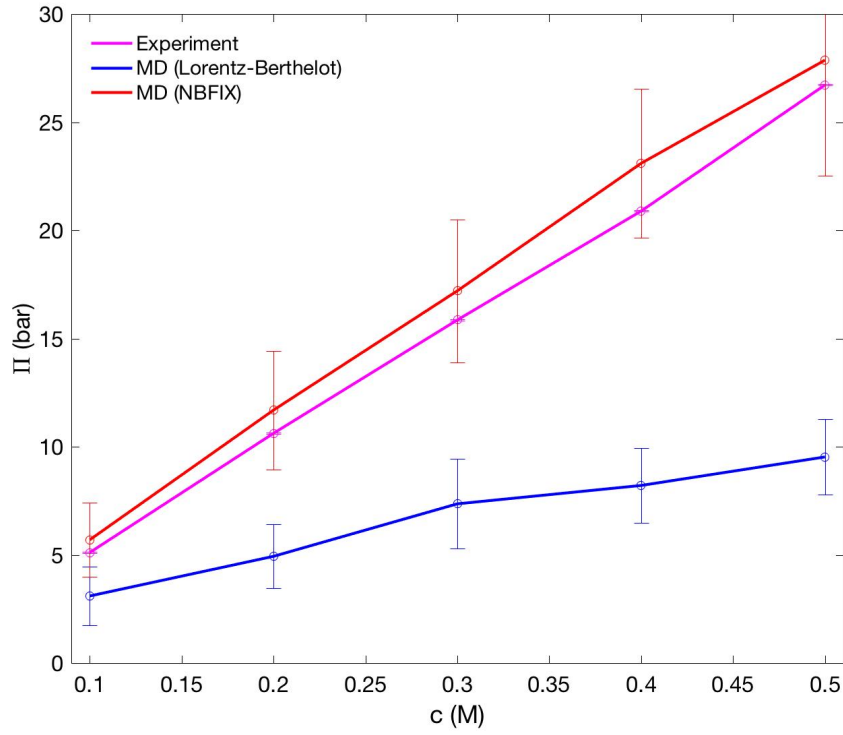


Figure 4.7. Osmotic pressure as a function of concentration for $\text{Ca}(\text{OAc})_2$. Blue line shows the use of LB mixing rule, red line NBFIX and pink line experimental values (unpublished work by Dr. Rong Shen, University of Chicago).

As can be seen in Fig.4.8, where the osmotic pressure from simulations with different r_{ij}^{min} is compared to that from experiments, the simulations reproduce the experimental results best for the full range of concentrations when $r_{ij}^{min} = 3.19\text{\AA}$. When this r_{ij}^{min} is used as NBFIX to the raw CHARMM FF and the osmotic pressure calculated in the different concentrations, we observe much better agreement to experimental results (Fig.4.7; red curve).

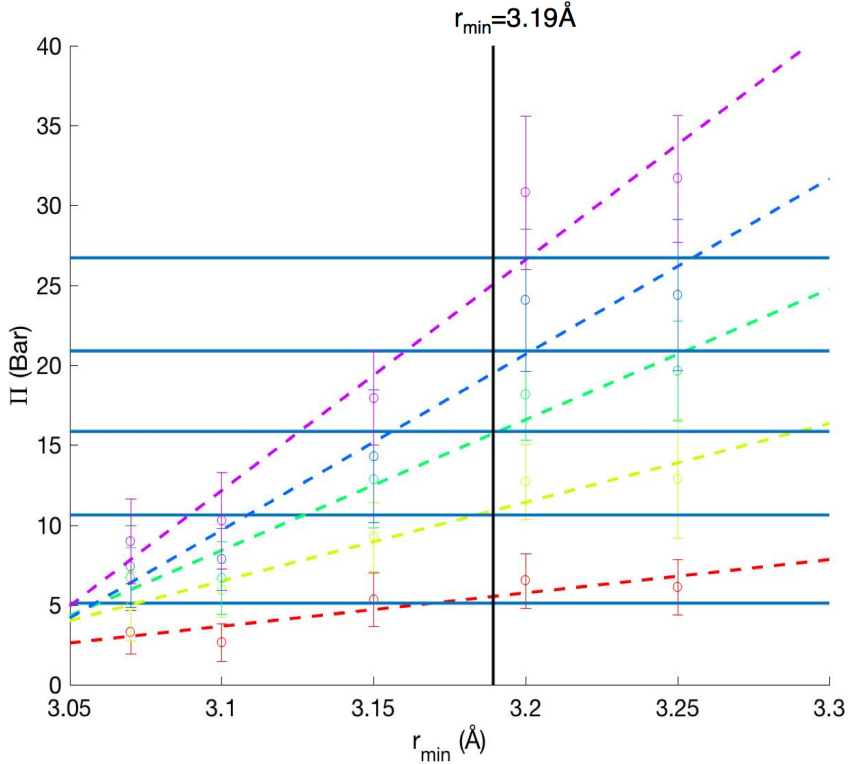


Figure 4.8. Determination of NBFIX for Ca^{2+} - OAc^- black horizontal lines are target experimental values (unpublished work by Dr. Rong Shen, University of Chicago), coloured dashed lines are fits of the computational results for each concentration and black vertical line indicates the best fit for r_{\min} .

The red curve in Fig 4.9 shows the PMF for the pair interaction between Ca^{2+} and OAc^- with the new NBFIX. The binding is greatly decreased and now better agree with the results form the CPMD calculation. The new calculated K_D is improved, however, it is still very small, $K_D=0.0027\pm0.0322$ M, this is likely due to the low dehydration barrier. This result does not match the experimental results of $K_D=0.076, 0.12, 0.12, 0.13$ M [208]. As discussed above convergence is a big problem when using CPMD, in particular when exploring the dehydration barrier. However, these issues are not a factor in the contact binding well. The experimental K_D s for $\text{Ca}^{2+}\text{-OAc}^-$ are highly variable and the largest value is almost twice the size as the smallest value. Furthermore, investigations of different techniques for measuring the binding affinity have found that dissociation constants determined from Raman spectroscopy is ~ 1.5 orders of magnitude larger than those obtained from potentiometry [201]. Due to this high variability experimentally measured binding affinities, K_D might not be a suitable guide for parametrisation.

Our reparametarisation and investigations confirm the difficulty in properly modelling divalent ions. Using parameters that properly depict one type of environment does not mean that they will properly represent a different environment. We have created a new r_{ij}^{min} that fits well with experimentally measured osmotic pressures in physiologically relevant concentrations. Our parameters also match CPMD calculations, explicitly taking polarisation into account, fairly well. However, they do not match the binding affinity from potentiometry titration experiments. Recent investigations by Yoo *et al.* using the similar osmotic pressure methods with Ca(OAc)_2 finds the optimal r_{ij}^{min} to be 3.16 Å [195]. Furthermore, these parameters were implemented and MD simulations of DNA translocation of Ca^{2+} was found to reproduce experimental results [195].

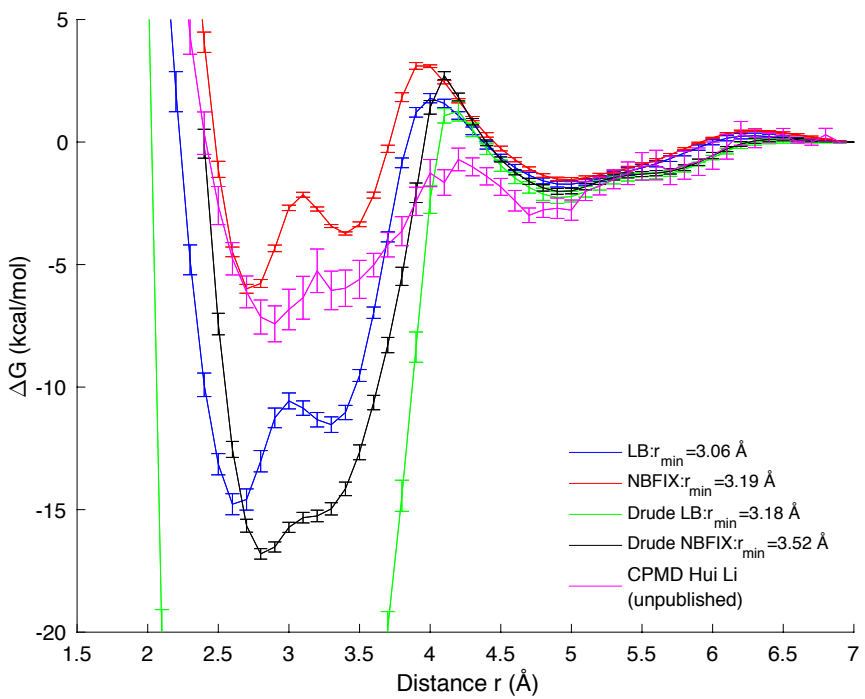


Figure 4.9. The free energy of OAc^- interacting with Ca^{2+} , only free energies over -20 kcal/mol are shown.

4.3 Conclusions

To be able to trust our computer models we need to be certain that the model quantitatively reproduces well-defined data at the atomic and macroscopic

levels. In particular, the interaction between K^+ , Na^+ and Ca^{2+} and Asp and Glu are important for ion selectivity in Na^+ selective channels and is of particular interest due to the significance of these channels. We have investigated these interactions using US to determine the PMF and binding affinity both with classical non-polarisable FFs, with the addition of polarisation via the Drude oscillator model and quantum mechanical CPMD simulations. Our results show a pair interaction that is highly dependent on which of the published interaction parameters that are used.

For Na^+ -OAc⁻ we see a preference for contact binding using the LB mixing rule with CHARMM FF both with and without Drude oscillators and CPMD. When we instead use the pair specific NBFIX parameters created by fitting to osmotic pressure data solvent separated binding is preferred. Furthermore, when we compare to experimentally measured K_D we find that these are highly variable and the use of LB mixing rule with CHARMM FF is in the lower of the experimental range but also that the use of NBFIX on CHARMM FF is in the upper range. Parameters that better match high concentration properties, as those fitted to the osmotic pressure data, may not properly represent polarisation properties. Furthermore, CPMD calculations in high dilution may accurately depict the polarisability but not in high concentration environments. This seems to be an inherent issue in FFs.

For K^+ -OAc⁻ the result of the pair interaction PMF and calculated K_D show less marked difference. The use of LB mixing rule with CHARMM FF and the use of Drude oscillators both show a preference for direct binding, although the addition of polarisability shifts this minimum out by $\sim 0.2 \text{ \AA}$. The use of NBFIX on the CHARMM FF shows a preference for solvent separated binding, although only barely. The less distinct difference between the FFs is likely due to the lower influence from polarisability on K^+ originating in its smaller charge/size ratio.

Results from Ca^{2+} -OAc⁻ pair interaction show very deep binding for all FFs. In particular, the binding was more than twice as deep for all the results using classical FFs compared to results from CPMD. Furthermore, the calculated K_D strongly disagreed with experimental data. To investigate this further osmotic pressure simulations were performed and compared to experimental data. These

showed an osmotic pressure that is underestimated in the non-polarisable CHARMM FF indicating excessive aggregation of Ca^{2+} ions with OAc^- . The LJ r_{ij}^{min} parameter was adjusted and showed an optimal value of 3.19 Å. When the pair interaction was explored and PMFs made for this new NBFIX we saw greatly improved agreement between MD simulations and CPMD. However, the calculated K_D did not match experimental results. This, again, shows the difficulties in fitting parameters to different environments and expecting a set of parameters that fits all. This is especially prevalent for Ca^{2+} where polarisability plays an important role.

Our investigation of the pair interactions for Na^+ and K^+ with OAc^- showed agreement for the use of standard CHARMM FF parameters with comparison to CPMD. They also showed agreement to experimentally measured K_D . We therefore conclude that these parameters are suitable for use. However, the use of the Ca^{2+} - OAc^- parameters from the LB mixing rule and CHARMM FF show extreme over binding. Our new NBFIX shows improvement both in matching experiments and CPMD. However, they also highlight the difficulties in creating one set of parameters that accurately represents all environments for the small, divalent Ca^{2+} ion.

Chapter 5

5 Selective ion permeation involves complexation with carboxylates and lysine in a human sodium channel

5.1 Overview

Bacterial and human Na_vs exhibit similar cation selectivities, despite their distinct EEEE and DEKA SF sequences. The recent solution of high-resolution structures for bacterial Na_vs has allowed us to learn about ion conduction mechanisms in these simpler homotetrameric channels, but our understanding of the function of their mammalian counterparts remains limited. To probe these conduction mechanisms, a model of the human $\text{Na}_v1.2$ channel has been constructed by grafting residues of its SF and external vestibular region onto the bacterial Na_vRh channel. Multi- μs fully atomistic simulations capture long time-scale ion and protein movements associated with the permeation of Na^+ and K^+ ions, and their differences. We observe a Na^+ ion knock-on conduction mechanism facilitated by low energy multi-carboxylate/multi- Na^+ complexes, akin to the bacterial channels. These complexes involve both the DEKA and vestibular EEDD rings, acting to draw multiple Na^+ ions into the SF and promote permeation. When the DEKA ring lysine is protonated, we observe that the ammonium group from the lysine is actively participating in Na^+ permeation, taking the role of another Na^+ ion. It participates in the formation of a stable complex involving carboxylates that collectively bind both a Na^+ ion and the ammonium group of lysine, permitting pass-by translocation of Na^+ in a high-field strength site. In contrast, multiple K^+ ion complexes with the DEKA and EEDD rings are disfavoured, with the K^+ -lysine-carboxylate

complex non-existent, owing to the large, up to 8.3 kcal/mol, difference in thermodynamic stability of these clusters between Na^+ and K^+ ions. As a result, the charged lysine acts as an electrostatic plug that stops the flow of K^+ ions, which must instead wait for the isomerization of lysine downward to admit K^+ passage. These distinct mechanisms give us insight into the nature of ion conduction and selectivity in human Na_v channels, while revealing the essential high field strength carboxylate binding that defines Na^+ selectivity across all Na^+ channels.

5.2 Introduction

Na_v channels are widely distributed in the central and peripheral nervous systems where they participate in essential functions, including heartbeat, muscle contraction and brain activity [7, 79]. Dysfunctional Na_v s are associated with several physiological disorders, including epileptic seizures and chronic pain [71, 72], and they are therefore a major target for new drugs [209]. However, our understanding of the fundamental mechanisms governing these channels remains incomplete, largely due to the lack of high-resolution structural data on mammalian Na_v s.

There have, however, been recent breakthroughs in structural determination for bacterial Na_v channels, with the first high-resolution x-ray structure of Na_vAb [54], illustrated in Fig.5.1, followed by numerous other high resolution structures, including for Na_vRh [55], $\text{Na}_v\text{Aep1}$ [56] and Na_vMs [57, 58]. Bacterial and human Na_v channels share several features including Na^+ -selective conduction, voltage-dependent activation, pore-based inactivation and drug modulation [20, 210-212]. While there is only a 25-30% sequence identity between bacterial and human Na_v s [58], there exists evidence for overall shared structure [20]. Human Na_v s consist of four domains, DI-DIV, linked together to form one long polypeptide chain, whereas the simpler bacterial channels are made up of four identical subunits [20]. Each of these domains/subunits consists of 6 helical trans-membrane spanning segments, S1-S6, where S1-S4 make up a voltage sensor domain (VSD) and S5-S6 the pore domain (PD). Between these two latter segments is a P-loop that includes a narrow ion SF [20], which establishes an ion preference fingerprint (permeability $\text{Li}^+ \sim \text{Na}^+ > \text{K}^+ \sim \text{Cs}^+ \sim \text{Rb}^+$) that is the same for both bacterial and human Na_v s [7, 26, 27]. Both eukaryotic

and bacterial Na_v s are Na^+ over K^+ selective with eukaryotic Na_v s selecting for Na^+ with $P_{\text{Na}^+}/P_{\text{K}^+} \sim 10-30$ [7, 51] and bacterial Na_v s with $P_{\text{Na}^+}/P_{\text{K}^+} \sim 5-170$ [26, 27, 78]. Due to the structural and functional similarities, the bacterial Na_v channels offer an excellent template, or scaffold to support investigation into the core functional activities of mammalian Na_v s.

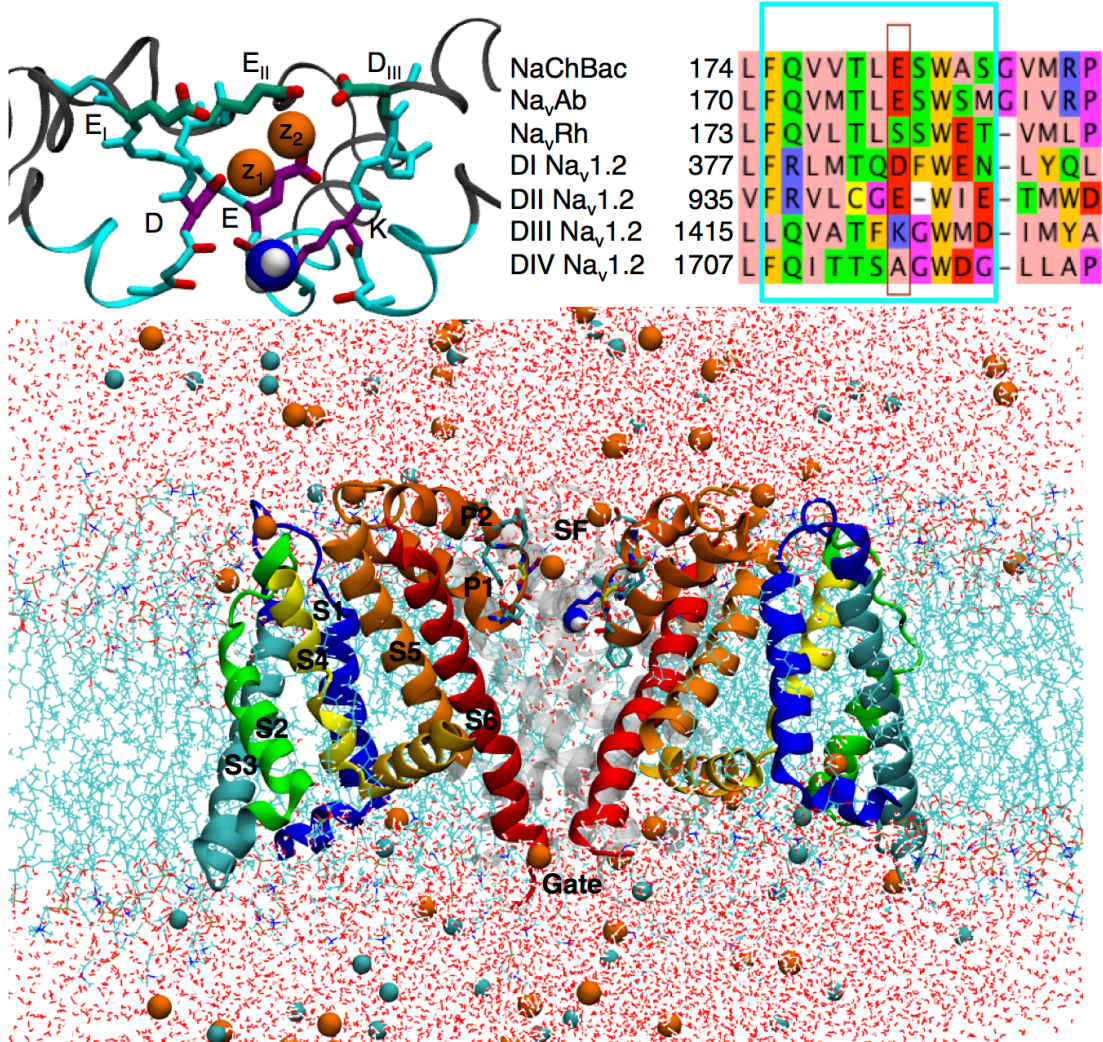


Figure 5.1. $\text{Na}_v\text{Rh}/\text{Na}_v1.2$ channel embedded in a hydrated DPPC bilayer (cyan sticks), surrounded by water (red and white sticks) with Na^+ and Cl^- ions (orange and cyan balls). 3 out of 4 monomers are represented (rear subunit in grey), with VSD in green/blue/yellow and the PD in orange/red ribbons. On the top left the SF and vestibule of the $\text{Na}_v\text{Rh}/\text{Na}_v1.2$ hybrid model with mutated residues in cyan and the residues in the DEKA and EEDD rings are indicated in purple and green, respectively. Top right shows a sequence alignment of bacterial NaChBac , Na_vAb and Na_vRh , as well as the four domains of human $\text{Na}_v1.2$ (labelled DI-DIV). The amino acids are coloured according to their properties using the Zappo colouring scheme [83]. Cyan box selection marks the mutated residues. Red box selection marks the EEEE/DEKA signature sequences responsible for selectivity.

Despite overall conservation of structure and function, the channels present distinct SF sequences (Fig.5.1, sequence alignment), with bacterial Na_v channels making use of a ring of four Glu side chains (EEEE), to create a high field strength binding site thought to favour Na^+ [20], whereas all mammalian Na_v utilise a ring of Glu, Asp, Lys and Ala (DEKA; Fig.5.1, inset) [20, 51, 70], containing not only acidic residues, but also a basic lysine side chain that is known to be crucial to selectivity in mammalian channels [51, 70]. So how do these different channels achieve similar ion selectivity, and does the existence of disparate sequences mean that bacterial and mammalian channels impose their ion preference via different molecular strategies [27]? We seek to reveal and compare the fundamental rules of selective ion permeation for the whole family of sodium channels, by exploring ion conduction mechanisms in a human Na_v channel to compare to previous simulations in bacterial channels.

There are 9 different Na_v s comprising $\text{Na}_v1.1$ to $\text{Na}_v1.9$ [213], with highly conserved sequences throughout these different subtypes [214]. $\text{Na}_v1.2$ is abundant in the human nervous system and has been investigated extensively using methods of mutagenesis and electrophysiology (e.g. [70, 91, 93]). Although no mammalian Na_v structure is yet available, an eukaryotic Na_vPaS structure from cockroach has recently been solved using cryo EM [14]. This channel has a 36-46% sequence identity to human Na_v channels, but is 300-500 residues shorter, has several residues in and around the SF unresolved, and has reduced charge in the vestibule (Gln replacing Asp in DIII; D1426Q; Fig.5.2). We therefore instead take advantage of the conserved structural and functional features between mammalian and bacterial channels to generate a model of $\text{Na}_v1.2$, which incorporates the key SF and vestibular regions, into a high resolution bacterial structure. Such grafting has previously been successful experimentally for imparting Ca^{2+} selectivity on a bacterial Na_v channel [21]. The bacterial Na_vRh structure was chosen as the scaffold due to its higher sequence similarity in and around the SF. In particular, other bacterial Na_v s have one residue extra just above the SF (Gly182) compared to $\text{Na}_v1.2$ (see Fig.5.1, sequence alignment). Furthermore, those channels have an arginine (Arg185) close to the SF that was found to interfere with the side chains of the $\text{Na}_v1.2$ SF in separate models using Na_vAb . We also note that proposed open structures of a bacterial Na_v have been presented [57, 212], but our simulations have suggested that these structures do not stay open without strong

constraints, as discovered previously [215]. Furthermore, previous studies of ion selectivity in bacterial Na_vs using a closed lower gate have shown good sampling of ion translocation throughout the SF [49, 59], and are thus capable of shedding light on selectivity mechanisms.

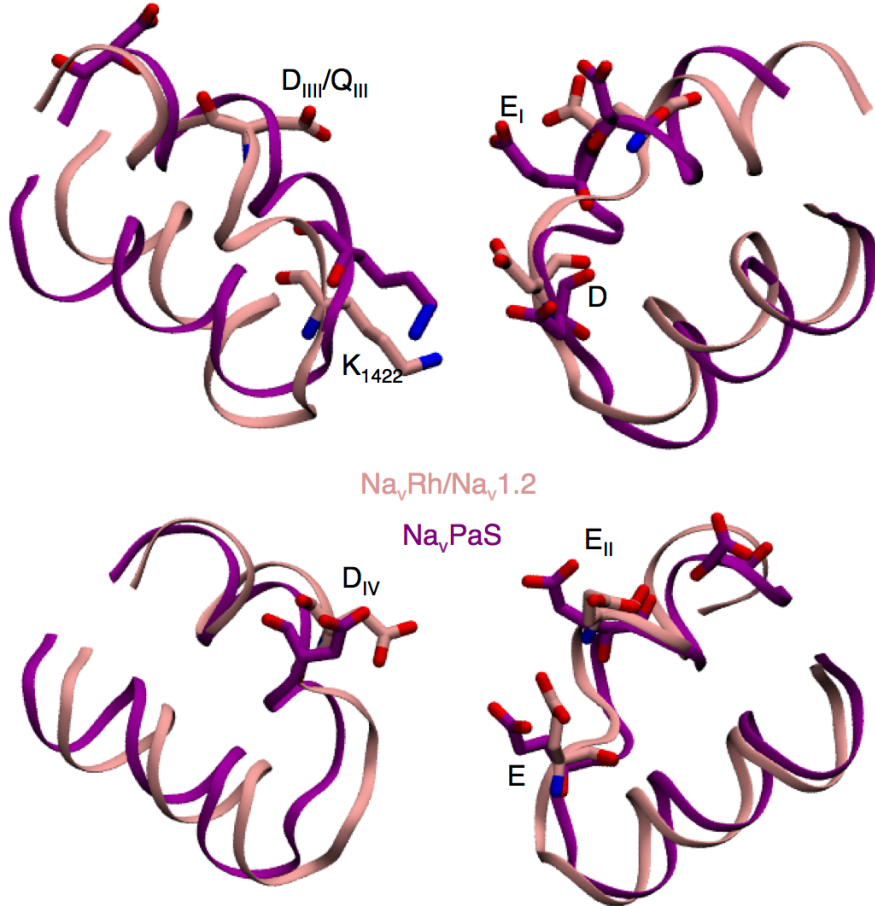


Figure 5.2. Alignment of Na_v1.2 and Na_vPaS. Insets show structural alignment of Na_v1.2 (pink) and Na_vPaS (purple) of DI and DIII (top) and DII and DIV (bottom). The side chains of Glu, Asp and Lys are shown.

Previous simulations of the bacterial channels can teach us much about the potential behaviour of the human sodium channel. The bacterial SF contains a highly conserved ring of four Glu side chains which forms a S_{HFS} [54]. Simulations have shown that the SF is flexible and wide enough to allow partly hydrated Na⁺ ions to permeate [85], and is occupied by an average of two to three ions [49, 59, 84]. Long unbiased MD simulations have described a stable 2-

ion state, where the ions are trapped [49]. While some studies have focused only on this 2-ion state [60, 87], it has been shown that when a third ion enters that efficient knock-on of the bottom ion in to the central cavity occurs [49, 59]. The top ion can either knock-on or pass-by the middle ion in S_{HFS}, with both permeation pathways experiencing similar energy barriers (Fig.5.3; [49]). Regardless, binding of Na⁺ to the S_{HFS} Glu side chains is central to understanding Na⁺ over K⁺ selectivity [27, 49, 60, 87]. Conduction is reliant on the flexibility of these side chains [59], where Na⁺ ions form favourable 2 ion-2 carboxylate clusters (see Fig.5.3b, state C₂) that are not stable for K⁺ [49]. Human Na_v channels do not possess a symmetric E ring, but contain a set of carboxylates that might mediate similar complex formation. In particular, the DEKA signature sequence (Fig.5.1, right inset) contains two carboxylates that may be sufficient. However, human channels also possess a well-conserved [91] charged ring in the outer vestibule, immediately adjacent to the SF, consisting of Glu, Glu, Asp and Asp residues (E_IE_{II}D_{III}D_{IV}; with the exception of Na_v1.7 that contains E_IE_{II}I_{III}D_{IV}; Fig.5.1, right inset) [90]. The residues in these two rings have been shown to be asymmetrical in height [92] and highly flexible [39], and thus may facilitate multi-ion conduction, akin to the bacterial channels.

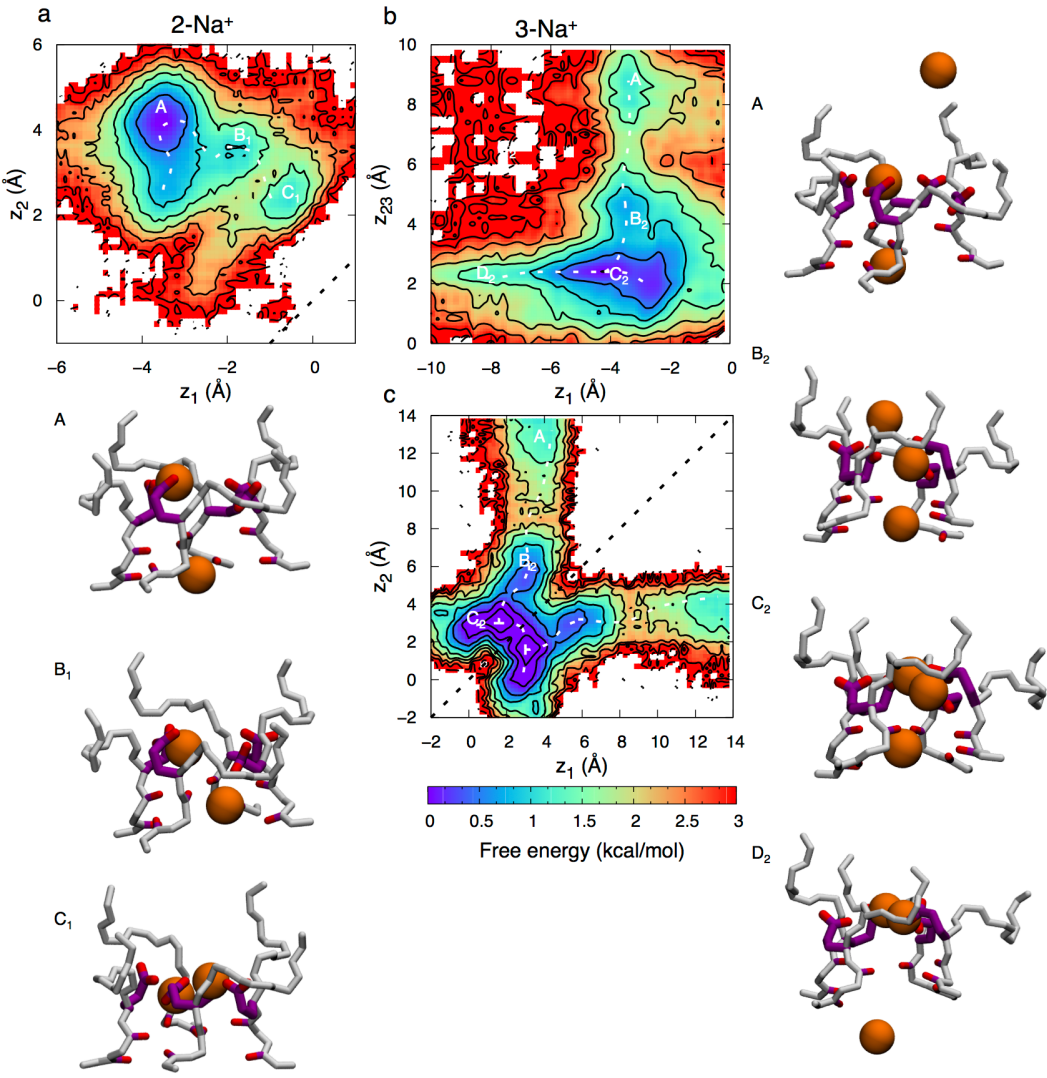


Figure 5.3. Na^+ in the SF of Na_vAb . 2D free energy projections showing a) 2-ion occupancy and b) 3-ion occupancy. When there are 2 ions in the SF, the ions seem trapped and it is not until a third ion enters from above that we can observe either a knock on or pass by conduction mechanism. z_1 corresponds to the z position of the bottom ion, z_{23} the z position of COM of the top two ions and z_3 the z position of the top ion. Snapshots with the EEEE ring in purple indicate the corresponding Na^+ ion (orange balls) movements.

Substitution experiments have shown that the DEKA ring is crucial for the selection of Na^+ ions in mammalian Na_v channels [51, 70, 93]. With at least one of the D and E necessary to preserve selectivity [51]. The most important carboxylate in the DEKA ring is the E, which together with the K₁₄₂₂, maintains wildtype (WT) selectivity, despite mutation of the D [51]. However, if the positions of these two residues are swapped, into DKEA, selectivity is

reduced nearly 4-fold [93], showing the importance of their precise locations, potentially due to interactions with surrounding amino acids, or implying a specific coordinating complex for Na^+ during conduction. Mutagenesis has also shown that both the charge and length of the K₁₄₂₂ are necessary for maintaining Na^+ selectivity; substitution of Lys with neutral side chains causing a complete loss of Na^+ selectivity, and substitution with negatively charged side chains even reversing selectivity [51]. Previous computational studies to examine the role of Lys in conduction have also been based on models using bacterial structures, and concluded on a passive blocking role for Lys. Xia *et al.* replaced the EEEE ring of the bacterial channel Na_vRh with DEKA and performed MD simulations to find that only when the Lys was constrained to E_{IV} was the SF permeable to Na^+ and K^+ ions [68, 216]. Mahdavi *et al.* threaded the amino acids from rat Na_v1.4 onto the backbone of a pore only model of Na_vAb, also suggesting that ion translocation requires displacement of Lys out of the permeation pathway, by hydrogen bonding to the neighbouring DIV Ser [101]. We will show in this study, using extended length simulations, that Lys in fact plays an active role in conduction that is quite different for Na^+ and K^+ ions.

The vestibular EEDD-ring has also been shown to be important for ion conduction, possibly because it increases the electrostatic attraction of extracellular cations [94] [91, 93, 95]. However, all four residues are not equally important, with cysteine mutations showing the greatest decrease in conduction when domain II Glu is mutated (effect on conduction: E_{II}>E_I>D_{IV}~D_{III}) [92, 93]. Furthermore, mutagenesis experiments have shown that replacement of EEDD residues can be detrimental to Na^+ selectivity. In particular $P_{\text{Na}}/P_{\text{K}}$ has been shown to decrease when D_{IV} is replaced with Cys [90, 92, 97], while other experiments have shown little or no effect [93, 96]. Functionally, therefore, the exact roles of the outer ring carboxylates in selectivity are not well defined. Previous models based on bacterial structures have implied a greater thermodynamic preference for Na^+ in the lower SF, and an additional outer binding site at the EEDD-ring [68, 101]. However, we will show that on long timescales, SF rearrangements allow for stable complexes with carboxylates from both the S_{HFS} and outer ring that are important to permeation.

Bacterial and human Na_v channels therefore both possess several carboxylate side chains in (or adjacent to) the SF, allowing for multiple high field strength sites that may bind one or more ions, possibly leading to increased Na^+ selectivity [217]. In a multi-ion/multi-ligand complex there will be competition between favourable ion-ligand and unfavourable ligand-ligand and ion-ion energies [218], needing long time scale simulations to capture the ion and protein configurations [49, 59]. The mechanism is further complicated by the presence of the Lys, which may increase the sampling challenges due to side chain isomerisations. We thus turn to long MD simulations to capture those ion and slowly-interconverting protein movements using the DE Shaw Anton supercomputer. We have performed multi- μs simulations where Na^+ and K^+ are permitted to freely diffuse into and out of the SF of the $\text{Na}_v\text{Rh}/\text{Na}_v1.2$ model, observing the involvement of DEKA and outer EEDD rings, as well as the signature Lys in the multi-ion binding complexes that underpin permeation, revealing distinct permeation mechanisms for Na^+ and K^+ ions.

5.3 Methods

5.3.1 Model of a human Na_v

We have created a model of human $\text{Na}_v1.2$ that includes the most important residues for ion permeation and selectivity, based on a stable structural scaffold from a bacterial channel. Although other parts of the channel may be important for attracting ions [14], the main functional region involves the SF and outer vestibular regions of the channel [91]. The sequence alignment in Fig.5.1 was created with Jalview [83] and was used to create a model of human $\text{Na}_v1.2$ based on the bacterial Na_vRh structure (PDB:4DXW [55]), due to their high sequence similarity in and around the SF region. We note that the bacterial channel Na_vAb with high resolution structure previously studied with MD simulations, possesses an extra Gly residue in this region, which misaligns Na_vAb with $\text{Na}_v1.2$ (Fig.5.1, sequence alignment), making it less suitable for this model as it introduces either an additional residue that would need to be removed or a foreign residue close to the SF. Furthermore, there is also a neighbouring Arg residue present in Na_vAb but not $\text{Na}_v1.2$ that was observed to interfere with the SF structure in separate simulations based on Na_vAb by binding to DEKA Glu side chain (see SI Text). As a result, the Na_vRh high

resolution structure was found to be most suitable for grafting of Na_v1.2 SF and vestibular regions. The mutated region (framed in cyan in the Fig.5.1 sequence alignment), spanning residues 174-184 (Na_vRh numbering used herein), was chosen to include the important DEKA and EEDD rings (residue 180 and 183/184), as well as Thr178 and Leu179 that make up the lower SF. Furthermore, residues 174-177 are located behind the SF and may interact with the side chains of the SF. In particular, within that range is Na_vRh Q174, which is a positively charged Arg in Na_v1.2 DI and DII, and may influence both structure and ion conduction. The chosen residues incorporate all of these key SF and vestibular functional groups from Na_v1.2, whilst minimizing the perturbation of the overall structure. Herein the residues from the DEKA ring will be referred to by their 1-letter abbreviation, except for Lys, due to the common symbol for potassium, it will be referred to also by its hNa_v1.2 residue number (K₁₄₂₂). The Asp and Glu residues from the vestibular EEDD-ring will be referred to according to their amino acid 1 letter abbreviation and domain number (E_I, E_{II}, D_{III} and D_{IV}).

Between the DEKA ring and the EEDD-ring the sequence is one residue shorter in DII of Na_v1.2 than in the bacterial channels. This residue (number 181) was removed, and neighbouring residues (180-182) joined with constrained MD simulation (see below). We note that the original Na_vRh SF structure was closed at the lower gate as well as having a slightly collapsed SF. The collapsed SF has been proposed to be associated with the orientation of the Ser181 side chains, blocking the SF [219], however, after removing the Ser side chains as well as patching Na_v1.2 residues and equilibration (described below), the filter forms an open SF conformation that allows us to study ion permeation (Fig.5.1; inset).

Prior to sequence patching, modifications to the Na_vRh structure were required, owing to the absence of intracellular loops connecting S2 and S3 helices in the voltage sensing domains (VSD). The Na_vRh structure was completed by rebuilding the missing loops (residue 70-75, Na_vRh numbering) in VSD II using Rosetta [220], chosen as it is the domain with most residues resolved in the crystal structure of Na_vRh. This loop was then grafted on to the other voltage sensor domains, based on the assumption that these loops will be similar in each domain [54], minimizing the number of residues being rebuilt. The loop

conformation chosen was representative of the best cluster in Rosetta and favours the positioning of aromatic residues F72 and F73 at the lipid interface, while charged residues D71 and K74 reside in the aqueous environment. Torsional angles of the connecting parts of the model were energy minimized without changing the side chain or backbone conformation of the rest of the protein. During loop optimization, the original x-ray structure rotamers orientation was used for the protein not being rebuilt to keep the model as close as possible to the initial structure.

There is a hydrogen bond present in both Na_vRh and Na_vAb structures between Thr178 and Trp182. This bond has been postulated to be important for keeping the shape of the SF in bacterial Na_v [54, 55]. These residues are conserved throughout the Na_v family and all but one is present in human $\text{Na}_v1.2$ (T382-W386, C940-W943, T1420-W1424, T1712-W1716; $\text{Na}_v1.2$ numbering). To make sure that the mutations do not disturb the shape of the SF, this bond was therefore constrained throughout the mutation, minimization and equilibration of our model, and then released for unbiased production simulations.

It is difficult to predict or measure the pK_a shift of Lys in a non-aqueous microenvironment with the coming and going of conducting ions, such as in the SF of a Na_v channel [148]. Large pK_a shifts have been recorded in channel environments, and protonation states depend on the exact environment and ion occupancy, which will fluctuate over time [149]. Furthermore, quantum mechanical calculations using simplified models of the DEKA ring alone, have demonstrated that a thermodynamic preference for Na^+ may be achieved with either protonation state of the Lys [217]. However, the signature Lys has been shown to be crucial to Na^+ selectivity [51], intuitively suggesting that its charge may be important. To cover both possibilities, we have examined ion movements with charged and neutral lysine, which will help us isolate the role of that charge in ion conduction.

We also note that we have followed similar procedures to create an additional model based on the bacterial Na_vAb channel (PDB:4NTW). However, Na_vAb suffers from having an additional residue (glycine) at 185 that interferes with a simple overlay of the $\text{Na}_v1.2$ sequence (see Fig.1, lower right inset). Moreover, Na_vAb has a charged residue, Arg188, near by the SF, just outside of the

mutated area, which we found deforms the SF via interaction with E from the DEKA ring, making Na_vRh a much more fitting candidate as a scaffold for Na_v1.2.

5.3.2 Simulation details

Proteins were embedded in lipid bilayers of dipalmitoylphosphatidylcholine (DPPC), being the best characterized lipid for MD simulations [221], with explicit TIP3P water molecules [142] and 150 mM of NaCl or KCl solution. Systems were built and pre-equilibrated with CHARMM [140] and further equilibrated using NAMD [131] using the CHARMM36 [221] lipid and CHARMM22 protein and ion parameters [131] with CMAP corrections [138].

Modifications to ion parameters to accurately capture the interactions of Na⁺ and K⁺ ions with the SF have been made. Changes to the pair specific non-bonded Lennard Jones interactions have been made with NBFIIX, specifically for Na⁺ and K⁺ interacting with Glu/Asp carboxylate oxygen atoms and backbone carbonyl groups. A number of attempts to adjust the extent of ion pairing have been made in the past, according to hydration free energy and osmotic pressure data [193, 194, 196], with overall similar conclusions on ion selectivity obtained using modified or unmodified parameters for LeuT [194], a Na⁺/Ca²⁺ exchanger [196], and an acid sensing ion channel [15]. Previous simulations of ion pairing between Na⁺ and acetate have shown reasonable agreement between standard LJ parameters and quantum mechanical calculations, and suggest that addition of NBFIIX adjustment makes the ion-carboxylate pairing too repulsive [15]. The binding affinity was evaluated and dissociation constants (K_D) using the Lorentz-Berthelot mixing rule and NBFIIX showed general agreement with experiment [15]. However, to evaluate model dependence in this study, modified LJ parameters for the ion-carboxylate interaction, that better reproduce experimental osmotic pressure [196], have also been used in 2 μ s simulations with Na⁺ and K⁺ in our Na_v1.2 model for comparison.

Adjustments to the LJ NBFIIX for ions with backbone carbonyl oxygen atoms have also been made, to reproduce free energies of ion hydration (of -80 kcal/mol and -101 kcal/mol for K⁺ and Na⁺) in the protein backbone mimetic, N-methyl-acetamide [47], as has previously been a useful reference for narrow

K^+ channels [222]. However, the relevance of such liquid amide partitioning data to a wide Na_v SF solvation environment is less certain. Optimized parameters ($\epsilon_0 = -0.102$ kcal/mol and $r_{min} = 3.64$ Å for $K^+ \text{-O}$ and $\epsilon_0 = -0.0750$ kcal/mol and $r_{min} = 3.30$ Å for $Na^+ \text{-O}$) were used for Na^+ and K^+ interacting with backbone carbonyl oxygen atoms (during Anton production runs, described below, these were only applied to SF residues 178-181 due to a limitation in number of NBFIX modifications permitted).

During equilibration simulations using NAMD 2.9 [223], the NPT ensemble was imposed using a Langevin piston to maintain constant pressure of 1 atm [166, 169], and a Nosé-Hoover thermostat to maintain constant temperature of 323 K [164, 165]. The RATTLE algorithm [203] was used to maintain the bonds to hydrogen atoms. Electrostatic interactions were calculated for the tetragonal periodic box using Particle Mesh Ewald [204] with grid spacing of 1.5 Å and 6th order B-spline for mesh interpolation. The non-bonded pair list was built to 16 Å, with a real space cut off at 12 Å and force switching from 10 Å. The protein was constrained while the membrane was energy minimized for 1000 steps and then equilibrated by initially constraining all heavy atoms with a 10 kcal/mol/Å² harmonic restraint, which was then slowly released over 2.5 ns. Residue 182 in segment II was removed and residue 181 and 183 pulled together in steps of 0.1 Å with a force constant of 100 kcal/mol/Å², decreased over 20 ns, while the other domains and residues outside of the SF were constrained during this adjustment, with protein heavy atoms constrained using 10 kcal/mol/Å² harmonic constraints. Distance constraints with force constant 10 kcal/mol/Å² on the hydrogen bonds between T382-W386, C940-W943, T1420-W1424 and T1712-W1716 were added, and the protein was equilibrated for an additional 100 ns. Unbiased production simulations were then carried out on the purpose-built supercomputer Anton [224, 225] for 4 μs , as well as an additional 1 μs with NBFIX, for $Na_vRh/Na_v1.2$ with charged Lys both for NaCl and KCl and 2 μs , due to better sampling, for $Na_vRh/Na_v1.2$ with neutral Lys, totalling to 12 μs . The NPT ensemble was maintained on Anton with a Nose-Hoover thermostat [164, 165] and a Martyna-Tobias-Klein barostat [167] at 323 K with a 2 fs time step. A cut-off of 12.72 Å optimised specifically for this simulation by Anton scripts was used and long-range electrostatic forces evaluated with Gaussian split Ewald method every 6 fs [48, 226, 227].

5.3.3 Analysis

To determine the number of ions involved in ion conduction, the occupancy in the filter was calculated based on the mean and standard deviation of the number of ions within $r < 10 \text{ \AA}$ and $-15 < z - z_{ref} < 15 \text{ \AA}$, where z_{ref} is the z-position of the centre of mass (COM) of the backbone atoms of residues 178-182. This range incorporates the DEKA ring as well as two additional residues above and two residues below for rigidity. The free energy map, or PMF, for ion movement through the filter was calculated for each system using trajectory data with specific ion occupancies, to ensure well defined free energy maps. The relevant occupancies for permeation were found to be either 2 or 3 ions for the channel with neutral Lys, and 1 or 2 ions for the channel with charged Lys. The PMFs for the relevant ion occupancies identified from the occupancy analysis were calculated from unbiased simulations by

$$W(\{z_i\}) = -k_B T \ln \rho(\{z_i\}) + C, \quad (5.1)$$

where ρ is the unbiased probability distribution as a function of reaction coordinate(s) $\{z_i\}$, being the vertical positions of one or more ions (z_1, z_2 , or z_3 ; defined with z_1 being the lowermost ion), or their centroids (e.g. $z_{12} = (z_1 + z_2)/2$), (Fig.5.1; inset), each relative to z_{ref} and where C is a constant.

Errors for the maps were created by dividing the well-sampled part of the trajectory (the last $2 \mu\text{s}$ of the trajectory for NaCl and the last $2.2 \mu\text{s}$ trajectory for KCl) into two parts and determine the standard deviation between the maps. The total error of the maps was calculated by the square of the sum of the standard deviation of energies $< 3 \text{ kcal/mol}$.

Structural changes were investigated by root mean square deviation (RMSD) of the mutated area (residue 174-184). To evaluate the flexibility of the SF, the Root Mean Square Fluctuation (RMSF) was calculated for the backbone of each residue in the SF and vestibular ring (including residues 178-184). The RMSF was measured after orientation with respect to the backbone residues of 178-184 of both all subunits and each subunit, to investigate both relative and internal fluctuation respectively. For comparative purposes, the same calculation was done for $2.5 \mu\text{s}$ long simulations with the bacterial channel

Na_vAb . The $\text{Na}_v\text{Rh}/\text{Na}_v1.2$ model was also compared structurally to the eukaryotic Na_vPaS by performing RMSD calculations of the equilibrated $\text{Na}_v\text{Rh}/\text{Na}_v1.2$ model to the cryo-EM structure of Na_vPaS , using the backbone of each residue in and around the SF (residue 171-193). The stability of the H-bonds between T382-W386, C940-W943, T1420-W1424 and T1712-W1716 (corresponding to Thr175-Trp179 in Na_vAb) were evaluated by calculating the donor-acceptor distance over the course of the simulation.

To determine the important states involved in ion permeation, clustering analysis was performed. The frames were broken down according to ion occupancies and the representative occupations further analysed separately. The radial distribution function for ion-ion and ion-carboxylate pair interactions was evaluated and a cut-off based on the first minima was then determined ($\text{Na}^+ \cdot \text{Na}^+$: $r_{\min} = 4.7 \text{ \AA}$, $\text{K}^+ \cdot \text{K}^+$: $r_{\min} = 5.5 \text{ \AA}$, Na^+ -carboxylate: $r_{\min} = 3.8 \text{ \AA}$, K^+ -carboxylate: $r_{\min} = 4.2 \text{ \AA}$) (Fig.5.4). This cut-off was used to break the frames down and assign them to clusters based on number of DEKA and EEDD carboxylates within the ion-carboxylate cut-off of the ion(s) and, in the case of multi-ion occupancies, whether or not the ions were within the ion-ion cut-off distance of each other. The clusters were further broken down according to which residues the ions were bound to. The most stable frame of the most representative clusters was identified by choosing the middle frame of the configuration with the highest probability of occurrence within each cluster.

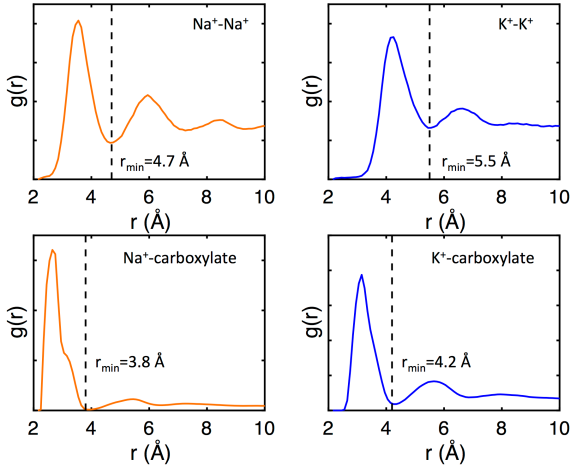


Figure 5.4. Radial distribution function for Na^+-Na^+ (top left), K^+-K^+ (top right), Na^+ -carboxylate (bottom left) and K^+ -carboxylate (bottom right). Multi ion complexes defined by $r < 4.7 \text{ \AA}$ for Na^+ and $r < 5.5 \text{ \AA}$ for K^+ , and carboxylate binding by $r < 3.8 \text{ \AA}$ for Na^+ and $r < 4.2 \text{ \AA}$ for K^+ .

The most important states involved in the permeation of Na^+ and K^+ ions across the SF were identified from the PMFs and cluster analysis (Table 5.1). These states include complexes involving one or more carboxylate groups, Na^+ or K^+ ions and/or the signature Lys ammonium group. To evaluate the relative binding affinities of these states, Free Energy Perturbation (FEP) [228] calculations were performed. The starting frame was chosen as the most stable frame of the cluster, as described above. The relative binding affinity, $\Delta\Delta G_{\text{Na}^+\rightarrow\text{K}^+}$, was calculated from

$$\begin{aligned}\Delta\Delta G_{\text{Na}^+\rightarrow\text{K}^+} &= \Delta G_{\text{Na}^+:\text{Bulk}\rightarrow\text{Site}} - \Delta G_{\text{K}^+:\text{Bulk}\rightarrow\text{Site}} \\ &= \Delta G_{\text{Na}^+\rightarrow\text{K}^+:\text{Site}} - \Delta G_{\text{Na}^+\rightarrow\text{K}^+:\text{Bulk}}\end{aligned}\quad (5.2)$$

The NAMD FEP module was used to determine $\Delta G_{\text{Na}^+\rightarrow\text{K}^+:\text{Site}}$ and $\Delta G_{\text{Na}^+\rightarrow\text{K}^+:\text{Bulk}}$ by alchemically transforming Na^+ to K^+ and K^+ to Na^+ using a coupling parameter, λ . The coupling parameter was divided into 20 windows that were initiated by consecutively increasing λ in steps of 0.05 for 0.2 ns each. Each window was then equilibrated and simulated concurrently for 2.4 ns giving a total of 48 ns simulation per calculation. A convergence criterion of $\Delta\Delta G$ within 1 kcal/mol was used. The first 1.2 ns of each window were discarded for the single-ion/multi-carboxylate complexes, the first 0.6 ns for each window of

the 1st ion transformation and the first 1.4 ns of each window for the 2nd ion transformations in the 2-ion/multi-carboxylate complex, the first 1.0 ns of each window were discarded for the ion+Lys/multi-carboxylate cluster and the first 1.2 ns were discarded for each window for the ion+Lys in the lower SF transformations. The windows were combined and the free energy difference calculated with WHAM [172]. Both forward and backward transformations were performed ($\text{Na}^+ \rightarrow \text{K}^+$ and $\text{K}^+ \rightarrow \text{Na}^+$), and for the case of a site bound by 2 ions, each individual ion was transformed separately and the final transformation calculated by the mean of the two transformations (1st ion: mean of $\text{Na}^+\text{Na}^+ \rightarrow \text{K}^+\text{Na}^+$ and $\text{Na}^+\text{Na}^+ \rightarrow \text{Na}^+\text{K}^+$, or mean of $\text{K}^+\text{K}^+ \rightarrow \text{K}^+\text{Na}^+$ and $\text{K}^+\text{K}^+ \rightarrow \text{Na}^+\text{K}^+$; 2nd ion: mean of $\text{K}^+\text{Na}^+ \rightarrow \text{K}^+\text{K}^+$ and $\text{Na}^+\text{K}^+ \rightarrow \text{K}^+\text{K}^+$; or mean of $\text{K}^+\text{Na}^+ \rightarrow \text{Na}^+\text{Na}^+$ and $\text{Na}^+\text{K}^+ \rightarrow \text{Na}^+\text{Na}^+$). The endpoint histograms for the adjacent λ for the forward and backward transformations were combined with the VMD plugin ParseFEP [229] using BAR [177].

During these FEP calculations, ions were constrained with a 20 kcal/mol/Å² half-harmonic flat-bottomed constraint with outer radius of 2.75 Å from the COM of the multiple carboxylate carbon atoms for the ion/ion+Lys-carboxylate complexes. The results were adjusted for the constraint force by subtracting the Boltzmann average of the difference in constraint energy for $\lambda = 0$ and $\lambda = 1$. Most of the time the constraints were not interfering and thus only a small correction (computed as the difference in $-k_B T \ln \langle \exp(-\Delta U / k_B T) \rangle_{(U_0(\lambda))}$ between $\lambda = 0$ and 1, where $U_0(\lambda)$ is the unperturbed system potential and ΔU is the constraint energy) was subtracted from the results. In particular differences in constraint energies between starting state, Na^+ and end state, K^+ , were found to be 0.30 ± 0.02 kcal/mol for the single ion complex, 0.15 ± 0.42 kcal/mol for ion+Lys complex and -0.017 ± 0.042 kcal/mol and -0.023 ± 0.075 kcal/mol for the 1st and 2nd ion transformation in the two ion complexes. For the case of ion+Lys in the lower SF, a constraint was applied to the ion and the ammonium group of the Lys, keeping them at that location (-4.0 < z < -2.5 Å), using a flat-bottomed harmonic constraint with force constant 20 kcal/mol/Å². The difference in constraint force was found to be 0.34 ± 0.12 kcal/mol. During the $\text{Na}^+ \rightarrow \text{K}^+$ and $\text{K}^+ \rightarrow \text{Na}^+$ transformations, a harmonic constraint of 100 kcal/mol/Å² was applied between the vanishing and appearing ions to maintain overlap. A convergence criterion of $\Delta\Delta G$ within 1 kcal/mol was used. The first 1.2 ns of each window were discarded for the single-ion/multi-

carboxylate complex. For the 2-ion complex, the first 0.6 ns for the 1st and 1.4 ns for the 2nd ion transformation were removed from each window. For the ion+Lys complex, the first 1.0 ns was discarded, while for the ion adjacent to Lys in the lower SF the first 1.2 ns were discarded for each window.

To examine the electrostatic influence of the SF signature sequences and vestibular charge rings on permeation, Poisson's equation was solved for long ranged electrostatic interactions using a smooth PME method, using VMD plugin PMEPot [230], yielding electrostatic potential maps for the Na_vRh/Na_v1.2 and Na_vAb channels. A grid size of 1 Å was used and the final map in the SF was averaged over every 100th frame. The ion density was evaluated with the VMD VolMap plugin [231].

5.4 Results and Discussion

5.4.1 A stable human Na_v model with asymmetric and flexible selectivity filter

After patching of Na_v1.2 SF and vestibular residues into the bacterial channel, followed by equilibration, the overall structures of the pore domain and SF are stable and settle down to RMSD ~ 3 Å after initial structural changes during the first μ s of simulation, with later changes occurring especially for K⁺ due to permeation events described below (Fig.5.5). The first 1 μ s of the Na_v1.2 model with charged Lys with NaCl and KCl and the first 0.25 μ s of the shorter simulation with uncharged Lys have been discarded as equilibration (Fig.5.5). Furthermore, we observe that the Na_v1.2 SF is relaxing into an asymmetrical shape where the DEKA and EEDD-ring span ~10-15 Å, allowing interactions with residues other than their immediate neighbours (Fig.5.6). Previous experiments involving cysteine mutations have shown that the residues in the filter of a Na_v channel are indeed asymmetrical in height and that the inner and outer rings span up to ~15 Å [92]. This asymmetry destabilizes the Thr/Cys178-Trp183 bond, important for keeping the shape of the SF in bacterial channels [54, 55], which during the simulation break and form several times.

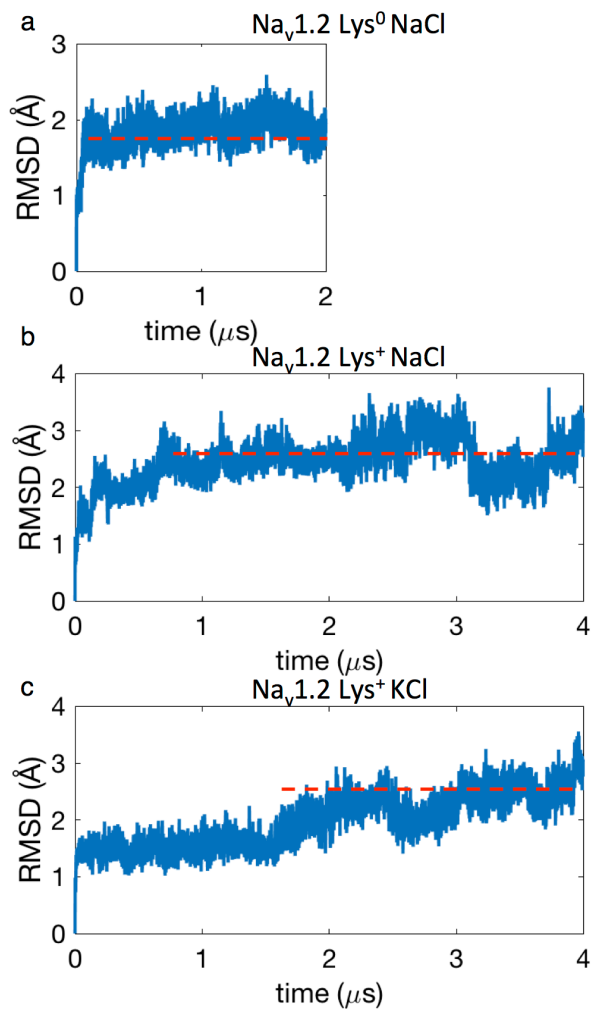


Figure 5.5. RMSD for the backbone of the mutated residues, 178-184, in Na_vRh/Na_v1.2 for a) Na⁺ with deprotonated Lys, b) Na⁺ with protonated Lys and c) K⁺ with protonated Lys.

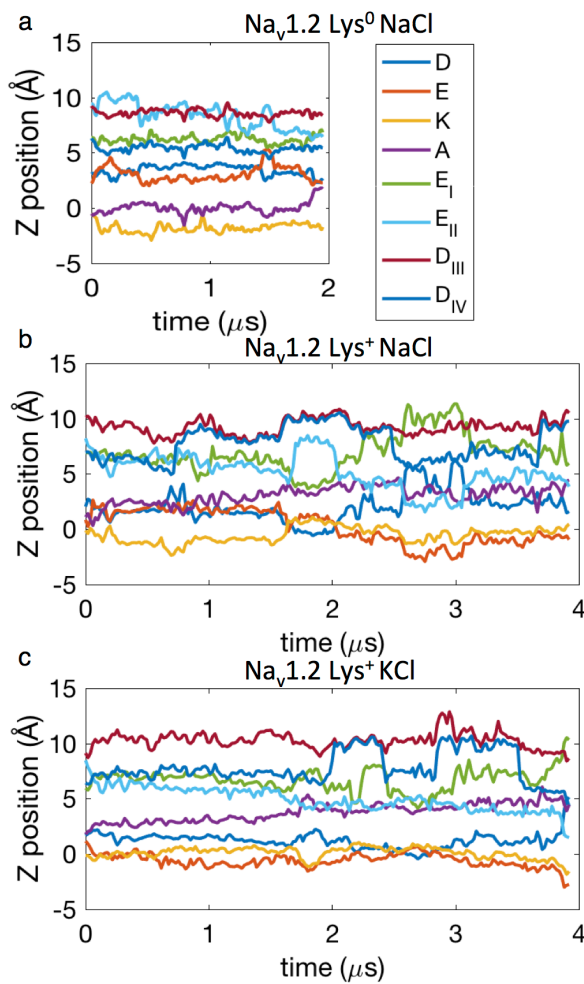


Figure 5.6. Residue position of the DEKA and EEDD rings over time in Na_vRh/Na_v1.2 for a) Na⁺ with deprotonated Lys, b) Na⁺ with protonated Lys and c) K⁺ with protonated Lys.

Flexibility has been shown to be a critical property of the bacterial Na_v channel SF to facilitate ion conduction [49, 59]. Furthermore, pairwise cysteine mutations have shown extreme flexibility (up to 7 Å) of the residues in the SF of a mammalian Na_v [39, 97]. Likewise, we observe high flexibility in the SF of the Na_vRh/Na_v1.2 model (Fig.5.7). In fact, the mean SF backbone fluctuations are approximately twice as large as those for Na_vAb (RMSF~1.5 Å and RMSF~0.8 Å for Na_vRh/Na_v1.2 and Na_vAb) (Fig.5.7a&b). These large RMSF values (Fig.5.7a) are mostly due to asymmetric subunit movements, with the RMSF values halved when computed based on subunit-by-subunit orienting (Fig.5.7b).

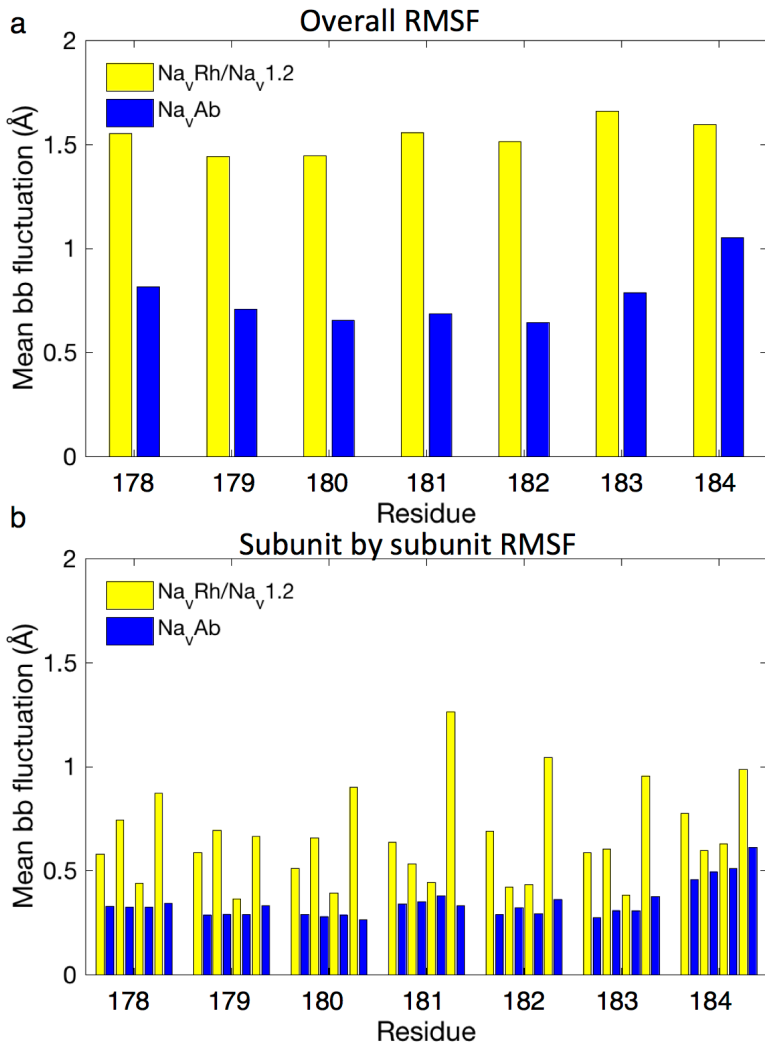


Figure 5.7. RMSF of residue 178 to 184 in Na_vRh/Na_v1.2 (blue) and Na_vAb (yellow) for a) the mean of the four subunits and b) for each subunit.

The recent eukaryotic Na_vPaS cryo EM structure [14] offers related structural data to validate our model, although at limited resolution where several SF side chains were not resolved, preventing immediate conclusions about specific interactions. Structural alignment between the Na_vRh/Na_v1.2 model and Na_vPaS (Fig.5.2) shows structural similarities between the two proteins, with key residues at the same positions, and an RMSD of the SF backbone of ~1.8 Å. The residues of the DEKA and EEQD/EEDD rings in both structures are asymmetrical in height, with these residues spanning 10-15 Å in the model, and ~10 Å in Na_vPaS (Fig.5.2). The spread of these side chains in both our model and the Na_vPaS structure, combined with the high flexibility and lack of

experimental resolution in this region, indicates that SF dynamics may play an important role in conduction.

5.4.2 Selectivity filter with neutral lysine exhibits bacterial-like multi-ion complex formation and conduction

The DEKA Lys has been shown to be crucial to Na^+ selectivity in mammalian Na_v channels [51]. However, the protonation states of amino acids in a dynamic microenvironment, like that of a ion channel SF, have proven hard to determine [148] and to have large fluctuations [149]. We have therefore investigated the ion selectivity in $\text{Na}_v1.2$ not only with a protonated (charged) Lys but also with a deprotonated (neutral) Lys. Importantly, this allows us to isolate the role that the positive charge may play in the SF of $\text{Na}_v1.2$.

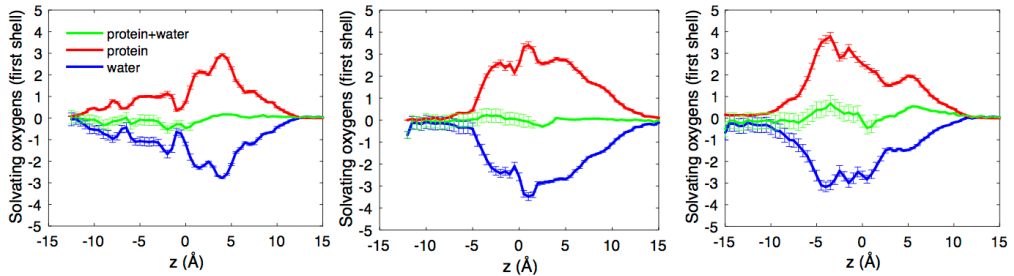


Figure 5.8. Solvation of the first shell relative to bulk for Na^+ in $\text{Na}_v\text{Rh}/\text{Na}_v1.2$ with a) deprotonated Lys, b) protonated Lys and c) K^+ in $\text{Na}_v\text{Rh}/\text{Na}_v1.2$ with protonated Lys. Bulk solvation was found to be 5.67 ± 0.04 water molecules for Na^+ and 6.94 ± 0.07 water molecules for K^+ .

Permeation of Na^+ in the SF of the $\text{Na}_v1.2$ model when K_{1422} is neutral involves both 2-ion and 3-ion conduction mechanisms with an average number of 2.1 ± 0.2 ions in the SF, similar to that seen in the bacterial channel Na_vAb (2.3 ± 0.5 ions; [49]). The ions are partly hydrated as they permeate the SF (Fig.5.8). In the time series for ion movements shown in Fig.5.9, several ions (coloured lines) are observed to enter and exit the central cavity, often coexisting within the SF. We see ~ 70 complete permeation events through the SF and the ions appear to move independently of the neutral Lys side chain (black line). Snapshots in Fig.5.9 show representative configurations of a 2-ion and 3-ion state, where we see multi Na^+ -ion/multi-carboxylate complexes similar to those in for the bacterial Na_v ([49]; see also Fig.5.10e&f, to be discussed below). However, in the $\text{Na}_v1.2$ channel it most commonly not only

involves carboxylates only from the DEKA ring, but also from the outer EEDD-ring, whose carboxylates reach down to help coordinate the ions, as opposed to only using two carboxylates from the inner EEEE ring, as was the case of the bacterial Na_vAb.

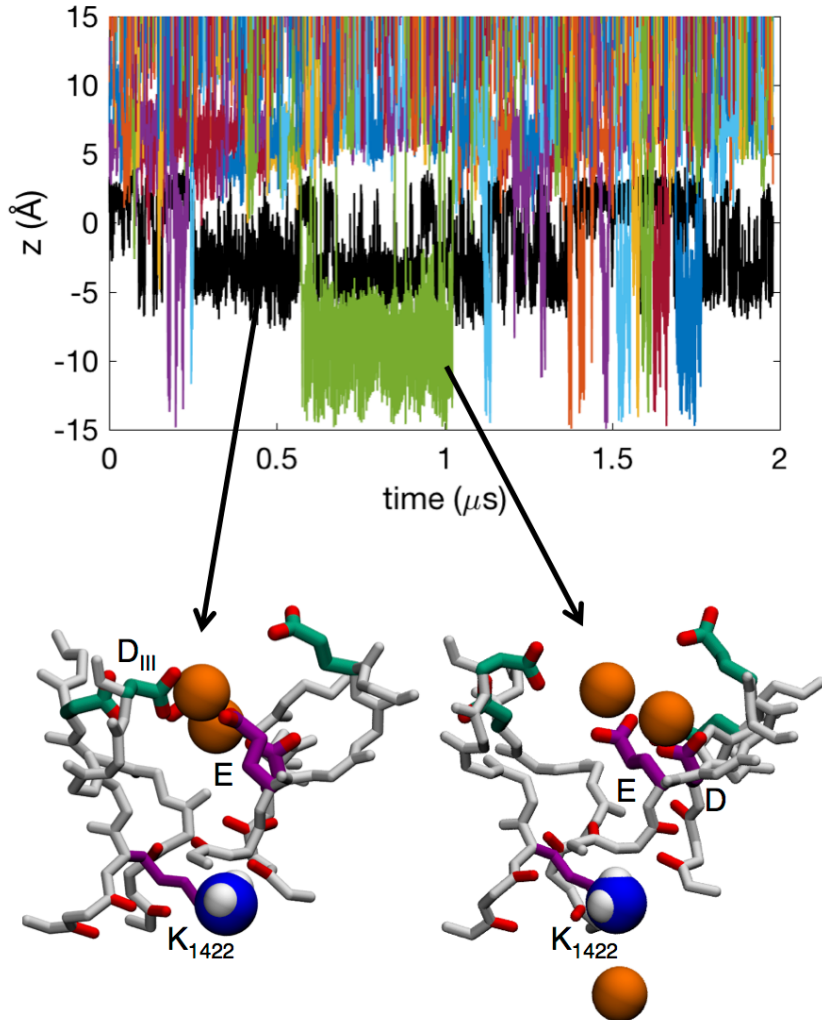


Figure 5.9. Time series showing the z-positions of K₁₄₂₂ (black) and Na⁺ ions (colours) in the SF of Na_v1.2 with deprotonated (neutral) Lys. Insets show snapshots of Na⁺ ions (orange balls) in representative configurations with active residues from the DEKA (purple) and EEDD (green) rings labelled.

This cooperation between the DEKA and EEDD-rings creates a longer filter with a broad span of negative electrostatic potential (Fig.5.10a&b), leading to less distinct binding sites. While Na_vAb has all of its charged side chains in one symmetrical ring, Na_v1.2 has its charges spread out in two asymmetrical and highly flexible rings creating a broad S_{HFS} (ion density map shown in Fig.5.10c),

compared to Na_vAb (Fig.5.10d). Commonly a binding site is created with two Na^+ and one or two carboxylates from the DEKA and EEDD rings (Table 5.1; column 2 and Fig.5.11). The specific residues involved vary and we see several distinct carboxylate ion complexes forming during the simulation (Table 5.1; column 2 and Fig.5.11).

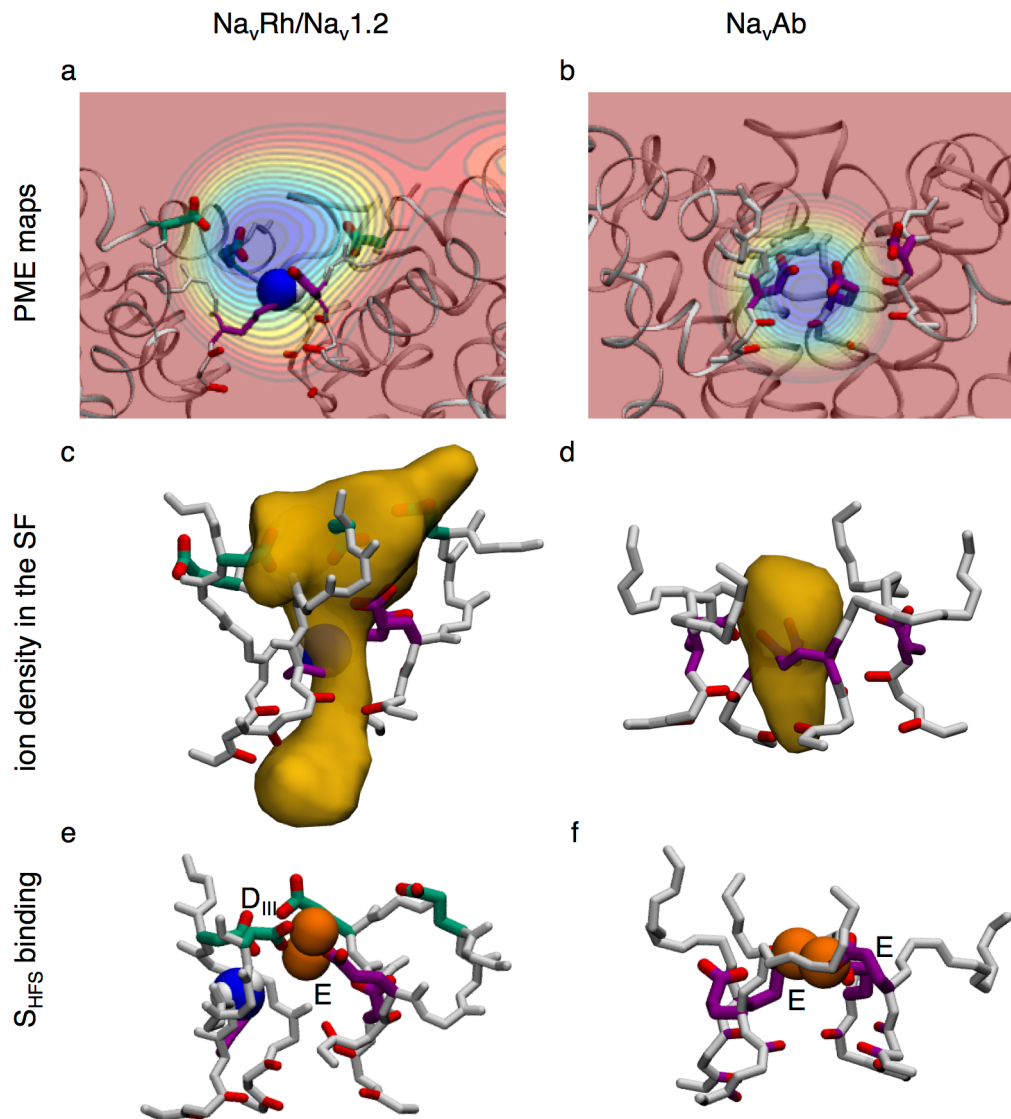


Figure 5.10. Electrostatic map of the filter of $\text{Na}_v1.2$ with deprotonated Lys (a) and Na_vAb (b). Each contour makes up 10 kcal/mol/Å/e. Density maps of Na^+ occupancy in the filter of $\text{Na}_v1.2$ with deprotonated Lys (c) and Na_vAb (d). Multi ion-multi carboxylate binding site in the SF of $\text{Na}_v1.2$ with deprotonated Lys (e) and Na_vAb (f).

Double ion occupancy dominates in the SF, but 3-ion occupancy is also common (Fig.5.11a). When the SF is occupied by a single ion it is most commonly unbound, however, it is also likely to be bound to one or more

carboxylate side chain (Fig.5.11b). When there are two ions in the filter they most likely form single ion complexes with multiple carboxylates (Fig.5.11c). They are also often singly bound or bound together in a tight multi-ion/multi-carboxylate complex (defined by the radial distribution function in Fig.5.3: ions within 4.7 Å of each other and 2 or more carboxylate carbons from the DEKA and EEDD-rings within 3.8 Å of the ions). When there are three ions in the SF, two of these are most likely to be bound together in a tight multi-carboxylate complex (Fig.5.11d). We have previously shown that multi-ion/multi-carboxylate complexes play a role in Na^+ selectivity in ASICs [15]. When these complexes are present, the ions are mostly bound by E and/or D from the DEKA ring, together with the outer ring D_{III} (Table 5.1; column 2). This cooperativity of inner and outer charge rings is common and while all carboxylate side chains from either of the two rings are not necessary, at least one is needed for Na^+ binding in the S_{HFS} . In particular, the DEKA ring is involved ~80% of the time, the EEDD ring ~80% of the time, and both rings cooperatively involved ~60% of the time. This need for only one of the carboxylates in the DEKA ring to maintain cation permeability has previously been seen in mutagenesis experiments [51].

Table 5.1. Summary of ion bindings in the SF of the NavRh/Nav1.2 mutant. The 1st column defines which carboxylate(s) the ion is bound to. Column 2, 3 and 4 show the tight 2-ion/multi-carboxylate complexes for Na_v1.2/Na_vRh with deprotonated Lys in NaCl, Na_v1.2/Na_vRh with protonated Lys surrounded by NaCl and KCl, respectively. Column 5 and 6 show the tight ion+Lys/multi-carboxylate complexes for Na_v1.2/Na_vRh with protonated Lys in NaCl and KCl, respectively. Complexes that occur less than 4% of the time are not shown. Most commonly, Na⁺ is bound to D and/or E together with E_{II} whereas K⁺ is bound to the outer EEDD ring or singly bound to the DEKA D.

	Probability ±SD (%)				
	Tight 2-ion/multi-carboxylate complex			Tight ion+Lys/multi-carboxylate complex	
Bound by residues	Deprot Lys Na ⁺	Prot Lys Na ⁺	Prot Lys K ⁺	Na ⁺	K ⁺
E,D _{III}	26±3	0	0	0	0
D,E,D _{III}	48±4	0	0	0	0
D _{III}	0	0	7±5	0	0
E _{II} ,D _{III} ,D _{IV}	0	0	5±4	0	0
D _{III} ,D _{IV}	6±8	0	8±4	0	0
D _{IV}	0	0	4±4	0	0
E _{II} ,D _{III}	0	4±4	35±14	0	0
D,E	4±4	0	0	0	4±4
D,E,E _{II}	6±6	3±2	0	23±5	0
D	0	0	8±12	40±7	83±7
E _{II}	0	6±3	0	0	0
E,E _{II}	0	4±2	5±2	5±4	0
E,E _{II} ,D _{III}	0	6±8	4±3	0	0
D,E _{II}	0	69±11	8±11	25±19	4±3
Unbound	0	0	0	0	6±5

Despite the longer SF in Na_v1.2, we see a conduction mechanism resembling that of the bacterial Na_v, relying on multi ion-multi carboxylate complexes for an efficient knock on conduction. When there are 2 ions within the SF, at z_1 (lower) and z_2 (upper), the free energy map (as function of z_1 and z_2) in Fig.12a exhibits three states; A, B₁ and C₁. In state A, the upper ion is in the vestibular region of the SF (z_2 ~14Å) and the lower ion is collectively bound by the inner (purple side chains) and outer rings (green side chains) (z_1 ~7Å). In state B₁ the top ion has joined the bottom ion and they are both bound by the inner and outer rings (z_1 ~ z_2 ~7Å) forming cooperative tight multi-ion/multi-carboxylate

complexes, commonly made up by D, E and D_{III}, and reminiscent of those seen in the bacterial Na_v (compare Fig.5.10e&f). In state C₁ the top ion has either pushed the bottom ion in to the cavity by Coulomb repulsion (dashed line) or it has passed by the bottom ion and entered the cavity itself (dotted line crossing the diagonal, $y=x$, represented by black dashed line), in both cases translocating from $z_2 \sim 7 \text{ \AA}$ to $z_2 \sim 10 \text{ \AA}$, while the other ion remains collectively bound to the inner and outer rings. These distinct permeation pathways are equally likely, with the largest barrier encountered being $1.9 \pm 0.8 \text{ kcal/mol}$.

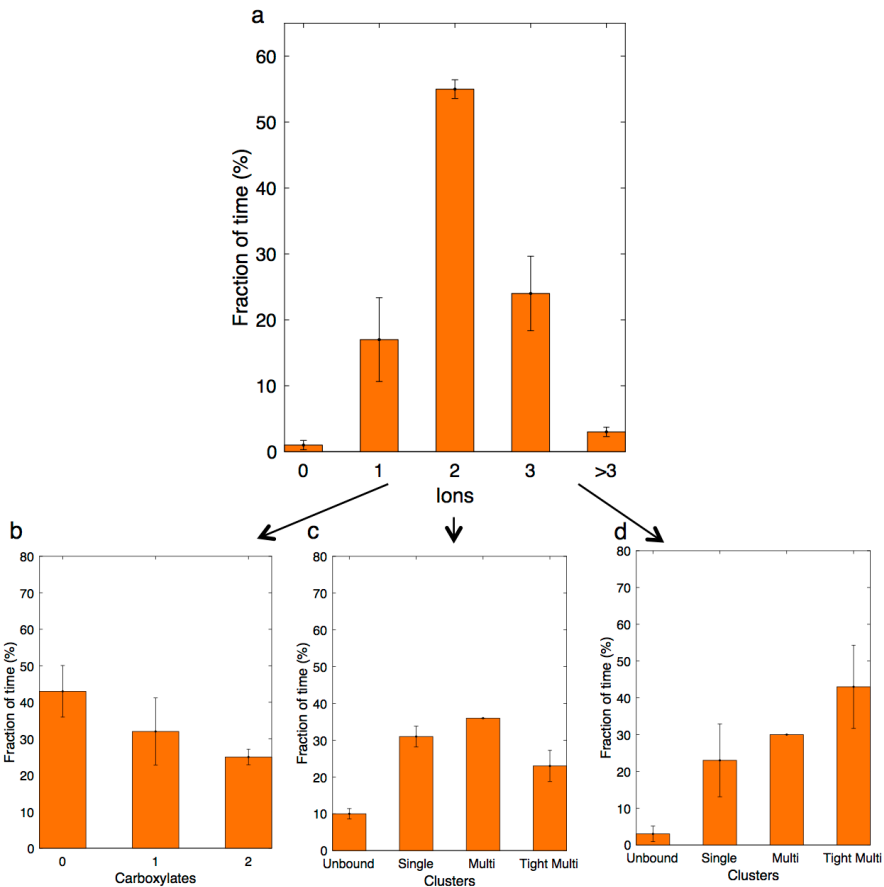


Figure 5.11. Occupancy analysis in the SF ($-15 < z < 15$) with deprotonated K₁₄₂₂. a) Distribution of ion occupancy in the SF of NavRh/Nav1.2 and dominant cluster confirmations for b) 1-ion occupancies and c) 2 ion occupancies, single clusters represent 1-ion/multi-carboxylate clusters and 1-ion/1-carboxylate clusters, and multi clusters represent tight 2-ion/multi-carboxylate clusters.

Fig.5.12b-d show free energy projections for the 3-ion occupancy state, with ion positions specified as z_1 (lower ion), z_2 (middle ion), z_3 (upper ion) or z_{23} (COM

of the two upper ions). Here state A corresponds to the same 2-ion state A from Fig.5.12a, with one ion in the middle of the two rings ($z_1 \sim 7$ Å) and one ion in the vestibule ($z_2 \sim 14$ Å), but with an additional ion entering from the bulk above ($z_3 \sim 15$ Å). In Fig.12b&c we see how the upper ion pushes the middle ion downward to bind together with the lower ion at the inner ring ($z_1 \sim z_2 \sim 6$ Å), represented by state B_2 , before eventually entering this site itself and pushing the bottom ion into the cavity, state C_2 , and completing the conduction event. The broad free energy surface in panel c is due to the range of binding sites offered by the inner and outer carboxylate rings, as well as the fact that the centroid of 2 ions may span a wide range. Fig.5.12d shows another projection involving only the top two ions (z_2 and z_3). The dashed line in Fig.5.12d shows how the top ion moves from state B_2 to state C_2 by entering the SHFS and knocking the bottom ion downward. The dotted line shows an alternative path where the top ion instead passes by the middle ion before knocking the bottom ion into the cavity. Regardless of the permeation pathway, the largest barrier experienced during permeation through the SF in the 3-ion state is 1.4 ± 0.6 kcal/mol, similar to that experienced for Na^+ in the bacterial channel (Fig.5.x). These results demonstrate that low barrier conduction may occur via knock-on or pass-by mechanisms in either 2- or 3-ion occupancy states for $\text{Na}_v1.2$, but where 3-ion conduction is energetically more favourable, with slightly reduced activation barriers. However, considering a 2-ion occupancy is more common (Fig.5.11), the 2-ion mechanism is likely contributing significantly to the overall ion flux.

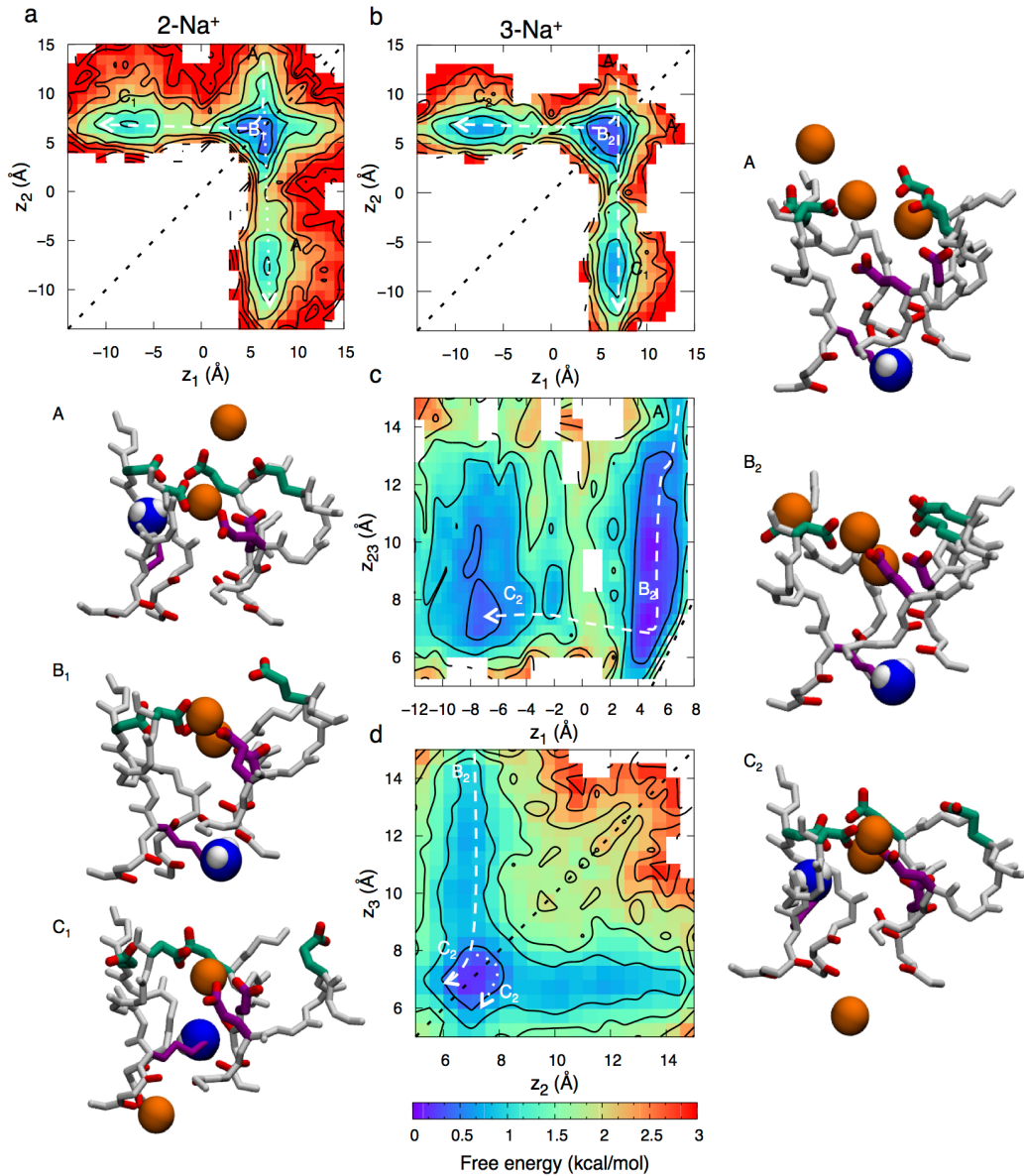


Figure 5.12. Permeation of Na^+ in the SF of $\text{Na}_v1.2$ with deprotonated (neutral) Lys. 2D free energy projections showing a) 2-ion conduction mechanism and b) 3-ion conduction mechanism, where z_1 , z_2 , and z_3 corresponds to the z positions of the bottom, middle and top ions, respectively, and where z_{23} is the z position of the COM of the top two ions. Snapshots with the DEKA ring in purple and the EEDD-ring in green indicate the corresponding Na^+ ion (orange balls) movements.

5.4.3 Charged lysine forms a high field-strength complex to enhance pass-by conduction

When Lys is charged, there is an average of 1.5 ± 0.4 ions in the SF and permeation involves either 1 or 2-ion conduction. This reduction in ion occupancy (compared to Na_v1.2 with neutral Lys and Na_vAb) is due to the reduced negative charge inside the SF. If the ammonium group of the Lys was considered as another ion, we would have, in total, a similar ion occupancy of 2–3 ions in the SF. The time series in Fig.5.13 reveals that several ions (coloured lines) enter and exit the SF, but it is not until the second half of the 4 μ s simulation that ions begin to cross the charged Lys and enter the cavity beneath, after which we observe ~30 complete permeation events (defined as any ion crossing downward or upward past the Lys).

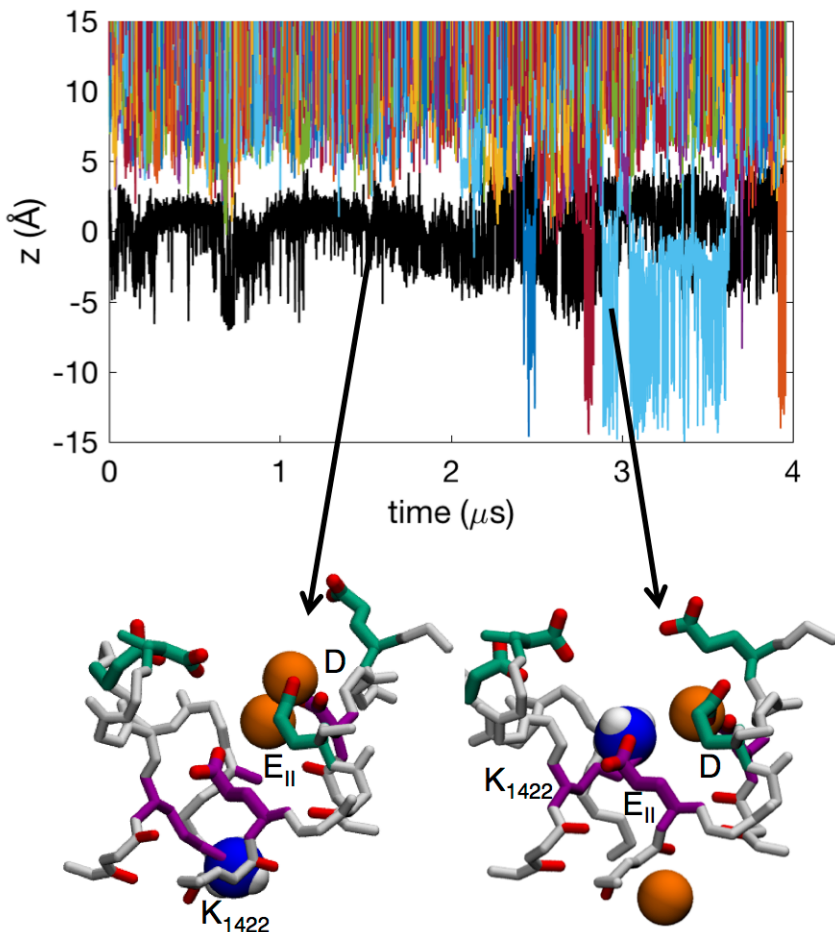


Figure 5.13. Time series showing the z-positions of K₁₄₂₂ (black) and Na⁺ ions (colours) in the SF of Na_v1.2 with protonated (charged) Lys. Insets show snapshots of Na⁺ ions (orange balls) in representative configurations with active residues from the DEKA ring (purple) and EEDD-ring (green) labelled.

Snapshots in Fig.5.13 show representative configurations of 1- and 2-ion carboxylate complex. As with the neutral Lys case, we see multi-ion/multi-carboxylate complex formation where the residues from the EEDD ring (green) bend down into the SF region, leading to the binding of ions together with the carboxylates from the DEKA ring (purple; see also Table 5.1; column 3). The DEKA ring is involved in binding ~50% of the time, the EEDD ring ~90% of the time, and both rings are cooperatively involved ~40% of the time. These complexes are most commonly ($69 \pm 11\%$) involving D from DEKA ring and E_{II} from EEDD ring. The ammonium group of the Lys from the DEKA is also involved, binding $61 \pm 10\%$ of the time to the E or D from the DEKA ring. The salt bridge between Lys and one or both of these residues has previously been identified by mutagenesis experiments as being important for Na^+ selectivity [51], and may be responsible for the importance of the precise location of the Lys in the DEKA ring [93]. We also observe that when ions enter the SF, the ammonium group of Lys (black line in Fig.5.13) is displaced downward; being knocked-on, like any other ion. Thus, the charged Lys is intimately involved in the multi-ion mechanism. Importantly, it also participates in a Lys+ Na^+ /carboxylate complex, similar to the 2-ion/multi-carboxylate complexes, commonly coordinated by D and E_{II} and sometimes additionally by E (Table 5.1; column 5). The ability to form these complexes is likely dependent on the location of the Glu and Lys in the DEKA ring, and swapping their positions might affect this complex formation thus decreasing selectivity, as observed in mutagenesis experiments [93]. We will see below how this tight complexes plays an important role in the conduction mechanism.

Free energy projections reveal the relationship between the ions and the position of the ammonium group of Lys, z_{K1422} , demonstrating conduction with 1-ion and 2-ion occupancies in the SF. When there is a lone ion in the SF, at z_1 , the free energy map (as function of z_1 and z_{K1422}) in Fig.5.14 exhibits four states; A, B_1 , C_1 and D_1 . In state A, the ion is in the outer vestibular region of the SF ($z_1 \sim 14 \text{ \AA}$) and the Lys is bound to one of the inner ring carboxylates ($z_{K1422} \sim 1 \text{ \AA}$). In state B_1 , the ion has entered deeper into the SF and is bound to the inner and outer rings ($z_1 \sim 6 \text{ \AA}$). The dotted line shows an alternative state, B_1' , in which the ion entering the filter replaces the ammonium group of K1422, which is displaced downward (from $z_1 \sim 6 \text{ \AA}$ & $z_{K1422} \sim 1 \text{ \AA}$ to $z_1 \sim 4 \text{ \AA}$ & $z_{K1422} \sim 2 \text{ \AA}$). It is interesting to note that there is no conduction when this happens. The

ion is bound tightly to the DEKA ring and the ammonium group of the Lys is too repulsive for it to pass by in the lower part of the filter, where the electrostatic potential is less negative. However, the dashed line shows how the ion can cross the ammonium group of K1422 in a region of higher field strength created by multiple carboxylates ($z\sim 2$ Å), leading to state C₁. In state C₁ the ammonium group of K1422 remains bound to the inner ring ($z_{K1422}\sim 2$ Å) and the ion is bound to the backbone carbonyl of the two residues underneath the DEKA ring ($z_1\sim -2$ Å). In state D₁ the ion has left the SF and entered the cavity ($z_1\sim -8$ Å), completing the permeation event. The dashed arrow shows the minimum free energy path for conduction, where the largest barrier encountered is 1.7 ± 0.3 kcal/mol.

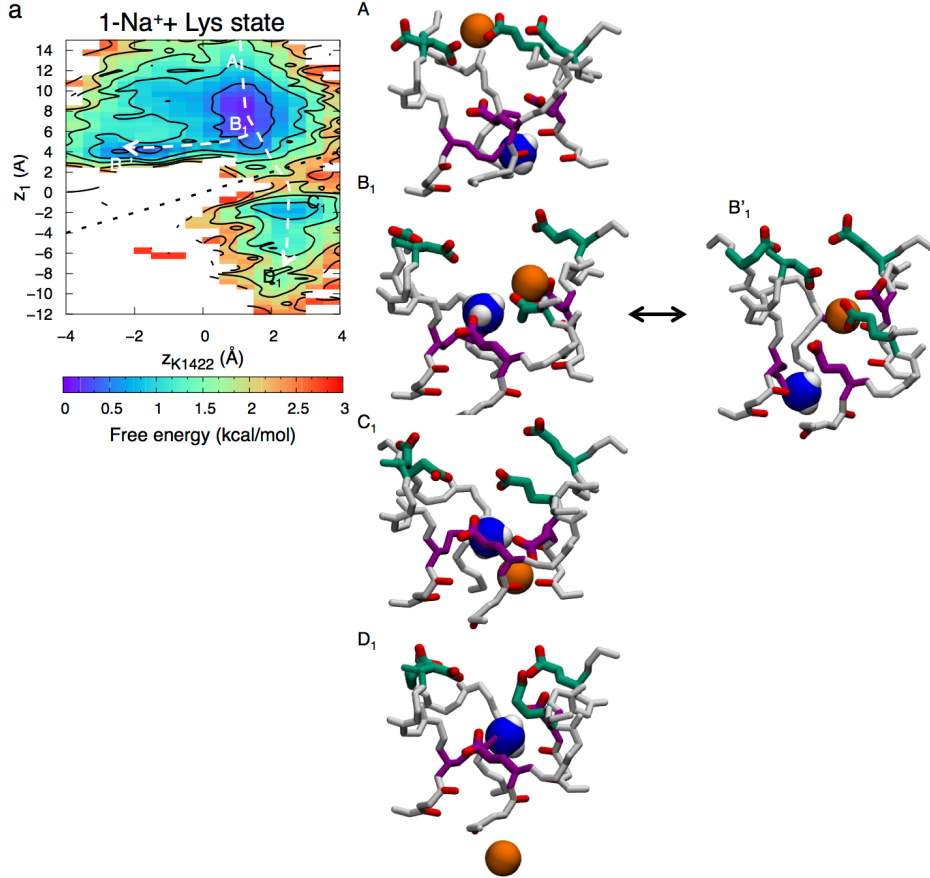


Figure 5.14. Permeation of Na^+ in the SF of $\text{Na}_v1.2$ with protonated (charged) Lys. 2D free energy projections showing 1-ion conduction mechanism where z_1 corresponds to the z position of the ion and $z_{\text{K}1422}$ the z position of the ammonium group of the Lys. Snapshots with the DEKA ring in purple and the EEDD-ring in green indicate the corresponding Na^+ ion (orange balls) movements.

Fig.5.15 shows the 2-ion conduction mechanism, where the free energy projection in Fig.5.15a shows the position of the bottom ion (z_1) as a function of the ammonium group of the Lys ($z_{\text{K}1422}$), Fig.5.15b shows the COM of the two ions (z_{12}) as a function of the lysine, while Fig.5.15c shows the function of bottom versus top ions. In this 2-ion case, we see five distinct states; state A corresponds to the same 1-ion state A, but with an additional ion entering from the bulk above, Fig.5.15b ($z_{12} \sim 14 \text{ \AA}$). We see how the two ions enter deeper into the SF and bind collectively to the inner and outer rings, just above the Lys in state B_2 ($z_1 \sim z_2 \sim 7 \text{ \AA}$ & $z_{\text{K}1422} \sim 2 \text{ \AA}$). There is an additional state B'_2 , related to B_2 , where the ammonium group of the Lys is displaced downward (from $z_1 \sim 6 \text{ \AA}$ & $z_{\text{K}1422} \sim 2 \text{ \AA}$ to $z_1 \sim 4 \text{ \AA}$ & $z_{\text{K}1422} \sim -2 \text{ \AA}$; dotted line). However, just as for the 1-ion state, this downward Lys displacement is not sufficient for conduction, instead

requiring that the ammonium group of Lys rise up and join one of the ions in a new intermediate stable state C₂ as shown in Fig.5.15a ($z_1 \sim z_K \sim 2 \text{ \AA}$). This state only appears when there are 2 Na⁺ ions in the filter and seems to be vital for efficient permeation, because it allows the ion to pass the Lys with reduced energetic barrier (dashed line). The ion then binds below the Lys to the backbone carbonyls of the lower SF represented by state D₂ ($z_1 \sim 2 \text{ \AA}$ & $z_{K1422} \sim 2 \text{ \AA}$). In state E₂ the top ion pushes the bottom ion into the cavity and binds to the inner ring ($z_1 \sim -6 \text{ \AA}$, $z_2 \sim 6 \text{ \AA}$ & $z_{K1422} \sim 2 \text{ \AA}$). Fig.5.15c shows only the two ions, at z_1 (lower) and z_2 (upper), and the corresponding states. The top ion can either enter and knock on or pass by the bottom ion. The dashed arrows show the lowest free energy path for conduction. The greatest barrier to overcome in the 2-ion state is $1.6 \pm 0.7 \text{ kcal/mol}$. Importantly, while conduction was seen to be possible with a singly-occupied SF (seen in Fig.5.14; dashed line), the entrance of a second Na⁺ ion enables a stable state (Fig.5.15a; state C₂) where the ammonium group of the Lys and the bottom ion are collectively bound by the carboxylates, this allows the ion to pass by the Lys and in to the cavity with a lower barrier. We see a mechanism where Lys is an active participant necessary for efficient conduction of Na⁺ ions. As we shall see below, this mechanism does not exist for K⁺ ions.

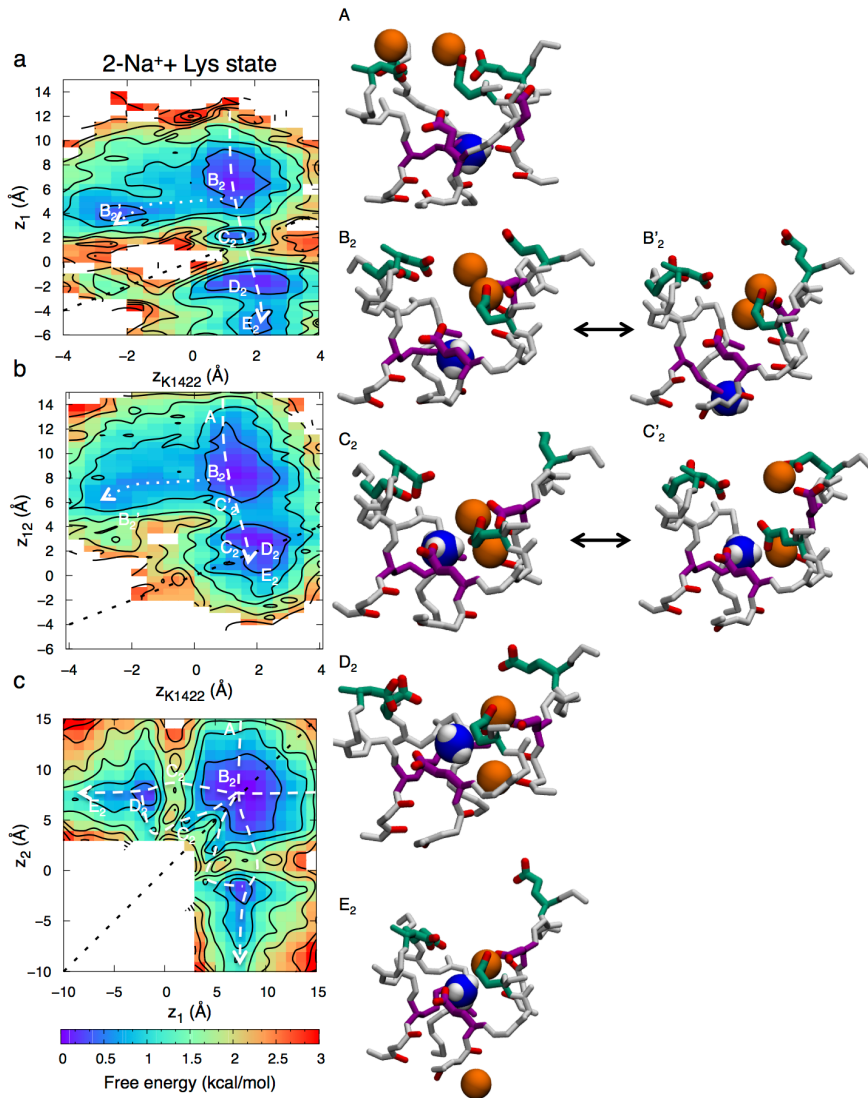


Figure 5.15. Permeation of Na^+ in the SF of $\text{Na}_v\text{Rh}/\text{Na}_v1.2$ with protonated (charged) Lys. 2D free energy projections showing 2-ion conduction mechanism where z_1 corresponds to the z position of the bottom ion, z_{12} the z position of the two ions and z_{K1422} the z -position of the ammonium group of the Lys. Snapshots with the DEKA ring in purple and the EEDD-ring in green indicate the corresponding Na^+ ion (orange balls) movements.

5.4.4 K^+ exhibits less multi-ion complex formation, and is partially blocked by lysine

The $\text{Na}_v1.2$ SF, with charged Lys, in the presence of KCl solution has an average occupancy of 1.3 ± 0.1 K^+ ions, being slightly lower than the occupancy for Na^+ ions, but within errors. Fig.5.16 shows several ions (coloured lines) entering and exiting the SF but not interacting extensively with the Lys (black

line). We see \sim 20 complete K^+ ion permeation events, being similar but somewhat lower than the Na^+ case above.

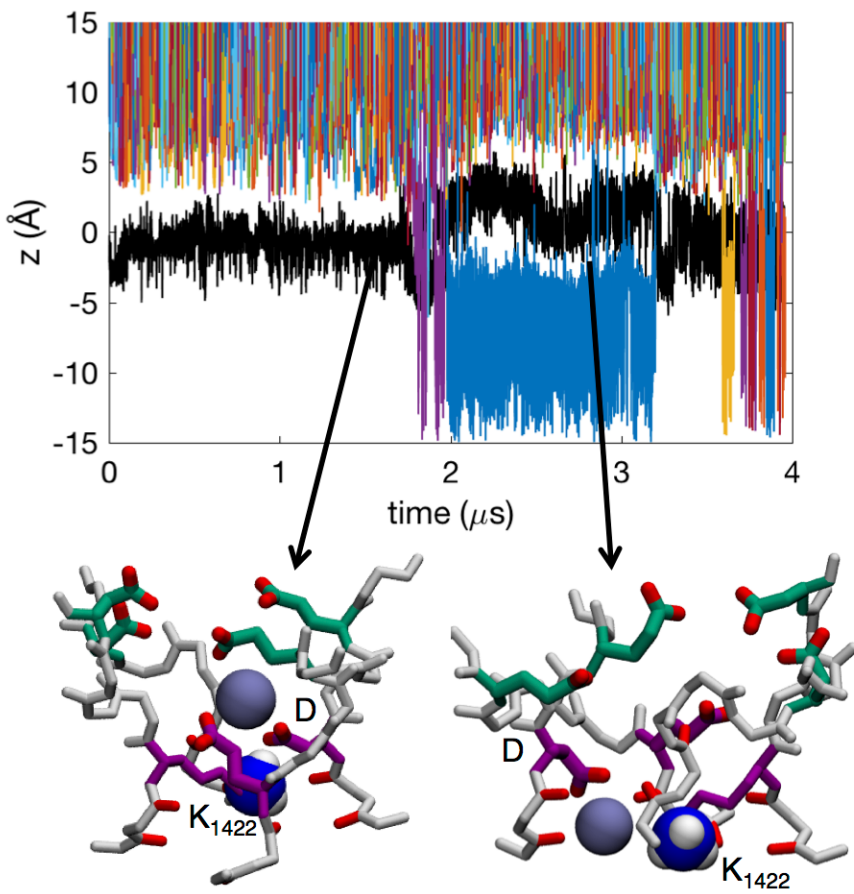


Figure 5.16. Time series showing the z-positions of K_{1422} (black) and K^+ ions (colours) in the SF of $\text{Na}_v1.2$ with protonated (charged) Lys. Insets show snapshots of K^+ ions (purple balls) in representative configurations with active residues from the DEKA ring (purple) and EEDD-ring (green) labelled.

Most of the time there exists a single K^+ ion in the SF (Fig.5.17). When there are two K^+ ions in the SF they are generally further from each other with a mean ion-ion distance of 15.1 ± 0.8 Å, compared to 11.4 ± 1.2 Å for Na^+ . Snapshots in Fig.5.18 show representative configurations. The K^+ ions most commonly bind to single carboxylates or stay unbound (Fig.5.17). The lower occupancy and the larger ion-ion distances mean that we do not see the same tight multi-ion/multi-carboxylate complexes as frequently as we did for Na^+ (Fig.5.17), and when they do occur they are almost always singly coordinated by outer ring carboxylates (Table 5.1; column 4). Instead, a single K^+ ion

typically enters the SF and binds solely to the D from the DEKA ring (Table 5.1; column 6). The DEKA ring is involved in binding ~40% of the time, the EEDD ring ~70% of the time, and both rings cooperatively involved only ~10% of the time. This reduced binding and absence of deep complex formation prevents K⁺ permeation. We instead observe K⁺ ions held bound to the D of DEKA, electrostatically repelled by the Lys ammonium group, until the Lys side chain changes rotamer downward to allow ion movement.

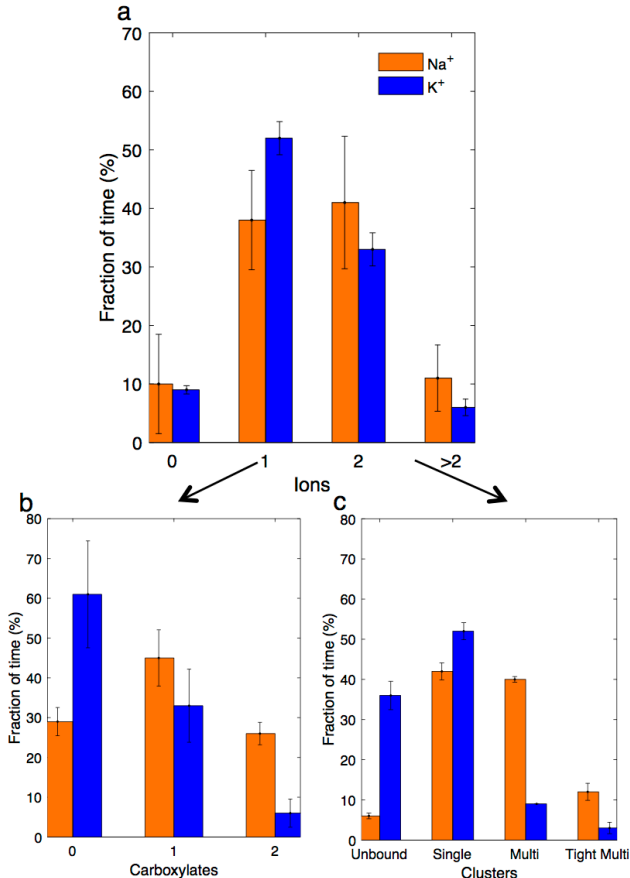


Figure 5.17. Occupancy analysis in the SF ($-15 < z < 15$) with charged K₁₄₂₂. a) Distribution of ion occupancy in the SF of NavRh/Nav1.2 and dominant cluster confirmations for b) 1-ion occupancies and c) 2 ion occupancies, single clusters represent 1-ion/multi-carboxylate complex and 1-ion/1-carboxylate complex, and multi clusters represent tight 2-ion/multi-carboxylate complex.

We again see conduction with either 1 or 2 K⁺ ion occupancy. However, unlike for Na⁺ ions, we see similar permeation mechanisms when 1 and 2 K⁺ ions are in the SF. This, together with the large mean K⁺-K⁺ distance of 15.1 ± 0.8 Å, compared to 11.4 ± 1.2 Å for Na⁺, suggest that the second ion does not

participate in conduction but rather is loosely associated around the vestibular region. Fig.5.18a shows the 1 ion conduction mechanism, with the ion at z_1 , and the ammonium group of Lys, at z_{K1422} . We observe four states in the 2D PMF in Fig.5.18; A, B, C and D. In state A the ion is in the vestibular region of the SF ($z_1 \sim 14 \text{ \AA}$) and the Lys is bound to one of the inner ring carboxylates ($z_1 \sim 0 \text{ \AA}$). The ion then moves down and binds to the outer ring ($z_1 \sim 8 \text{ \AA}$) represented by state B. In state C, the ion has entered deeper into the SF and is now bound only to the carboxylate of the D from the DEKA ring ($z_1 \sim 4 \text{ \AA}$). The Lys is still bound to the inner ring in both these two states ($z_K \sim 0 \text{ \AA}$). The ions do not have considerable effect on the position of the ammonium group of the Lys. However, occasionally (~10% of the time) the Lys changes rotamer downward ($z_{K1422} < -2 \text{ \AA}$), allowing leakage of K^+ ions and thus permeation, represented by dashed line, leading to state D. After the conduction event, the ammonium group of the Lys again bends upward to bind to the inner ring carboxylates ($z_{K1422} \sim 2 \text{ \AA}$). For this to happen the K^+ ion has to pass by the ammonium group of the Lys in the lower part of the SF ($z_1 \sim z_{K1422} \sim -2 \text{ \AA}$) where the electrostatic potential is less negative, leading to a larger energy barrier of $2.8 \pm 0.3 \text{ kcal/mol}$, as seen in Fig.18a along the pathway represented with a dashed arrow.

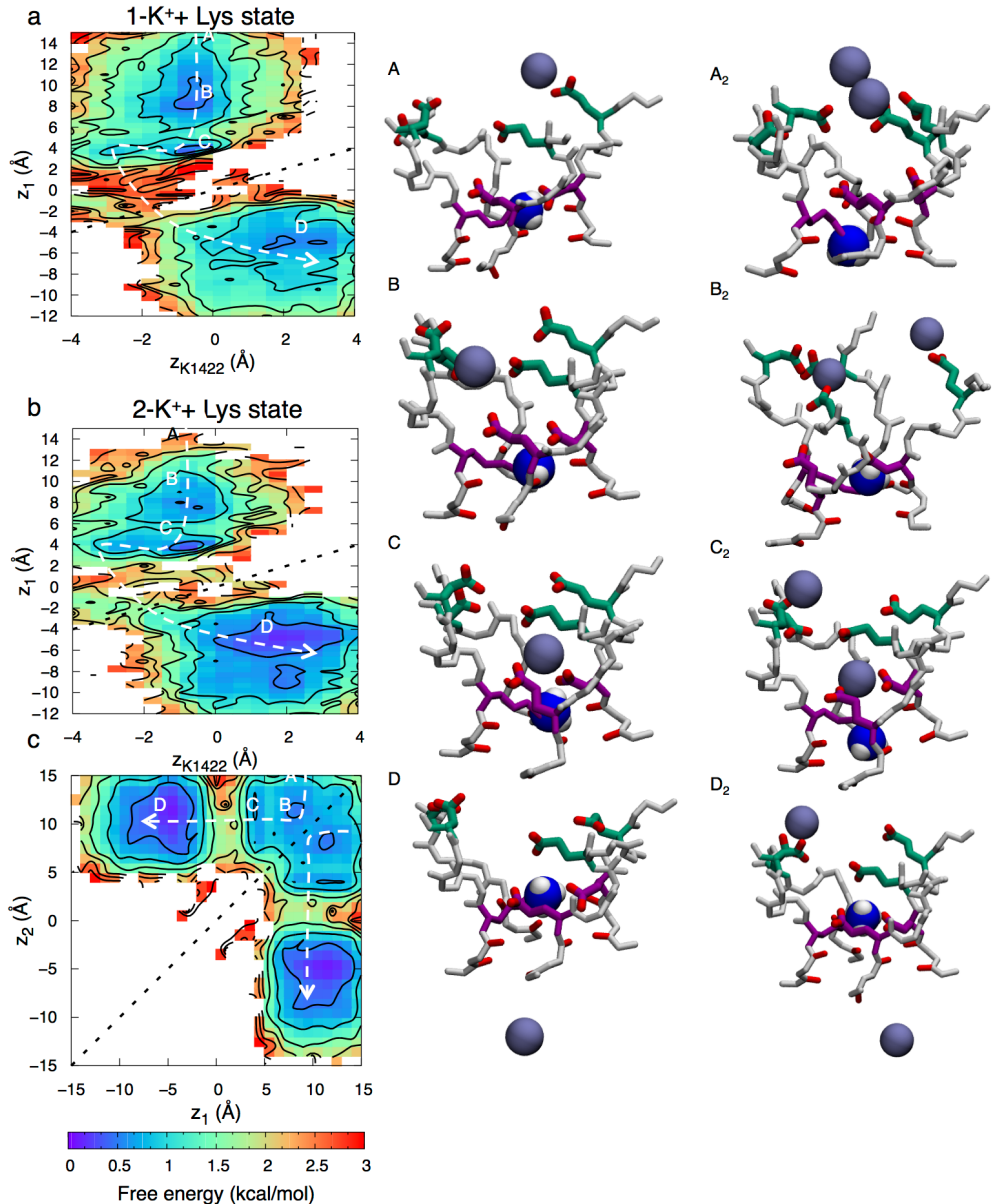


Figure 5.18. Permeation of K^+ in the SF of $\text{Na}_v\text{Rh}/\text{Na}_v1.2$ with protonated (charged) Lys. 2D free energy projections showing a) 1 and b&c) 2-ion conduction mechanism. z_1 corresponds to the z-position of the bottom ion, z_2 the z-position of the top ion and $z_{\text{K}1422}$ the z-position of the ammonium group of the Lys. Snapshots with the DEKA ring in purple and the EEDD ring in green indicate the corresponding Na^+ ion (purple balls) movements.

The 2-ion conduction mechanism looks very similar, with the large mean K^+ - K^+ distance of $15.1 \pm 0.8 \text{ \AA}$ indicating that it is the same as the 1-ion conduction mechanism, only with an additional ion in the vicinity. Fig.18b shows the 2D PMF with the bottom ion, at z_1 , and the ammonium group of Lys, at $z_{\text{K}1422}$.

This map is almost identical to the 1-ion case in Fig.18a, further supporting the lack of a proper 2-ion conduction mechanism. The lower ion enters the channel, binds collectively to the DEKA and EEDD ring in state B_2 , before binding solely to the DEKA ring in state C_2 . To enter the cavity, the ion has to wait for the Lys to change rotamer, it can then pass the Lys ammonium group in the lower SF, and then further down into the cavity (state D_2). Meanwhile, the upper ion generally sits in the vicinity of the SF. In Fig.18c we see how the two ions can cross each other in the top part of the channel. The top ion can be anywhere between $z_2 \sim 7 \text{ \AA}$ and $z_2 \sim 15 \text{ \AA}$ during conduction, however, with a slight preference around $z_2 \sim 12 \text{ \AA}$. The energetic barrier for the 1 and 2-ion conduction is similar with a height of $2.7 \pm 0.3 \text{ kcal}$. The Na^+ and K^+ barriers differ by 1.1 kcal/mol, however, the slowest coordinate in the K^+ translocation pathway appears to involve the structural isomerization of the Lys side chain downward to permit conduction, leading to a permeation event far more costly for K^+ .

Key to the low barrier for Na^+ permeation is its ability to form tight multi-ion/multi-carboxylate complexes as well as a complex with Lys and two carboxylates, allowing pass-by conduction in the S_{HFS} . We do not see the same tight K^+-K^+ complexes nor the simultaneous binding of K^+ and Lys near the DEKA ring. Instead we see a lone K^+ ion that is singly bound and forced to pass by the Lys lower in the SF, where the electrostatic fields are less favourable (Fig.5.10a), making the whole process far less likely.

We now explore the thermodynamic stabilities of the complexes observed during permeation events to understand the causes of the different Na^+ and K^+ mechanisms that may underlie selectivity.

5.4.5 Multi-ion complex stability underpins selective conduction

Multi-ion complex formation with carboxylates is required for efficient permeation through the SF as it helps draw in and stabilize the ions in the SF. This acts as a precursor for the ion+Lys/multi-carboxylate complex that aid in the crossing of the SF. The analysis in Fig.5.17 suggests that such multi-ion/multi-carboxylate complexes appear more favourable for Na^+ over K^+ . When the SF is occupied by a single ion, Na^+ is most commonly bound to one

or more carboxylate side chains (45% and 26%), whereas K⁺ is more likely to be unbound (61%) (Fig.5.17b), and Na⁺ is several times more likely than K⁺ to form multi-carboxylate complexes (26% vs. 6%). Of the multi-ion occupancies observed, Na⁺ ions are most likely to be either singly bound or in loose multi-carboxylate complexes (42% and 40%), whereas K⁺ is most likely to be either singly bound or unbound (52% and 36%). Na⁺ is several times more likely to form tight multi-ion/multi-carboxylate complexes than K⁺ (12% vs. 3%) (Fig.5.17c). For Na⁺ ions, these complexes are predominantly made up by outer ring carboxylates together with either the E or D from the DEKA ring, most commonly E_{II} together with D (Table 5.1; column 5). For K⁺ such complexes are almost always made up only by the outer ring carboxylates (Table 5.1; column 6).

Thus, tight 2-ion/multi-carboxylate complexes, similar to that seen ahead of the low free energy pass-by conduction events for Na⁺ (Fig.5.15; state B₂), are more common for Na⁺ than K⁺, and may be very important for selectivity (Fig.5.17). FEP calculations were used to investigate the relative stabilities of Na⁺ and K⁺ in such a complex. The most representative multi-ion/multi-carboxylate complex was identified to be bound collectively by D and E_{II} (69%) (Fig.5.19b; inset and Table 5.1; column 3). Results from FEP calculations show preferential binding by Na⁺ with 4.8±0.2 kcal/mol for single ion occupancy (Fig.5.19a), showing a strong inherent preference by carboxylates to bind Na⁺, in agreement with Eisenman high field strength theory on ion selectivity [232]. Quantum mechanical calculations using a model DEKA ring has shown a similar preference for Na⁺ over K⁺ (4.8 kcal/mol [233]) showing consistency between models. The same complex containing two ions shows a large preference of 8.3 ± 0.2 kcal/mol for Na⁺ over K⁺ (Fig.5.19b); 4.2 kcal/mol from the transformation of the 1st ion and 4.1 kcal/mol from the transformation the 2nd ion. This shows that an additional ion creates extra stability for Na⁺ relative to K⁺. When another ion is added to the complex, the cumulative ion-carboxylate attraction increases faster than the carboxylate-carboxylate and ion-ion repulsion, more so for Na⁺ than K⁺, giving additional stability to Na⁺ complexes (Fig.5.19a&b). These complexes create deeper binding in the SF that aids crossing of the ammonium group of the Lys.

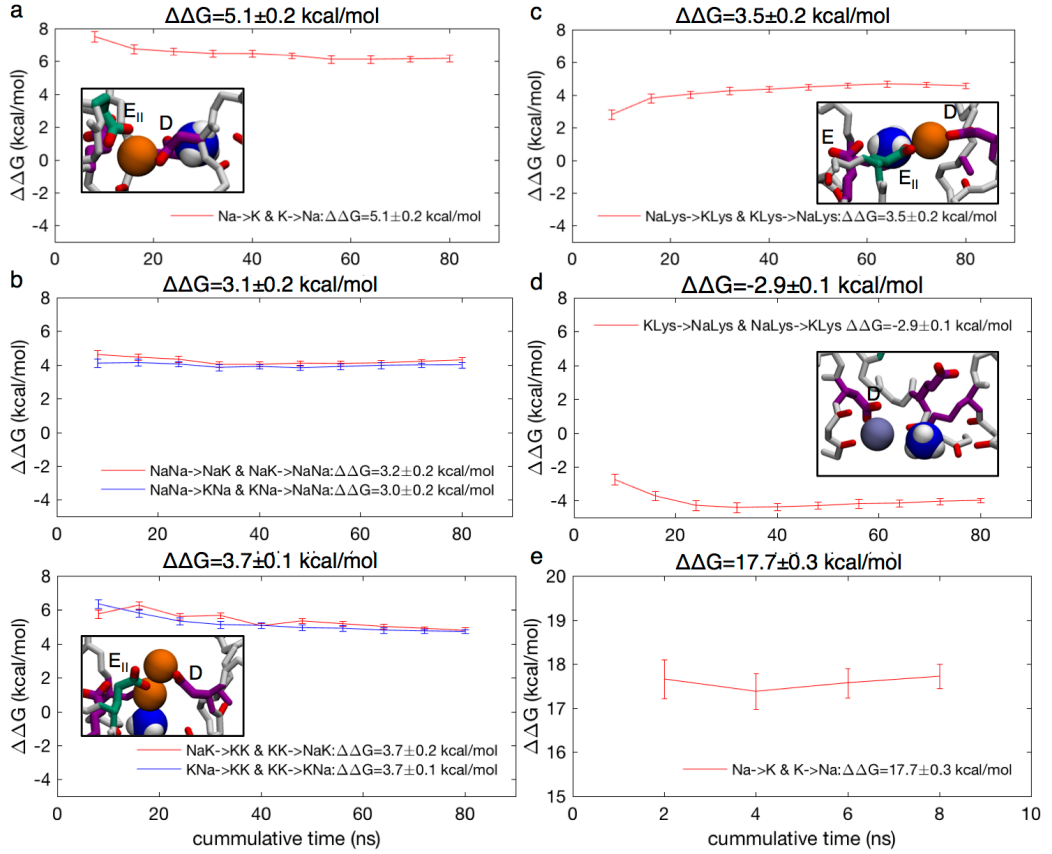


Figure 10. Results from FEP simulations. Binding free energy for a) $\text{Na}^+ \rightarrow \text{K}^+$ & $\text{K}^+ \rightarrow \text{Na}^+$ in $\text{Na}^+ - \text{D}_{\text{II}}$ complex, b) 1st ion $\text{Na}^+ \text{-Na}^+ \rightarrow \text{K}^+ \text{-Na}^+$, $\text{Na}^+ \text{-Na}^+ \rightarrow \text{Na}^+ \text{-K}^+$, $\text{K}^+ \text{-K}^+ \rightarrow \text{K}^+ \text{-Na}^+$, $\text{K}^+ \text{-K}^+ \rightarrow \text{Na}^+ \text{-K}^+$ (top) and 2nd ion $\text{K}^+ \text{-Na}^+ \rightarrow \text{K}^+ \text{-K}^+$, $\text{Na}^+ \text{-K}^+ \rightarrow \text{K}^+ \text{-K}^+$, $\text{K}^+ \text{-Na}^+ \rightarrow \text{Na}^+ \text{-Na}^+$, $\text{Na}^+ \text{-K}^+ \rightarrow \text{Na}^+ \text{-Na}^+$ (bottom) in $\text{Na}^+ \text{-Na}^+ - \text{D}_{\text{II}}$ complex, c) $\text{Na}^+ \rightarrow \text{K}^+$ & $\text{K}^+ \rightarrow \text{Na}^+$ for $\text{Na}^+ \text{-Lys-D E}_{\text{II}}$ complex, d) $\text{K}^+ \rightarrow \text{Lys}$ in the lower SF and e) $\text{Na}^+ \rightarrow \text{K}^+$ & $\text{K}^+ \rightarrow \text{Na}^+$ in bulk. Insets show starting configurations and indicate the amino acids involved in the ion-carboxylate complexes.

During the ion crossing of the charged Lys, the ion creates a stable transition state together with the Lys and multiple carboxylates (Fig.5.19c; inset). This ion-Lys state is bound collectively by the D and E from the DEKA ring, as well as E_{II} from the outer ring, and shows preferential binding of a single Na^+ by 4.1 ± 0.1 kcal/mol (Fig.5.19c). This ability to create a joint ion-Lys complex to facilitate crossing of the Lys in the S_{HFS} is the salient difference in Na^+ and K^+ permeation mechanisms.

The K^+ ion instead usually resides alone in the SF and crosses the ammonium group of the Lys further down, (Fig.5.19d; inset), where the electrostatic fields arising from carboxylates in the central and upper SF is less attractive. If we

examine the relative free energies of Na^+ and K^+ ions in this region of the SF near the Lys, where such crossing occurs for K^+ , we calculate a similar but reduced value of 3.4 ± 0.3 kcal/mol, still favoring Na^+ (Fig.5.19d). This value remains negative because the ion remains in contact with the carboxylate side chains of D from the DEKA ring as it passes the positively charged side chain of the Lys. Theoretically, both K^+ and Na^+ should be able to translocate in this fashion when the Lys moves downward, but this was not observed for Na^+ . We may understand this from the relative destabilization of Na^+ in this region relative to the highly selective multi-carboxylate complexes that form above it, preventing downward movement of Na^+ into a cleared path.

We therefore hypothesize that selective permeation arises from the distinct mechanisms (Lys-complex pass-by permeation versus electrostatically plugged Lys permeation), which originates from the difference in stabilities of multi-ion and ion-Lys complexes in the high field strength region of the SF. Multi-ion/multi-carboxylate complexes have also been seen to be crucial for Na^+ permeation in the bacterial Na_vAb channel, where a preference for single Na^+ ions of -2.2 ± 0.6 kcal/mol has been estimated [49]. However, we suggest that optimal conduction requires the greater occupancy of the three ion state, which is achieved when the crystallographic E177-S178 H-bond (Na_vAb numbering) is lost on two opposite monomers, allowing the S_{HFS} carboxylate groups to reach toward the centre of the SF and coordinate two Na^+ ions concurrently. This two- Na^+ /two-carboxylate complex offers additional stability, allowing those two ions to coexist in S_{HFS} , and we calculate the relative stability of Na^+ vs. K^+ in S_{HFS} to become -3.8 ± 0.2 kcal/mol. This observation suggests that Na^+ ions adopt a specific three-ion arrangement with two ions at the level of S_{HFS} that does not occur in simulations of K^+ , which parallels our observations in the $\text{Na}_v1.2$ channel.

5.5 Conclusions

The ability to select for their native ion while discriminating against other similar ions is one of the key features of voltage gated ion channels. Uncovering what governs this ion selectivity in Na_v channels is essential to gather a better understanding of their nature and functions. Ion selectivity and conduction are co-dependent, dynamic processes that involve conformational isomerization of

the residues of the SF as well as translocation of several ions, hence the need for long unbiased simulations, allowing the study of the whole energetic landscape. In the absence of a high-resolution structure of a eukaryotic channel to study selectivity and conduction at the molecular level, we designed a model of the human $\text{Na}_v1.2$ by patching the essential sequence of residues in and around the SF, including the key DEKA and EEDD rings, into the Na_vRh bacterial channel. This $\text{Na}_v\text{Rh}/\text{Na}_v1.2$ SF relaxes into an asymmetrical configuration, where the DEKA and EEDD rings are highly flexible and cooperate to ensure efficient conduction and selectivity for Na^+ over K^+ , in line with previous studies of bacterial Na_v channels where similar flexibility has been shown to be critical for ion conduction [49, 59].

The presence of a positively charged residue such as Lys in Na_v channels has long been a source of confusion. While proven to be essential for selectivity, its specific role remained largely unexplained. Previous computational studies of eukaryotic Na_v models point toward a passive, mostly hindering behaviour, where the Lys side chain needs to bind away from the pore in order to allow the conduction of Na^+ ions. We reveal a much more involved, active role for this residue, changing depending on its protonation state. When Lys is unprotonated (neutral), we observe a 2 to 3-ion occupancy in the SF where both 2 and 3-ion knock on conductions are common, these permeation events are facilitated by tight multi-ion/multi-carboxylate complexes made possible by the highly flexible side chains of the SF. When Lys is instead protonated (charged), we see a reduction to a 1 to 2-ion occupancy, due to the extra charge introduced by the ammonium group of the Lys. In fact, we see the Lys actively participating in the conduction mechanism with a role similar to that of a permeating ion. Again, we see multi-ion/multi-carboxylate complexes playing a key role in Na^+ permeation. In the presence of K^+ ions, the conduction mechanism mainly relies on single ion permeation, where multi-ion/multi-carboxylate complexes are far less likely.

These multi- Na^+ /multi-carboxylate complexes help attracting Na^+ ions in to the SF of $\text{Na}_v1.2$ where deep binding stabilizes the ions. Interestingly, the carboxylates involved in these key multi- Na^+ /multi-carboxylate complexes generally involves only one carboxylate from DEKA ring and one or two from the EEDD ring in the vestibular region, rather than both D and E from the

DEKA ring. This observation is consistent with mutagenesis experiments showing the need for only one of the D and E from the DEKA ring, supporting the theory of direct involvement of the outer ring [51]. These Na^+ favourable complexes are more commonly bound collectively by D and E_{II} . Cysteine mutations of the residues in the EEDD ring show the greatest decrease in conduction when this domain II Glu (E_{II} in our model) is mutated [92, 93], supporting our observation that this residue from the outer ring is particularly important.

In the case of charged Lys we see conduction that is possible with a singly occupied SF, however, the binding of a second Na^+ ion reduces the conduction barrier, therefore allowing a more efficient multi-ion conduction. The second Na^+ ion helps to push the ion already in the SF and stabilize a state where the ammonium group of the Lys and the bottom ion are collectively bound by the carboxylates, this allows the ion to pass by the Lys and in to the cavity. Even though more space for conduction can be created in the SF by the steric unplugging of the ammonium group of the Lys, no conduction occurs in the Lys down state. This behaviour is consistent and comparable with previous results in Na_vAb , where pass by of ion by another would only occur at the level of S_{HFS} . When the charged ammonium group of Lys is in the S_{HFS} , where the electrostatic potential is most negative, it creates a smooth electrostatic environment leading into the cavity, when it is in the down state the electrostatic potential is being “cut off” by the Lys. This shows the fundamental role of the Lys as an active participant in the conduction mechanism of Na^+ ions.

K^+ is far less likely to form these multi-ion/multi-carboxylate complexes; in particular, we see preferential binding of 8.3 ± 0.1 kcal/mol for $\text{Na}^+ \text{-} \text{Na}^+$ over $\text{K}^+ \text{-} \text{K}^+$ in these complexes. Furthermore, K^+ does not form the stable ion+Lys/multi-carboxylate complex; in fact this complex favours Na^+ over K^+ by 4.3 ± 0.4 kcal/mol. The consequence of this difference in affinity is a completely different conduction mechanism for K^+ , having to pass the ammonium group of Lys in the lower part of the SF, where the electrostatic environment is not as favourable. Furthermore, even with Lys in this down state favoured by K^+ , we see a preferential binding of Na^+ over K^+ of 3.8 ± 0.2 kcal/mol.

Our knowledge of Na^+ conduction in bacterial Na_v channels can shed some light onto the origins of these different permeation mechanisms in human Na_v channels. Efficient permeation of Na^+ in the bacterial Na_vAb channel depends on an interconversion between 2 and 3-ion occupancy states, where 2 ions stably bind to the S_{HFS} Glu side chains, and a 3rd ion enters the filter to knock-on or pass-by the middle ion and to push the bottom ion in to the central cavity. The efficiency of this multi ion knock-on mechanism is reliant on 2- Na^+ /2-carboxylate complexes, whose thermodynamic stability is increased for Na^+ compared to K^+ , as we have shown. Even though bacterial channels possess four carboxylates at this site, not all are needed for high affinity binding, linking back to the eukaryotic channel selectivity mechanism [49].

It has been proposed that mammalian Na_v s select for Na^+ via a different mechanism to bacterial Na_v s owing to their differing S_{HFS} (EEEE vs. DEKA) [27, 234]. While this appears to be the case based on our observations, we see evidence for common features that may be central to Na^+ selectivity. Both bacterial and human channels make use of an efficient multi ion mechanism enabled by flexible carboxylates binding two Na^+ ions. The bacterial channel uses two of its four S_{HFS} Glus, whereas the mammalian channel uses carboxylates both from the DEKA and EEDD rings. The Lys in DEKA acts as an additional Na^+ and participates in this multi ion knock-on mechanism. The bacterial like multi-ion/multi-carboxylate complexes that favour Na^+ work together with Lys acting as a gate that only lets Na^+ ions through, when in its predominant up state, to create a highly Na^+ selective channel.

Experiments have suggested that Na_v s have multiple binding sites in the SF and that they therefore can hold several ions [29, 30]. However, investigations of concentration dependence, flux coupling and anomalous mole fraction effects give ambiguous evidence when it comes to ion occupancy [29-32, 37, 38]. A flux ratio exponent close to unity and a lack of anomalous mole fraction effect have previously been interpreted as meaning that the conduction mechanism through the Na_v s rely on a single ion mechanism [30, 32, 37]. However, both of these methods measure the coupling and cooperativity of the ion in a single file SF. Thus, in a wider SF, like the one of Na_v s, where the high electrostatic environment allows for ion-ion pass by, it is questionable that the flux coupling and anomalous mole fraction effects are directly related to the ion occupancy.

In fact, simulations have shown that n' does not always correlate directly to the number of ions that occupy the channel, but can change independently of ion occupancy [40]. And anomalous mole fraction effects have been attributed to other causes [44-46]. Furthermore, a concentration dependence on the conductance indicative of multi-ion cooperativity has been found [32]. The occupancy analysis of our free simulations revealed an occupancy of 1-2 Na^+ ions in the SF of $\text{Na}_v1.2$. However, there are inherent limitations in our simulations originating from the closed state of the channel. We have therefore not been able to investigate ion selectivity under physiological conditions, with a potential difference driving the ions through the channel. It is therefore pertinent that future studies should be performed with an open model of $\text{Na}_v1.2$.

Although we have explored both possible protonation states of the side chain of the DEKA Lys, we have not investigated a potential change of protonation states for any of the SF Glus or Asps. Experiments on mammalian Na_v s have shown a progressively decreasing conductance during extracellular acidification [95, 235]. Electrostatic calculations have found that the DEKA ring Glu and Asp are likely deprotonated at lowered pH, protected by the electrostatic field created by the DEKA Lys [95]. In contrast, the vestibular EEDD ring has been proposed to be responsible for proton block. These Asps and Glus can protonate at extracellular acidification which leads to a blocked channel [95]. This further may suggest that an efficient conduction is reliant on the deprotonated state of these residues. Mutations changing the Asps and Glus of the EEDD ring to neutral or positively charged amino acids show decreased ion conduction further demonstrating the importance of the negative charge of these residues [91, 93-95].

Experiments on bacterial Na_v s have shown that the Na^+/K^+ selectivity is lowered during extracellular acidification [27]. Computational studies have shown that this is likely due to the loss of ion exchange between the cytoplasm and the SF. When more than one of the S_{HFS} Glus are protonated a decrease in ion occupancy can be observed which leads to proton block [49]. The conduction mechanism in bacterial Na_v s is reliant on alternating ion occupancy between two and three ions [49, 59, 84]. This mechanism is lost when more than one of the Glus are protonated. The conduction mechanism is therefore likely reliant

on a mainly deprotonated EEEE-ring. However, it has been proposed that the protonation and deprotonation of the EEEE-ring is coupled to the alternating ion occupancy and protonation/deprotonation events may happen concurrently as the occupancy alternates [49]. As we see alternating ion occupancies also in the mammalian Na_v a similar link is possible; protons may bind to the EEDD ring during single ion occupancy and unbind so that an additional ion can enter the channel. It is therefore likely that protonation and ion conduction are coupled in mammalian Na_v s. Furthermore, as the we see high involvement of the outer ring in ion selectivity, and the Na^+/K^+ selectivity was altered at extracellular acidification [27], the selectivity mechanism is likely delicate and a change in protonation state may alter also the selectivity. Although the fully conducting state is likely deprotonated, the investigation of protonation of the vestibular ring of the mammalian Na_v would add interesting information to the investigation of ion selectivity and conduction in $\text{Na}_v1.2$. Simulations should therefore either be performed for all the possible protonation states of the channels or using constant pH MD simulations, where titratable groups are allowed to change protonation state, for example by using non equilibrium MD [236]. Furthermore, the protonation states of the residues in a variety of ion channel like environments could be explored with QM calculations [217]. This way we would be able to better understand the protonation dependence in these environments.

5.6 Supplementary information

5.6.1 Model dependence of the results

To insure that our results are independent of changes to the model we also used a non-bonded VDW NBFIX created by fitting ion carboxylate parameters to osmotic pressure data (Na^+ -carboxylate $r_{\min}=3.19\text{\AA}$ and K^+ -carboxylate $r_{\min}=3.52\text{\AA}$) [196]. It should be noted that previous investigations of these parameters have shown repulsive ion pairings between Na^+ and acetate and a diffusion coefficient not adequately matching experimental results [15]. Only short simulations were performed and while we see a decrease in binding, cluster analysis show consistency with original results, with Na^+ being more likely than K^+ to form the important multi-carboxylate complexes (Fig.S5.1).

Single ion occupancies now dominate for both Na^+ and K^+ and the lone ions are generally unbound for both species, however, it is more likely for Na^+ than for K^+ to be bound to 1 or more carboxylate side chains (Fig.S5.1a&b). Of the multi-ion occupancies, Na^+ ions are several times more likely than K^+ to form multi-carboxylate complexes and slightly more likely to form tight ones (Fig.S5.1c).

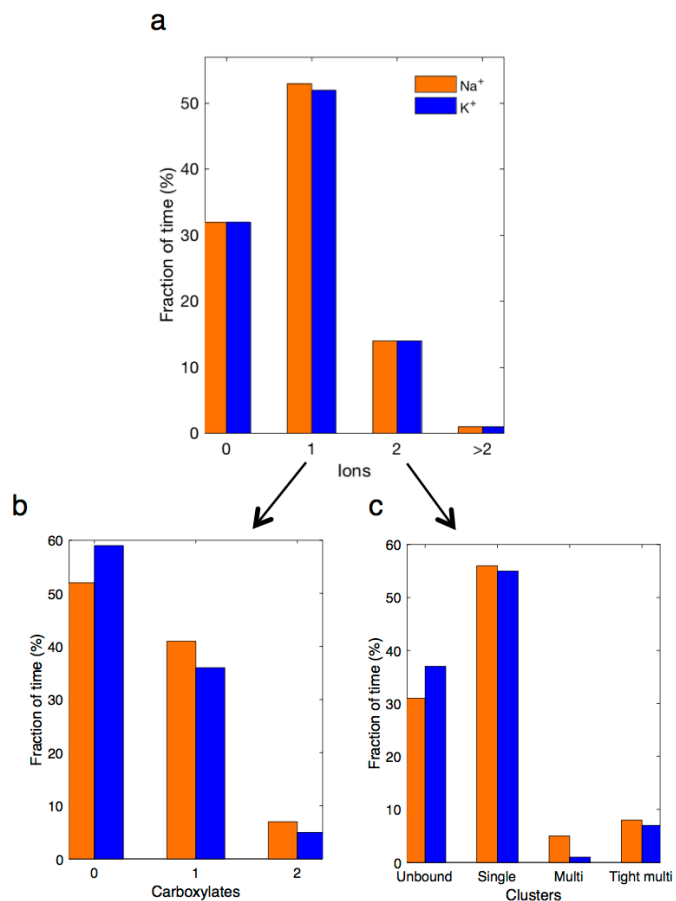


Figure S5.1 a) Distribution of ion occupancy in the SF of $\text{Na}_v\text{Rh}/\text{Na}_v1.2$ with Na^+ (orange) and K^+ (blue) where NBFIX has been used b) 1-ion occupancies and c) 2 ion occupancies, in the case of tight multi carboxylate complexes, states are defined by the radial distribution function $g(r)$ for ion-ion distance as well as being bound to multiple carboxylates.

Chapter 6

6 Ion selectivity in the acid sensing ion channel ASIC1

6.1 Overview

ASICs are proton-gated channels that mediate Na^+ currents. They play essential roles in a wide range of physiological processes ranging from pain sensation to anxiety. Recently solved crystal structures for the ASIC1a channel provides us with an excellent opportunity to investigate functional mechanisms using MD simulations. The ion selectivity of ASICs has been proposed to be governed by a size constriction site in the middle of the pore. This size constriction site is comprised of three Gly, Ala and Ser (GAS) residues. Surprisingly, free energy simulations show no difference in thermodynamic stability in the GAS region, challenging this size-based selectivity hypothesis. Instead, our simulations show that the channel utilises rings of Glu and Asp residues in the lower pore to discriminate against K^+ ions. Suggesting a SF in the intracellular end of the ASIC pore. These residues can form multi-ion/multi-carboxylate complexes that favour Na^+ . Our results are supported by mutagenesis and novel unnatural amino acid substitution experiments performed by collaborators [15]. Unnatural amino acid substitutions allow us to probe the involvement of GAS without affecting the function of the channel. Furthermore, we suggest that the

experimentally observed selectivity is better explained by a channel with narrower intracellular pore opening. A narrower pore would allow Glu and Asp side chains from different subunits to form complexes with ions. These studies provide important insights into ASIC structure and function and may assist the design of therapeutics for neurological disorders such as chronic pain syndrome, cerebral ischemia and epileptic seizures.

6.2 Introduction

ASICs are Na^+ -selective, voltage independent ion channels activated by a change in extracellular pH [237]. ASICs are widely distributed in both the central and peripheral nervous system where they primarily participate in neuronal sensitivity to acidosis, as well as pain, taste, anxiety, retinal function and memory amongst other functions [106-109]. For this reason they have great potential to be pharmacological targets [106]. Six different ASICs have been identified (ASIC1a, ASIC1b, ASIC2a, ASIC2b, ASIC3 and ASIC4) encoded by four different genes (ASIC1-4) [105]. However, the understanding of their functions in the body is far from complete. Recently solved crystal structures for the ASIC1a channel [112, 114] enables investigation of their functional mechanisms using MD simulations.

ASICs consist of three domains each containing two trans-membrane spanning subunits (TM1 and TM2/(TM2a and TM2b)) connected by a large extracellular loop (Fig.6.1). This loop makes up 60-70% of the protein and is responsible for the binding of the protons and subsequent opening of the channel [112]. ASICs are a part of the larger family of ENaC/DEGs [102]. Experiments on ENaCs have previously suggested that selectivity is governed by the well-conserved residues G-X-S located in the middle of TM2 [238]. Mutations of these residues effected the permeation of larger cations [122, 238]. The notion of a GXS SF has been extended to ASICs. ASIC selectivity is proposed to be governed by a constriction site in the middle of TM2 made up of G10', A11' and S12' [111, 114]. Furthermore, the recently presented x-ray structure of an ASIC1 channel (PDB:4NTW) demonstrated these residues created a narrow constriction site in the middle of TM2, supposedly confirming the GAS SF [114]. It is proposed that the size of this constriction site ($\sim 3.8 \text{ \AA}$) is more suited to Na^+ as it favourably accommodates a hydrated Na^+ ion (~ 3.8

\AA) over a hydrated K^+ ion ($\sim 4.2 \text{ \AA}$) [239]. Therefore, a selectivity mechanism dependant on a size constriction site has been proposed. However, this type of size-based selectivity is generally deemed out dated as experiments and simulations have shown that ion channels are highly flexible macromolecules [39, 47-49]. Furthermore, ASIC selectivity relying solely on the GAS residues has not been experimentally tested as mutagenesis of G10' and S12' renders the channel non-functional [123-125]. Furthermore, it is the backbone carbonyl of G10' that is presumed to point into the pore and interact with the ion [114]. This was further confirmed by the new structure [114]. Thus, conventional mutagenesis is not suitable to explore its contribution to channel function. To overcome this problem collaborators have performed unnatural amino acid substitutions that alter the dipole moment of the backbone on G10'. Using this novel technique the role of GAS can be examined [15]. Furthermore, MD simulations may be a useful tool to explore ion selectivity in ASIC1.

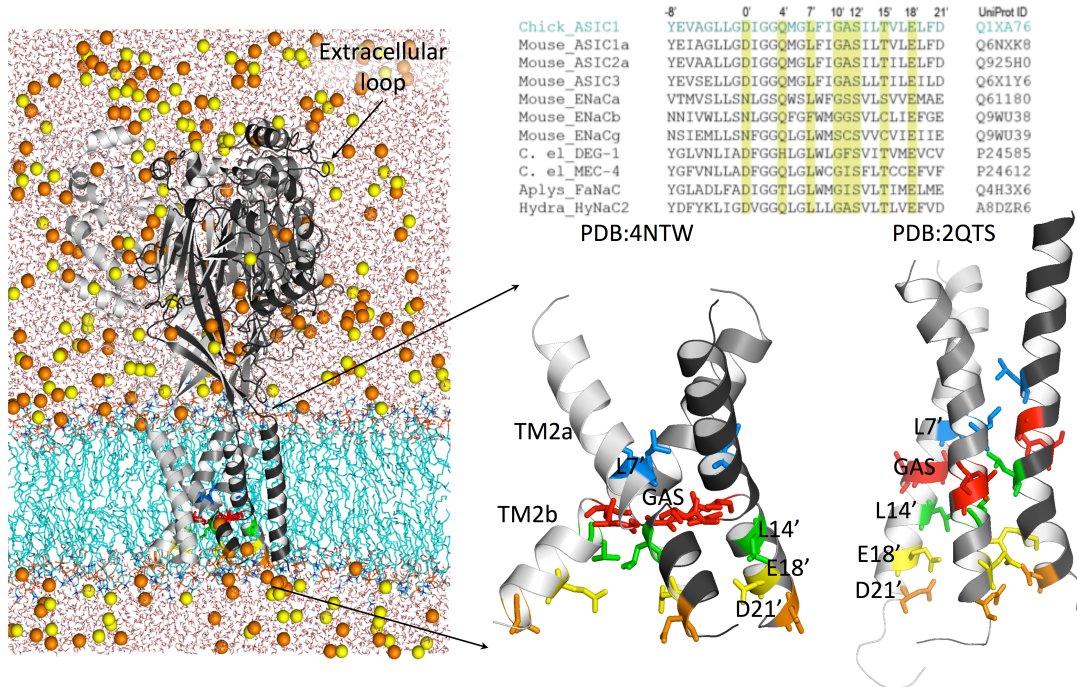


Figure 6.1. ASIC1 channel embedded in a hydrated DPPC bilayer (cyan sticks), surrounded by water (red and white sticks) with Na^+ and Cl^- ions (orange and yellow balls). Insets show the TM2 of 4NTW to the left and 2QTS to the right, highlighting L7' in blue, GAS in red, L14' in green, E18' in yellow and D21' in orange. Sequence alignment shows ASIC, ENaC and DEG aligned, with conserved residues highlighted in yellow.

There are a number of atomic scale structures of the mammalian ASIC1 including the closed PDB:2QTS [112] and the open MitTx bound PDB:4NTW

[114]. In PDB:4NTW, TM2 kink to form a planar belt at the level of the GAS residues, creating a locally defined gate not seen in PDB:2QTS (Fig.6.1). The GAS belt breaks the TM2 helix into TM2a and TM2b that forms inter domain interactions with each other (Fig.6.1 inset). The kinks between TM2a and TM2b from the different subunits together create a narrow ring, the GAS-belt. The main chain carbonyls of G10' are pointed into the channel pore and interact with the ion when it permeates the GAS belt [114]. In this conformation the lower part of the pore is splayed open, causing the residues at the lower end of the pore to be too far from each other to interact and form inter-subunit sites (Fig.6.1, inset). This splaying may be a consequence of the missing intracellular N and C-termini which help forming a conducting pore (Fig.6.2) [240]. PDB:2QTS is solved for an additional 10 residues towards the intracellular side and the orientation of TM2 creates a narrow pore. The TMD of the channel in this state is obstructed by a ring of L7' side chains pointing in to the channel pore, rendering the channel non-conductive. Therefore, the channel is postulated to be in a closed, desensitised state. However, we can still investigate ion binding in the lower part of the channel (Fig.6.1, inset).

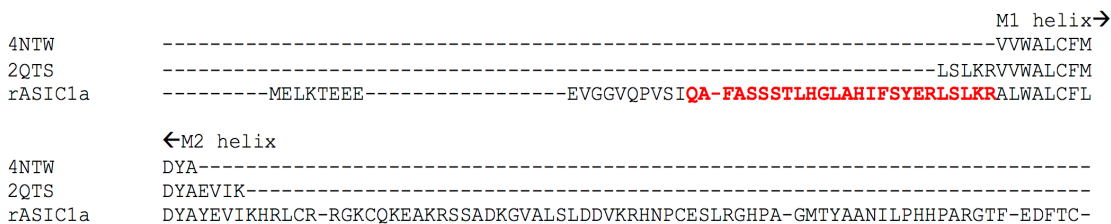


Figure 6.2. Sequence alignment of the intracellular domain of PDB:4NTW, PDB:2QTS and rat ASIC1. Both PDB structures are missing large parts of the intracellular domain.

We have explored ion selective binding in ASIC1 using MD simulations, starting with unbiased simulations of Na^+ and K^+ in PDB:4NTW. Permeation through the GAS-belt is a single ion mechanism thus making US suitable to increase statistical power and further pinpoint the mechanisms involved. The splayed lower pore of the PDB:4NTW may be an artefact of the missing intracellular termini (Fig.6.2). To account for structural dependence we also explored another ASIC x-ray structure; PDB:2NTW, which we will show may be more consistent with both our simulation and experimental evidence. We will demonstrate that there is no preference for Na^+ in the GAS belt. Instead, a preference for Na^+ in the lower part of the pore will be observed. Furthermore,

collaborators Lynac *et al.* at the Centre for Biopharmaceuticals at University of Copenhagen have performed unnatural amino acid substitution and mutagenesis experiments on ASIC1 [15]. These experiments are perfectly suited to probe the contributions of charge, length and cooperativity of the side chains and the backbones of the amino acids lining the ASIC1 pore [15]. We will show how these experiments reinforce the predictions from our simulations.

6.3 Methods

6.3.1 System

Ion permeation and selectivity was explored by performing both free simulations and US simulations of Na^+ and K^+ going through the trans membrane spanning part of two ASIC1 structures (Fig.6.1). The first proposed open structure, PDB:4NTW [114] (available residues 45 to 456) was embedded in a bilayer of palmitoyloleoyl- phosphatidylcholine (POPC) lipids. It was surrounded with explicit TIP3P water molecules [142] (47184 molecules) and 150 mM of NaCl or KCl (162 Na^+ or K^+ ions and 123 Cl^- ions). This gives a total of 213,043 atoms in a $115 \times 115 \times 160$ Å box. The second structure, PDB:2QTS [112] (available residues 42 to 458, 42 to 461 and 40 to 457) was embedded in a bilayer of 412 dipalmitoylphosphatidylcholine (DPPC) lipids. It was surrounded by explicit TIP3P water molecules [142] (49850 molecules) and 150 mM of NaCl or KCl (188 Na^+ or K^+ ions and 136 Cl^- ions) for a total of 223315 atoms in a $115 \times 115 \times 164$ Å box.

6.3.2 Simulation details

The system was built and equilibrated with the CHARMM program [140, 241] using CHARMM36 lipid parameters [221] and CHARMM22 protein parameters [131] with CMAP corrections [138]. The ion parameters for CHARMM27 with revised non-bonded LJ Na^+ and K^+ parameters that were adjusted to fit experimentally measured hydration free energies of -98.1 kcal/mol and -80.6 kcal/mol, respectively were used ($r_{min} = 3.12$ Å and 3.46 Å for Na^+ and K^+) [194]. Pair specific parameters, NBFIx parameters, were also added to improve the descriptions of Na^+ and K^+ ions interacting with protein backbone carbonyl oxygen atoms which reproduce correct free energies of solvation in protein

backbone mimetic [194]. NBFIX parameters were also explored for Na^+ and K^+ interactions with carboxylate oxygen, this is further discussed below in section Model Dependence. The systems were energy minimized for 3000 steps before heavy atoms were constrained with harmonic constraints with force constants of 10 kcal/mol/ \AA^2 , which were slowly released during 0.5 ns simulations. They were further equilibrated for 1.5 ns before production runs started. All simulations with POPC were run at a temperature of 303 K and DPPC at 323 K [242, 243]. These temperatures were chosen to ensure lipids were in the liquid phase. The SHAKE algorithm [244] was used to maintain the bonds to hydrogen atoms. Electrostatic interactions were calculated with Particle Mesh Ewald [204] with a grid spacing of 1 \AA and 6th order B-spline for mesh interpolation. Non-bonded pair lists were used with a cut-off of 16 \AA , a real space cut off at 12 \AA and a smooth switching from 10 \AA .

Production simulations were run with NAMD 2.9 [223] with the same force fields as used for building the systems. Additionally, tetragonal boundary condition was used. The NPT ensemble was used and maintained by a Langevin piston to maintain constant pressure [166, 169] and a Nose-Hoover thermostat to maintain constant temperature [164, 165]. The RATTLE algorithm [203] was used to maintain bonds to hydrogen atoms. Electrostatic interactions were again calculated with Particle Mesh Ewald [204] with grid spacing of 1.5 \AA and 6th order B-spline for mesh interpolation. Non-bonded pair lists were created out to 16 \AA , with a real space cut off at 12 \AA and a smooth switching from 10 \AA .

6.3.3 Analysis

Free energy maps for ion movement through the TMD were calculated from the unbiased simulations as

$$W(z) = -k_B T \ln \rho(z) + C \quad (6.1)$$

Where ρ is the unbiased probability distribution as a function of reaction coordinate z , being the position of an ion along the z coordinate with respect to the COM of the backbone atoms of GAS, and where C is an arbitrary constant.

Unbiased simulations were run for 255 ns and 237 ns for PDB:4NTW and PDB:2QTS, respectively. The first 20 ns were thrown away for PDB:4NTW and the first 12 ns for PDB:2QTS due to large changes in the beginning of the simulation. All simulations were performed both with NaCl and KCl surrounding the protein. The closed PDB:2QTS does not allow ion permeation through the pore. To ensure sampling of ion interactions with the protein regardless of this two of the cations were constrained at the bottom of the TM domain. They were kept in a cylinder of radius 15 Å and height 10 Å centred on the COM of E18' and D21', with other ions unrestrained in movement.

US simulations [171] of the ion going through the TM part of the channels were performed to increase statistical power. US was performed going from bulk, at $z=-25$ Å (z-positions are relative to centre of mass of GAS), to the beginning of the extracellular domain, at $z=20$ Å, for PDB:4NTW. For the closed PDB:2QTS US was performed from bulk, at $z=-25$ Å, to the closing of the channel, at $z=0$ Å. A window spacing of 1 Å was used giving 46 independent simulations for PDB:4NTW and 26 for PDB:2QTS. The ion was held with a force constant of 2.57 kcal/mol/Å² to ensure sufficient overlap according to the equipartition theorem $\langle x^2 \rangle = \sqrt{k_B T/k}$. Furthermore, to ensure that the ion stayed in the pore laterally a flat-bottomed cylindrical constraint with a radius of 9 Å and a force constant of 10 kcal/mol/Å² was used. Based on preliminary results, extra windows were added to simulations in PDB:2QTS for K⁺ at $z=9.5$ Å and $z=11.5$ Å and for Na⁺ the force constant was increased to 5.14 kcal/mol/Å² at $z=7$ Å to ensure sampling. The lower pore of PDB:2QTS is highly asymmetrical with several charged residues, therefore extra windows were needed to get sufficient sampling. Each window was simulated for 20 ns (extended to 27 ns for windows between -15 Å and -5 Å in PDB:4NTW). This region represents the most challenging part of the channel of PDB:4NTW due to the wide pore and the need to bind and dissociate from a trimer of carboxylate pairs. The criterion for convergence for the US simulations was a free energy change of <1 kcal/mol. This was achieved for PDB:4NTW within 6 ns for Na⁺ and 3 ns for K⁺ and for PDB:2QTS within 6 ns for Na⁺ and 7 ns for K⁺, with all preceding data discarded for final calculations (Fig.6.3a&d). Movements of Na⁺ and K⁺ in the xy-plane at the level of residues E18' and

D21' demonstrated sufficient lateral sampling of the pore after half the simulation period for both structures (Fig.6.3b,c,e&f). WHAM [172] was used to reassemble and unbiased the PMF.

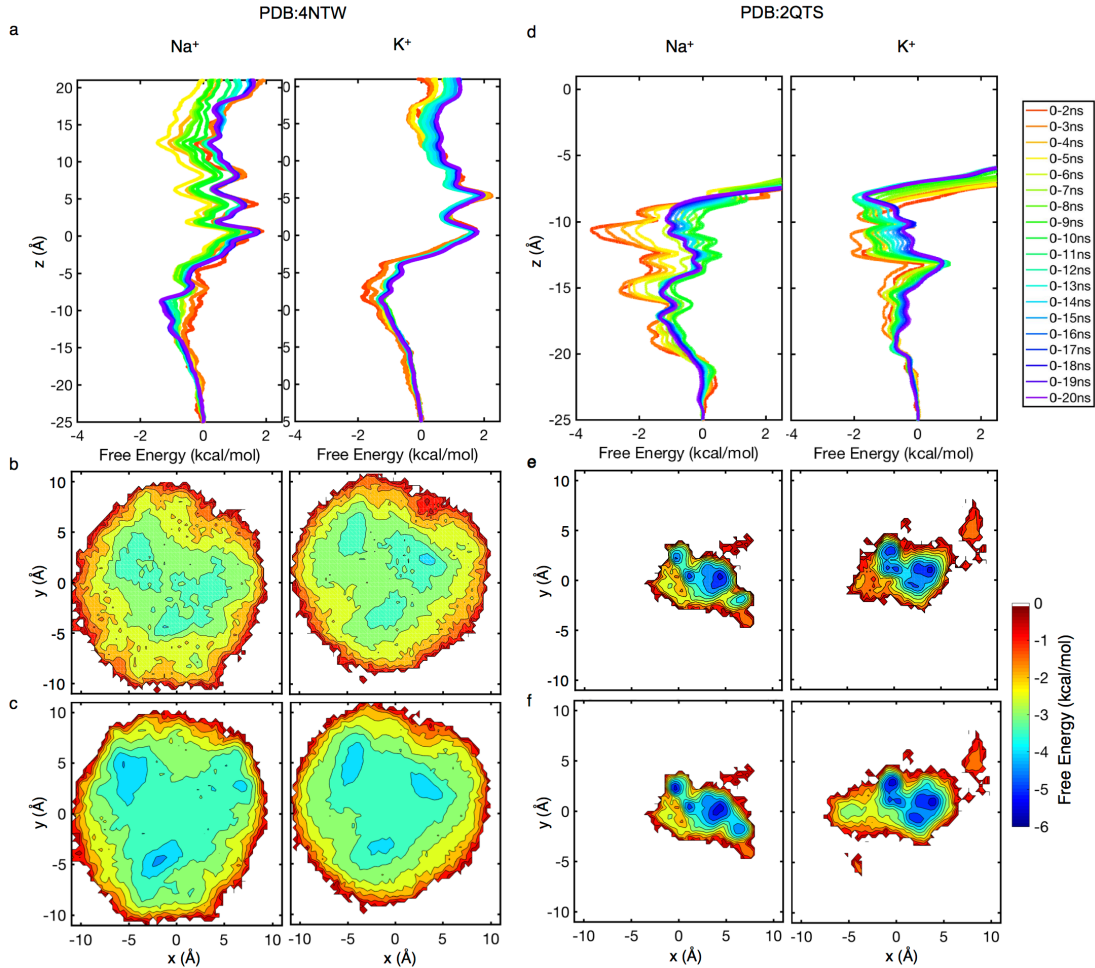


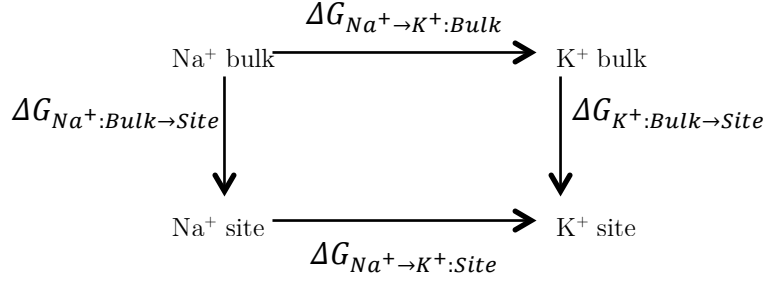
Figure 6.3. Free energy convergence and lateral sampling of ions for umbrella sampling of PDB:4NTW (left) and PDB:2QTS (right). a) Convergence of free energy profiles over time for Na⁺ (left) and K⁺ (right) through the trans-membrane part of the channel of PDB:4NTW. b&c) Lateral sampling of Na⁺ (left) and K⁺ (right) in the xy-plane at the level of residues E18' and D21' (z=-15 to -5 Å) b) for the first half of the simulation and c) the full simulation. d) Convergence of free energy profiles over time for Na⁺ (left) and K⁺ (right) ions through the lower entrance of the trans-membrane part of the channel of PDB:2QTS (note the change of scale for the z-axis). e&f) Lateral sampling of Na⁺ (left) and K⁺ (right) in the xy-plane at the level of residues E18' and D21' (z=-15 to -5 Å) e) for the first half of the simulation and f) the full simulation.

The protein/water coordination of the Na⁺ and K⁺ ions was determined by counting the number of oxygen atoms from water and protein in the first solvation shell of the ions. The solvation shell was defined using the radial

distribution functions in Fig.6.4. The total coordination number was determined relative to bulk values, these were determined to be 5.67 ± 0.04 and 6.94 ± 0.07 water molecules for Na^+ and K^+ , respectively.

To determine the important states involved in ion binding frames with similar configurations were grouped together by performing clustering analysis for the free simulations. In PDB:4NTW the clusters were initially broken down according to ion occupancies. They were further broken down according to how many carboxylates (one or two) they were bound to. Due to less well-defined sites in PDB:2QTS, clusters were instead defined solely by the radial distribution function for ion-ion interaction (Fig.6.9). These definitions are shown in Fig.6.9. where *i* represents a tight multi-ion/multi-carboxylate complex where the two ions are close to each other (within 4.7 Å and 5.5 Å for Na^+ and K^+). *ii* represents a loose multi-ion/multi-carboxylate complex where the ions are in the vicinity of each other, including clusters where the two ions are bound to one carboxylate each, one common carboxylate when they share more carboxylates but are further away from each other (with a lower limit imposed by the *ii* state and an upper limit of 7.2 Å and 8.0 Å for Na^+ and K^+). *iii* represents ions that are unbound or participate in single ion complexes (with a lower limit imposed by state *ii*) (Fig.6.9).

To investigate the relative binding affinity for Na^+ and K^+ free energy perturbation (FEP) calculations [228] were performed in the different sites identified from the clustering analysis. These sites are made up of amino acid side chains or backbones and are occupied by one or more ions. In the case of multi-ion occupancies the ions were transformed one at a time. The change in free energy between Na^+ and K^+ can be evaluated using the thermodynamic cycle



and the change in free energy, $\Delta\Delta G_{Na^+\rightarrow K^+}$, was calculated from the change in free energy of $Na^+\rightarrow K^+$ in the site compared to bulk according to

$$\begin{aligned}\Delta\Delta G_{Na^+\rightarrow K^+} &= \Delta G_{Na^+:Bulk\rightarrow Site} - \Delta G_{K^+:Bulk\rightarrow Site} \\ &= \Delta G_{Na^+\rightarrow K^+:Site} - \Delta G_{Na^+\rightarrow K^+:Bulk}\end{aligned}\quad (6.2)$$

NAMD2.9 was used with the alchemical FEP module [228] to determine $\Delta G_{Na^+\rightarrow K^+:Site}$ and $\Delta G_{Na^+\rightarrow K^+:Bulk}$. A coupling parameter, λ , was used to ensure overlap between the initial state and the final state. λ was divided into 20 steps with a step size of 0.05 Å. The windows were initiated by pulling λ from 0 to 1 in steps of 0.05 Å for 0.2 ns in each window. Each window was then equilibrated for 0.2 ns followed by a 2 ns production run concurrently, totalling in 40 ns production run for each simulation. The windows were assembled with WHAM [172]. Both forward and backward transformations ($K^+Na^+\rightarrow K^+K^+$ and $Na^+K^+\rightarrow K^+K^+$) were performed. The VMD plugin ParseFEP [229] was used to combine the endpoint histograms for the adjacent windows for the backwards and forwards transformations using BAR [177]. In the case of two ion occupancy, the final $\Delta\Delta G_{Na^+\rightarrow K^+}$ was calculated as the sum of the two transformations. In the case of a E18' and D21' site the ions were constrained with a 20 kcal/mol/Å² half-harmonic flat-bottomed constraint to stay within 2.75 Å from the centre of mass of the E18' and D21' carboxylate carbon atoms. Due to it always being multiple carboxylates involved in these sites, the constraint force is estimated to have minimal impact on the energies. In the case of the GAS site the ion was constrained in a slab of 4 Å thickness and 5 Å radius in the xy-plane around the GAS belt. The constraint was maintained with a 20kcal/mol/Å² half-harmonic flat-bottomed constraint at each of the

boundaries. A harmonic constraint of 100 kcal/mol/Å² was applied between the vanishing and appearing ions to maintain overlap.

6.3.4 Model dependence

As discussed in Chapter 4, the interaction between ions and Glu/Asp can be difficult to accurately depict. Furthermore, there have been a number of attempts to correct for this by adjusting the LJ interaction parameter r_{ij}^{min} including by Marinelli *et al.* (Na⁺-carboxylate $r_{ij}^{min} = 3.19 \text{ \AA}$ and K⁺-carboxylate $r_{ij}^{min} = 3.52$). However, as discussed in Chapter 4, standard CHARMM parameters using the LB mixing rule for Na⁺ and K⁺ interactions with the carboxylate side chains of Asp and Glu show general agreement to both experimental data and MD simulations taking quantum mechanical effects into account. However, to judge the robustness of our results these more repulsive parameters were explored by correcting for the change in interaction energy that the altered parameter would give. The ensemble averages were recalculated after introducing a weight, w_F , for each of the frames, F . This weight represents the likelihood of finding the system in that particular configuration if the new parameters, leading to different interaction energy, were used. The weight was determined by the Boltzmann distribution and calculated by determining the change in potential energy, ΔU , due to a change in non-bonded parameters.

$$w_F = e^{-\Delta U_F / k_B T} \quad (6.3)$$

The difference in free energy can then be calculated as

$$\Delta W = -k_B T \langle w \rangle \quad (6.4)$$

Each frame was re-weighted and a change in free energy calculated. The free energies for use of NBFIX parameters were then created by adding this to the free energies without NBFIX.

Although useful as a guide, this method does not take relaxation of the configurations into account. When the r_{ij}^{min} is increased there may be problems with overlapping of the ions and carboxylate oxygen atoms leading to high energetic costs. If the system were allowed to relax the overlapping atoms would move apart and this cost reduce. Furthermore, low energy states using the new parameters may not be sufficiently sampled using the old parameters. However, this correction tests the robustness of our results.

6.3.5 Experimental methods

Collaborators, Lynac *et al.* [15], have performed electrophysiology and mutagenesis experiments using the same mouse ASIC1 protein as previously used for the computational studies. Voltage clamping experiments were performed and the reversal potential used to determine the relative permeabilities of Na^+/K^+ , Na^+/Li^+ and Na^+/Cs^+ . The importance of specific residues for ion selectivity was determined by individually mutating 16 residues in TM2. To investigate the involvement of GAS in ion selectivity, without rendering the channel non functional, *in vivo* nonsense suppression [245] was used to decrease the dipole of G10'. A11' was replaced by α -hydroxyl which replaces the main chain carbonyl of G10' with an ester carbonyl (Fig.6.4a) [246]. Single channel currents were then measured. Acid-amide substitution was used to test the contribution of the charge of E18' to permeation by replacing the Glu with the uncharged analogue 4-nitro-2-aminobutyric acid (Fig.6.4b). Concatameric mutations, involving the mutations of 1/3, 2/3 and 3/3 of the subunits, were generated to test their individual contributions to selectivity and cooperativity from each subunit (more about the method in [15]).

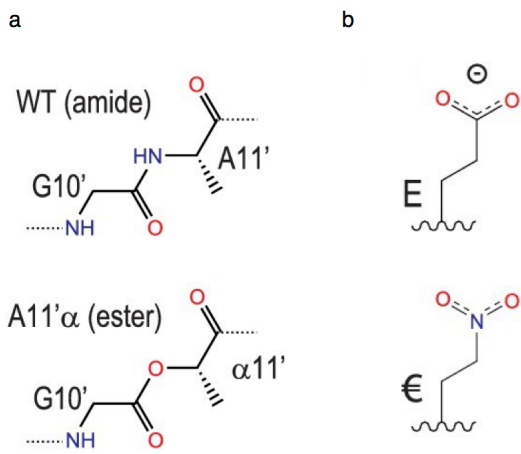


Figure 6.4. a) amide-ester substitution A11'a to probe the contribution of G10' and b) 4-nitro-2-aminobutyric acid of E18', to probe the contribution of charge to Na⁺ conduction and selectivity.

6.4 Results

6.4.1 Free simulations of ions in PDB:4NTW show no preference for Na⁺ in the GAS-belt

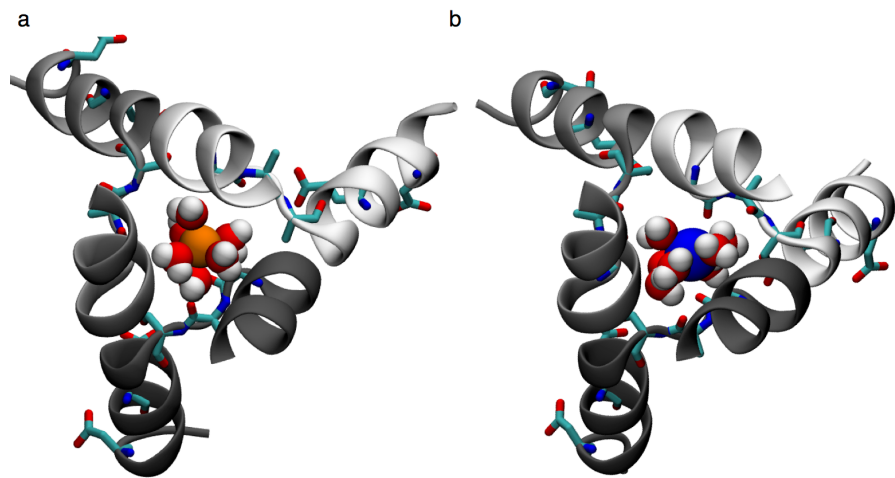


Figure 6.5. The GAS-belt of PDB:4NTW with a) Na⁺ ion and b) K⁺ ion in. Both ions are partly hydrated and alone when they cross GAS.

To obtain an initial indication of the free energy required for ion translocation through the ASIC pore, free simulations of PDB:4NTW were performed. The free energy profiles show permeation of both Na⁺ and K⁺ ions. We observed

both ions going through the channel partly hydrated, although Na^+ more so than K^+ , via the GAS-belt (Fig.6.5). Fig.6.6a shows a comparable free energy profile for both Na^+ and K^+ . Each ion encounters a free energy barrier when crossing the GAS belt where the energy barrier for Na^+ permeation is minorly higher than for K^+ , however, within errors. Furthermore, we see a minor preference for Na^+ around residues E18' and D21' but again within error margins. The errors of these free energy profiles are large due to a lack of sampling. Only a couple of ions permeated the channel due to the relatively short simulations compared to physiological time scales of ion permeation. The ion conduction through the GAS belt and surroundings of the channel rely on a single ion mechanism (Fig.6.6c), offering an excellent opportunity to increase statistics and decrease the error by using 1D US.

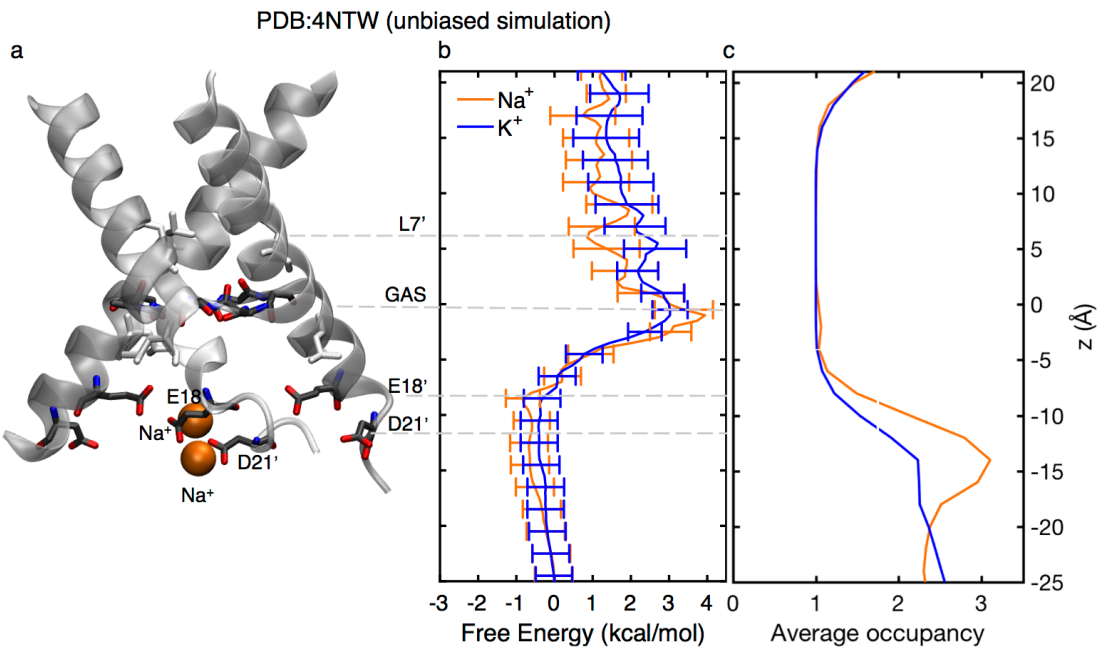


Figure 6.6. a) Snapshots of the TMD of PDB:4NTW from free simulation. B) free energy profiles for Na^+ (orange) or K^+ (blue) permeating the pore of PDB:4NTW. c) The average occupancy of Na^+ (orange) or K^+ (blue). We see single ion occupancy within the GAS belt and surrounding regions of the channel. Positions of key residues are indicated with grey dashed lines.

6.4.2 Umbrella sampling in ASIC PDB:4NTW reveals Na^+ preference in the lower part of the pore

Results from US simulations in PDB:4NTW in Fig.6.7b show similar results to the free simulations but with a lower error allowing us to resolve differences

between Na^+ and K^+ . When the ions enter the TMD from above, both Na^+ and K^+ interact with D0' and consequently replace water molecules with carboxylate oxygen atoms from D0' ($z \sim 17$ Å) (Fig.6.7c&d). The pore is wide and the ions can only bind to the Asp in one of the three subunits at a time. As the ions move further down the channel they slowly dehydrate without compensating for the loss by binding to the protein. The ions therefore have a partly empty first solvation shell, more so for K^+ than Na^+ . Regardless, their energetic profiles are similar. This is due to that K^+ compensate for the difference in lost water molecules, compared to Na^+ , by binding to the protein. Around L7' this changes and we see a preference for Na^+ of ~ 1 kcal/mol ($z \sim 6$ Å). This is likely due to the K^+ ions losing ~ 1 of their first hydration shell water molecules, whereas, Na^+ is only losing ~ 0.5 water molecules and there are no amino acids available to bind and compensate for this loss of water molecules. Therefore, L7' may be important for selectivity. Both Na^+ and K^+ continue to dehydrate until they reach the GAS belt ($z \sim 0$ Å). We have observed evidence of Na^+ ions passing through the GAS constriction site without having to dehydrate as much as K^+ (~ 1 compared to ~ 1.5 water molecules on average)(Fig.6.7c&d). However, there is no free energy preference for Na^+ over K^+ around the GAS constriction site. Typical configurations in the GAS belt show water molecules within 3.2 Å for Na^+ and 3.6 Å of K^+ (defined by the radial distribution function in Fig.6.8) reveal interaction with amide carbonyl of G10' for K^+ (Fig.6.7c&d insets). The K^+ ions are losing part of their first hydration shell and interacting with 1 to 2 carbonyl oxygen atoms when crossing the GAS belt, while Na^+ ions can go through this constricted part of the pore with an almost complete first hydration shell. Thus, the loss of first shell hydration for K^+ appears well compensated for by protein backbone carbonyl oxygen atoms at the narrow GAS belt, explaining the lack of significant energetic difference. This opposes the hypothesis of the GAS-belt being responsible for ion selectivity in ASICs. After crossing the GAS belt the ions rehydrate before encountering an energetic minimum at E18' and D21', where they trade water for carboxylate oxygen atoms ($z \sim 9$ Å). There is a preference for Na^+ by 0.5 ± 0.1 kcal/mol that comes from the ions binding to high field strength ligands that are thought to prefer Na^+ [98]. We see indications of the two amino acids cooperatively binding two Na^+ ions creating a Na^+ -selective site (Fig.6.7a). This can be seen also in the results from the unbiased simulations.

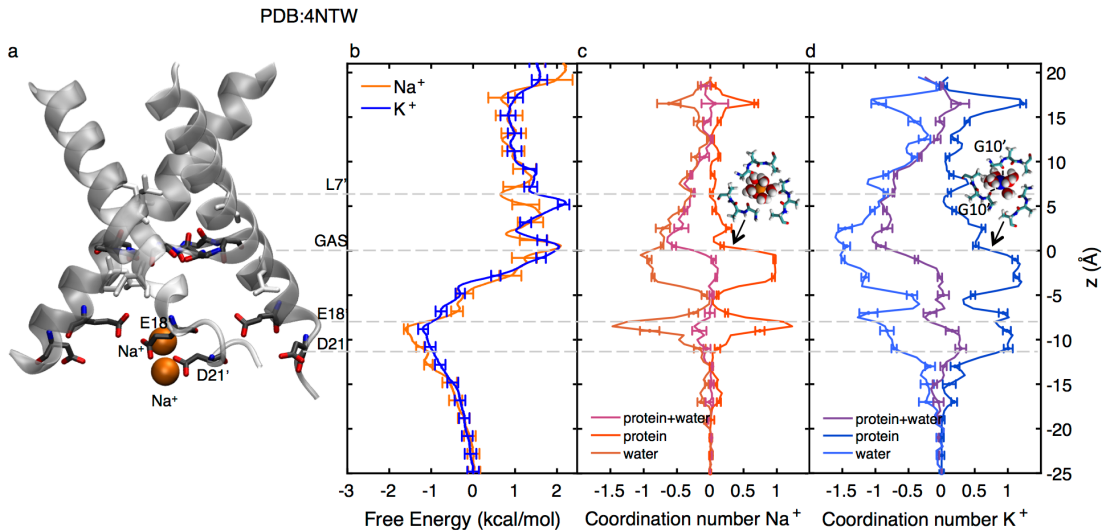


Figure 6.7. a) Snapshots of the TMD of PDB:4NTW from simulation. b) Single ion free energy profiles for Na^+ (orange) or K^+ (blue) permeating the pore of PDB:4NTW. First shell coordination of c) Na^+ and d) K^+ by oxygen atoms from water and protein (backbone and side chains) in the ASIC pore; offset relative to bulk coordination numbers (5.8 and 7.0 for Na^+ and K^+ , respectively) for clarity. Positions of key residues are indicated with grey dashed lines. Based on the positions of the first minima in the radial distribution functions for oxygen atoms, cut offs of 3.2 and 3.6 Å were applied to Na^+ and K^+ , respectively. Insets show backbone and water coordination at the level of the GAS belt.

Results from US show no energetic preference for Na^+ at the GAS-belt. Contrary to previously beliefs we therefore suggest that the GAS filter may not be responsible for ion selectivity. However, we observe energetic preference for Na^+ in the lower part of PDB:4NTW, suggesting that this region of the pore might be important for ion selectivity. Furthermore, we observe energetic preference also at L7' which therefore also may play a role in selectivity. We therefore need to investigate the influence of these residues further.

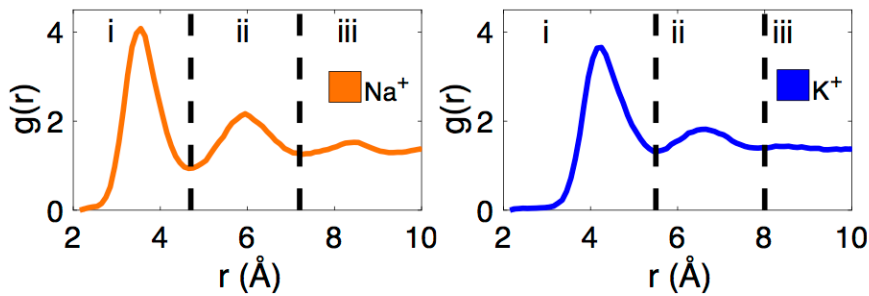


Figure 6.8. Radial distribution function for Na^+ (left) and K^+ (right). The clusters are defined as i) tight and ii) loose 2-ion binding as well as iii) single ion binding.

6.4.3 Umbrella sampling in ASIC PDB:2QTS shows a strong Na^+ preference in the lower part of the pore

To investigate the energetic preference for Na^+ in the lower pore we performed US simulations in another, narrower, structure. Even though PDB:2QTS is closed and these simulations do not show any complete channel permeation, we can explore the different mechanisms of ion binding selectivity in the lower part of the pore (Fig.6.9a). Results from US simulations show a similarly shaped PMF for both ions, with both ions binding to E18' and D21' (Fig.6.9b). However, there is an overall preference for Na^+ over K^+ of 1 kcal/mol throughout the channel, increasing to 1.8 ± 0.4 kcal/mol around E18' and D21'. Both Na^+ and K^+ dehydrate as they enter the pore but Na^+ makes up for it almost completely by binding to the carboxylates of E18' and D21', whereas the first solvation shell of K^+ remains partly empty (Fig.6.9c&d).

These results show a large influence from E18' and D21' on ion permeation through the lower pore of PDB:2QTS. There is an energetic preference for Na^+ compared to K^+ throughout the whole lower pore, however, this is especially prevalent at E18'. The increase in energetic preference in the lower pore compared to results from PDB:4NTW is likely due to the difference in width of the two pores; PDB:2QTS has a much narrower vestibule of the pore which allows E18' and D21' to better contribute to ion binding. This further supports a SF in the lower part of the pore.

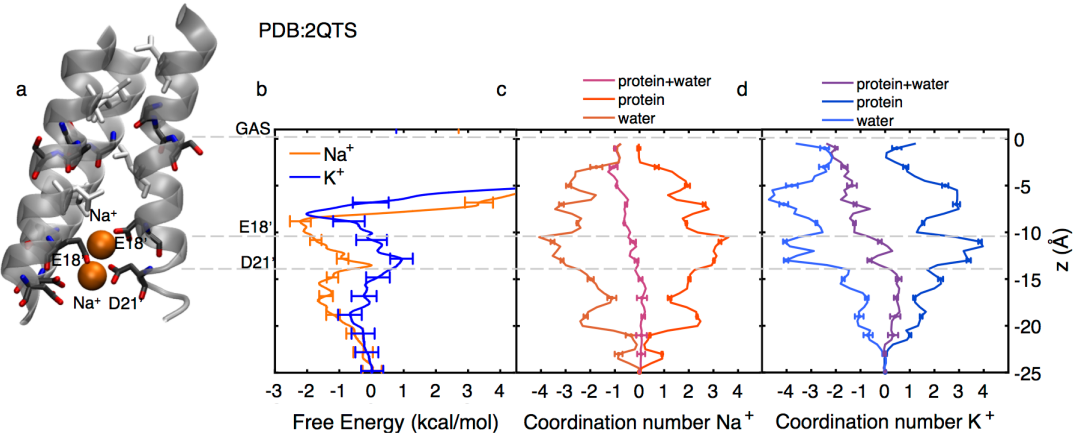


Figure 6.9. a) Snapshots of the TMD of PDB:2QTS from simulation. b) Single ion free energy profiles for Na^+ or K^+ permeating the pore of PDB:2QTS. First shell coordination of c) Na^+ and d) K^+ by oxygen atoms from water and protein (backbone and side chains) in the ASIC pore; offset relative to bulk coordination numbers (5.8 and 7.0 for Na^+ and K^+ , respectively) for clarity. Positions of key residues are indicated with grey dashed lines. Based on the positions of the first minima in the radial distribution functions for oxygen atoms, cut offs of 3.2 and 3.6 Å were applied to Na^+ and K^+ , respectively. Note that only $z < 0$ is shown because of the closed upper pore.

6.4.4 Mutagenesis and unnatural amino acid substitution experiments validate MD results

To investigate ion selectivity in ASIC1 and the influence of specific residues, 16 residues in TM2 were mutated and relative ion permeabilities measured (Fig.6.10). Results of the relative permeability of Na^+/Li^+ , Na^+/K^+ and Na^+/Cs^+ from single channel recordings are shown in Fig.6.10. L7', L14', E18' and D21' are the only residues whose mutation change ion selectivity (Fig.6.10). For L7' only the more dramatic of the mutations, L7'A, altered ion selectivity, whereas the more moderate mutations of L7'I and L7'V left the Na^+/K^+ selectivity unaltered. This suggests that loss in selectivity is due to the L7' hydrophobic interactions with the neighbouring helix that would break with the more dramatic L7'A mutations, this would lead to a deformed pore. Similarly, the loss of selectivity we observe with the L14'A mutation is likely due to loss of interactions between L14' and neighbouring helices, which are not altered with the less dramatic L14'I mutant. This is consistent with previous experiments showing the importance of L14' in maintaining an open channel [123].

The mutations of E18' and D21' in the lower pore, that were noted in US both in PDB:2QTS and PDB:4NTW, show strong influence on relative ion permeabilities. Mutation of both E18'Q and E18'D decreased Na⁺ selectivity drastically, suggesting that both charge and size of E18' is important for Na⁺ selectivity. This is an indicator that E18' participates in complex formation where E18' need to be able to be long enough be able to reach and form ion complexes together with other carboxylate side chains. Furthermore, D21'N removed selectivity whereas D21'E maintained WT selectivity, suggesting that the charge but not size is important for D21'. Therefore D21' may not be participating, or have an as large influence, in the complexes (Fig.6.10).

To further investigate the influence of the importance of the charge of E18' it was replaced with its uncharged analogue 4-nitro-2-aminobutyric acid and voltage clamp experiments performed. Fig.6.11b show the current voltage relationship and it can be seen that the E18'E mutation completely removed selectivity. This confirms the importance of both the charge and the length of E18'.

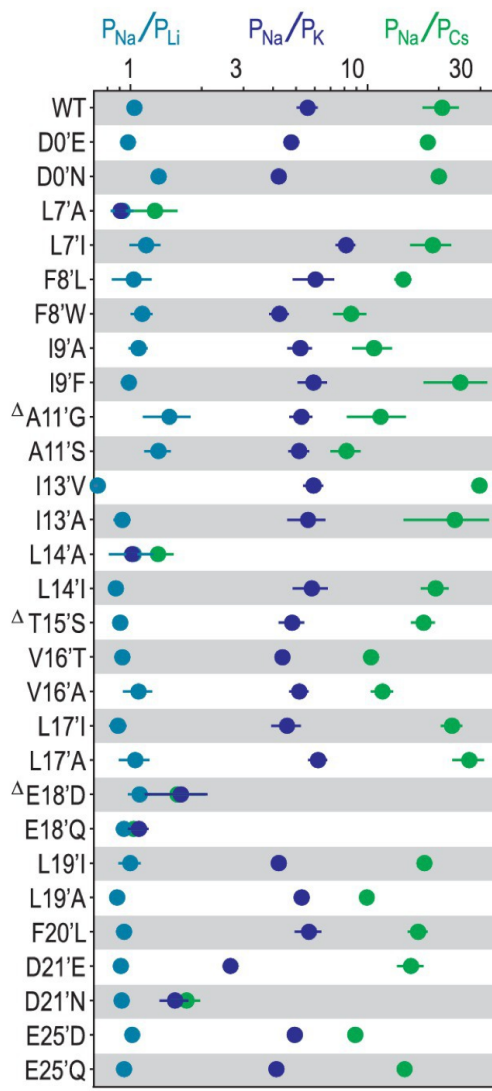


Figure 6.10. Relative permeability ratios for WT and mutant ASIC1a channels (mean \pm SEM; $n = 3-6$). Δ : G10'A/S, A11'V/F, S12'G/A/C/T, T15'V and E18'A channels were non-functional.

To investigate the influences from GAS on ion permeation unnatural amino acid substitution was performed. The A11' α substitution was used to decrease the dipole of G10' to be able to investigate the influence of GAS on ion permeability. Results showing the relative permeabilities from single channel recordings of ASIC with the A11' α mutation can be seen in Fig.6.11a. There is no decrease in Na^+ selectivity compared to the Wild Type (WT) channel. Thus, a reduction of the electrostatic surface potential of G10' does not decrease the relative permeability, suggesting that G10' is not vital for Na^+ selectivity in ASIC1. We, in fact, see a slight increase in Na^+ over K^+ selectivity, potentially

due to the A11'α mutant disturbing the interaction between K⁺ and the backbone carbonyls of the GAS. These results are consistent with results from MD simulations and suggest that the GAS-belt is not responsible for ion selectivity. Contrary to mutagenesis of G10', these experiments showed no change in general functionality of the channel suggesting minimal structural changes [15].

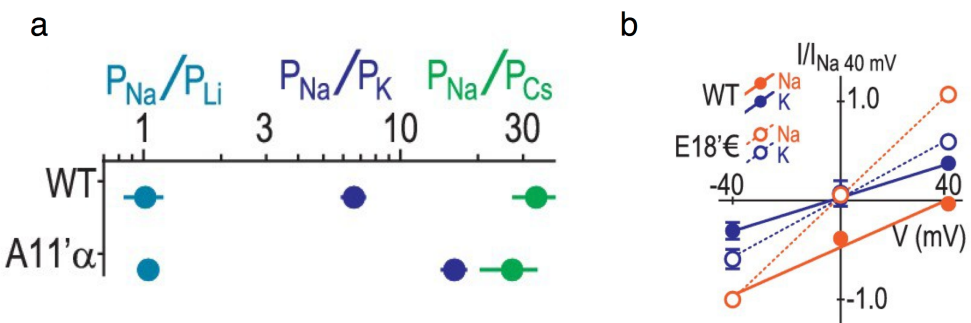


Figure 6.11. a) relative permeability ratios of WT and A11'α channels and b) current voltage relationship channel in NaCl (orange) and KCl (blue) of WT (solid line) and channel with mutant E18'€ (dashed line).

The results from the mutagenesis experiments are consistent with the results from MD simulations except for residue L14'; the PMF for ion permeation through PDB:4NTW did not show any energetic preference for Na⁺ around L14'. This may be due to an artificially splayed open lower pore in the PDB:4NTW structure, eliminating any dehydration of K⁺ that could occur in a narrower pore. Furthermore, the results from the mutagenesis again highlight the importance of residues in the lower pore, specifically E18' and D21', for Na⁺ selectivity in ASIC1. The importance of both charge and length of E18' further support the existence of multi carboxylate binding sites that are only possible when E18' is charged and of a certain length to be able to create these complexes.

To investigate the effect from individual subunits on these identified important mutations concatamers were created. Results show that E18' from every subunit is contributing to selectivity as selectivity decreases for every mutation. Mutation in 1, 2 or all 3 subunits show progressive non-linear decrease in $P_{\text{Na}^+}/P_{\text{K}^+}$ and $P_{\text{Na}^+}/P_{\text{Cs}^+}$ from 0/3 through 1/3, 2/3 and 3/3 for E18'Q-mutated

channels. Furthermore, this non-linear effect is stronger for the larger Cs^+ . A larger ion would be less likely to form multi-ion complexes, this highly non-linear dependence therefore suggest cooperative intersubunit complex formation for Na^+ . Furthermore, it is only when two or more subunits are mutated that the WT selectivity profile ($P_{\text{Na}^+} > P_{\text{K}^+} > P_{\text{Cs}^{2+}}$) is lost. This suggests that multiple, but not necessarily all, carboxylates are needed in this part of the channel for selectivity. The same experiments for L7'A and S12'A caused no change in relative permeability for 1/3 and 2/3 mutated subunits but rendered the channel non-functional when all subunits were mutated (Fig.6.12). This lack of influence on the relative permeability when 2/3 mutations are performed indicates that L7' and S12' are not involved in ion selectivity.

Results from unnatural amino acid substitutions and mutagenesis show a strong influence of E18' on relative permeabilities in ASIC1, where all mutations performed renders the channel non-selective. Charge, length and cooperativity influence the relative permeability. This suggests multi ion complex formation in the lower part of the ASIC1 pore that is responsible for Na^+ selectivity. Furthermore, we do not see an influence on selectivity from the less drastic mutations of L7'. Furthermore, when L7' in 1/3 or 2/3 of the subunits are mutated the channel remains Na^+ selective. This suggests that L7' is not the key to ion selectivity in ASIC1. Mutations of L14' affects channel permeability, however, we do not see any energetic preference around L14' in the free energy profiles from US in PDB:4NTW (Fig.6.7). We therefore suggest that the experimentally observed selectivity is better explained by a channel with narrower intracellular pore opening. Furthermore, this would also allow for E18' and D21' side chains from different subunits to form complexes with ions; not possible with the currently accepted, yet incomplete, ASIC1a open state structure.

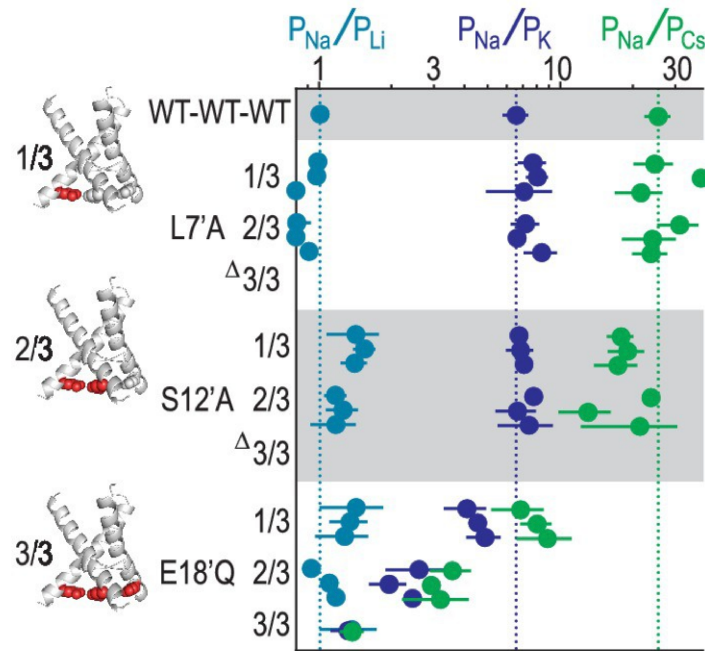


Figure 6.12. Relative permeability ratios for concatemeric channels carrying no mutations (WT-WT-WT) or one, two or three S12'A or E18'Q mutations (mean \pm SEM, $n = 3-6$). Δ : Concatemeric channels containing three L7'A- and three S12'A-mutated subunits non-functional.

6.4.5 Free simulations suggest an important role of multi-ion/multi-carboxylate complexes in selective ion permeation

To investigate the specific atomic interactions that take part in creating this preference for Na^+ around E18' and D21' we performed free simulations in PDB:2QTS, and performed further analysis of the free simulations in PDB:4NTW. Results show that both Na^+ and K^+ prefer to bind as single ions to single carboxylates from E18' and D21' in PDB:4NTW (Fig.6.13a&b). However, 2-ion occupancy states occur several times more frequently for Na^+ than K^+ . In particular, when two ions are bound to these sites the formation of 2-ion complexes, involving two residues, is more than twice as probable in the presence of Na^+ than K^+ . In the snapshots of Fig.6.13b we can see representative configurations of two ion complexes. The lower pore of PDB:4NTW is too wide to allow inter subunit cooperation between the carboxylates, and we therefore only ever see 1 or 2 carboxylate binding the ions.

Due to the narrower lower vestibule of the structure of PDB:2QTS the carboxylates of E18' and D21' frequently create tight multiple carboxylate complexes with multiple ions (Fig.6.13c). These complexes often consist of two or three carboxylates binding the ions, and we see an asymmetrical lower pore consisting of three carboxylate binding sites. Furthermore, during multi ion binding, sometimes some of the carboxylates are shared and sometimes all of them are shared. This makes the binding sites less well defined and we instead define the states according to the RDF. Single carboxylate binding is distinguished from loose 2-ion binding where the ions are in the vicinity of each other, and from tight multi-ion/multi-carboxylate complexes, where ions close to each other are stabilised by multiple carboxylate (Fig.6.13d). In this narrow pore structure, both Na^+ and K^+ prefer double ion occupancy, but of the multi-ion complexes Na^+ tend to form tight complexes more often than K^+ ($28 \pm 8\%$ compared to $13 \pm 3\%$ for Na^+ and K^+). These complexes seem to be a defining difference between Na^+ and K^+ in ASIC1.

When FEP calculations are performed at the GAS site in PDB:4NTW, we see only marginal preference for Na^+ over K^+ , with $\Delta\Delta G(\text{Na}^+ \rightarrow \text{K}^+) = 0.20 \pm 0.04$ kcal/mol (Fig.6.14e). This supports our findings both from US (Fig.6.7) and from unnatural amino acid substitutions (Fig.6.11). This shows that the GAS residues may not be responsible for ion selectivity in ASIC1.

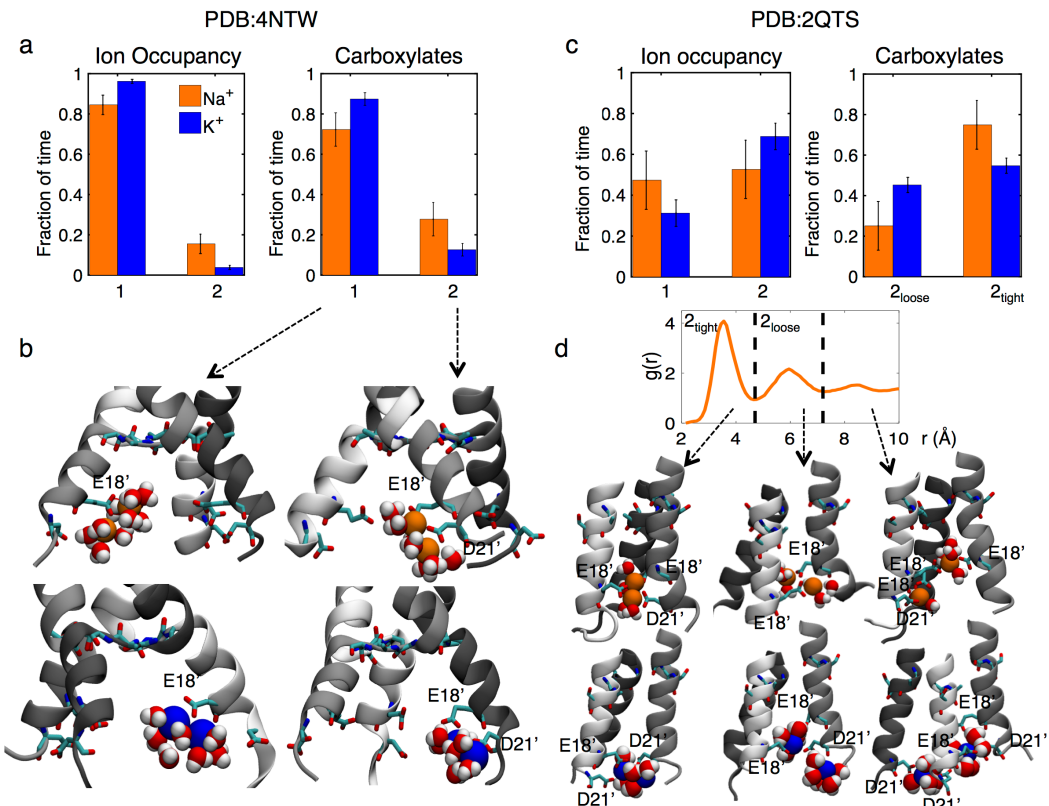


Figure 6.13. Occupation and conformation of the sites formed by residues E18' and D21' in unbiased simulation of a&b) PDB:4NTW and c&d) PDB:2QTS. a) Distribution of occupancy states in the sites formed by residues E18' and D21' in the presence of Na⁺ (orange) and K⁺ (blue) for 4NTW. b) Typical configurations in the vicinity of E18' and D21' for Na⁺ (top, orange) and K⁺ (bottom, blue) showing single and double occupancy involving 1 or 2 residues, as used as starting points for separate FEP calculations for relative binding free energies. c) Distribution of occupancy states formed by residues E18' and D21' in the presence of Na⁺ (orange) and K⁺ (blue) for 2QTS. d) Common configurations Na⁺ (top) and K⁺ (bottom) for single occupancy binding sites (left) and double occupancy binding sites (right) showing complex formation involving one, two and three side chains from E18' and D21'.

The tight multi-ion/multi-carboxylate complexes are more common for Na⁺ than K⁺. When the relative binding affinity of these complexes are investigated with FEP we see an overall energetic preference for Na⁺ in both structures and for both 1 and 2 ion occupancies. In particular, sites formed by residues E18' and D21' in PDB:4NTW favour Na⁺ over K⁺ by 1.4 ± 0.2 kcal/mol for single ion occupancy and 3.0 ± 0.5 kcal/mol for double occupancy (Fig.6.15a&c). In the narrower pore of PDB:2QTS, the greater number and flexibility of carboxylates involved in the binding sites leads to an even higher preference for Na⁺ over K⁺ by 2.6 ± 0.3 and 5.9 ± 0.9 kcal/mol, for single and double occupancies (Fig.6.15b&d), respectively.

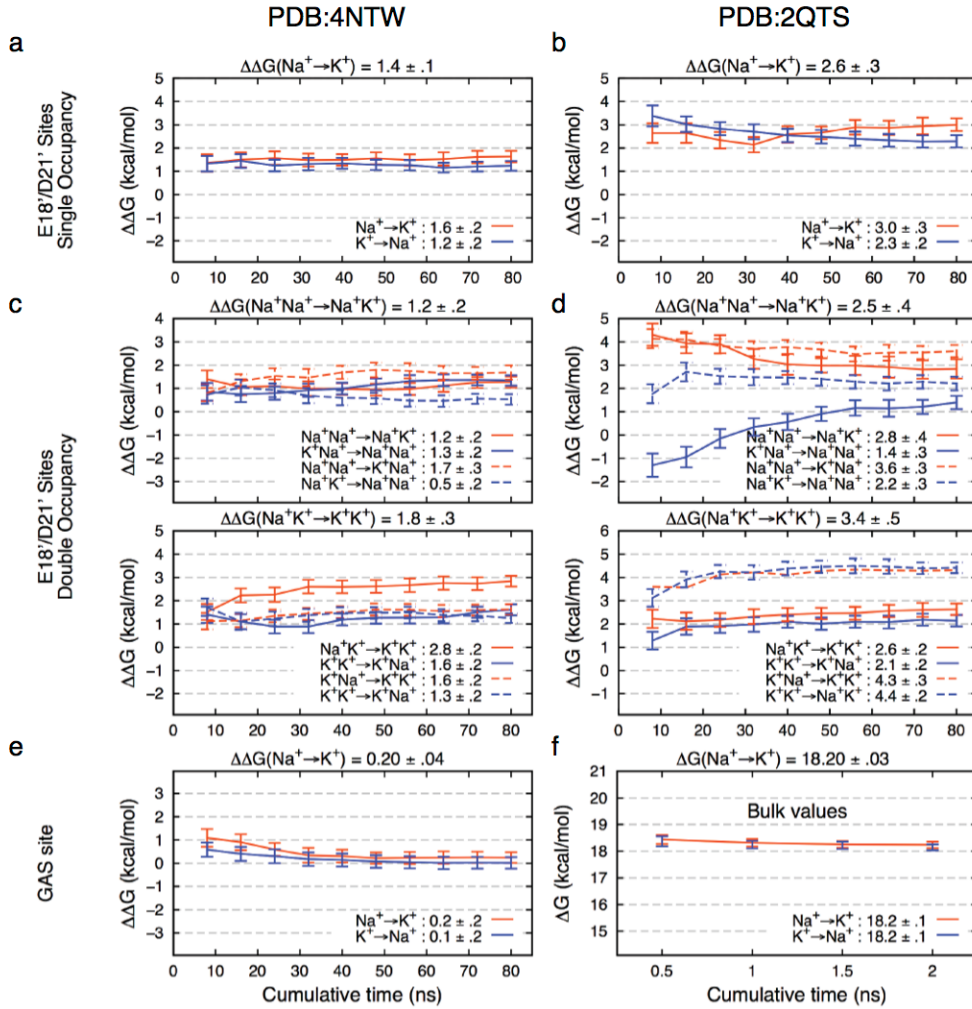


Figure 6.14. FEP binding free energy difference $\Delta\Delta G$ and convergence. a&b) $\text{Na}^+\rightarrow\text{K}^+$ (with results for $\text{K}^+\rightarrow\text{Na}^+$ negated) for the site formed by E18'/D21' occupied by a single ion in a) PDB:4NTW and b) PDB:2QTS. c&d) Results for transformations $\text{Na}^+\text{Na}^+\rightarrow\text{Na}^+\text{K}^+$ (top) and transformations $\text{Na}^+\text{K}^+\rightarrow\text{K}^+\text{K}^+$ (bottom) for c) PDB:4NTW and d) PDB:2QTS. Mean values from independent transformations are shown above each panel, with values for complete transformation $\text{Na}^+\text{Na}^+\rightarrow\text{K}^+\text{K}^+$ being the sum of individual transformations $\text{Na}^+\text{Na}^+\rightarrow\text{K}^+\text{Na}^+$ and $\text{Na}^+\text{K}^+\rightarrow\text{K}^+\text{K}^+$: 3.0 ± 0.4 for PDB:4NTW and 5.9 ± 0.6 for PDB:2QTS. e) Results for the PDB:4NTW GAS site. f) bulk values in agreement with experiment (18.2 kcal/mol) [247].

6.4.6 Model dependence

To estimate the effects of changing to pair specific Na^+/K^+ -carboxylate parameters optimised to match osmotic pressure experiments post simulation adjustments were made. The results from the post-simulation adjustment for the use of the new NBFIx parameters can be seen in Fig.6.15. The solid curve

shows the new free energy profiles ($W_{NBFIX}(z) = W(z) + \Delta W(z)$), and the dashed curve show the free energy profiles from Fig.6.7. Overall the use of more repulsive LJ parameters shows less binding. In PDB:4NTW the correction term adds up to $\sim 0.4\text{kcal/mol}$ (Fig.6.15a). This decreases the overall binding affinity for both species, however, a preference, although smaller, for Na^+ around E18' and D21' is still maintained (Fig.6.15a). In the narrower PDB:2QTS the cost of introducing the new more repulsive parameters is larger. However, Na^+ is still preferred at E18' and D21'. Results for deeper inside the closed pore ($z > -10\text{\AA}$) has increased errors and are considered unreliable due to the channel being closed (Fig.6.15b). Cluster analysis in Fig.6.15c&d also shows consistent results, but also here results are less predominant. Tight multi-ion/multi-carboxylate complexes are still more common for Na^+ than for K^+ both in PDB:4NTW (Fig.6.15c) and PDB:2QTS (Fig.6.15d).

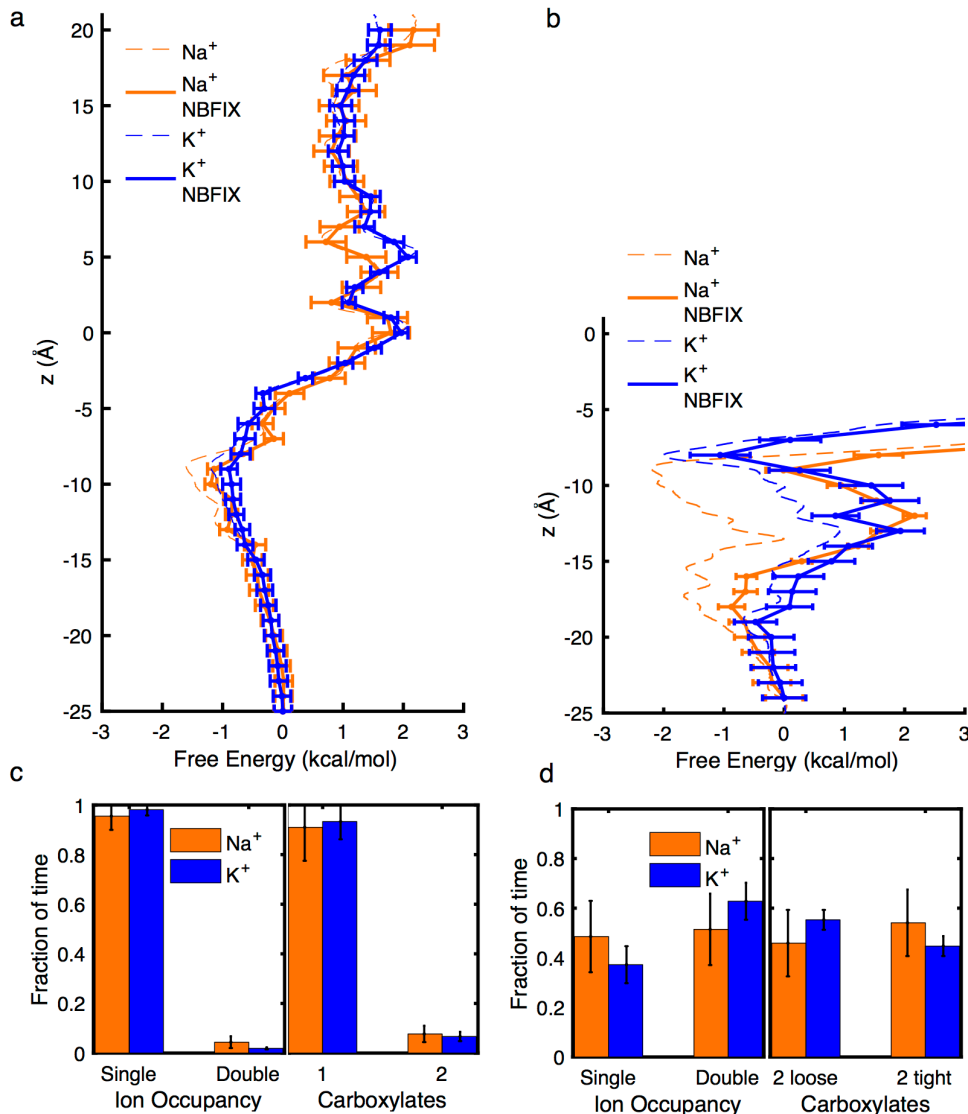


Figure 6.15. Estimates of free energy and coordination results for modified CHARMM27* NBFIIX (Na^+ -carboxylate $r_{\min}=3.19 \text{ \AA}$ and K^+ -carboxylate $r_{\min}=3.52 \text{ \AA}$), using post-simulation adjustment for the LJ parameter. US for Na^+ and K^+ crossing the pore of a) PDB:4NTW and b) PDB:2QTS. Values deep in the channel (above -10 \AA) are considered unreliable in this closed pore. Adjusted analysis of ion occupancies for c) PDB:4NTW and d) PDB:2QTS.

Modification to the FEP calculations shows that the tight multi-ion/multi-carboxylate complexes are still more favourable for Na^+ than K^+ (Fig.6.16), reinforcing the importance of these complexes for Na^+ selectivity in ASIC. In PDB:4NTW Na^+ is preferred by 0.2–0.5 kcal/mol for single ion complexes (Fig.6.16a) and 0.8 kcal/mol for double ion complexes (Fig.6.16c). In PDB:2QTS we see favourable complexes for Na^+ by 1.1 kcal/mol for the single ion (Fig.6.16b), and 1.3 kcal/mol for the 2-ion complex, with a net dual ion

transformation free energy of 3.0 kcal/mol (Fig.6.16d). This shows a lower pore of ASIC1 that strongly favour Na^+ -carboxylate complexes independent of the choice of LJ parameters.

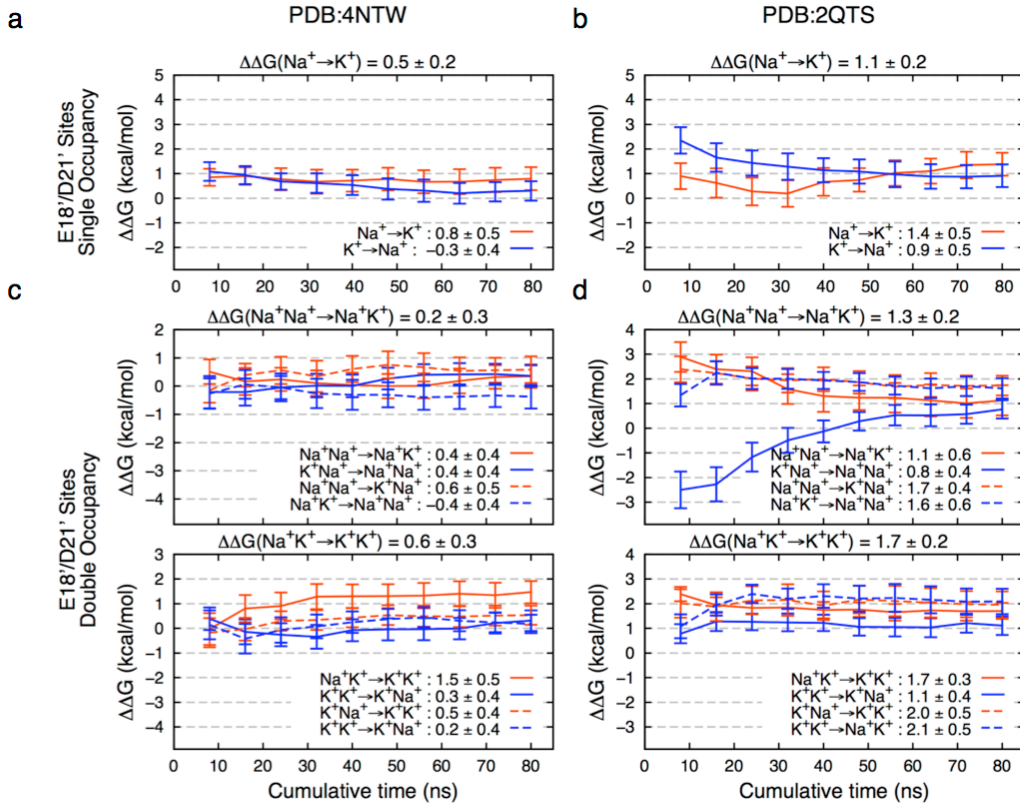


Figure 6.16. Estimated $\text{Na}^+\rightarrow\text{K}^+$ free energy perturbations for PDBs 4NTW and 2QTS with modified ion parameters, with $r_{\min}=3.19$ Å for Na^+ and $r_{\min}=3.52$ Å for K^+ , instead of the usual mixing rules for CHARMM27*. $\text{Na}^+\rightarrow\text{K}^+$ (with results for $\text{K}^+\rightarrow\text{Na}^+$ negated) for the site formed by E18'/D21' occupied by a single ion in a) 4NTW and b) 2QTS. Results for transformations $\text{Na}^+\text{Na}^+\rightarrow\text{Na}^+\text{K}^+$ (top) and transformations $\text{Na}^+\text{K}^+\rightarrow\text{K}^+\text{K}^+$ (bottom) for c) PDB:4NTW and d) PDB:2QTS. Mean values from independent transformations are shown above each panel, with values for complete transformation $\text{Na}^+\text{Na}^+\rightarrow\text{K}^+\text{K}^+$ being the sum of individual transformations.

6.5 Conclusions

The idea that selectivity in ASIC is governed by the GAS central constriction is an extension of the prevailing hypothesis for the super family of DEG/ENaCs, for which the ASIC is a member [111]. Mutations of the Ser of GAS in ENaCs have suggested an influence of the GAS residues on ion permeation and selectivity [122, 238]. However, this has not been tested in ASICs as mutation of this residue renders the channel non-functional [123-125]. We have explored

the roll of the GAS belt with MD simulations and unnatural amino acid substitutions. Results from MD simulations show no preference for Na^+ ions over K^+ at the GAS-belt, owing to the fact that the K^+ ions make up for their extra dehydration by binding to the backbone carbonyls of the GAS belt. Unnatural amino acid substitution show that if we decrease the dipole of the backbone carbonyl of G10' the Na^+ selectivity does not decrease. Mutation of S12' in one or two out of the three subunits show no effect on permeability, further suggesting that the GAS-belt is not involved in ion selectivity. Our results thus show that a size-exclusion filter made up by the GAS-belt may not be responsible for ion selectivity in ASIC1. The GAS belt may still contribute to selectivity, but we propose a SF located elsewhere.

The most notable preference for Na^+ over K^+ , both in results from MD simulations and mutagenesis, is at residues E18' and D21' in the lower part of the pore. We see a energetic preference for Na^+ in PDB:4NTW of ~ 0.5 kcal/mol and in PDB:2QTS of ~ 2 kcal/mol. Mutagenesis shows a complete loss of selectivity when E18' and D21' are neutralised. Analysis from MD simulations show that both ions bind to the carboxylate side chains of these residues, but that Na^+ ions participate in multi-ion/multi-carboxylate complexes more often than K^+ . Concatamers, where mutation is performed only in 1/3, 2/3 and 3/3 of the subunits, supports this as we see a non-linear decrease in relative permeabilities, suggesting inter subunit cooperativity. FEP verifies that the energetic preference is due to these tight multi-ion/multi-carboxylate complexes that favour Na^+ ions. Multi-ion/multi-carboxylate complexes are up to 3.0 ± 0.5 kcal/mol and 5.9 ± 0.9 kcal/mol more energetically favourable for Na^+ than for K^+ in PDB:4NTW and PDB:2QTS. Concatamers show that removing 2/3 of the E18' drastically reduces selectivity suggesting that 2 or more Glus are involved in the binding. We show that these results are maintained even with the more repulsive pair specific Na^+ and K^+ -carboxylate parameters created to reproduce osmotic pressure experiments.

These multi-ion/multi-carboxylate complexes that are crucial to Na^+ selectivity in the ASIC is a reoccurring factor in Na^+ selective ion channels [49]. As E18' is highly conserved throughout ASIC we suggest a SF at the bottom of the pore of ASIC. Analysis of the occupancy in the channel suggests that there are multiple ions at the lower part of the channel. Previous studies focusing on proton

sensing sites have noted that one or more Na^+ ions bind to the E18' and D21' rings [121], supporting our finding of multi-ion/multi-carboxylate binding sites. In a narrow pore, like that of PDB:2QTS, these kind of multi-ion/multi-carboxylate binding sites would be likely to facilitate a multi ion knock-on permeation. Both voltage gated Na^+ and K^+ channels have been shown to make use of a multi-ion knock on conduction [47, 49, 59]. It would be interesting to further investigate this multi-ion mechanism using long unbiased simulations or multi-ion US simulations.

The conclusions from these investigations can be drawn back to the larger family of ENaCs. ENaCs are generally more Na^+ selective than ASICs [248] and they have a Glu in the place of the Asp in position 21'. This may suggest that an additional Glu in this position increases the flexibility and potent of the multi-ion/multi-carboxylate complexes in the lower part of the pore. Furthermore, experiments have shown that mutations of E18' in ENaCs decreases Na^+ currents and in some cases increased K^+ permeability [249] [250]. We therefore speculate that ion selectivity in ENaCs may also be influenced by the residues in the lower pore.

Chapter 7

7 Concluding remarks and future directions

In this study we have performed an extensive investigation of ion selectivity in Na^+ selective ion channels. We have used MD simulations with different types of enhanced sampling methods. We have also compared our results to experimental data and quantum mechanical calculations. We have investigated ion selectivity in a bacterial Na_v , a mammalian Na_v and in an ASIC.

Results from previous studies where we have investigated the Na^+ selectivity in a bacterial Na_v show evidence for discrimination between Na^+ over K^+ based on the formation of 2-ion/2-carboxylate complexes with the Glu in the S_{HFS} . In this study we have further investigated this by performing FEP simulations to investigate the relative binding affinity in this S_{HFS} and we find that this binding to carboxylates favours Na^+ , in particular when the site is made up by several carboxylate side chains.

We have created a model of a human Na_v channel that has not yet been structurally solved. Using this model we have conducted studies of ion selectivity and conduction during multi μs unbiased simulations. We have observed evidence of Na^+ selectivity reliant on the same multi-ion/multi-carboxylate complexes as for bacterial Na_v s. These complexes are not solely formed by the carboxylates from the Glu and Asp in the DEKA ring but also involve the Glus and Asps from the vestibular EEDD ring. Our results also demonstrated the importance of the Lys residue in the DEKA ring. In fact, during conduction Lys appears to act as an additional ion, and participates in

the formation of Lys+ion/multi-carboxylate complexes. When an additional Na^+ ion enters the SF from above, it pushes the ion in the SF into a stable state with the Lys and the carboxylates. This allows the Na^+ ion to pass the Lys, in a beneficial electrostatic surrounding provided by the high field strength Glus and Asps, and enters into the pore without high energetic barriers. For K^+ ions, there is generally only a single ion in the SF and thus no formation of the stable multi-ion complexes. The permeation mechanism through the SF therefore involves higher barriers for K^+ , as it is forced to pass the Lys in the lower pore. Mutagenesis of the E and the K from the DEKA ring has shown that selectivity is greatly decreased if either of these are mutated [51]. We therefore hypothesise that it is in the formation of tight multi-ion/multi-carboxylate complexes, and the involvement in these of Lys, that the origin for Na^+ selectivity in human Na_vs can be found.

Our studies of the ASIC disproved the previously accepted theory that the SF is a size constriction site made up by the residues GAS in the middle of the pore [114]. Instead, we report that the residues responsible for ion selectivity are a ring of Glu and Asp at the lower end of the pore. These results are supported by experimental data from mutagenesis and unnatural amino acid substitutions performed by collaborators [15]. Furthermore, with the aid of concatameric mutants, unbiased MD and FEP; we substantiate these residues are integral for Na^+ selectivity as they form multi ion-multi/multi-carboxylate complexes which are more favourable for Na^+ over K^+ .

We have demonstrated that these multi-ion/multi-carboxylate complexes are crucial for Na^+ selectivity in multiple different sodium channels. We have used FEP to show that these carboxylate binding sites are more stable for Na^+ than for K^+ in all investigated channels. The availability of several carboxylate side chains in these sites creates tight binding where single ion conduction would entail crossing a high barrier to leave these complexes. Therefore, the kinetics of the conduction plays a crucial role in Na^+ selectivity. The wide SF of Na_vs allows simultaneous lateral positioning of the ions this creates a knock on mechanism very different from the single file conduction mechanism observed in K_vs [47, 52, 53]. An ion, or the ammonium group of the Lys in the mammalian case, can stay stationary in the SF, while a knock-on or pass-by mechanism occurs. The SF in the lower pore of the ASIC, that we are proposing is similarly

structured, also allows for comparable lateral binding of inter subunit carboxylate side chains. We therefore hypothesise a similar multi-ion knock on process also for ASICs. Thus, we propose, contrary to the previously postulated hypothesis that the strategies underlying selectivity may be distinct [27], that ion channels share a common mechanism for Na^+ selectivity that spans the different membrane ion transporter.

There are several additional exciting directions and opportunities for future research. To gain further knowledge in this area, we would like to investigate ion selectivity in the recently described structures of the eukaryotic Na_v , Na_vPaS [14]. The Na_vPaS structure provides an opportunity to create a complete model of $\text{Na}_v1.2$. Simulations in this complete $\text{Na}_v\text{PaS}/\text{Na}_v1.2$ could then complement and verify results from our $\text{Na}_v\text{Rh}/\text{Na}_v1.2$ model. Furthermore, recent open confirmation bacterial Na_vs [58, 82] has been presented. This allows for a more realistic permeation mechanism where we can study the movement of the ions through the SF in the conditions of a conducting channel. An application of membrane potential would also increase the speed of the permeation and allow for better sampling. In the future, these two structures could be used to create an open model of a human Na_v . When using these open structures a voltage may be applied to more accurately simulate physiological conditions.

Furthermore, Na^+ channels can discriminate against Ca^{2+} , which has almost the same radius (differ only by 0.04 Å) and are known to favour the same high field strength ligand as Na^+ [21]. However, due to the problems of accurately depicting the interaction between Ca^{2+} ions and the carboxylate side chain of Asps/Glus there is a gap in knowledge regarding the molecular determinants of $\text{Na}^+/\text{Ca}^{2+}$ selectivity. We have conducted osmotic pressure simulations and compared results to experimental data and quantum mechanical calculations and used this to reparameterise the Ca^{2+} carboxylate interaction. In preliminary results from 0.5 μs free simulations with Na_vAb surrounded by CaCl_2 we do not observe any conduction in free simulations (Fig.7.1), instead, a Ca^{2+} ion bound to the S_{HFS} with a high barrier for exiting the SF (Fig.7.1b). The lack of Ca^{2+} conduction is likely due to the high relative permeability for $\text{Na}^+/\text{Ca}^{2+}$ of bacterial Na_vs , $P_{\text{Na}^+}/P_{\text{Ca}^{2+}} \sim 7-70$ [26, 27, 78]. To further investigate Ca^{2+} selectivity and conduction through the SF of Na_vAb we need to perform

simulations using enhanced sampling methods. Ions permeation of open and activated ion channels take 10s of ns to μ s, the closed channel and the high $\text{Na}^+/\text{Ca}^{2+}$ selectivity would make Ca^{2+} permeation a slow process. Enhanced sampling will help investigate the mechanism of how $\text{Na}^+/\text{Ca}^{2+}$ selectivity is achieved.

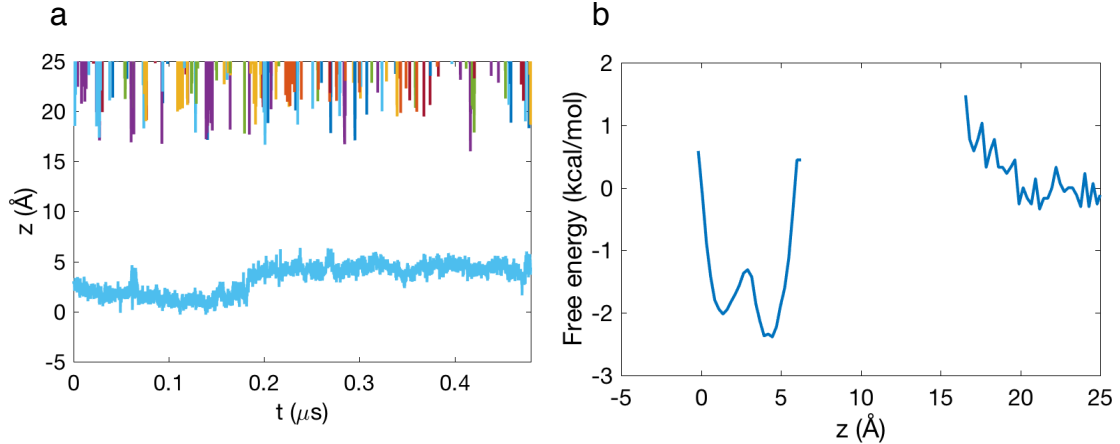


Figure 7.1. CaCl_2 in Na_vAb . a) z -positions of the Ca^{2+} ions in the SF and b) the free energy for Ca^{2+} in the SF. z is relative to the COM of the backbone of residue 175-179 and the SF is restricted by $r < 10 \text{ \AA}$.

Furthermore, these new Ca^{2+} parameters could be used to investigate how Ca^{2+} channels discriminate against Na^+ while choosing Ca^{2+} . Therefore MD simulations in Ca_vAb [21] should be conducted. Ca_v s have a SF similar to that of the bacterial Na_v s but instead consisting of three charged rings made up by Asps (Fig.2.4) [21]. The conduction mechanism has been shown to rely on a multi-ion knock-on mechanism that alternates between single and double or double and triple ion occupancy in three sites [21, 251]. In these sites the Ca^{2+} ion is coordinated by four carboxylates [251, 252] rather than two that has been proposed for Na^+ [49, 59]. Furthermore, as Na^+ ions can pass freely through the Ca_v in the absence of Ca^{2+} , the $\text{Ca}^{2+}/\text{Na}^+$ selectivity have been proposed to be achieved by Ca^{2+} blocking the entrance of Na^+ [252]. By performing MD simulations in Ca_v we could learn more about the underlying molecular mechanisms of this $\text{Ca}^{2+}/\text{Na}^+$ selectivity. This would provide further insight into the selectivity for (or against) Na^+ .

The interaction between ions and the carboxylate side chains of the Glus and Asps is clearly of great importance for ion selectivity. It is therefore crucial that the MD simulations depict this interaction properly. We have carefully

investigated the interaction between Na^+ , K^+ and Ca^{2+} and the carboxylate side chains of Asp and Glu. We have found that the interaction is highly dependent on which of the currently available set of parameters are used. The interaction between Na^+/K^+ and carboxylate is best represented by the use of LB mixing rule with the CHARMM FF whereas the interaction between Ca^{2+} and carboxylate showed extreme over binding for all FFs. We have therefore created a new pair-specific interaction parameter that better matches both experiments and results from CPMD simulations. The classical FFs do not explicitly take electronic polarisation into account. Instead the atomic charges are fixed and placed so that they approximately represent the electronic distribution of the molecule [131]. It is well known that the charge distribution of an atom changes depending on its environment. The divalence and small size of Ca^{2+} leads to strong electric fields that render electronic polarisation important. Previous simulations using classical FFs with LB mixing rule have shown difficulties in accurately representing Ca^{2+} interactions leading to excessive ion binding [49, 197, 198]. Furthermore, it is difficult to create one set of parameters that properly represents the variety of environments in an ion channel. FFs that take polarisability into account have the potential of adding accuracy. However, it is apparent that the parameters for the Drude polarisable FF currently face the same limitations, when it comes to cross interactions, as nonpolarisable FFs do. The parameters for the polarisable FFs must therefore be rigorously parameterised against benchmarks and pair specific interaction parameters created. Regardless of which FF is used, it needs to entail more accurate LJ interactions through the use of interaction specific parameters for more cross interactions.

The availability of other structures for ASICs also presents an exciting opportunity to further investigate the role of the carboxylates in the lower pore, and the possibility of a similar mechanism for the other members of the ASIC family. The formation of multi- Na^+ /multi-carboxylate complexes suggests an underlying conduction mechanism of a multi-ion knock-on nature. In Chapter 6, we proposed that the selectivity mechanism in ASIC would be better explained by a channel with a narrow lower pore, like that of PDB:2QTS. However, PDB:2QTS is closed, we have therefore started to create a model of an open channel with features like those of PDB:2QTS based of the open PDB:4NTW using Rosetta [220]. In a narrow pore, like the one of PDB:2QTS we could

properly examine the full multi-ion knock-on process that we propose in Chapter 6.

To further investigate Na^+ selectivity we suggest expanding the investigation across different membrane transport proteins, including the sodium ion pump (Na^+/K^+ -ATPase). This is a trans-membrane protein that maintains ion concentrations in and around the cell by transporting the ions using ATP to pump the ions back against their chemical gradient [253]. Sodium-potassium pumps transport three Na^+ out of the cell and two K^+ into the cell with the use of two binding sites that are non-selective and can bind either Na^+ or K^+ and one additional Na^+ binding site [219]. The ions are coordinated by both carboxylate side chains and backbone carbonyls in these sites (Fig.7.2) [219, 254-256]. However, four Glus and Asps have been identified as being particularly important to the selectivity [257, 258]. This makes the Na^+/K^+ -ATPase especially interesting to examine as we see Glus and Asps reoccurring in binding sites both in Na_vs and an ASIC. It is therefore intriguing that the Na^+/K^+ -ATPase can select three Na^+ and two K^+ with a set of residues usually found to be Na^+ selective. Furthermore, recent investigations of ion binding in the Na^+/K^+ -ATPase show that the Na^+/K^+ selectivity is dependent on the protonation states of these four Glus and Asps. It has been suggested that protonation state is directly affecting selectivity in the K^+ bound state [257, 258]. Whereas in the Na^+ bound state, protonation of residues on the cytoplasmic side leads to a change in conformation of the binding sites to better suit the Na^+ ions [258]. Understanding of this proton coupling may help shed light on the pH dependence and potential effects from protonation on selectivity in Na^+ channels. Ion selectivity is a delicate mechanism likely relying on subtle, but important, differences. A change in pH has been shown to alter ion selectivity in the bacterial Na_vs [27], therefore the protonation of a single residue could lead to a loss of the important differences. The presence of these carboxylates in the binding site of Na^+/K^+ -ATPase suggests that there may be a common mechanism for Na^+ selectivity, not only within the family of ion channels but potentially the whole family of membrane transport proteins.

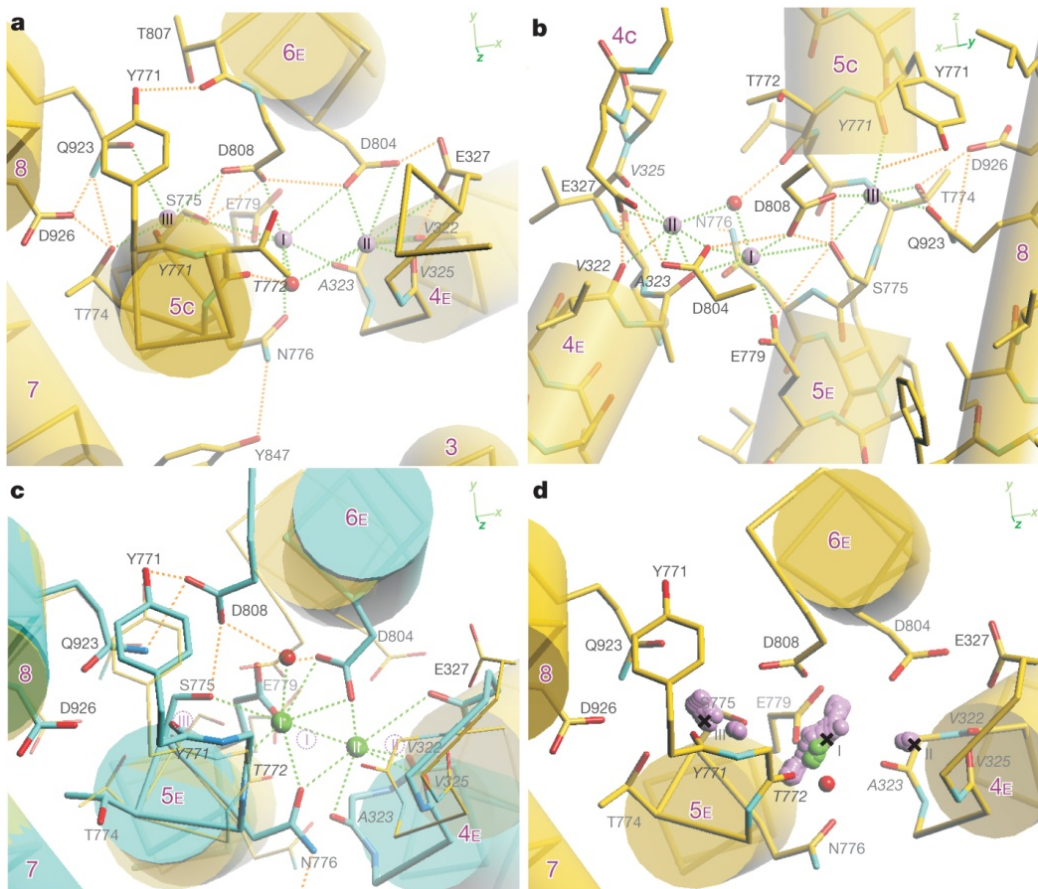


Figure 7.2. Na^+ binding sites in Na^+ (purple) bound Na^+/K^+ -ATPase, a) bottom view, b) side view, c) comparison between K^+ (green) binding sites and K^+ bound Na^+/K^+ -ATPase (cyan) and d) valence map for Na^+ and K^+ [219].

Increased understanding of Na^+ selectivity will have great applications. The development of a single new drug cost over US\$1 billion [259]. The high cost originates from the low success rate of ~3% for a molecule from to go from discovery phase to market. The reasons for this low success rate include unclear target biology, inadequate efficacy and unexpected toxicity [74]. These stem from lack of understanding both of the drug, the target and their interaction. As several physiological disorders are connected to ion channels, these are the targets for several existing and potential future drugs [73]. The drugs can work either by affecting the gating mechanism or by partly or fully blocking the pore of the ion channels [74]. To better understand these mechanisms we need to understand how these ion channels function. Better knowledge of the ion selectivity mechanisms will lead to better understanding of the ability of drugs to inhibit the Na^+ current and therefore provide us with a better position to

develop better and more potent drugs. Furthermore, methods and parameters developed for investigation of ion selectivity can be extended for the use of molecules and drugs binding to the ion channels. Computer simulations already play a roll in drug discovery as a pre-screening tool [260], however, increasing our knowledge of the ion channels and the accuracy of the methods will help make it less of a screening tool and more of a design tool where specific interactions and functions can be tailored. Eventually, this could help decrease the use of animal models making drug design cheaper and more ethical.

Another area where the understanding of ion selectivity can have great benefit is in the development of processes for desalination of water. 1 billion people are suffering from lack of clean freshwater and 41% of the earth population live in areas where access to fresh water may be an issue. These numbers are expected to grow [261]. Furthermore, many parts of the world, including Australia, are depleting their groundwater resources which is having an detrimental environmental impact [262]. Techniques for desalination of water are therefore becoming increasingly important. Desalination is the process of turning seawater and brackish water into fresh water by removing salts and solids [261]. The most common way of desalinating water is by using reverse osmosis where the water is pushed through membranes permeable only to water [263]. However, this process has a very high energy consumption [261]. A potentially more efficient way is by using specially manufactured nanotubes in membranes that allows water to permeate while discriminating against ions. To be able to manufacture these ion channel mimetic membranes the mechanisms of ion selectivity and discrimination in can act as a learning platform. The ion selectivity in ion channels is extremely delicate and several bodily functions rely on the fidelity of ion selectivity and discrimination. If we can understand how this selectivity and discrimination works we can use it to create efficient nanotubes that discriminate against ions while letting water though [263]. This has the potential of providing cost effective supply of water for human consumption.

8 References

1. Lodish, H., et al., *Transport across cell membranes*. 2000.
2. Alberts, B., et al., *Molecular biology of the cell*. new york: Garland science; 2002. Classic textbook now in its 5th Edition, 2002.
3. Purves, D., *Neuroscience 2nd edition*. Associates Inc. 2001.
4. Bähring, R. and M. Covarrubias, *Mechanisms of closed-state inactivation in voltage-gated ion channels*. The Journal of physiology, 2011. **589**(3): p. 461-479.
5. Yarov-Yarovoy, V., et al., *Structural basis for gating charge movement in the voltage sensor of a sodium channel*. Proceedings of the National Academy of Sciences, 2012. **109**(2): p. E93-E102.
6. Lodish, H., et al., *Molecular cell biology 4th edition*. National Center for Biotechnology Information's Bookshelf, 2000.
7. Hille, B., *Ion channels of excitable membranes*. Vol. 507. 2001: Sinauer Sunderland, MA.
8. Ringer, S., *A further contribution regarding the influence of the different constituents of the blood on the contraction of the heart*. The Journal of physiology, 1883. **4**(1): p. 29.
9. Hodgkin, A.L. and A.F. Huxley, *A quantitative description of membrane current and its application to conduction and excitation in nerve*. The Journal of physiology, 1952. **117**(4): p. 500.
10. Neher, E. and B. Sakmann, *Single-channel currents recorded from membrane of denervated frog muscle fibres*. A century of Nature: twenty-one discoveries that changed science and the world, 2010: p. 224.
11. Noda, M., et al., *Primary structure of α -subunit precursor of *Torpedo californica* acetylcholine receptor deduced from cDNA sequence*. Nature, 1982. **299**(5886): p. 793-797.
12. Doyle, D.A., et al., *The structure of the potassium channel: molecular basis of K^+ conduction and selectivity*. science, 1998. **280**(5360): p. 69-77.
13. Berman, H.M., et al., *The Protein Data Bank, 1999–*, in *International Tables for Crystallography Volume F: Crystallography of biological macromolecules*. 2006, Springer. p. 675-684.
14. Shen, H., et al., *Structure of a eukaryotic voltage-gated sodium channel at near-atomic resolution*. Science, 2017. **355**(6328): p. eaal4326.
15. Lynagh, T., et al., *A selectivity filter at the intracellular end of the acid-sensing ion channel pore*. eLife, 2017. **6**: p. e24630.
16. Lingrel, J.B. and T. Kuntzweiler, *Na^+ , K (+)-ATPase*. Journal of Biological Chemistry, 1994. **269**(31): p. 19659-19662.

17. Nernst, W., *Zur kinetik der in lösung befindlichen körper*. Zeitschrift für physikalische Chemie, 1888. **2**(1): p. 613-637.
18. Pollard, T.D. and W.C. Earnshaw, *Cell biology*. 2004.
19. Marban, E., T. Yamagishi, and G.F. Tomaselli, *Structure and function of voltage-gated sodium channels*. The Journal of physiology, 1998. **508**(3): p. 647-657.
20. Charalambous, K. and B.A. Wallace, *NaChBac: the long lost sodium channel ancestor*. Biochemistry, 2011. **50**(32): p. 6742-6752.
21. Tang, L., et al., *Structural basis for Ca²⁺ selectivity of a voltage-gated calcium channel*. Nature, 2014. **505**(7481): p. 56-61.
22. Goldman, D.E., *Potential, impedance, and rectification in membranes*. The Journal of general physiology, 1943. **27**(1): p. 37-60.
23. Hodgkin, A.L. and B. Katz, *The effect of sodium ions on the electrical activity of the giant axon of the squid*. The Journal of physiology, 1949. **108**(1): p. 37-77.
24. Noskov, S.Y. and B. Roux, *Importance of hydration and dynamics on the selectivity of the KcsA and NaK channels*. The Journal of general physiology, 2007. **129**(2): p. 135-143.
25. Marcus, Y., *Thermodynamics of solvation of ions. Part 5.—Gibbs free energy of hydration at 298.15 K*. Journal of the Chemical Society, Faraday Transactions, 1991. **87**(18): p. 2995-2999.
26. Ren, D., et al., *A prokaryotic voltage-gated sodium channel*. Science, 2001. **294**(5550): p. 2372-2375.
27. Finol-Urdaneta, R.K., et al., *Sodium channel selectivity and conduction: Prokaryotes have devised their own molecular strategy*. The Journal of general physiology, 2014. **143**(2): p. 157-171.
28. Hille, B., *The permeability of the sodium channel to organic cations in myelinated nerve*. The Journal of general physiology, 1971. **58**(6): p. 599-619.
29. Begenisich, T. and M. Cahalan, *Sodium channel permeation in squid axons. I: Reversal potential experiments*. The Journal of physiology, 1980. **307**(1): p. 217-242.
30. Begenisich, T. and M. Cahalan, *Sodium channel permeation in squid axons. II: Non-independence and current-voltage relations*. The Journal of physiology, 1980. **307**(1): p. 243-257.
31. French, R., et al., *Ion permeation, divalent ion block, and chemical modification of single sodium channels. Description by single-and double-occupancy rate-theory models*. The Journal of general physiology, 1994. **103**(3): p. 447-470.

32. Ravindran, A., et al., *Modeling ion permeation through batrachotoxin-modified Na⁺ channels from rat skeletal muscle with a multi-ion pore*. Biophysical journal, 1992. **61**(2): p. 494-508.
33. Hodgkin, A.L. and R. Keynes, *The potassium permeability of a giant nerve fibre*. The Journal of Physiology, 1955. **128**(1): p. 61-88.
34. Ussing, H.H., *The distinction by means of tracers between active transport and diffusion*. Acta Physiologica, 1949. **19**(1): p. 43-56.
35. Begenisich, T. and P. De Weer, *Potassium flux ratio in voltage-clamped squid giant axons*. The Journal of general physiology, 1980. **76**(1): p. 83-98.
36. Zhou, Y., et al., *Chemistry of ion coordination and hydration revealed by a K⁺ channel-Fab complex at 2.0 Å resolution*. Nature, 2001. **414**(6859): p. 43.
37. Rakowski, R.F., D.C. Gadsby, and P. De Weer, *Single ion occupancy and steady-state gating of Na channels in squid giant axon*. The Journal of general physiology, 2002. **119**(3): p. 235-250.
38. Begenisich, T. and D. Busath, *Sodium flux ratio in voltage-clamped squid giant axons*. The Journal of general physiology, 1981. **77**(5): p. 489-502.
39. Tsushima, R.G., R.A. Li, and P.H. Backx, *P-loop flexibility in Na⁺ channel pores revealed by single-and double-cysteine replacements*. The Journal of general physiology, 1997. **110**(1): p. 59-72.
40. Vora, T., B. Corry, and S.-H. Chung, *Brownian dynamics study of flux ratios in sodium channels*. European Biophysics Journal, 2008. **38**(1): p. 45.
41. Hagiwara, S., et al., *Anomalous permeabilities of the egg cell membrane of a starfish in K (+)-Tl (+) mixtures*. The Journal of general physiology, 1977. **70**(3): p. 269.
42. Hille, B. and W. Schwarz, *Potassium channels as multi-ion single-file pores*. The Journal of General Physiology, 1978. **72**(4): p. 409-442.
43. Eisenman, G., R. Latorre, and C. Miller, *Multi-ion conduction and selectivity in the high-conductance Ca⁺⁺-activated K⁺ channel from skeletal muscle*. Biophysical journal, 1986. **50**(6): p. 1025-1034.
44. Gillespie, D., J. Giri, and M. Fill, *Reinterpreting the anomalous mole fraction effect: the ryanodine receptor case study*. Biophysical journal, 2009. **97**(8): p. 2212-2221.
45. Gillespie, D. and D. Boda, *The anomalous mole fraction effect in calcium channels: a measure of preferential selectivity*. Biophysical Journal, 2008. **95**(6): p. 2658-2672.

46. Nonner, W., D.P. Chen, and B. Eisenberg, *Anomalous mole fraction effect, electrostatics, and binding in ionic channels*. Biophysical Journal, 1998. **74**(5): p. 2327-2334.
47. Noskov, S.Y., S. Berneche, and B. Roux, *Control of ion selectivity in potassium channels by electrostatic and dynamic properties of carbonyl ligands*. Nature, 2004. **431**(7010): p. 830-834.
48. Berneche, S. and B. Roux, *Energetics of ion conduction through the K⁺ channel*. Nature, 2001. **414**: p. 73-77.
49. Boiteux, C., I. Vorobyov, and T.W. Allen, *Ion conduction and conformational flexibility of a bacterial voltage-gated sodium channel*. Proceedings of the National Academy of Sciences, 2014. **111**(9): p. 3454-3459.
50. Chung, S.-H., et al., *Permeation of ions across the potassium channel: Brownian dynamics studies*. Biophysical Journal, 1999. **77**(5): p. 2517-2533.
51. Favre, I., E. Moczydowski, and L. Schild, *On the structural basis for ionic selectivity among Na⁺, K⁺, and Ca²⁺ in the voltage-gated sodium channel*. Biophysical journal, 1996. **71**(6): p. 3110.
52. Kim, I. and T.W. Allen, *On the selective ion binding hypothesis for potassium channels*. Proceedings of the National Academy of Sciences, 2011. **108**(44): p. 17963-17968.
53. Åqvist, J. and V. Luzhkov, *Ion permeation mechanism of the potassium channel*. Nature, 2000. **404**(6780): p. 881-884.
54. Payandeh, J., et al., *The crystal structure of a voltage-gated sodium channel*. Nature, 2011. **475**(7356): p. 353-358.
55. Zhang, X., et al., *Crystal structure of an orthologue of the NaChBac voltage-gated sodium channel*. Nature, 2012. **486**(7401): p. 130-134.
56. Shaya, D., et al., *Structure of a prokaryotic sodium channel pore reveals essential gating elements and an outer ion binding site common to eukaryotic channels*. Journal of molecular biology, 2014. **426**(2): p. 467-483.
57. McCusker, E.C., et al., *Structure of a bacterial voltage-gated sodium channel pore reveals mechanisms of opening and closing*. Nature communications, 2012. **3**: p. 1102.
58. Sula, A., et al., *The complete structure of an activated open sodium channel*. Nature Communications, 2017. **8**.
59. Chakrabarti, N., et al., *Catalysis of Na⁺ permeation in the bacterial sodium channel NaVAb*. Proceedings of the National Academy of Sciences, 2013. **110**(28): p. 11331-11336.

60. Corry, B. and M. Thomas, *Mechanism of ion permeation and selectivity in a voltage gated sodium channel*. Journal of the American Chemical Society, 2012. **134**(3): p. 1840-1846.
61. Eisenman, G., *Cation selective glass electrodes and their mode of operation*. Biophysical journal, 1962. **2**(2): p. 259-323.
62. Bezanilla, F. and C.M. Armstrong, *Negative conductance caused by entry of sodium and cesium ions into the potassium channels of squid axons*. The Journal of General Physiology, 1972. **60**(5): p. 588-608.
63. Yu, H., S.Y. Noskov, and B. Roux, *Two mechanisms of ion selectivity in protein binding sites*. Proceedings of the National Academy of Sciences, 2010. **107**(47): p. 20329-20334.
64. Allen, T.W., O. Andersen, and B. Roux, *On the importance of atomic fluctuations, protein flexibility, and solvent in ion permeation*. The Journal of general physiology, 2004. **124**(6): p. 679-690.
65. Kuppuraj, G., M. Dudev, and C. Lim, *Factors Governing Metal—Ligand Distances and Coordination Geometries of Metal Complexes*. The Journal of Physical Chemistry B, 2009. **113**(9): p. 2952-2960.
66. Sigel, A., H. Sigel, and R.K. Sigel, *The alkali metal ions: their role for life*. Vol. 16. 2016: Springer.
67. Boiteux, C. and T. Allen, *Chapter Six-Understanding Sodium Channel Function and Modulation Using Atomistic Simulations of Bacterial Channel Structures*. Current topics in membranes, 2016. **78**: p. 145-182.
68. Xia, M., et al., *The mechanism of Na⁺/K⁺ selectivity in mammalian voltage-gated sodium channels based on molecular dynamics simulation*. Biophysical journal, 2013. **104**(11): p. 2401-2409.
69. Nimigean, C.M. and T.W. Allen, *Origins of ion selectivity in potassium channels from the perspective of channel block*. The Journal of general physiology, 2011. **137**(5): p. 405-413.
70. Heinemann, S.H. and H. Terlau, *Calcium channel characteristics conferred on the sodium channel by single mutations*. Nature, 1992. **356**(6368): p. 441.
71. Lossin, C., et al., *Molecular basis of an inherited epilepsy*. Neuron, 2002. **34**(6): p. 877-884.
72. Akopian, A.N., et al., *The tetrodotoxin-resistant sodium channel SNS has a specialized function in pain pathways*. Nature neuroscience, 1999. **2**(6).
73. M Waszkielewicz, A., et al., *Ion channels as drug targets in central nervous system disorders*. Current medicinal chemistry, 2013. **20**(10): p. 1241-1285.

74. Borhani, D.W. and D.E. Shaw, *The future of molecular dynamics simulations in drug discovery*. Journal of computer-aided molecular design, 2012. **26**(1): p. 15-26.
75. Kellenberger, S., et al., *Permeability properties of ENaC selectivity filter mutants*. The Journal of general physiology, 2001. **118**(6): p. 679-692.
76. Palmer, L.G. and G. Frindt, *Amiloride-sensitive Na channels from the apical membrane of the rat cortical collecting tubule*. Proceedings of the National Academy of Sciences, 1986. **83**(8): p. 2767-2770.
77. Kellenberger, S. and L. Schild, *International Union of Basic and Clinical Pharmacology. XCI. structure, function, and pharmacology of acid-sensing ion channels and the epithelial Na⁺ channel*. Pharmacological Reviews, 2015. **67**(1): p. 1-35.
78. Yue, L., et al., *The cation selectivity filter of the bacterial sodium channel, NaChBac*. The Journal of general physiology, 2002. **120**(6): p. 845-853.
79. Catterall, A.W., *Structure and function of voltage-gated ion channels*. Annual review of biochemistry, 1995. **64**(1): p. 493-531.
80. West, J.W., et al., *A cluster of hydrophobic amino acid residues required for fast Na (+)-channel inactivation*. Proceedings of the National Academy of Sciences, 1992. **89**(22): p. 10910-10914.
81. Catterall, W.A., *Ion channel voltage sensors: structure, function, and pathophysiology*. Neuron, 2010. **67**(6): p. 915-928.
82. Lenaeus, M.J., et al., *Structures of closed and open states of a voltage-gated sodium channel*. Proceedings of the National Academy of Sciences, 2017: p. 201700761.
83. Waterhouse, A.M., et al., *Jalview Version 2—a multiple sequence alignment editor and analysis workbench*. Bioinformatics, 2009. **25**(9): p. 1189-1191.
84. Naylor, C.E., et al., *Molecular basis of ion permeability in a voltage-gated sodium channel*. The EMBO journal, 2016: p. e201593285.
85. Payandeh, J. and D.L. Minor Jr, *Bacterial Voltage-Gated Sodium Channels (BacNaVs) from the Soil, Sea, and Salt Lakes Enlighten Molecular Mechanisms of Electrical Signaling and Pharmacology in the Brain and Heart*. Journal of Molecular Biology, 2015. **427**(1): p. 3-30.
86. Deller, M.C. and B. Rupp, *Models of protein–ligand crystal structures: trust, but verify*. Journal of computer-aided molecular design, 2015. **29**(9): p. 817-836.
87. Furini, S. and C. Domene, *On conduction in a bacterial sodium channel*. PLoS computational biology, 2012. **8**(4): p. e1002476.
88. Corry, B., *Na⁺/Ca²⁺ selectivity in the bacterial voltage-gated sodium channel NavAb*. PeerJ, 2013. **1**: p. e16.

89. Guardani, C., et al., *On the selectivity of the NaChBac channel: an integrated computational and experimental analysis of sodium and calcium permeation*. Physical Chemistry Chemical Physics, 2017. **19**(44): p. 29840-29854.
90. Chiamvimonvat, N., et al., *Control of ion flux and selectivity by negatively charged residues in the outer mouth of rat sodium channels*. The Journal of physiology, 1996. **491**(1): p. 51-59.
91. Terlau, H., et al., *Mapping the site of block by tetrodotoxin and saxitoxin of sodium channel II*. FEBS letters, 1991. **293**(1-2): p. 93-96.
92. Chiamvimonvat, N., et al., *Depth asymmetries of the pore-lining segments of the Na⁺ channel revealed by cysteine mutagenesis*. Neuron, 1996. **16**(5): p. 1037-1047.
93. Schlief, T., et al., *Pore properties of rat brain II sodium channels mutated in the selectivity filter domain*. European biophysics journal, 1996. **25**(2): p. 75-91.
94. Noda, M., et al., *A single point mutation confers tetrodotoxin and saxitoxin insensitivity on the sodium channel II*. FEBS letters, 1989. **259**(1): p. 213-216.
95. Khan, A., et al., *Role of outer ring carboxylates of the rat skeletal muscle sodium channel pore in proton block*. The Journal of physiology, 2002. **543**(1): p. 71-84.
96. Penzotti, J.L., et al., *Differences in saxitoxin and tetrodotoxin binding revealed by mutagenesis of the Na⁺ channel outer vestibule*. Biophysical journal, 1998. **75**(6): p. 2647-2657.
97. Tsushima, R.G., R.A. Li, and P.H. Backx, *Altered ionic selectivity of the sodium channel revealed by cysteine mutations within the pore*. The Journal of general physiology, 1997. **109**(4): p. 463-475.
98. Hille, B., *The permeability of the sodium channel to metal cations in myelinated nerve*. The Journal of general physiology, 1972. **59**(6): p. 637-658.
99. Lipkind, G.M. and H.A. Fozard, *KcsA crystal structure as framework for a molecular model of the Na⁺ channel pore*. Biochemistry, 2000. **39**(28): p. 8161-8170.
100. Lipkind, G.M. and H.A. Fozard, *Voltage-gated Na channel selectivity: the role of the conserved domain III lysine residue*. The Journal of general physiology, 2008. **131**(6): p. 523-529.
101. Mahdavi, S. and S. Kuyucak, *Mechanism of ion permeation in mammalian voltage-gated sodium channels*. PloS one, 2015. **10**(8): p. e0133000.

102. Sluka, K.A., O.C. Winter, and J.A. Wemmie, *Acid-sensing ion channels: A new target for pain and CNS diseases*. Current opinion in drug discovery & development, 2009. **12**(5): p. 693.
103. Price, M.P., P.M. Snyder, and M.J. Welsh, *Cloning and expression of a novel human brain Na channel*. Journal of Biological Chemistry, 1996. **271**(14): p. 7879-7882.
104. Waldmann, R., et al., *A proton-gated cation channel involved in acid-sensing*. 1997.
105. Sherwood, T.W., E.N. Frey, and C.C. Askwith, *Structure and activity of the acid-sensing ion channels*. American Journal of Physiology-Cell Physiology, 2012. **303**(7): p. C699-C710.
106. Baron, A. and E. Lingueglia, *Pharmacology of acid-sensing ion channels—Physiological and therapeutical perspectives*. Neuropharmacology, 2015. **94**: p. 19-35.
107. Pidoplichko, V.I., et al., *ASIC1a activation enhances inhibition in the basolateral amygdala and reduces anxiety*. Journal of Neuroscience, 2014. **34**(9): p. 3130-3141.
108. Ziemann, A.E., et al., *The amygdala is a chemosensor that detects carbon dioxide and acidosis to elicit fear behavior*. Cell, 2009. **139**(5): p. 1012-1021.
109. Wemmie, J.A., M.P. Price, and M.J. Welsh, *Acid-sensing ion channels: advances, questions and therapeutic opportunities*. Trends in neurosciences, 2006. **29**(10): p. 578-586.
110. Kew, J.N. and C.H. Davies, *Ion channels: from structure to function*. 2010: Oxford University Press, USA.
111. Kellenberger, S. and L. Schild, *Epithelial sodium channel/degenerin family of ion channels: a variety of functions for a shared structure*. Physiological reviews, 2002. **82**(3): p. 735-767.
112. Jasti, J., et al., *Structure of acid-sensing ion channel 1 at 1.9 Å resolution and low pH*. Nature, 2007. **449**(7160): p. 316-323.
113. Baconguis, I. and E. Gouaux, *Structural plasticity and dynamic selectivity of acid-sensing ion channel-spider toxin complexes*. Nature, 2012. **489**(7416): p. 400-405.
114. Baconguis, I., et al., *X-Ray structure of acid-sensing ion channel 1-snake toxin complex reveals open state of a Na⁺-selective channel*. Cell, 2014. **156**(4): p. 717-729.
115. Zha, X.-m., *Acid-sensing ion channels: trafficking and synaptic function*. Molecular brain, 2013. **6**(1): p. 1.
116. Noël, J., et al., *Current perspectives on acid-sensing ion channels: new advances and therapeutic implications*. Expert review of clinical pharmacology, 2010. **3**(3): p. 331-346.

117. Benson, C.J., et al., *Heteromultimers of DEG/ENaC subunits form H⁺-gated channels in mouse sensory neurons*. Proceedings of the National Academy of Sciences, 2002. **99**(4): p. 2338-2343.
118. Waldmann, R. and M. Lazdunski, *H⁺-gated cation channels: neuronal acid sensors in the NaC/DEG family of ion channels*. Current opinion in neurobiology, 1998. **8**(3): p. 418-424.
119. Baron, A., et al., *Acid sensing ion channels in dorsal spinal cord neurons*. The Journal of Neuroscience, 2008. **28**(6): p. 1498-1508.
120. Deval, E., et al., *Acid-sensing ion channels (ASICs): pharmacology and implication in pain*. Pharmacology & therapeutics, 2010. **128**(3): p. 549-558.
121. Shaikh, S.A. and E. Tajkhorshid, *Potential cation and H⁺ binding sites in acid sensing ion channel-1*. Biophysical journal, 2008. **95**(11): p. 5153-5164.
122. Kellenberger, S., I. Gautschi, and L. Schild, *A single point mutation in the pore region of the epithelial Na⁺ channel changes ion selectivity by modifying molecular sieving*. Proceedings of the National Academy of Sciences, 1999. **96**(7): p. 4170-4175.
123. Carattino, M.D. and M.C. Della Vecchia, *Contribution of residues in second transmembrane domain of ASIC1a protein to ion selectivity*. Journal of Biological Chemistry, 2012. **287**(16): p. 12927-12934.
124. Yang, H., et al., *Inherent dynamics of the acid-sensing ion channel 1 correlates with the gating mechanism*. PLoS Biol, 2009. **7**(7): p. e1000151.
125. Li, T., Y. Yang, and C.M. Canessa, *Outlines of the pore in open and closed conformations describe the gating mechanism of ASIC1*. Nature communications, 2011. **2**: p. 399.
126. Car, R. and M. Parrinello, *Unified approach for molecular dynamics and density-functional theory*. Physical review letters, 1985. **55**(22): p. 2471.
127. Karplus, M. and J.A. McCammon, *Molecular dynamics simulations of biomolecules*. Nature Structural & Molecular Biology, 2002. **9**(9): p. 646-652.
128. Verlet, L., *Computer" experiments" on classical fluids. I. Thermodynamical properties of Lennard-Jones molecules*. Physical review, 1967. **159**(1): p. 98.
129. Allen, M.P. and D.J. Tildesley, *Computer simulation of liquids*. 1989: Oxford university press.
130. Frenkel, D. and B. Smit, *Understanding molecular simulation: from algorithms to applications*. Vol. 1. 2001: Academic press.

131. MacKerell Jr, A.D., et al., *All-atom empirical potential for molecular modeling and dynamics studies of proteins*. The journal of physical chemistry B, 1998. **102**(18): p. 3586-3616.
132. Oostenbrink, C., et al., *A biomolecular force field based on the free enthalpy of hydration and solvation: the GROMOS force-field parameter sets 53A5 and 53A6*. Journal of computational chemistry, 2004. **25**(13): p. 1656-1676.
133. Cornell, W.D., et al., *A second generation force field for the simulation of proteins, nucleic acids, and organic molecules*. Journal of the American Chemical Society, 1995. **117**(19): p. 5179-5197.
134. Shirley, W.A. and C.L. Brooks, *Curious structure in “canonical” alanine-based peptides*. Proteins: Structure, Function, and Bioinformatics, 1997. **28**(1): p. 59-71.
135. Beachy, M.D., et al., *Accurate ab initio quantum chemical determination of the relative energetics of peptide conformations and assessment of empirical force fields*. Journal of the American Chemical Society, 1997. **119**(25): p. 5908-5920.
136. Buck, M., et al., *Importance of the CMAP correction to the CHARMM22 protein force field: dynamics of hen lysozyme*. Biophysical journal, 2006. **90**(4): p. L36-L38.
137. Feig, M., A.D. MacKerell, and C.L. Brooks, *Force field influence on the observation of π -helical protein structures in molecular dynamics simulations*. The Journal of Physical Chemistry B, 2003. **107**(12): p. 2831-2836.
138. MacKerell, A.D., M. Feig, and C.L. Brooks, *Extending the treatment of backbone energetics in protein force fields: Limitations of gas-phase quantum mechanics in reproducing protein conformational distributions in molecular dynamics simulations*. Journal of computational chemistry, 2004. **25**(11): p. 1400-1415.
139. Mackerell, A.D., *Empirical force fields for biological macromolecules: overview and issues*. Journal of computational chemistry, 2004. **25**(13): p. 1584-1604.
140. Brooks, B.R., et al., *CHARMM: the biomolecular simulation program*. Journal of computational chemistry, 2009. **30**(10): p. 1545-1614.
141. Luo, Y. and B. Roux, *Simulation of osmotic pressure in concentrated aqueous salt solutions*. The Journal of Physical Chemistry Letters, 2009. **1**(1): p. 183-189.
142. Jorgensen, W.L., et al., *Comparison of simple potential functions for simulating liquid water*. The Journal of chemical physics, 1983. **79**(2): p. 926-935.

143. Berendsen, H.J., et al., *Interaction models for water in relation to protein hydration*, in *Intermolecular forces*. 1981, Springer. p. 331-342.
144. Mark, P. and L. Nilsson, *Structure and dynamics of the TIP3P, SPC, and SPC/E water models at 298 K*. The Journal of Physical Chemistry A, 2001. **105**(43): p. 9954-9960.
145. Franci, M.M., et al., *Self-consistent molecular orbital methods. XXIII. A polarization-type basis set for second-row elements*. The Journal of Chemical Physics, 1982. **77**(7): p. 3654-3665.
146. Becker, O.M., et al., *Computational biochemistry and biophysics*. 2001: CRC Press.
147. Yin, D. and A.D. MacKerell, *Combined ab initio/empirical approach for optimization of Lennard-Jones parameters*. Journal of Computational Chemistry, 1998. **19**(3): p. 334-348.
148. Isom, D.G., C.A. Castañeda, and B.R. Cannon, *Large shifts in pKa values of lysine residues buried inside a protein*. Proceedings of the National Academy of Sciences, 2011. **108**(13): p. 5260-5265.
149. Cymes, G.D., Y. Ni, and C. Grosman, *Probing the structure and electrostatics of ion-channel pores one proton at a time*. Nature, 2005. **438**(7070): p. 975.
150. Baker, C.M., V.M. Anisimov, and A.D. MacKerell Jr, *Development of CHARMM polarizable force field for nucleic acid bases based on the classical Drude oscillator model*. The journal of physical chemistry B, 2010. **115**(3): p. 580-596.
151. Ahlström, P., et al., *A molecular dynamics study of polarizable water*. Molecular Physics, 1989. **68**(3): p. 563-581.
152. Rick, S.W., S.J. Stuart, and B.J. Berne, *Dynamical fluctuating charge force fields: Application to liquid water*. The Journal of chemical physics, 1994. **101**(7): p. 6141-6156.
153. Drude, P., C. Riborg, and R.A. Millikan, *The Theory of Optics... Translated from the German by CR Mann and RA Millikan*. 1902: London; New York [printed].
154. Lemkul, J.A., et al., *An empirical polarizable force field based on the classical drude oscillator model: development history and recent applications*. Chemical reviews, 2016. **116**(9): p. 4983-5013.
155. Thole, B.T., *Molecular polarizabilities calculated with a modified dipole interaction*. Chemical Physics, 1981. **59**(3): p. 341-350.
156. Harder, E., et al., *Understanding the dielectric properties of liquid amides from a polarizable force field*. The journal of physical chemistry B, 2008. **112**(11): p. 3509-3521.

157. Lamoureux, G., et al., *A polarizable model of water for molecular dynamics simulations of biomolecules*. Chemical Physics Letters, 2006. **418**(1): p. 245-249.
158. Vanommeslaeghe, K. and A. MacKerell, *CHARMM additive and polarizable force fields for biophysics and computer-aided drug design*. Biochimica et Biophysica Acta (BBA)-General Subjects, 2015. **1850**(5): p. 861-871.
159. Jiang, W., et al., *High-performance scalable molecular dynamics simulations of a polarizable force field based on classical Drude oscillators in NAMD*. The journal of physical chemistry letters, 2010. **2**(2): p. 87-92.
160. Roux, B., et al., *Theoretical and computational models of biological ion channels*. Quarterly reviews of biophysics, 2004. **37**(1): p. 15-103.
161. Ewald, P.P., *Die Berechnung optischer und elektrostatischer Gitterpotentiale*. Annalen der Physik, 1921. **369**(3): p. 253-287.
162. Darden, T., D. York, and L. Pedersen, *Particle mesh Ewald: An $N \cdot \log(N)$ method for Ewald sums in large systems*. The Journal of chemical physics, 1993. **98**(12): p. 10089-10092.
163. Berendsen, H.J., et al., *Molecular dynamics with coupling to an external bath*. The Journal of chemical physics, 1984. **81**(8): p. 3684-3690.
164. Nosé, S., *A unified formulation of the constant temperature molecular dynamics methods*. The Journal of chemical physics, 1984. **81**(1): p. 511-519.
165. Hoover, W.G., *Canonical dynamics: equilibrium phase-space distributions*. Physical review A, 1985. **31**(3): p. 1695.
166. Andersen, H.C., *Molecular dynamics simulations at constant pressure and/or temperature*. The Journal of chemical physics, 1980. **72**(4): p. 2384-2393.
167. Martyna, G.J., D.J. Tobias, and M.L. Klein, *Constant pressure molecular dynamics algorithms*. The Journal of Chemical Physics, 1994. **101**(5): p. 4177-4189.
168. Quigley, D. and M. Probert, *Langevin dynamics in constant pressure extended systems*. The Journal of chemical physics, 2004. **120**(24): p. 11432-11441.
169. Feller, S.E., et al., *Constant pressure molecular dynamics simulation: the Langevin piston method*. The Journal of chemical physics, 1995. **103**(11): p. 4613-4621.
170. Trzesniak, D., A.P.E. Kunz, and W.F. van Gunsteren, *A comparison of methods to compute the potential of mean force*. ChemPhysChem, 2007. **8**(1): p. 162-169.

171. Torrie, G.M. and J.P. Valleau, *Nonphysical sampling distributions in Monte Carlo free-energy estimation: Umbrella sampling*. Journal of Computational Physics, 1977. **23**(2): p. 187-199.
172. Kumar, S., et al., *The weighted histogram analysis method for free-energy calculations on biomolecules. I. The method*. J Comput Chem, 1992. **13**(8): p. 1011-1021.
173. Roux, B., *The calculation of the potential of mean force using computer simulations*. Computer Physics Communications, 1995. **91**(1): p. 275-282.
174. Zwanzig, R.W., *High-temperature equation of state by a perturbation method. I. nonpolar gases*. The Journal of Chemical Physics, 1954. **22**(8): p. 1420-1426.
175. Pohorille, A., C. Jarzynski, and C. Chipot, *Good practices in free-energy calculations*. The Journal of Physical Chemistry B, 2010. **114**(32): p. 10235-10253.
176. Valleau, J. and S. Whittington, *A guide to Monte Carlo for statistical mechanics: 1. Highways*, in *Statistical mechanics*. 1977, Springer. p. 137-168.
177. Bennett, C.H., *Efficient estimation of free energy differences from Monte Carlo data*. Journal of Computational Physics, 1976. **22**(2): p. 245-268.
178. Åqvist, J., *Ion-water interaction potentials derived from free energy perturbation simulations*. Journal of Physical Chemistry, 1990. **94**(21): p. 8021-8024.
179. Beglov, D. and B. Roux, *Finite representation of an infinite bulk system: solvent boundary potential for computer simulations*. The Journal of chemical physics, 1994. **100**(12): p. 9050-9063.
180. Marchand, S. and B. Roux, *Molecular dynamics study of calbindin D9k in the apo and singly and doubly calcium-loaded states*. Proteins Structure Function and Genetics, 1998. **33**(2): p. 265-284.
181. Åqvist, J., *Ion-water interaction potentials derived from free energy perturbation simulations*. The Journal of Physical Chemistry, 1990. **94**(21): p. 8021-8024.
182. Jorgensen, W.L. and J. Tirado-Rives, *The OPLS [optimized potentials for liquid simulations] potential functions for proteins, energy minimizations for crystals of cyclic peptides and crambin*. Journal of the American Chemical Society, 1988. **110**(6): p. 1657-1666.
183. Roux, B., et al., *Ion selectivity in channels and transporters*. The Journal of general physiology, 2011. **137**(5): p. 415-426.
184. Becke, A.D., *Density-functional exchange-energy approximation with correct asymptotic behavior*. Physical review A, 1988. **38**(6): p. 3098.

185. Todorova, T., et al., *Molecular dynamics simulation of liquid water: hybrid density functionals*. The Journal of Physical Chemistry B, 2006. **110**(8): p. 3685-3691.
186. Silvestrelli, P.L. and M. Parrinello, *Water molecule dipole in the gas and in the liquid phase*. Physical Review Letters, 1999. **82**(16): p. 3308.
187. Schwegler, E., et al., *Towards an assessment of the accuracy of density functional theory for first principles simulations of water. II*. The Journal of chemical physics, 2004. **121**(11): p. 5400-5409.
188. Megyes, T., et al., *The structure of aqueous sodium hydroxide solutions: A combined solution x-ray diffraction and simulation study*. The Journal of chemical physics, 2008. **128**(4): p. 044501.
189. Bankura, A., V. Carnevale, and M.L. Klein, *Hydration structure of salt solutions from ab initio molecular dynamics*. The Journal of chemical physics, 2013. **138**(1): p. 014501.
190. Bucher, D., et al., *Coordination numbers of K⁺ and Na⁺ ions inside the selectivity filter of the KcsA potassium channel: Insights from first principles molecular dynamics*. Biophysical journal, 2010. **98**(10): p. L47-L49.
191. Timko, J., D. Bucher, and S. Kuyucak, *Dissociation of NaCl in water from ab initio molecular dynamics simulations*. The Journal of chemical physics, 2010. **132**(11): p. 114510.
192. Chung, S.-H. and S. Kuyucak, *Recent advances in ion channel research*. Biochimica et Biophysica Acta (BBA)-Biomembranes, 2002. **1565**(2): p. 267-286.
193. Venable, R.M., et al., *Simulations of anionic lipid membranes: Development of interaction-specific ion parameters and validation using NMR data*. The Journal of Physical Chemistry B, 2013. **117**(35): p. 10183-10192.
194. Noskov, S.Y. and B. Roux, *Control of ion selectivity in LeuT: two Na⁺ binding sites with two different mechanisms*. Journal of molecular biology, 2008. **377**(3): p. 804-818.
195. Yoo, J. and A. Aksimentiev, *Improved parametrization of Li⁺, Na⁺, K⁺, and Mg²⁺ ions for all-atom molecular dynamics simulations of nucleic acid systems*. The Journal of Physical Chemistry Letters, 2011. **3**(1): p. 45-50.
196. Marinelli, F., et al., *Sodium recognition by the Na⁺/Ca²⁺ exchanger in the outward-facing conformation*. Proceedings of the National Academy of Sciences, 2014. **111**(50): p. E5354-E5362.
197. Saxena, A. and D. Sept, *Multisite ion models that improve coordination and free energy calculations in molecular dynamics simulations*. Journal of chemical theory and computation, 2013. **9**(8): p. 3538-3542.

198. Warshel, A., M. Kato, and A.V. Pisliakov, *Polarizable force fields: history, test cases, and prospects*. Journal of Chemical Theory and Computation, 2007. **3**(6): p. 2034-2045.
199. Li, H., et al., *Representation of Ion-Protein Interactions using the Drude Polarizable Force-Field*. The Journal of Physical Chemistry B, 2015.
200. Van Eerden, J., et al., *Potential of mean force by thermodynamic integration: Molecular-dynamics simulation of decomplexation*. Chemical Physics Letters, 1989. **164**(4): p. 370-376.
201. Fournier, P., et al., *Experimental determination of aqueous sodium-acetate dissociation constants at temperatures from 20 to 240 C*. Chemical geology, 1998. **151**(1): p. 69-84.
202. Chialvo, A., et al., *Na⁺-Cl⁻ ion pair association in supercritical water*. The Journal of chemical physics, 1995. **103**(21): p. 9379-9387.
203. Andersen, H.C., *Rattle: A “velocity” version of the shake algorithm for molecular dynamics calculations*. Journal of Computational Physics, 1983. **52**(1): p. 24-34.
204. Darden, T., D. York, and L. Pedersen, *Particle mesh Ewald: An N-log(N) method for Ewald sums in large systems*. J Chem Phys, 1993. **98**: p. 10089.
205. Marx, D. and J. Hutter, *Ab initio molecular dynamics: basic theory and advanced methods*. 2009: Cambridge University Press.
206. Kleinman, L. and D. Bylander, *Efficacious form for model pseudopotentials*. Physical Review Letters, 1982. **48**(20): p. 1425.
207. Robinson, R.A. and R.H. Stokes, *Electrolyte solutions*. 2002: Courier Corporation.
208. Daniele, P.G., et al., *Weak alkali and alkaline earth metal complexes of low molecular weight ligands in aqueous solution*. Coordination Chemistry Reviews, 2008. **252**(10): p. 1093-1107.
209. England, S. and M.J. de Groot, *Subtype-selective targeting of voltage-gated sodium channels*. British journal of pharmacology, 2009. **158**(6): p. 1413-1425.
210. Lee, S., S.J. Goodchild, and C.A. Ahern, *Local anesthetic inhibition of a bacterial sodium channel*. The Journal of general physiology, 2012. **139**(6): p. 507-516.
211. Pavlov, E., et al., *The pore, not cytoplasmic domains, underlies inactivation in a prokaryotic sodium channel*. Biophysical journal, 2005. **89**(1): p. 232-242.
212. Bagnérис, C., et al., *Prokaryotic NavMs channel as a structural and functional model for eukaryotic sodium channel antagonism*. Proceedings of the National Academy of Sciences, 2014. **111**(23): p. 8428-8433.

213. Frank, H.Y. and W.A. Catterall, *Overview of the voltage-gated sodium channel family*. Genome biology, 2003. **4**(3): p. 207.
214. Catterall, W.A., et al., *International Union of Pharmacology. XLVIII. Nomenclature and structure-function relationships of voltage-gated calcium channels*. Pharmacological reviews, 2005. **57**(4): p. 411-425.
215. Ulmschneider, M.B., et al., *Molecular dynamics of ion transport through the open conformation of a bacterial voltage-gated sodium channel*. Proceedings of the National Academy of Sciences, 2013. **110**(16): p. 6364-6369.
216. Li, Y., et al., *Lysine and the Na+/K+ Selectivity in Mammalian Voltage-Gated Sodium Channels*. PloS one, 2016. **11**(9): p. e0162413.
217. Dudev, T. and C. Lim, *Factors governing the Na+ vs K+ selectivity in sodium ion channels*. Journal of the American Chemical Society, 2010. **132**(7): p. 2321-2332.
218. Roux, B., *Exploring the ion selectivity properties of a large number of simplified binding site models*. Biophysical journal, 2010. **98**(12): p. 2877-2885.
219. Kanai, R., et al., *Crystal structure of a Na+-bound Na+, K+-ATPase preceding the E1P state*. Nature, 2013. **502**(7470): p. 201.
220. Combs, S.A., et al., *Small-molecule ligand docking into comparative models with Rosetta*. Nature protocols, 2013. **8**(7): p. 1277-1298.
221. Klauda, J.B., et al., *Update of the CHARMM all-atom additive force field for lipids: validation on six lipid types*. The journal of physical chemistry B, 2010. **114**(23): p. 7830-7843.
222. Bernèche, S. and B. Roux, *A gate in the selectivity filter of potassium channels*. Structure, 2005. **13**(4): p. 591-600.
223. Phillips, J.C., et al., *Scalable molecular dynamics with NAMD*. Journal of computational chemistry, 2005. **26**(16): p. 1781-1802.
224. Shaw, D.E., et al. *Millisecond-scale molecular dynamics simulations on Anton*. in *High performance computing networking, storage and analysis, proceedings of the conference on*. 2009. IEEE.
225. Shaw, D.E., et al. *Anton 2: raising the bar for performance and programmability in a special-purpose molecular dynamics supercomputer*. in *Proceedings of the international conference for high performance computing, networking, storage and analysis*. 2014. IEEE Press.
226. Allen, T.W., O.S. Andersen, and B. Roux, *Molecular dynamics - potential of mean force calculations as a tool for understanding ion permeation and selectivity in narrow channels*. Biophys Chem, 2006. **124**(3): p. 251-67.

227. Shan, Y., et al., *Gaussian split Ewald: A fast Ewald mesh method for molecular simulation*. The Journal of chemical physics, 2005. **122**(5): p. 054101.
228. Kollman, P., *Free energy calculations: applications to chemical and biochemical phenomena*. Chemical reviews, 1993. **93**(7): p. 2395-2417.
229. Liu, P., et al., *A toolkit for the analysis of free-energy perturbation calculations*. Journal of chemical theory and computation, 2012. **8**(8): p. 2606-2616.
230. Aksimentiev, A. and K. Schulten, *Imaging α -hemolysin with molecular dynamics: ionic conductance, osmotic permeability, and the electrostatic potential map*. Biophysical journal, 2005. **88**(6): p. 3745-3761.
231. Cohen, J., et al., *Imaging the migration pathways for O₂, CO, NO, and Xe inside myoglobin*. Biophysical journal, 2006. **91**(5): p. 1844-1857.
232. Eisenman, G. and S. Krasne. *Further considerations on the ion selectivity of carrier molecules and membranes*. in *IV International Biophysics Congress Symposium on Membrane Structure and Function*, Moscow. 1973.
233. Dudev, T. and C. Lim, *Ion selectivity strategies of sodium channel selectivity filters*. Accounts of chemical research, 2014. **47**(12): p. 3580-3587.
234. Ahern, C.A., et al., *The hitchhiker's guide to the voltage-gated sodium channel galaxy*. The Journal of general physiology, 2016. **147**(1): p. 1-24.
235. Khan, A., et al., *Isoform-dependent interaction of voltage-gated sodium channels with protons*. The Journal of physiology, 2006. **576**(2): p. 493-501.
236. Radak, B.K., et al., *Constant-pH Molecular Dynamics Simulations for Large Biomolecular Systems*. Journal of chemical theory and computation, 2017. **13**(12): p. 5933-5944.
237. Kreple, C.J., et al., *Acid-sensing ion channels contribute to synaptic transmission and inhibit cocaine-evoked plasticity*. Nature neuroscience, 2014. **17**(8): p. 1083-1091.
238. Snyder, P.M., D.R. Olson, and D.B. Bucher, *A pore segment in DEG/ENaC Na⁺ channels*. Journal of Biological Chemistry, 1999. **274**(40): p. 28484-28490.
239. Mähler, J. and I. Persson, *A study of the hydration of the alkali metal ions in aqueous solution*. Inorganic Chemistry, 2011. **51**(1): p. 425-438.
240. Pfister, Y., et al., *A gating mutation in the internal pore of ASIC1a*. Journal of Biological Chemistry, 2006. **281**(17): p. 11787-11791.
241. Brooks, B.R., et al., *CHARMM: A program for macromolecular energy, minimization, and dynamics calculations*. Journal of computational chemistry, 1983. **4**(2): p. 187-217.

242. Davis, J.-H., *Deuterium magnetic resonance study of the gel and liquid crystalline phases of dipalmitoyl phosphatidylcholine*. Biophysical journal, 1979. **27**(3): p. 339-358.
243. Petersen, N.O., et al., *Thermal phase transitions in deuterated lecithin bilayers*. Chemistry and physics of lipids, 1975. **14**(4): p. 343-349.
244. Ryckaert, J.-P., G. Ciccotti, and H.J.C. Berendsen, *Numerical integration of the cartesian equations of motion of a system with constraints: molecular dynamics of n-alkanes*. J Comp Phys, 1977. **23**(3): p. 327-341.
245. Dougherty, D.A. and E.B. Van Arnam, *In Vivo Incorporation of Non-canonical Amino Acids by Using the Chemical Aminoacylation Strategy: A Broadly Applicable Mechanistic Tool*. ChemBioChem, 2014. **15**(12): p. 1710-1720.
246. Lu, T., et al., *Probing ion permeation and gating in a K⁺ channel with backbone mutations in the selectivity filter*. Nature neuroscience, 2001. **4**(3): p. 239-246.
247. Friedman, H. and C. Krishnan, *Water, a Comprehensive Treatise*/Ed. by F. 1973, Franks. NY: Plenum Press.
248. Gründer, S. and M. Pusch, *Biophysical properties of acid-sensing ion channels (ASICs)*. Neuropharmacology, 2015. **94**: p. 9-18.
249. Langloh, A.L.B., et al., *Charged residues in the M2 region of α-hENaC play a role in channel conductance*. American Journal of Physiology-Cell Physiology, 2000. **278**(2): p. C277-C291.
250. Sheng, S., et al., *Second transmembrane domains of ENaC subunits contribute to ion permeation and selectivity*. Journal of Biological Chemistry, 2001. **276**(47): p. 44091-44098.
251. Sather, W.A. and E.W. McCleskey, *Permeation and selectivity in calcium channels*. Annual review of physiology, 2003. **65**(1): p. 133-159.
252. Dang, T.X. and E.W. McCleskey, *Ion channel selectivity through stepwise changes in binding affinity*. The Journal of general physiology, 1998. **111**(2): p. 185-193.
253. Gadsby, D.C., *Ion channels versus ion pumps: the principal difference, in principle*. Nature reviews Molecular cell biology, 2009. **10**(5): p. 344-352.
254. Apell, H.-J. and S. Karlish, *Functional properties of Na⁺, K⁺-ATPase, and their structural implications, as detected with biophysical techniques*. The Journal of membrane biology, 2001. **180**(1): p. 1-9.
255. Morth, J.P., et al., *Crystal structure of the sodium–potassium pump*. Nature, 2007. **450**(7172): p. 1043-1049.
256. Toyoshima, C., R. Kanai, and F. Cornelius, *First crystal structures of Na⁺, K⁺-ATPase: new light on the oldest ion pump*. Structure, 2011. **19**(12): p. 1732-1738.

257. Yu, H., et al., *Protonation of key acidic residues is critical for the K+-selectivity of the Na/K pump*. Nature Structural and Molecular Biology, 2011. **18**(10): p. 1159.
258. Razavi, A.M., et al., *Molecular simulations and free-energy calculations suggest conformation-dependent anion binding to a cytoplasmic site as a mechanism for Na+/K+-ATPase ion selectivity*. Journal of Biological Chemistry, 2017. **292**(30): p. 12412-12423.
259. Munos, B., *Lessons from 60 years of pharmaceutical innovation*. Nature reviews Drug discovery, 2009. **8**(12): p. 959.
260. Okimoto, N., et al., *High-performance drug discovery: computational screening by combining docking and molecular dynamics simulations*. PLoS computational biology, 2009. **5**(10): p. e1000528.
261. Service, R.F., *Desalination freshens up*. Science (New York, NY), 2006. **313**(5790): p. 1088.
262. Konikow, L.F. and E. Kendy, *Groundwater depletion: A global problem*. Hydrogeology Journal, 2005. **13**(1): p. 317-320.
263. Thomas, M., et al., *Modeling Selective Transport and Desalination in Nanotubes*. Nanotubes and Nanosheets: Functionalization and Applications of Boron Nitride and Other Nanomaterials, 2015: p. 305.